

**A COMPUTATIONAL STUDY OF CORTICAL CYTOSKELETAL  
REMODELING DURING CELL MORPHOGENESIS**

by  
**Jing Li**

**A Dissertation**

*Submitted to the Faculty of Purdue University*

*In Partial Fulfillment of the Requirements for the degree of*

**Doctor of Philosophy**



Weldon School of Biomedical Engineering

West Lafayette, Indiana

December 2021

**THE PURDUE UNIVERSITY GRADUATE SCHOOL**  
**STATEMENT OF COMMITTEE APPROVAL**

**Dr. Tae Yoon Kim, Chair**

Weldon School of Biomedical Engineering

**Dr. David M. Umulis**

Weldon School of Biomedical Engineering

**Dr. Daniel B. Szymanski**

Department of Botany and Plant Pathology

**Dr. Daniel M. Suter**

Department of Biological Sciences

**Approved by:**

Dr. David M. Umulis

*Carpe Diem*  
*Practice makes perfect.*

## ACKNOWLEDGMENTS

I would like to sincerely thank my major advisor and principal investigator, Dr. Tae Yoon Kim, for the continued support and guidance during my Ph.D. study. His patience, professionalism, enthusiasm, and knowledge are second to none, which significantly helped my whole research progress. As an expert in coarse-grained and agent-based modeling, he spared no effort to ensure our continuous personal development in the quantitative biology field. He always inspired us to explore new research topics in cytoskeletal dynamics. In addition, I would also like to thank the members of my advisory committee, Dr. David Umulis, Dr. Daniel B. Szymanski, and Dr. Daniel Suter, for their time, talent, expertise, and professional guidance. I want to thank especially Dr. Szymanski for his professional support in leading the microtubule project.

I would like to express my sincere gratitude to my parents and family members, who have always provided fundamental support for my personal development.

I would also like to thank members of the Szymanski group: Dr. Samuel A. Belteton, Eileen L. Mallery and Thomas Davis. They provided me with countless support and stimulating discussion during the project. My sincere thanks also go to Dr. Joseph A. Turner and members of his research group at University of Nebraska, Lincoln: Dr. Wenlong Li, Sedighe Keynia, Faezeh Afshar, Dr. Anastasia S. Desyatova, for their advice and support.

I sincerely thank my fellow lab mates in the Kim group: Dr. Wonyeong Jung, Dr. Abdel-Rahman Hassan, Pei-En Chou, Qilin Yu, Brandon Slater, Thomas Biel for creating such an enlightening research environment.

Last but not least, I would like to thank all members of the Weldon School of Biomedical Engineering as well as the Purdue research community.



# TABLE OF CONTENTS

LIST OF TABLES .....	8
LIST OF FIGURES .....	9
LIST OF ABBREVIATIONS .....	15
ABSTRACT.....	16
1. INTRODUCTION .....	17
1.1 Morphogenesis: animal and plant cells .....	17
1.2 Importance of cortex during morphogenesis.....	18
1.2.1 Cell cortex in animal and plants .....	19
1.2.2 Cortical cytoskeletal remodeling during morphogenesis .....	19
1.3 Coarse-grained models of the cytoskeleton .....	21
1.3.1 Models of actin cytoskeleton.....	22
1.3.2 Models of cortical microtubules .....	27
1.4 Shortcomings of current models and hitherto unaddressed gap.....	29
1.5 Research goal and outline .....	31
2. MODULATION OF CONTRACTILE BEHAVIOR OF ACTOMYOSIN NETWORKS...	32
2.1 Introduction .....	32
2.2 Method .....	33
2.2.1 Model Overview .....	33
2.2.2 Dynamics of ACPs .....	35
2.2.3 Dynamics of motors .....	36
2.3 Buckling-induced severing regulates actomyosin contraction.....	36
2.3.1 Background .....	36
2.3.2 Additional method .....	37
2.3.3 Results .....	39
2.3.4 Conclusion and discussion .....	49
2.4 Pulsatile contraction of actomyosin network .....	50
2.4.1 Background .....	50
2.4.2 Additional method.....	52
2.4.3 Results .....	55

2.4.4	Conclusion and discussion .....	63
2.5	Contraction regulated by motility of molecular motors .....	67
2.5.1	Background .....	67
2.5.2	Additional method .....	69
2.5.3	Results .....	74
2.5.4	Conclusion and discussion .....	82
3.	A DISCRETE MODEL OF CORTICAL MICROTUBULE ARRAY .....	87
3.1	Introduction .....	87
3.1.1	Cortical microtubule patterning in plant cells .....	87
3.1.2	Patterning of microtubule in response to mechanical stress.....	88
3.2	Method .....	91
3.2.1	Model overview .....	91
3.2.2	Constitutive equation for stress sensing .....	93
3.2.3	Simulation algorithm.....	94
3.2.4	Quantification of self-organization .....	94
3.2.5	Microscopic imaging .....	95
3.3	Stress pattern is potent to reorganize cortical microtubules.....	95
3.3.1	Sensitivity of stochastic parameter to mechanical cues .....	96
3.3.2	Stress reorientation leads to CMT reorganization .....	100
3.3.3	Stress gradient potentially generate organized microtubule arrays.....	102
3.4	Branched nucleation determines CMT array bundling .....	108
3.4.1	Background .....	108
3.4.2	Additional method: Nucleation and severing dynamics.....	108
3.4.3	Additional method: Quantitative analysis of bundling.....	110
3.4.4	Branched and parallel nucleation lead to differentiated bundle morphology. ....	110
3.4.5	Nucleation angle couples with zippering angle for bundle formation .....	114
3.4.6	Severing act as a potential mechanism to facilitate bundle morphology .....	115
3.5	Conclusion and Discussion .....	116
4.	CONCLUSION AND OUTLOOK.....	119
4.1	Summary .....	119
4.2	Future directions.....	120

4.2.1 Actomyosin contractility .....	120
4.2.2 Cortical microtubule patterning.....	121
A. MATRIX-CELL REMODELING .....	123
B. SEVERING AND MODEL PARAMETER .....	135
C. EFFECT OF ENCOUNTER BASED CATASTROPHE .....	138
REFERENCES .....	140
VITA.....	160
PUBLICATIONS.....	161

## LIST OF TABLES

Table 1.1 The structural and mechanical properties of F-actin and microtubules in the cytoskeleton. ....	20
Table 1.2 Properties of two general actin filament models including FJC and WLC models. ....	22
Table 3.1 List of microtubule dynamic parameters in the simulation for three-state models. ....	96
Table 3.2 Average microtubule lifetime and length under various stress conditions. ....	99
Table B.1 List of parameters employed in the model. For some of the parameters, references are provided if the parameters were determined based on specific previous studies. ....	136
Table B.2 List of parameter values used for adopting “parallel cluster model” [118, 119]. Note that we used slightly different values for $F_0$ , $d$ , and $k_m$ from those in the literature. ....	137
Table B.3 Stochastic and deterministic event parameters in addition to dynamic instability ....	137

## LIST OF FIGURES

Fig. 1.1 Various cell morphologies in animal and plants. From left to right: Lamellipodia, filopodia, leaf pavement cell, leaf epidermal trichome cell. Adapted from [7-9].	18
Fig. 1.2 Schematic of cortical microtubules anchored to plasma membrane in plant cells. Molecular and protofilament structure of microtubules are included. Adapted from [213].	24
Fig. 2.1 Contraction of actomyosin networks is investigated using an agent-based computational model. (a) Schematic diagram showing a circular network consisting of actin filaments (F-actin, cyan), actin crosslinking proteins (yellow), and motors (red). The three constituents are simplified via cylindrical segments. (b) Morphology of networks at $t = 0, 100$ , and $200$ s during contraction. Densities of motors and ACPs are $0.08$ and $0.04$ , respectively.	38
Fig. 2.2 Network contraction is regulated by densities of motors ( $R_M$ ) and ACPs ( $R_{ACP}$ ). Contraction was evaluated under various $R_M$ and $R_{ACP}$ . (a) Network morphology with actins and motors represented by blue and red, respectively. Note that motors can aggregate very tightly due to the absence of a volume-exclusion effect between them. (b) Time evolution of the extent of contraction ( $\xi$ ) for four different cases. (c) $\xi$ measured at a steady state ( $\xi_{ss}$ ). Large network contraction occurs above critical $R_M$ with intermediate $R_{ACP}$ .	41
Fig. 2.3 Bending stiffness ( $\kappa_{b,A}$ ) and length ( $\langle L_f \rangle$ ) of actin filaments modulate network contraction. (a) When $\langle L_f \rangle$ is reduced from $2.53 \mu m$ to $1.74 \mu m$ , critical levels of $R_{ACP}$ above which large contraction occurs are higher (c.f. Fig. 2.2c) because more ACPs are needed for the minimal network connectivity if the network has lower connectivity due to shorter actin filaments. (b) When $\kappa_{b,A}$ is increased 16-fold, the transition of contraction on the left still occurs at $R_{ACP} \sim 0.0025$ - $0.005$ . By contrast, the transition on the right takes place at lower $R_{ACP}$ (c.f. Fig. 2.2c) because buckling of actin filaments requires a larger amount of forces (i.e. higher $R_M$ ) at each $R_{ACP}$ . In (a-b), for comparison, red dashed lines indicate a regime where large network contraction emerges in Fig. 2.2c.	42
Fig. 2.4 If filaments can be severed due to buckling, intermediate bending rigidity can lead to the largest network contraction. We evaluated network contraction with diverse bending stiffness of filaments ( $\kappa_{b,A}$ ) and zero-angle severing rate constant ( $k_{s,A}^0$ ) at $R_M = 0.08$ and $R_{ACP} = 0.02$ . (a) Morphology of networks with actins and motors represented by blue and red, respectively. (b) Frequency of filament severing. (c) Number of foci measured at a steady state. (d) $\xi_{ss}$ evaluated at a steady state. If $\kappa_{b,A}$ is very high, buckling is inhibited, leading to small contraction and formation of motor foci and aster-like actin structures. Higher $k_{s,A}^0$ and lower $\kappa_{b,A}$ result in formation of multiple foci with small contraction because filament severing occurs very frequently under such conditions, severely deteriorating network connectivity. Thus, optimal intermediate $\kappa_{b,A}$ exists at high $k_{s,A}^0$ .	44
Fig. 2.5 The optimal intermediate bending rigidity is more apparent in loosely cross-linked networks. We probed network contraction over a wide range of $R_{ACP}$ and $\kappa_{b,A}$ with $k_{s,A}^0 = 10^{-30} s^{-1}$ and $R_M = 0.08$ . Here, the range of $R_{ACP}$ is narrowed to $0.005$ - $0.08$ to consider only a regime where significant network contraction appears without F-actin severing in Fig. 2c. (a) Network morphology showing actins (blue) and motors (red). (b) Frequency of filament severing. (c)	

Number of foci evaluated at a steady state. (d)  $\xi_{ss}$  measured at a steady state. If  $R_{ACP}$  is smaller, the range of  $\kappa_{b,A}$  leading to large contraction becomes narrower. By contrast, if  $R_{ACP}$  is sufficiently high, networks contract to a single focus regardless of  $\kappa_{b,A}$  despite much more frequent severing events because enhancement of network connectivity resulting from more ACPs is superior to deterioration of connectivity induced by F-actin severing during contraction. .... 46

Fig. 2.6 With more motors, the optimal intermediate bending rigidity is more conspicuous. Network contraction was measured over a wide range of  $R_M$  and  $\kappa_{b,A}$  with  $k_{s,A}^0 = 10^{-30} \text{ s}^{-1}$  and  $R_{ACP} = 0.02$ . (a) Morphology of networks with actins (blue) and motors (red). (b) Frequency of filament severing. (c) Number of foci measured at a steady state. (d)  $\xi_{ss}$  at a steady state. If there are a larger number of motors, more filaments are buckled and severed during contraction because larger compressive forces are exerted on filaments. Since  $R_{ACP}$  is constant in all cases, networks experiencing more severing events have poorer connectivity. Thus, an increase in  $R_M$  leads to formation of multiple foci and small contraction at low  $\kappa_{b,A}$  and low contraction at high  $\kappa_{b,A}$ , making the optimal intermediate  $\kappa_{b,A}$  more apparent..... 47

Fig. 2.7 Time required for reaching the steady state of contraction ( $\tau_{ss}$ ) and average contraction rate which corresponds to  $\xi_{ss} / \tau_{ss}$ , at various  $k_{s,A}^0$  and  $\kappa_{b,A}$  . .... 48

Fig. 2.8  $\tau_{ss}$  and average contraction rate over a wide range of  $R_{ACP}$  and  $\kappa_{b,A}$  . .... 48

Fig. 2.9  $\tau_{ss}$  and average contraction rate at various  $R_M$  and  $\kappa_{b,A}$  ..... 48

Fig. 2.10 Actomyosin networks contract to either of three possible states depending on bending stiffness of F-actin ( $\kappa_{b,A}$ ), zero-angle severing rate constant ( $k_{s,A}^0$ ), ACP density ( $R_{ACP}$ ), and motor density ( $R_M$ ). (a) The three possible states are i) small contraction with a single focus (left), ii) large contraction with a single focus (middle), and iii) small contraction with multiple foci (right). (b) Three-dimensional phase diagram showing regimes for the three states..... 49

Fig. 2.11 Network contraction is regulated by F-actin turnover. We varied actin turnover rate ( $k_{t,A}$ ) between  $15 \text{ s}^{-1}$  and  $240 \text{ s}^{-1}$  at  $R_M = 0.04$ ,  $R_{ACP} = 0.02$ , and  $\langle L_f \rangle = 1.6 \text{ }\mu\text{m}$ . (a) Morphology of networks at 65 s with four different  $k_{t,A}$ . (b) Heterogeneity of F-actin distribution (blue circle) and  $\langle \cos \phi \rangle$  indicating persistency of motor velocities between 10 s and 20 s (red triangle) depending on  $k_{t,A}$ . The heterogeneity monotonically decreases as  $k_{t,A}$  increases. At low  $k_{t,A}$ , motors tend to move persistently over time, but as  $k_{t,A}$  increases, motors exhibit less persistent motions because F-actins undergo rapid turnover without formation of large clusters. (c) Average speed of motors at early times (0-10 s, blue square) and late times (from 50 s till end, red triangle) as a function of  $k_{t,A}$ . While the average speed hardly changes at high  $k_{t,A}$ , it is significantly reduced over time at low  $k_{t,A}$ . .... 56

Fig. 2.12 ACPs regulate contractile behaviors of networks. We changed ACP density ( $R_{ACP}$ ) between 0.0025 and 0.16 at  $R_M = 0.04$ ,  $\langle L_f \rangle = 1.6 \text{ }\mu\text{m}$ , and  $k_{t,A} = 30 \text{ s}^{-1}$ . (a) Morphology of networks at 65 s depending on  $R_{ACP}$ . (b) Heterogeneity and persistency of motor velocities. (c) Average speed of motors at early and late times. .... 58

Fig. 2.13 Average length of F-actins ( $\langle L_f \rangle$ ) highly affects network contraction in a similar fashion to  $R_{ACP}$ . We varied  $\langle L_f \rangle$  between  $0.7 \text{ }\mu\text{m}$  and  $5.0 \text{ }\mu\text{m}$  at  $R_M = 0.04$ ,  $R_{ACP} = 0.02$ , and  $k_{t,A} = 30 \text{ s}^{-1}$ . (a) Morphology of networks at 65 s depending on  $R_{ACP}$ . (b) Heterogeneity and persistency of motor velocities. (c) Average speed of motors at early and late times..... 58

Fig. 2.14 Balance between force generation and relaxation causes weak pulsatile contraction with formation of very small clusters. Conditions used in a case shown here are  $R_M = 0.04$ ,  $R_{ACP} = 0.01$ ,  $\langle L_f \rangle = 1 \mu\text{m}$ , and  $k_{t,A} = 70 \text{ s}^{-1}$ . (a) Morphology of networks showing cluster formation taken at different time points. (b) Time evolution of a small pulsed cluster indicated by a blue box in (a). This cluster appears from  $\sim 30 \text{ s}$  and then becomes the largest at  $41 \text{ s}$  as indicated by a white arrow. Then, it disassembles gradually over time. (c) Time evolution of a fluctuating cluster highlighted by a red box in (a). (d) Time evolution of the percentage of actin segments located within clusters. Random colors are assigned to curves to distinguish each cluster. Nascent pulsed clusters are shown in solid lines, whereas fluctuating clusters are shown in dot-dashed lines. (e, f) Frequency of appearance of pulsed clusters per 100 s depending on their size (e) and duration (f). Most clusters are very small and do not last for long time periods. .... 60

Fig. 2.15 Severing of F-actin facilitates strong pulsed contraction via selective force relaxation within clusters. We varied the zero-angle severing rate constant ( $k_{s,A}^0$ ) between  $10^{-60} \text{ s}^{-1}$  and  $10^{-10} \text{ s}^{-1}$  at  $R_M = 0.04$ ,  $R_{ACP} = 0.02$ ,  $\langle L_f \rangle = 1 \mu\text{m}$ ,  $k_{t,A} = 30 \text{ s}^{-1}$ , and  $\lambda_{s,A} = 1.6 \text{ deg}$ . (a) Morphology of networks with various  $k_{s,A}^0$ . As  $k_{s,A}^0$  increases, clusters become apparently smaller. (b) Time evolution of a relatively large pulsed cluster. The cluster appears at  $\sim 5 \text{ s}$  and becomes the largest at  $13 \text{ s}$  as marked by a white arrow. Then, it disassembles completely at  $\sim 100 \text{ s}$ . (c) Frequency of appearance of pulsed clusters per 100 s (blue circle) and percentage of severing events occurring within pulsed clusters (red triangle) depending on  $k_{s,A}^0$ . As  $k_{s,A}^0$  increases, more pulsed clusters appear, and more severing events take place outside the pulsed clusters. However, few pulsed clusters are formed if  $k_{s,A}^0$  is too high. (d) Distribution of size of pulsed clusters depending on  $k_{s,A}^0$ . With lower  $k_{s,A}^0$ , larger pulsed clusters are more likely to emerge. (e) Average duration (blue circle) and size (red triangle) of the largest pulsed clusters found from each of 5 simulations with different  $k_{s,A}^0$ . With lower  $k_{s,A}^0$ , more larger clusters appear and last longer before complete disassembly. . 62

Fig. 2.16 Dependence of the severing rate on a bending angle regulates the pulsed contraction. We modulated insensitivity of the severing rate to a bending angle ( $\lambda_{s,A}$ ) at  $R_M = 0.04$ ,  $R_{ACP} = 0.02$ ,  $\langle L_f \rangle = 1 \mu\text{m}$ ,  $k_{t,A} = 30 \text{ s}^{-1}$ , and  $k_{s,A}^0 = 10^{-30} \text{ s}^{-1}$ . Severing takes place at larger bending angles if  $\lambda_{s,A}$  is larger. (a) Morphology of networks with various  $\lambda_{s,A}$ . With higher  $\lambda_{s,A}$ , more large pulsed clusters emerge. (b) Frequency of appearance of pulsed clusters per 100 s (blue circle) and percentage of severing events occurring within pulsed clusters (red triangle) depending on  $\lambda_{s,A}$ . Although relatively the same number of clusters are formed regardless of  $\lambda_{s,A}$ , more severing events take place within clusters as  $\lambda_{s,A}$  increases. (c) Distribution of size of pulsed clusters with different  $\lambda_{s,A}$ . With larger  $\lambda_{s,A}$ , there are a greater number of large pulsed clusters although small pulsed clusters appear at a similar frequency. (d) Average duration (blue circle) and size (red triangle) of the largest pulsed clusters found from each of 5 simulations depending on  $\lambda_{s,A}$ . With larger  $\lambda_{s,A}$ , there are more larger clusters, and they last longer. .... 64

Fig. 2.17 The parallel cluster model (PCM). (a) Myosin motor cycle assumed in the PCM. Three mechanochemical rates were defined, and there are 5 transition rates between the states. In this study, we varied only the value of  $k_{20}$ . (b, c) Force-dependent walking ( $k_{w,M}$ ) and unbinding rate ( $k_{u,M}$ ) of a motor arm calculated by the PCM for various ATP-dependent unbinding rates ( $k_{20}$ ) and two different numbers of myosin heads represented by one motor arm ( $N_h$ ). .... 72

Fig. 2.18 Effects of mobility of motors and mechanochemical rate with one-arm motors. (a) Average tensile force exerted by motor arms, (b) fraction of motors bound to F-actins, (c) average

speed of F-actin, and (d) heterogeneity of F-actin spatial distribution. ATP-dependent unbinding rate of myosin heads ( $k_{20}$ ) and motor mobility modulated by the drag coefficient of motors ( $\zeta_M$ ). Forces exerted by motor arms and the average speed of F-actins are larger at higher  $\zeta_M$  and intermediate levels of  $k_{20}$ . More motors are bound to F-actins with smaller  $\zeta_M$  and  $k_{20}$ . Distribution of F-actins is the most heterogeneous at intermediate levels of  $\zeta_M$  and  $k_{20}$ .  $\zeta_M^* = 8.10 \times 10^{-8}$  kg/s and  $k_{20}^* = 20$  s<sup>-1</sup> are reference values of  $\zeta_M$  and  $k_{20}$ , respectively..... 76

Fig. 2.19 Morphology of networks with one-arm motors depend on mobility of motors and mechanochemical rate. Network morphology measured in all cases at a last time point where steady state is reached,  $t = 100$  s, with various ATP-dependent unbinding rate of myosin heads ( $k_{20}$ ) and motor mobility modulated by the drag coefficient of motors ( $\zeta_M$ ). F-actins, ACPs, and motors are visualized by cyan, yellow, and red, respectively.  $\zeta_M^* = 8.10 \times 10^{-8}$  kg/s and  $k_{20}^* = 20$  s<sup>-1</sup> are reference values of  $\zeta_M$  and  $k_{20}$ , respectively..... 78

Fig. 2.20 Impacts of motor mobility and mechanochemical rate on network contraction with two-arm motors. (a) Average tensile force exerted by motor arms, (b) fraction of motors bound to F-actins, (c) Average speed of F-actin, and (d) heterogeneity of F-actin spatial distribution, with various ATP-dependent unbinding rate of myosin heads ( $k_{20}$ ) and motor mobility modulated by the drag coefficient of motors ( $\zeta_M$ ). In (a-b), the left, center, and right plots correspond to motors bound to one F-actin, motors bound to relatively parallel F-actins, and motors bound to relatively parallel F-actins, respectively. Average force exerted by two-arm motors bound to parallel F-actins shows weak dependence on  $\zeta_M$ , and the number of those motors increases as  $\zeta_M$  decreases. Thus, the total forces exerted by all motors are higher with lower  $\zeta_M$ . F-actins move faster, and the distribution of F-actins is much more heterogeneous with lower  $\zeta_M$ .  $\zeta_M^* = 8.10 \times 10^{-8}$  kg/s and  $k_{20}^* = 20$  s<sup>-1</sup> are reference values of  $\zeta_M$  and  $k_{20}$ , respectively..... 80

Fig. 2.21 Morphology of networks with two-arm motors depending on the mobility and mechanochemical rate of motors. Network morphology measured in all cases at a last time point where steady state is reached,  $t = 100$  s, at wide ranges of ATP-dependent unbinding rate of myosin heads ( $k_{20}$ ) and motor mobility modulated by the drag coefficient ( $\zeta_M$ ). F-actins, ACPs, and motors are visualized by cyan, yellow, and red, respectively.  $\zeta_M^* = 8.10 \times 10^{-8}$  kg/s and  $k_{20}^* = 20$  s<sup>-1</sup> are reference values of  $\zeta_M$  and  $k_{20}$ , respectively. .... 81

Fig. 2.22 Schematic diagrams summarizing results. (a, b) Comparison between one-arm motor and two-arm motor. Since one-arm motors can bind to only one F-actin, they rely much on resistance originating from drag force ( $F_d$ ) when they pull F-actin. For example, one-arm motors with a higher drag coefficient ( $\zeta_M$ ) feel a larger drag force when they try to move. Thus, they have less mobility, enabling them to exert a larger force on F-actin. If two-arm motors pull two F-actins in relatively opposite directions, they do not need to rely on  $F_d$ . (c, d) Initial state (top) and final states of networks (the rest) with one-arm motors or two-arm motors with different  $\zeta_M$ . Note that all two-arm motors in the diagram are initially located in anti-parallel F-actins to show a case opposite to that with one-arm motors. In (c, d), it is assumed that a periodic boundary condition exists on the left and right boundaries. .... 84



Fig. 3.1 Model schematic and microtubule dynamics. (a and b) Schematic of MT dynamics, including stochastic events and angle-dependent collision/deterministic events. (a) Stochastic events include polymerization ( $v_{p+}$ ) and depolymerization ( $v_{d+}$ ) at the plus end and constant slow depolymerization ( $v_{d-}$ ) at the minus end, rescue and catastrophe. (b) Angle-dependent collision-based events of MTs include zippering at a shallow angle ( $<40^\circ$ ) and catastrophe or crossover beyond a critical angle ( $>40^\circ$ ). (c) Mathematical relationship between local principal stress and stress acting on individual microtubules depending on their angle of orientation. (d) MT simulation domain is a  $10 \times 10 \mu\text{m}$  (initial domain size) square network with periodic boundary conditions in both x and y directions. MTs in the simulation domain are composed of serially connected small segments representing tubulin monomers, as shown in green. .... 92

Fig. 3.2 Simulation flowchart. Stochastic and deterministic event with separate timesteps. .... 94

Fig. 3.3 Anisotropic stress affects self-organization of microtubules and correlates with global orientation. (A and B) Steady state MT network morphology. All snapshots are taken at 100 min. MTs are subject to network stress predominant in y direction (right), isotropic (left). In A and B, polymerization rate is enhanced, and catastrophe frequency is reduced in alignment with principal stress, respectively. (C) A representative case with the time evolution of the network order parameter  $S_p$ . The first time constant is calculated as the time required to reach half of the  $S_p$  value at steady state. (D) Summary of the network order parameter  $S_p$  at 100 min for all different conditions with isotropic vs. anisotropic stress in which principal stress influences individual stochastic parameter independently. (E) Boxplot of the time constants acquired from cases with isotropic vs. anisotropic stress in all conditions. Data for each condition are averaged over 20 simulations in each case. P: polymerization, D: depolymerization, C: catastrophe, R: rescue; ns  $p>0.05$ , \*  $p<0.05$ , \*\*  $p<0.01$ , \*\*\*  $p<0.001$ , \*\*\*\*  $p<0.0001$ . .... 98

Fig. 3.4 Order parameter and first time constant with different stress anisotropy ratios. .... 99

Fig. 3.5 Dynamic stress pattern reorientation leads to remodeling of the microtubule network. (A and B) Time evolution of the MT network morphology (at various timepoints including 25, 100, 105, 150, 250 min for a rapid transition and 100, 215, 225, 250, 350 min for a gradual transition). Grey dashed line indicates the timepoint (100 min) after which reorientation of anisotropic stress takes place. The blue dash line indicates the timepoint after which anisotropic stress is stabilized. Initial network stress pattern is predominant in y direction. In A, stress pattern reorients instantaneously and becomes predominant in x direction after 100 min. In B, stress pattern gradually reorients until 250 min and becomes steady afterwards. (C and D) Relative frequency showing the distribution of microtubule orientation angle at various timepoints during stress pattern reorientation in A and B respectively. 90 degree is equivalent to the direction parallel to y axis, and 0 or 180 degree is equivalent to the direction parallel to x axis. A flat curve indicates homogeneous distribution of MT orientation angles. (E, F) Time evolution of the network order parameter  $S_{p,y}$  (E) and network microtubule segment densities (F) in four cases: rapid transition (as indicated in A, blue), gradual transition of stress (150 min, as indicated in B, red; 100 min, black; 50 min, cyan). .... 101

Fig. 3.6 (a) Schematic of the stress pattern gradient pertinent to a finite element model of trichome morphogenesis. Magnitude of stress decreases from left to right, along the direction parallel to cell long axis while the stress is highly anisotropic and predominant in the transverse direction, indicated by the ellipses. The lower panels show an unfolded stress pattern based on the model results. The unfolded meshed stress pattern is mapped onto the simulation domain. (b)

Representative confocal image showing microtubule localization in stage 4 young trichome branches (left panel). Transverse band is prominent near the cell apex. The microtubule depleted zone (MDZ) is highlighted and marked in yellow. Scale bar: 10  $\mu\text{m}$ . Right panel shows the intensity profile from the apex to the base in the image shown in the left panel along the yellow line..... 103

Fig. 3.7 Different types of boundary conditions imposed in the simulation..... 105

Fig. 3.8 Order parameter (a) and local intensity (b) of the network under various conditions: stress free control and isotropic stress. Boundary conditions include catastrophe inducing boundary (CIB) and periodic boundary (PB). ..... 105

Fig. 3.9 A catastrophe-inducing boundary condition is implemented on the two short edges of the simulation domain (30  $\mu\text{m}$  x 10  $\mu\text{m}$ ). (a, e, i) Early-time (20 min) and (b, f, j) steady-state (100 min) morphology of network in stress free (a, b), stress gradient (e, f), and stress gradient with isotropic stress in the tip zone (i, j, 2 $\mu\text{m}$  tip zone marked by black bar). (c, g, k) Local order parameter of microtubules in subregions of cases in b, f, j respectively. For this, the network was divided into fifteen subregions, incrementally separated by 2 $\mu\text{m}$  along the x direction. Blue curve indicates and shaded region represents standard deviation (n=10). (d, h, l) Normalized intensity of MT segments (tubulin dimers) as a function of the distance from the tip (left boundary), which is nearest to apex of a real cell..... 106

Fig. 3.10 Distance of peak microtubule dimer intensity from the tip under various conditions. 107

Fig. 3.11 Stress profile from the FEM model. (a) Paired values of longitudinal and transverse stress in the apex of trichome model. Color indicates the distance from apex. (b) Distribution of the stress anisotropy ratio in the tip zone (blue) and flank region (orange). Stress is isotropic in the tip zone while anisotropic in the flank region, as implemented in our simulations. .... 107

Fig. 3.12 Schematic for (a) isotropic nucleation (stochastic), (b) branched nucleation and (c) severing at crossover sites of MTs..... 109

Fig. 3.13 Steady state network morphology at various combinations of probability of branched nucleation and branching nucleation angle..... 112

Fig. 3.14 Skewness of microtubule bundles as a function of branched nucleation angle under cases with various probabilities of branched nucleation. .... 113

Fig. 3.15 Heatmaps showing the average length, lifetime of microtubules and steady state order parameter of the cortical array, under various combination of probability of branched nucleation and branched nucleation angle..... 113

Fig. 3.16 Heatmaps showing the average length, lifetime of microtubules and steady state order parameter of the cortical array, under various combination of branched nucleation angle and zippering threshold angle..... 115

Fig. 3.17 Skewness of microtubule bundles in severing free condition, with stochastic and crossover site severing conditions. The heatmap shows dependence on the parametric space of probability of branched nucleation and branched nucleation angle..... 116

## LIST OF ABBREVIATIONS

2D	Two-Dimensional
3D	Three-Dimensional
MD	Molecular Dynamics
BD	Brownian Dynamics
ACP	Actin Crosslinking Protein
G-actin	Globular actin
F-actin	Filamentous actin
MT	Microtubule
MF	Microfibril
CMT	Cortical Microtubule
CMF	Cellulose Microfibril
CESA	Cellulose Synthase
MDZ	Microtubule Depleted Zone
ECM	Extracellular Matrix
ITZ	Isotropic Tip Zone
CIB	Catastrophe-Inducing Boundary
PBC	Periodic Boundary Conditions
FEM	Finite Element Model
MBD	Microtubule Binding Domain
ROP	Rho-of-plants
DAG	Days After Germination
CLASP	Cytoplasmic Linker Associated Protein

## ABSTRACT

During development in both animals and plants, cell morphogenesis is fundamental to various aspects of cellular functions, including contractility, motility, and their ability to respond to physiological and mechanical stimuli. The cell cortex, consisting of actin and microtubule cytoskeletons, plays a critical role in the spatiotemporal regulation of cell morphogenesis. Remodeling of the cytoskeleton is responsible for a large fraction of morphogenetic processes. However, due to experimental limitations, the underlying mechanism of the remodeling of the cortical cytoskeleton remains elusive. These limitations can be overcome by computational models. We computationally investigated two systems: the actin cytoskeleton in animal cells and cortical microtubule arrays in plant cells. For the actin cytoskeleton, we implemented a well-established agent-based model consisting of inter-connected cylindrical segments representing actin filaments, actin crosslinking proteins, and molecular motors. We found that the active remodeling of actin networks is regulated by network connectivity as well as the dynamic behaviors of crosslinking proteins and motors. In addition, we demonstrated that the fragmentation (i.e., severing) and turnover of actin filaments mediate various clustering behaviors due to a balance between force generation and force relaxation. For microtubule arrays, we developed a coarse-grained model of microtubules based on the Gillespie algorithm. Using the model, we studied the self-organization of the cortical microtubule arrays in response to tensile stress. By implementing a cellular stress pattern and a constitutive relationship between stress and plus-end dynamics of microtubules, we were able to identify the most sensitive parameters that constitute dynamic instability and recapitulate a distinct morphological transverse band. We further validated the importance of branched nucleation and severing during bundle formation and network evolution. Overall, our results regarding the two cytoskeleton systems provide insights into understanding the precise control of cytoskeletal remodeling at subcellular scales as well as integrative molecular mechanisms underlying cell morphogenesis.

# 1. INTRODUCTION

## 1.1 Morphogenesis: animal and plant cells

Morphogenesis is a ubiquitous feature of both animal and plant, which requires tight coordination between differentiation and growth. Morphogenesis is fundamental property of biological systems from cells, tissues to organisms [1, 2]. Narrowing down the scope to cell biology, individual cells are yet fully capable of developing numerous complex structures from a rather simple initial form during cell growth. Cell growth is also a well-coordinated process in animal and plant kingdoms, which involves increase in cell size and numbers during the typical life span of an organism [3, 4]. Cell growth is responsible for crucial consequences in a developing organism's ability to adapt to diverse living environment during evolution. In the cell cycle, mitosis is a universal characteristic shared by all animal and plant cells. However, plant growth and development are mainly driven by multiple extended phases of cell expansion. Plant cell expansion is irreversible and usually results in 10- to 100-fold of volume expansion [5]. As such, the distinctive feature of plant cell growth is marked by extensive increase in cell size unaccompanied by cell division, while animal cell growth is intrinsically subjected to time and size constraints, accompanied by cell movement [6]. The distinct growth mode leads to numerous cell morphologies such as the finger-like protrusion named as filopodia and sheet-like lamellipodia [7], or the zig-zag shaped pavement cells [8] and leaf epidermal trichome with three symmetric branches in plants [9] (Fig. 1.1).

Morphogenesis is a key determinant of cell and tissue shape. In animals, the dramatic change in the three-dimensional (3D) structure of cell and tissue is the prerequisite for embryonic development: a process called gastrulation or gut formation. Gastrulation is marked by folding and inward movement of the cell outside the embryo [10]. This morphogenetic invagination requires precisely timed interactions between embryonic cells. Another striking example of morphogenesis is the formation of lamellipodia during collective cell migration *in vivo*. The formation of lamellipodia is characterized by a continuous rim of sheet-like membrane protrusions as it drives forwards the leading edge of motile cells such as epithelial cell and neurons [7, 11]. This sheet-like transient structure bridges multiple cell bodies to facilitate the propagation of mechanotransduction during collective cell migration.

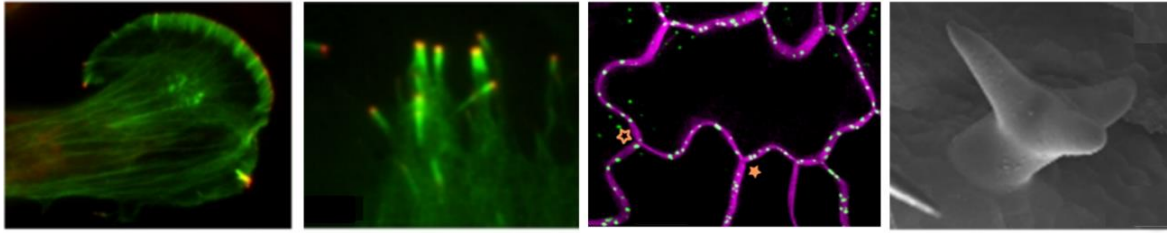


Fig. 1.1 Various cell morphologies in animal and plants. From left to right: Lamellipodia, filopodia in B16F1 mouse melanoma cells, leaf pavement cell, leaf epidermal trichome cell. Adapted from [7-9].

In plants, morphogenesis is driven by the biomechanical properties of cells, tissues, and organs. As sessile organisms, their form arises from a fixed location where the seed germinates, and the root and shoot develop in opposite directions. Plants grow rapidly and move through space, but the movement and development are not driven by the migration of individual cells or groups of cells relative to one another. Instead, meristems generate groups of progenitor cells that are progressively displaced from the meristematic zone as they divide and grow. Growth is symplastic (no cell movements or new contacts) since they expand as groups of cells that are mechanically coupled to their neighbors through a pectin-rich middle lamella. In elongating roots and stems, the coordinated anisotropic expansion of files of cells drives organ elongation. The overall shape and local boundaries of most cell types are relatively simple and rather smooth, lacking filopodia-like projections that are present in animal cells. Most plant cell types associated with organ elongation are cylindrical, and ground tissues are comprised primarily of simple polyhedral cells. As the plant develops, a subset of cell types synthesizes highly thickened and/or lignified secondary cell walls after cell expansion ceases to generate mechanical stability to the stems and leaves [12].

## 1.2 Importance of cortex during morphogenesis

The cell cortex is present in both animal and plant cells. As a highly specialized layer of cytoplasmic proteins beneath the plasma membrane, it plays a fundamental role during cell and tissue morphogenesis. In addition, it determines the cell shape, modulates various cell surface properties and plasma membrane behavior. In the following sections, a summary of the main components and functionality of cell cortex is presented. We briefly cover the cytoplasmic proteins and their intrinsic dynamics that are essential to regular cell behavior.

### **1.2.1 Cell cortex in animal and plants**

In general, the cortex is relatively thin layer with a thickness in the range of 100 nm to 1  $\mu$ m [13]. The fundamental structural component is quite distinctive across animal and plant cells. The animal cell cortex is mainly composed of filamentous actin (F-actin), myosin molecular motors, and various actin binding proteins. Since the cell is devoid of a cell wall, the actomyosin constitutes contribute to the mechanical rigidity of the cortex via rapid transient dynamics [14]. The dynamic behaviors of F-actin rely extensively on the interaction with other accessory and regulatory protein molecules in the cytoskeletal network including cross-linking proteins and motor proteins [15]. Cross-linking proteins build up the connection among filaments. They also provide linkage between the biopolymers and other cellular components. Motor proteins engender contractile forces when they slide F-actin. In plant cells, cortex is slightly different from that of animal cell. The cell cortex is underneath the membrane with mechanical strengthening from the rigid cell wall. The cell wall material couples tightly with the plant cortex via the plasma membrane as the cortical array is strongly anchored to the membrane [16, 17]. The mechanical rigidity and structural integrity of plant cell cortex is reinforced by cortical microtubules (CMT) and microtubule (MT) associated proteins. Motor proteins interacting with microtubules are the driving force for the transport of large molecular cargo as well as delivery of new cell wall material. The transport is also facilitated by specialized cortical actin filaments [9]. Therefore, the cortex not only has the ability to store nutrients, but it also facilitates the nutrient transport into the core of the plant root [18]. The properties of F-actin and microtubules are summarized in Table 1.1.

### **1.2.2 Cortical cytoskeletal remodeling during morphogenesis**

Given the intricate structure of the cortex, the cortical cytoskeletal protein constitutes cascade various transient dynamics. Here, we discuss two different types of cytoskeletons: actin and microtubule. In animal cells, F-actin subpopulations can be of significant size. Its relatively large structure directly controls cell shape and morphology. It is also responsible for the main machinery that drives and powers cell migrations through mechanosensing. To help cells gain locomotion, the actin cytoskeleton reconstructs continuously in motile cells by frequent assembly and disassembly at different scales. This predominantly depends on dynamics of actin molecules as well as mechanical properties of F-actin. Actin filaments are semi-flexible polymers (Table 1.1).

They slide, rotate, bend, extend, aggregate, and become polarized. They interact with multiple classes of proteins, generating and exerting forces within the actin cytoskeleton and on the membranes [13]. Actin filaments in the cortex undergo rapid turnover, polymerization, depolymerization and branching facilitated by actin binding proteins [19]. Formin is a protein associated with actin polymerization, while capping proteins and cofilin might induce depolymerization and severing. Arp2/3 is a protein that provides the actin filament the unique ability to form highly complex meshwork. Actin crosslinking protein (ACP) such as  $\alpha$ -actinin and filamin drives the phase and morphological transition of actin cytoskeleton, reminiscent of active remodeling of the network. These behaviors, combined, lead to actin cytoskeleton network remodeling, branching and filament bundling and clustering which directly control cellular structures and manipulate cell movements [19].

Table 1.1 The structural and mechanical properties of F-actin and microtubules in the cytoskeleton.

Name/Properties	F-actin	Microtubules
Outer diameter (nm)	7	25
Persistence length (Bending)	16 – 17 $\mu\text{m}$	2 – 6 mm
Persistence length (Torsional)	39 $\mu\text{m}$	0.5 mm
Rupture force (nN)	0.6	0.5
Globular protein	G-actin	$\alpha$ - and $\beta$ -tubulins
Motor protein	Myosin	Dynein, kinesin
Cross-linking protein	Fascin, filamin, $\alpha$ -actinin etc.	Ase1/PRC1/MAP65
Major function	Cell shape, adhesion, migration	Mitosis, organelle transport
References	[20-25]	[22, 26-30]

In plant cells, the remodeling of cortical microtubule array is also very often observed during growth and cell morphogenesis. In this system, growth is driven by isotropic turgor pressure and determined by the mechanical property of cell wall. In cases of diffuse growth, cell wall is



predominantly stiffer in the transverse direction than in the longitudinal direction, reminiscent of dynamic interactions between various wall structural components (polysaccharides) and wall modification proteins such as expansin and pectin [3, 31-34] at the molecular level. To this end, it has been shown that anisotropy in cell wall elasticity during anisotropic expansion is tightly regulated by deposition of the cellulose microfibrils. Cellulose microfibrils can reinforce cell wall anisotropically during polarized growth by dominantly aligning in the transverse direction, perpendicular to the major or long axis of growth. Meanwhile, the plant cytoskeletal microtubules in the cortex coordinate cellulose microfibril deposition to guide anisotropic expansion. Cortical microtubules are believed to interact with CESA complexes during cellulose biosynthesis [35-39]. Despite the highly ordered pattern during anisotropic growth, MTs are intrinsically dynamic as they remodel in very short timescale and efficiently respond to external mechanical and environmental stimuli such as abiotic stress, blue light and applied force [40-47]. This makes the cortical microtubule one of the most crucial players during plant cell morphogenesis as it impacts delivery and deposition of key cell wall materials. *In planta*, MTs usually form non-centrosomal array in the cortex, underneath the plasma membrane. The cortical MTs are laterally anchored to the plasma membrane without the ability to translocate either individually or as a bundle [48] (Fig. 1.2). The MTs are much stiffer compared with F-actin (Table 1.1). The dynamic remodeling of the cortical microtubule array signifies diverse patterning during plant cell development and simultaneously influence and direct the trajectory of cellulose synthase complex [37, 49] through interactive proteins [50]. In recent studies, rearrangement of cortical MTs has also been found to regulate deposition of non-cellulosic cell wall materials [51]. The dynamic rearrangement of microtubules has been observed to occur in various forms but one of the most important characteristics is its transverse patterning during polarized growth. In a substantial amount of plant cells including hypocotyls, roots and stems, microtubules develop transversely aligned array to permit anisotropic growth. Due to lack of ability to translocate owing to strong membrane anchoring, it is their intrinsic dynamics that contribute to the spatiotemporal regulation of the cortical array patterning at a network level.

### 1.3 Coarse-grained models of the cytoskeleton

To model the complex dynamics of cytoskeleton, it is crucial to identify the scale of phenomena before setting up the simulation networks or applying relevant mathematical equations

to the systems. A great advantage of multiscale mathematical modeling is its broad applicability to the characteristic behaviors of cytoskeleton from individual molecular dynamics to global network levels. At molecular level using molecular dynamic (MD) models, the spatiotemporal dynamics of cytoskeletal proteins strongly rely on their molecular structures from the smallest atomic scale to filamentous scale [52, 53]. However, MD models lack the ability of deriving comprehensive results for describing the interactions between actin or microtubule filaments and other binding proteins and molecular motors. Therefore, models with larger spatiotemporal scales are more useful for investigating microscopic interactions among multiple components of cytoskeleton while reducing the cost of computational work [53, 54]. In the section, we discuss the current state-of-the-art in terms of the coarse-grained models for actin cytoskeleton and cortical microtubules.

### 1.3.1 Models of actin cytoskeleton

When studying the actin cytoskeleton at a nano spatiotemporal scale up to micro scale, discrete modeling method circumvents the problems at molecular level. It is less intense as it neglects the atomic behavior of actin molecules with slightly lower resolution. Discrete models do not describe these collective behaviors within the actin cytoskeleton, but they combine the numerous actin molecules and simplify the actin filaments as semi-flexible segments represented by masses and springs [55]. With the help of experimentally determined mechanical properties of actin filaments, discrete models focus on probing a specific portion of actin cytoskeleton to study how reconstituted network properties at the filament scale respond to internal and external changes [56, 57]. Discrete modeling method is localized and provides sufficient details about dynamics of actin filaments based on a fundamental method called coarse graining.

Table 1.2 Properties of two general actin filament models including FJC and WLC models.

Model Property	FJC Model	WLC Model
Bending	No	Yes
Kuhn length, $b$	$b$	$2 L_p$
Goodness of fit to experimental data	Slight offset	Good

## Conformational Representation

To obtain an appropriate coarse-grained level of modeling actin filaments, researchers have developed methodologies in which they treat actin filaments as cylindrical segments of thin rods [58]. Both long range and short-range interactions between the segments can be simulated based on the model assumption [59]. In cytoplasm, actin filaments are subject to extensional, bending, torsional forces along with shear stress and severing [60, 61]. Therefore, it is significant to clearly define the conformational structure of single actin filaments to a specific coarse-grained magnitude. Two general methods include modeling actin segments as freely joined chain (FJC) and wormlike chain (WLC). A summary of the statistical properties of each model is listed in Table 1.2. FJC model represents actin filaments as straight segments jointed by random angles without bending resistance and rotational energy penalty. The length of each segment is called Kuhn length denoted by  $b$ . Therefore, the length of  $N$  segments under full extension can be calculated by  $L = Nb$ . Due to fluctuations and entropic effects, segments undergo rotation freely around joints. The parameter for quantifying the distance between one end of the chain to the other end of chain (representing barbed and pointed ends of actin filaments) is defined as the root mean squared end-to-end distance  $x = \sqrt{Nb}$ . FJC model assumes the chain acts as a spring with a spring constant of  $3k_B T/bL$  where  $k_b$  is the Boltzman's constant, and  $T$  is the absolute temperature. The advantage of WLC model is that it considers the flexural rigidity of actin filaments, which is also referred to as bending stiffness,  $K_b$ . The bending stiffness is related to the persistence length of actin filaments  $L_p$  via the following equation:

$$L_p = \frac{\kappa_b}{k_B T} \quad (1.1)$$

while the root mean squared end-to-end distance in WLC model is defined as:

$$x = \sqrt{2LL_p - 2L_p^2 \left(1 - e^{-\frac{L}{L_p}}\right)} \quad (1.2)$$

the force-extension relationship follows the relationship:

$$F = \frac{k_B T}{L_p} \left[ \frac{x}{L} + \frac{1}{4} \left(1 - \frac{x}{L}\right)^{-2} - \frac{1}{4} \right] \quad (1.3)$$

as a close approximation. The exact solution is more accurate compared to experimental data based on WLC model. Therefore, discrete models of actin cytoskeleton generally mimic actin filaments using WLC models, considering their semi-flexibility.

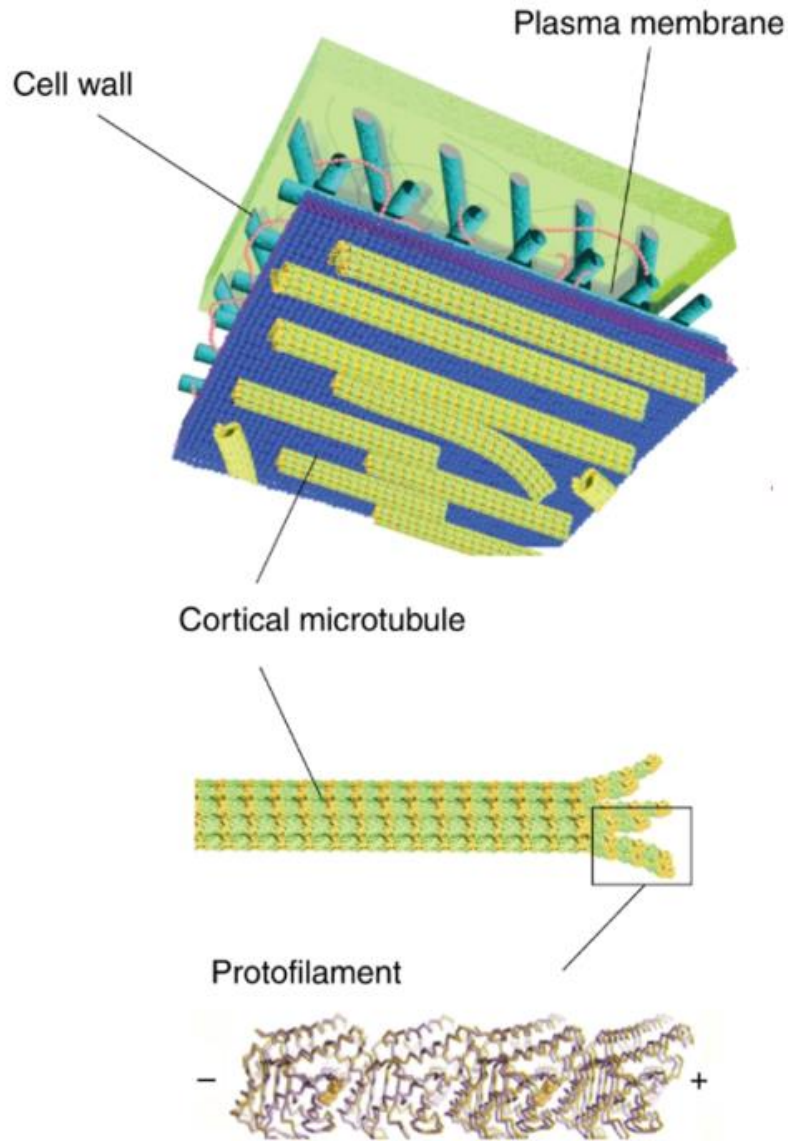


Fig. 1.2 Schematic of cortical microtubules anchored to plasma membrane in plant cells. Molecular and protofilament structure of microtubules are included. Adapted from [213].

### ***Rheological behaviors of actins in 2D Discrete Models***

To establish discrete cross-linked network models for actin cytoskeleton, we have to address the filament dynamics under real biological environments. The surrounding environments of actin cytoskeleton have high viscosity when they regulate mechanical properties of actin filaments. Furthermore, F-actin dynamics are influenced by other organelles, macromolecules, microtubules and intermediate filaments. This leads to motions of actin filaments that cannot be simplified based on Newton's second law. As a result, Brownian dynamics (BD) provide better description for the movements of actin filaments. In general, Brownian dynamics assume proportionality between force and velocity while inertia is negligible in the present discrete models. The movement of actin segments is restricted by viscous drag forces as well as forces due to thermal fluctuations. Incorporating Brownian dynamics, a discrete model [62] studied how severing lead to changes in actin filament turnover by polymerization and depolymerization. It also showed that F-actin elongation positively correlated with simulation time. In the model, depolymerization at the pointed ends occurs with constant density of unbinding monomers per unit time from mother filaments. Severing rates are fixed among filaments [63]. A critical distance is implemented in the model to allow polymerization. The motion of actin molecules is governed by Langevin equation.

Discrete models in two-dimensional space have also been utilized to study the elasticity of actin cytoskeleton focusing on the shear modulus [64] and deformation of network based on bending and stretching of actin filaments [65]. The affinity of actin cytoskeleton network deformation was found to depend on actin densities in cross-linked F-actin networks. The model also characterized a tri-phasic elastic regime of actin cytoskeleton based on actin densities and contour length of F-actin. Basically, actin cytoskeleton network deformation is affine with concentrated F-actin and high stiffness and nonaffine with diluted F-actin and low stiffness. In another study, small shear strains were applied to a two-dimensional discrete network model to induce random orientations of actin filaments, represented by elastic rods [66]. The energy balance equation involved a bending term and a stretching term. It concluded with a biphasic transition of network nonaffine deformation from a bending-induced behavior to a stretching-induced behavior due to rotation of actin filaments in the direction parallel to the applied strain. Heussinger et al. performed extensive simulations based on discrete models of actin bundles. The decrease in shear modulus of bundled filaments is due to increased probability of buckling for bundled network with higher degree of filament alignment [67]. They analyzed the anisotropic deformation of fibrous

network and calculated the elastic moduli of filamentous networks based on a floppy mode method, which assumed that detailed and localized low-energy excitations only affect one individual filament and the intimate surroundings [68]. A similar two-dimensional (2D) discrete model of classical beams coupled with fixed cross-links neglecting entropic distributions defines a regime where elastic energy of the F-actin is attributed to bending and stretching to the same degree [69]. In addition, the model predicts that there is evident dependence of elasticity of semi-flexible polymer on the filament length, which can be adapted to describe the intrinsic mechanical properties of F-actin. The same group also examined the distribution and transmission of forces among bundled filaments with a 2D discrete fiber network. There exists a threshold force defined as the average force for anisotropic bending of a bundle, below which the distribution of forces among fibers is homogenous and beyond which the distribution becomes heterogeneous [70]. Another 2D discrete model generated actin filaments with Poisson distribution and quantified the anisotropy of network by a nematic order parameter [71]. It illustrated that for various types of actin networks with different degree of alignments of actin filaments, a decrease in actin densities made the network undergo a transition from affine to nonaffine.

Additional models focus on contractility of actin cytoskeleton driven by mechanosensing. Simulations show that cell shape is regulated by contractility and remodeling of active actomyosin network [72]. In a two-filament system, motors are modeled via force dipoles, enabling the quantification and prediction of network contractile forces to be verified by experimentation [73, 74]. The contractility mechanism is also dependent on an intrinsic interplay between actin cytoskeleton connectivity and molecular motor density [75].

### ***3D Networks in Discrete Models***

The ability of predicting actin cytoskeleton dynamics with 2D discrete models is restricted by the oversimplifications. For instance, during network assembly, cross-links are conveniently established between two crossing filamentous segments in a confined space. Increasing the order of dimension by one not only adds complexity to the algorithm for network construction and homogenization but also leads to more possibilities of segment motions. Successful adaption of the 2D model by Onck et al. [66] in three-dimensional space adds a twisting mode in addition to bending and stretching modes to represent changes in cell shapes due to thermal fluctuations [76]. The model demonstrated dependence of 3D network behavior on actin and cross-links density,

filament length and connectivity. Two follow-up 3D discrete models contradicted the strain-stiffening response proposed in the classical 2D model by showing a positive correlation between nonaffinity of actin cytoskeleton deformation and macroscopic shear strain accompanied by collective reorientations of F-actin [77, 78]. The discrepancy can be attributed to increased sensitivity to local mechanical changes. Most of the models incorporate Brownian dynamics to describe dynamics of segments due to mechanical cues. Furthermore, Brownian dynamics are proven to be very beneficial to assess F-actin motions in both 2D and 3D discrete models. BD models have been used to investigate network remodeling of actin dynamics under shear flow [79]. More comprehensive studies have been performed in 3D cross-linked networks. For instance, Kim et al. constructed a BD-based 3D cross-linked actin cytoskeletal network and apply two different rheological simulations, either bulk stress-strain or segmental thermal fluctuations on individual actin segments, to investigate the viscoelastic properties and growth characteristics of actin network [80]. Furthermore, roles of cross-linking proteins [81] are evaluated in addition to the mechanosensing process driven by myosin motors contributing to phase transition, rigidity-sensing, and remodeling of actomyosin network into highly ordered structures [82-84].

### **1.3.2 Models of cortical microtubules**

#### ***Models based on MT-MT interactions***

Due to the transient dynamics of microtubules, live-cell imaging for quantification of continuous and/or instantaneous changes in cortical MT alignment has been a challenging task. However, *in silico* approaches took great advantages of the dynamic parameters quantified *in vivo* and were capable of simulating MT-MT interactions within the plant cortex at various spatiotemporal scales [85]. Earlier models of microtubules in plant cortex highlighted significance of zippering and bundling [86], which is believed to be strengthened by crosslinking proteins between microtubules [87]. Baulin et al. used a minimal model to show that microtubule growth can be constrained by perturbation of plus-end polymerization since it would affect frequency of collision between neighboring microtubules [88]. The importance of collision events followed by angle-dependent dynamics and entrainment have been fully investigated by a two-dimensional mechanochemical model that accounts for chemical bonding and crosslinking effects [89]. The same group developed a more realistic model that incorporated three-state (polymerization,

depolymerization and pause) dynamic instability [90] while previous models usually considered two-state assumptions (polymerization and depolymerization). They confirmed that plus-end zippering and bundling can significantly enhance ordering of cortical microtubules. Moreover, when a boundary-induced catastrophe effect was introduced, microtubule catastrophe would be triggered when it collides with specific edges or surfaces of the domain. Through this mechanism, they found that simulated boundary-induced catastrophe can fine-tune the dominant orientation angle of microtubules and is sufficient to provoke network alignment transverse to the direction of the cell growth. Mace et al. extended this model by incorporating microtubule severing and confirmed that it could enhance ordering of cortical MT array when coupled with optimal level of collision-induced catastrophe [91]. A more recent and complex model further interpreted the significance of katanin-mediated severing. It was found that only selective severing at MT crossover sites instead of random, stochastic and uniformly distributed severing, could promote the ordering of microtubules at a network level [92]. Nevertheless, it still requires a tight coordination of crossover-site severing and zippering at shallow angles which prevents frequent severing that would possibly deteriorate MT network connectivity and ordering. Several other studies also revealed the importance of nucleation modes of microtubules on the remodeling and emergence of ordering in cortical MT array [93-95].

### ***Models incorporating cell geometry***

To account for effects by cell geometry in addition to the aforementioned MT-MT interactions and dynamics, a study combined live cell imaging with computational models and predicted strong cell-edge effects on cortical MT orientation and organization associated with CLASP protein [96]. CLASP is proposed to accumulate at sharp edges to mitigate geometrical effects of the sharpness and stabilize microtubules. Basically, in CLASP mutants, sharp edge of cell induces catastrophe which directs growth of microtubules to be aligned parallel to the edge. It also reduces cortical anchoring of microtubules and allows them to adopt variable angles approaching each other, which leads to hyper-aligned cortical MT array [97]. More recently, two studies have focused on dependence of cortical MT alignment on variation of geometrical constraint and surface properties in three-dimensional domain [98, 99]. Using geometry derived from confocal images, one study reproduced distribution of microtubules in Arabidopsis leaf pavement cells [100]. However, the model lacks the ability to explain the extreme variability of



microtubules patterns as a function of time [99, 101, 102]. Mirabet et al. incorporated a directional bias for polymerization of microtubule, representing cues by cell polarization and external tension. Although it remains quite artificial, the directional bias, per se, is sufficient to induce global orientation and alignment [103]. In sum, these models account for coarse-grained description of microtubule dynamics and shed light on their sensitivities to geometrical effects in terms of their self-organization and emergence of global re-orientation.

## 1.4 Shortcomings of current models and hitherto unaddressed gap

### *Lack of physiological descriptions*

As an emerging topic, biophysical models of actin cytoskeleton on various spatiotemporal scales requires solid validation by experimental results. However, most of the coarse-grained models introduced lack detailed mechanical interactions between F-actin, motors proteins and ACPs. For instance, [69] considered fixed crosslinkers, ignoring the transient dynamics of actin-ACP interactions. For the BD models, although the stochastic dynamics of F-actin are considered, the parametric space is not broad enough to recapitulate the observed network morphology and dynamics of *in vivo* or *in vitro* actin cytoskeleton. [69] has explored the effect of F-actin density and average length. However, there are more important attributes such as ACP density, ACP unbinding dynamics, motor density and motor binding preference and configurations etc. In addition, F-actin turnover and severing are intrinsic to the dynamic remodeling of the actin cortex. This would require a systematic assumption from the mechanistic aspect where force and velocity based on the protein interactions are instantaneously updated at a physiologically relevant spatiotemporal scale. None of the coarse-grained models has incorporated a comprehensive description of the intracellular network prone to cytoskeletal protein-level interactions. Especially, the force-dependent dynamics of non-muscle myosins and ACPs remains a great challenge considering the computational expanses. Therefore, to recapitulate the active remodeling of actin cortex attributed to F-actin, motor, and ACP dynamics, it requires a robust mechanistic model at the discrete level which can bridge the gap.

### ***Over-simplification and lack of mechanical integrity***

In recent years, modeling the plant cortex has received much attention and effort. Most of the well-established models, nevertheless, are still very simplified. First, the cortical array model is purely based on stochastic and deterministic dynamics of MTs. The major assumptions in the previous models, since the first one introducing angle-dependent event-driven simulation was proposed by [104], were based on the parameter sets measured from various types of plant cells [90-92]. With the development of more advanced imaging techniques, a wide range MT treadmilling dynamics haven been quantified. However, those parameters are prone to cell types and surrounding conditions such as temperature, none of which has a fundamental relationship with external mechanical and geometrical stimuli. Therefore, it remains an open research gap to establish a computational basis for force-regulated or geometry-dependent dynamics. The models that accounted for cell faces does not include a realistic assumption for curvature dependency when simulating the microtubule dynamics. In a recent model, Chakraborty et al. [105] adapted a real-cell geometry and quantitatively explained the impact on global alignment of cortical array by cell geometry. However, the geometry is static and does not provide any insight for morphogenesis-relevant reorganization of CMTs. In such framework, the model constrains the network dynamics into a confined space instead of a dynamically changing real cell geometry during growth. To this end, the effect by cell geometry on regulating the alignment of cortical microtubules is still a necessary but not sufficient attribute. More recently, two studies have raised some controversy on the importance of geometry in isolated protoplasts devoid of cell walls. In [106], by varying the confined shape from rectangular, circular, triangular to squares, the authors concluded that predominant alignment of microtubules and actins as well as network anisotropy could only be observed in a rectangular space. This setup failed to produce transversely aligned cortical array due to the lack of cell and tissue level mechanical signals, proving that steric MT-MT interactions alone is not able to provide enough bias for self-organization to mimic *in vivo* conditions. Although a model implemented a weak directional bias sufficient to align microtubules in an elliptical domain [100], it nevertheless lacked the mechanical basis for the external stimuli. In contrast, Colin et al. proved that surface tension alone can override geometrical effect in regulation of cortical microtubule alignment [107]. However, the limitation of such system persists, as the real tension that couples with cortical MTs is only determined by the cell and tissue level stress. The lack of coupling between tensile stress and microtubules points to a demanding research gap.

## 1.5 Research goal and outline

To overcome the limitations of current model and address the research gap in cytoskeletal remodeling, we aim to implement and develop coarse-grained models based on the intrinsic dynamics of cytoskeleton protein constitutes at the mechanistic level. In this thesis, we introduce two different models for the distinct cytoskeleton: actin cytoskeleton in animal cells and cortical microtubule array in plant cells. The thesis is organized as follows.

In Chapter 2, we implement a well-established agent-based model for actomyosin network and introduced transient dynamics including actin severing, treadmilling and mobility of myosin motors to study the contractile behavior of the active system. The model is based on Langevin equation for Brownian dynamics. The simulations bring the full capability of mimicking *in vivo* and *in vitro* actomyosin networks.

In Chapter 3, we develop a discrete model of cortical microtubule array based on stochastic and deterministic dynamics, including nucleation, growth, shrinkage, pause, and angle-dependent catastrophe, rescue, crossover and severing. The three-state model is also integrated with a mechanical basis with evidence from tension-regulated microtubule dynamics.

In Chapter 4, we discuss the output from the two model systems and propose future directions in modeling the two cytoskeletons to study the mechanism underlying remodeling.

In Appendix A, we summarize the results for a model that simulates a contracting cell embedded in the extracellular matrix (ECM), allowing remodeling of the ECM as well as propagation of mechanical stress under various conditions. Appendix B lists the model parameters for the actomyosin network. Appendix C includes supplementary results for the cortical microtubule array model.

## 2. MODULATION OF CONTRACTILE BEHAVIOR OF ACTOMYOSIN NETWORKS

### 2.1 Introduction

Living cells need to generate mechanical forces for their physiological functions [108]. Forces are generated mainly by interactions between actin filaments (F-actin) and myosin II motor proteins in the cell cortex [13]. Myosin II proteins walk on F-actin by consuming chemical energy stored in adenosine triphosphate (ATP), which results in generation of tensile forces. The actomyosin contractility facilitates structural reorganization of the actin cytoskeleton in cells [109]. A pronounced example of actomyosin-based contraction is muscle contraction. The sarcomere, which is the fundamental unit of muscle, consists of overlapped actin and myosin filaments. Active forces generated by myosin filaments pulling the actin filaments is a well-defined mechanism for determining the extent of contraction. As in non-muscle cells like the cortex, contraction occurs in a much wider range of timescales (from seconds to hours): formation of an actomyosin ring whose contractility facilitates successful division during cytokinesis; rapid turnover of the actin and myosins in a structure near the apical region of the cell which constricts and induces contractility in an oscillatory manner that coincides with the assembly and disassembly of F-actin and non-muscle myosin II motors. The spatiotemporal activity of the myosin motors has been proven to align with RhoA distribution [110]. Different classes of myosin motors have specific binding preference and mode depending on their intracellular locations. As such, research on contractility of actomyosin networks has witnessed some influential progress in the design of *in vitro* systems such as reconstituted actomyosin gels and motility assays. The reconstituted gels are assembled via a specific sequence of adding protein constituents to form stable actomyosin bundles [111]. The bundles are coupled to elastic substrate via beads for precise force measurements. In this way, varying different quantities such as motor density and type, filament density and length, ACP density would provide sufficient support for understanding the mechanical feedback between contractility and mechanical force in disordered actomyosin bundles and clusters. In a motility assay experiment, motors are generally fixed which allows F-actin to glide on the template. By varying the motor types, various interesting contractile behavior has been observed. In addition, actomyosin remodeling under these conditions leads to a diverse range of network morphology.

Therefore, there is an urgent need for computational models that can recapitulate the design and output of those in *vitro* systems.

## 2.2 Method

### 2.2.1 Model Overview

We employed our previous Brownian dynamics model for studying the contraction of actomyosin network. Detailed descriptions about the model and parameter values used in this study can be found in the Supplementary Information. In the model, F-actin, ACP, and motor are simplified by interconnected cylindrical segments. F-actin is comprised of serially connected cylindrical segments with polarity (barbed and pointed ends). ACPs consist of two cylindrical segments. Each motor has a backbone connected with 8 arms. A motor arm represents 8 myosin heads, justified in our previous study [83]. Motions of the segments are governed by the Langevin equation with the Euler integration scheme. Deterministic forces include bending and extensional forces that maintain equilibrium angles and lengths formed by the segments, respectively, and repulsive forces that account for volume-exclusion effects between actin filaments. Stochastic forces are applied to induce thermal fluctuation. ACPs bind to F-actin at a constant rate and also unbind from F-actin in a force-dependent manner. A motor arm binds to F-actin and walks toward the barbed end.

#### *Brownian dynamics via the Langevin equation*

In the model, actin filaments are comprised of serially-connected cylindrical segments with barbed and pointed ends. ACPs consist of a pair of cylindrical segments. Each motor is modeled after myosin thick filaments; a motor has a backbone structure with 8 arms, and each of the arms represents 8 myosin heads. Displacements of the segments are governed by the Langevin equation with inertia neglected:

$$\mathbf{F}_i - \zeta_i \frac{d\mathbf{r}_i}{dt} + \mathbf{F}_i^T = 0 \quad (2.1)$$

where  $\mathbf{r}_i$  is a position vector of the  $i$ th element,  $\zeta_i$  is a drag coefficient,  $t$  is time,  $\mathbf{F}_i$  is a deterministic force, and  $\mathbf{F}_i^T$  is a stochastic force satisfying the fluctuation-dissipation theorem [112]:

$$\langle \mathbf{F}_i^T(t) \mathbf{F}_j^T(t) \rangle = \frac{2k_B T \zeta_i \delta_{ij}}{\Delta t} \boldsymbol{\delta} \quad (2.2)$$

where  $\delta_{ij}$  is the Kronecker delta,  $\boldsymbol{\delta}$  is a second-order tensor, and  $\Delta t = 1.5 \times 10^{-5}$  s is a time step. Drag coefficients are calculated using an approximated form for a cylindrical object [113]:

$$\zeta_i = 3\pi\mu r_{c,i} \frac{3 + 2r_{0,i} / r_{c,i}}{5} \quad (2.3)$$

where  $\mu$  is the viscosity of medium, and  $r_{0,i}$  and  $r_{c,i}$  are length and diameter of a segment, respectively. Positions of all the cylindrical segments are updated using Euler integration scheme:

$$\mathbf{r}_i(t + \Delta t) = \mathbf{r}_i(t) + \frac{d\mathbf{r}_i}{dt} \Delta t = \mathbf{r}_i(t) + \frac{1}{\zeta_i} (\mathbf{F}_i + \mathbf{F}_i^T) \Delta t \quad (2.4)$$

Note that we employed a 10-fold higher value for  $\mu$  than that used in our previous study where influences of F-actin severing on rheological behaviors of cross-linked actin networks were investigated [114]. Since simulations of aggregating networks in this study tend to significantly slow down later times, an increase in  $\Delta t$  is necessary for exploring wide parametric spaces, which can be achieved by the increase in  $\mu$  in an over-damped system. It was verified that network contraction in four representative cases is similar between the cases with  $\mu = 8.6 \times 10^{-1}$  [kg/m·s] and those with  $\mu = 8.6 \times 10^{-2}$  [kg/m·s].

### ***Deterministic forces***

Deterministic forces include extensional forces maintaining equilibrium lengths, bending forces maintaining equilibrium angles, and repulsive forces accounting for volume-exclusion effects between actin segments. The extensional and bending forces originate from harmonic potentials:

$$U_s = \frac{1}{2} \kappa_s (r - r_0)^2 \quad (2.5)$$

$$U_b = \frac{1}{2} \kappa_b (\theta - \theta_0)^2 \quad (2.6)$$

where  $\kappa_s$  and  $\kappa_b$  are extensional and bending stiffnesses,  $r$  and  $r_0$  is instantaneous and equilibrium lengths of cylindrical segments, and  $\theta$  and  $\theta_0$  are instantaneous and equilibrium angles formed by adjacent segments. An equilibrium length of actin segments ( $r_{0,A} = 140$  nm) and an equilibrium angle formed by two adjacent actin segments ( $\theta_{0,A} = 0$  rad) are regulated by extensional ( $\kappa_{s,A}$ ) and

bending stiffnesses of actins ( $\kappa_{b,A}$ ), respectively. The reference value of  $\kappa_{b,A}$  corresponds to the persistence length of 9  $\mu\text{m}$  [115]. An equilibrium length of ACP arms ( $r_{0,ACP} = 23.5 \text{ nm}$ ) and an equilibrium angle formed by two arms of each ACP ( $\theta_{0,ACP} = 0 \text{ rad}$ ) are maintained by extensional ( $\kappa_{s,ACP}$ ) and bending stiffnesses of ACPs ( $\kappa_{b,ACP}$ ), respectively. An equilibrium length of motor backbone segments ( $r_{s,M1} = 42 \text{ nm}$ ) and an equilibrium angle formed by adjacent backbone segments ( $\theta_{0,M} = 0 \text{ rad}$ ) are maintained by extensional ( $\kappa_{s,M1}$ ) and bending stiffnesses ( $\kappa_{b,M}$ ), respectively. The value of  $\kappa_{s,M1}$  is equal to that of  $\kappa_{s,A}$ , whereas the value of  $\kappa_{b,M}$  is larger than that of  $\kappa_{b,A}$ . Extension of each motor arm is regulated by the two-spring model with stiffnesses of transverse ( $\kappa_{s,M2}$ ) and longitudinal springs ( $\kappa_{s,M3}$ ). The transverse spring maintains an equilibrium distance ( $r_{0,M2} = 13.5 \text{ nm}$ ) between an endpoint of a motor backbone and actin segment where the arm of the motor binds, whereas the longitudinal spring helps maintaining a right angle between the motor arm and the actin segment ( $r_{0,M3} = 0 \text{ nm}$ ). Forces exerted on actin segments by bound ACPs and motors are distributed onto the barbed and pointed ends of the actin segments as described in our previous work. A repulsive force is represented by a harmonic potential [80]:

$$U_r = \begin{cases} \frac{1}{2} \kappa_r (r_{12} - r_{c,A})^2 & \text{if } r_{12} < r_{c,A} \\ 0 & \text{if } r_{12} \geq r_{c,A} \end{cases} \quad (2.7)$$

where  $\kappa_r$  is strength of repulsive force, and  $r_{12}$  is the minimum distance between two actin segments.

### 2.2.2 Dynamics of ACPs

ACPs bind to binding sites located every 7 nm on actin segments with no preference of contact angle. ACPs also unbind from F-actin in a force-dependent manner following Bell's equation [116]:

$$k_{u,ACP} = \begin{cases} k_{u,ACP}^0 \exp\left(\frac{\lambda_{u,ACP} |\vec{F}_{s,ACP}|}{k_B T}\right) & \text{if } r \geq r_{0,ACP} \\ k_{u,ACP}^0 & \text{if } r < r_{0,ACP} \end{cases} \quad (2.8)$$

where  $k_{u,ACP}^0$  is the zero-force unbinding rate,  $\lambda_{u,ACP}$  represents a sensitivity to applied force, and  $k_B T$  is thermal energy. The references values of  $k_{u,ACP}^0$  ( $= 0.115 \text{ s}^{-1}$ ) and  $\lambda_{u,ACP}$  ( $= 1.04 \times 10^{-10} \text{ m}$ ) correspond to filamin A [117].

Although we assumed the slip-bond nature of ACPs in this study, we also tested influences of force sensitivity of ACP unbinding on network contraction. We measured network contraction in four representative cases with catch-bond ACPs ( $\lambda_{u,ACP} = -0.115 \text{ s}^{-1}$ ) or with ideal-bond ACPs ( $\lambda_{u,ACP} = 0$ ). We observed that with a reference value of bending stiffness ( $\kappa_{b,A}$ ), the extent of network contraction varies only slightly due to a change in the force sensitivity. By contrast, with large  $\kappa_{b,A}$ , contraction is significantly greater in networks with catch-bond ACPs or ideal-bond ACPs. If  $\kappa_{b,A}$  is large, a network resists contraction stronger, resulting in a larger amount of forces on each ACP. If ACPs behave as a slip-bond, this large force accelerates unbinding events of ACPs, so network connectivity is impaired, leading to smaller network contraction. By contrast, if ACPs do not behave as a slip-bond, network connectivity is maintained, leading to large network contraction.

### 2.2.3 Dynamics of motors

Motor arms bind to binding sites on actin segments at a rate of  $40N_h \text{ s}^{-1}$ , where  $N_h = 8$  is the number of myosin heads represented by each arm. Walking ( $k_{w,M}$ ) and unbinding rates ( $k_{u,M}$ ) of the motor arms are regulated by the parallel cluster model to mimic the mechanochemical cycle of non-muscle myosin II [118, 119]. Details of implementation and benchmarking of the parallel cluster model in our models are extensively described in our previous study [83]. Note that  $k_{w,M}$  and  $k_{u,M}$  are lower with higher applied load since motors exhibit a catch-bond behavior. Unloaded walking velocity and stall force of motors are set to  $\sim 140 \text{ nm/s}$  and  $\sim 5.7 \text{ pN}$ , respectively.

## 2.3 Buckling-induced severing regulates actomyosin contraction

### 2.3.1 Background

Numerous *in vitro* experiments have demonstrated that reconstituted actin gels consisting of F-actins, ACPs, and myosin motors exhibit active contraction to single or multiple foci. For example, it was shown that contraction of the actin gels emerges above critical motor density with intermediate levels of ACP density [73] and takes place via multi-stage aggregation [120] by driving initially well-connected networks to a critical state [121]. In addition, we and our colleagues recently showed that networks contract at a rate proportional to network size via *in vitro* and numerical/analytical models, which is reminiscent of telescopic contraction of sarcomeres in muscle cells [122]. It was also found that buckling induced by compressive forces arising from



myosin activity plays a crucial role for contraction of actin gels [123], consistent with theoretical predictions [74, 124]. A recent computational study showed that suppression of F-actin buckling can significantly slow down contraction [125]. In general, myosin activity can drive actomyosin networks to either of three different states: negligible contraction, contraction to a single focus, or contraction to multiple foci. Known key factors determining the final state of networks are i) network connectivity regulated by cross-linking level and F-actin length and ii) destabilization of ACPs caused by forces exerted from motors [121, 125-127].

We recently demonstrated that severing of F-actin facilitated by buckling arising from external shear strain can induce distinct stress relaxation in passive cross-linked actin networks [114]. Interestingly, severing was also observed during the active contraction of actomyosin networks. However, the role of F-actin severing in the myosin-driven network contraction has not been investigated to date. In this study, using an agent-based computational model, we investigated how F-actin severing induced by buckling modulates contraction of cortex-like thin actomyosin networks. We found that the buckling-induced F-actin severing significantly modulates network contraction, which has not been demonstrated before.

### **2.3.2 Additional method**

#### ***Network assembly***

A very thin computational domain ( $20 \times 20 \times 0.1 \mu\text{m}$ ) is employed without a periodic boundary condition. F-actin, ACP, and motor are self-assembled to a cross-linked actomyosin network within a circular space whose radius is  $8 \mu\text{m}$  (Fig. 2.1). During the network assembly, actin monomers are nucleated and polymerized into F-actin. ACPs bind to F-actin to form functional cross-links between pairs of F-actin. Motors are assembled into thick filaments, and motor arms bind to F-actin without walking motion. After the network assembly, motors start walking on F-actin, facilitating network contraction.

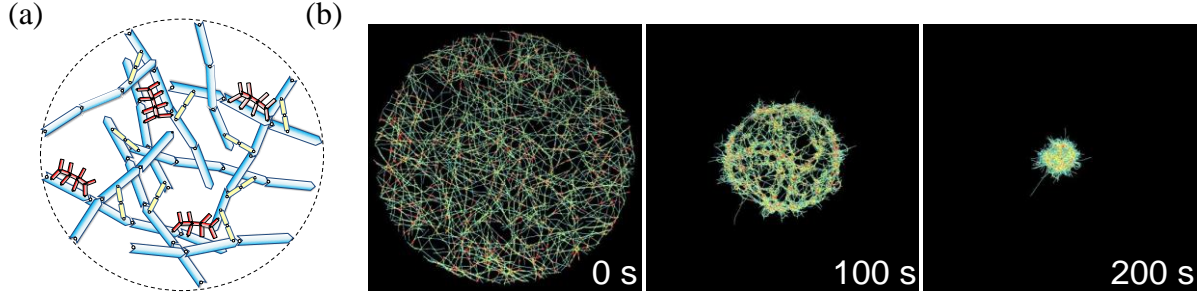


Fig. 2.1 Contraction of actomyosin networks is investigated using an agent-based computational model. (a) Schematic diagram showing a circular network consisting of actin filaments (F-actin, cyan), actin crosslinking proteins (yellow), and motors (red). The three constituents are simplified via cylindrical segments. (b) Morphology of networks at  $t = 0, 100$ , and  $200$  s during contraction. Densities of motors and ACPs are  $0.08$  and  $0.04$ , respectively.

### Severing of F-actin

F-actin can be severed at a rate depending on bending angle as in our previous model [114]. Severing of F-actin is simulated by breaking a chain between two adjacent points on the F-actin, which corresponds to disappearance of one actin segment. The sum of two adjacent bending angles on F-actin,  $\theta_{s,A}$ , is calculated, and we assume that a severing rate,  $k_{s,A}$ , exponentially increases as  $\theta_{s,A}$  increases:

$$k_{s,A} = k_{s,A}^0 \exp\left(\frac{\theta_{s,A}}{\lambda_{s,A}}\right) \quad (2.9)$$

where  $k_{s,A}^0$  is a zero-angle severing rate constant, and  $\lambda_{s,A}$  defines sensitivity to  $\theta_{s,A}$ . This severing model was verified by comparing with *in vitro* experiments as described in the supplementary information. For determination of the severing angle, the method is explained in Appendix B.

### Quantification of network contraction

Network contraction is calculated using the  $x$  and  $y$  coordinates of endpoints of actin segments. Assuming that they are located on a single  $x$ - $y$  plane, we create the spatial density map of the endpoints at the final time point of each simulation. By decreasing resolution of the map, a three-dimensional histogram is generated to automatically detect the number of foci. In the

histogram, locations with actin density above a threshold value are considered to be potential centers of foci. If several potential centers are adjacent to each other in the histogram, they are considered to be a single focus. Once the number of foci is identified, we back-trace the endpoints of actin segments that belong to each focus up to the first time point in order to calculate contraction at each time point. For each focus, we first calculate its center by averaging the x and y positions of the actin endpoints. Then, distances between the center and endpoints that belong to the focus are averaged to calculate its mean radius,  $R_i(t)$ . The extent of network contraction ( $\xi$ ) is calculated as follows:

$$\xi(t) = 1 - \frac{\sum_i^N \pi R_i(t)^2}{\sum_i^N \pi R_i(0)^2} \quad (2.10)$$

where  $N$  is the number of foci. Note that 0 corresponds to no contraction, whereas 1 means maximal contraction. An instantaneous contraction rate at each time point is determined by calculating the rate of a change in  $\xi$  over time ( $\dot{\xi}(t) = d\xi/dt$ ). We define a steady state to be a time point when  $\dot{\xi}(t)$  becomes less than ten percent of  $\dot{\xi}(0)$ . The time required for reaching the steady state is termed  $\tau_{ss}$ , and the average contraction rate is calculated by dividing  $\xi$  at the steady state ( $\xi_{ss}$ ) by  $\tau_{ss}$ .

### 2.3.3 Results

#### *Densities of motors and actin crosslinking proteins regulate contraction of actomyosin networks*

First, we evaluate the contraction of actomyosin networks at wide ranges of densities of motor ( $R_M$ ) and ACP ( $R_{ACP}$ ) in the absence of F-actin severing. Note that  $R_{ACP}$  and  $R_M$  are molar ratios defined with respect to actin concentration. In all cases, contraction initially rises at a different rate and eventually reaches a steady-state level (Fig. 2.2b). At the steady state, motors aggregate to single or multiple aggregates depending on conditions (Fig. 2.2a). Note that there is not a volume-exclusion effect between motors, so motors may overlap with each other in space, which can lead to very compact motor aggregates. Unlike motors, distribution of F-actin does not show noticeable discontinuity after contraction regardless of the number of motor aggregates. Large contraction greater than 50% occurs only above critical  $R_M$  with intermediate values of  $R_{ACP}$

(Fig. 2.2c). A minimum amount of motors are required to obtain cooperativity between local motor activities, resulting in the critical  $R_M$  ( $R_M^{\min}$ ) [75]. If there are an insufficient number of ACPs, connectivity between F-actins is too poor for motors to generate enough forces to contract networks. However, as  $R_M$  is higher, the minimum amount of ACPs required for large contraction ( $R_{ACP}^{\min}$ ) is smaller because motors can also behave as tentative cross-linkers. If average length of F-actins ( $\langle L_f \rangle$ ) is decreased from 2.53  $\mu\text{m}$  to 1.74  $\mu\text{m}$ , more ACPs are needed for large network contraction since a network with shorter F-actins has poorer connectivity compared to that with longer F-actins at the same cross-linking level (Fig. 2.3a). By contrast, if there are too many ACPs in a network, buckling of F-actins is suppressed either by a decrease in cross-linking distance or formation of F-actin bundles. Therefore, networks show smaller contraction above a certain level of  $R_{ACP}$  ( $R_{ACP}^{\max}$ ) because buckling is required for significant network contraction as predicted by theories (Fig. 2.2c) [74, 124]. A 16-fold increase in bending stiffness of F-actin ( $\kappa_{b,A}$ ) reduces  $R_{ACP}^{\max}$  because buckling can be suppressed more easily with stiffer F-actins even at larger cross-linking distance or with a less extent of F-actin bundling (Fig. 2.3b). A decrease in  $\langle L_f \rangle$  also reduces  $R_{ACP}^{\max}$  since motors generate weaker forces in a network with poorer connectivity although cross-linking distance and F-actin bundling are similar (Fig. 2.3a). These results showing large contraction only at  $R_M \geq R_M^{\min}$  and  $R_{ACP}^{\min} \leq R_{ACP} \leq R_{ACP}^{\max}$  are very similar to observations from *in vitro* experiments using an actin gel consisting of actin, skeletal muscle myosin II, and  $\alpha$ -actinin [73]. A computational study using a highly simplified model predicted that network contraction can be large at high  $R_{ACP}$  and intermediate  $R_M$  if volume-exclusion effects are negligible [75]. However, we did not observe the secondary regime for large contraction. This might be attributed to indirect consideration of volume-exclusion effects between motors and ACPs due to a limited number of binding sites on each actin segment (40). In addition, large contraction emerging at the intermediate range of  $R_{ACP}$  is also consistent with conclusion of a recent computational study that the degree of connectivity determines network contraction [125]. In sum, we found that large network contraction requires a sufficient amount of motors, enough network connectivity, and F-actin buckling. For the following studies, we focused on the narrower range of  $R_{ACP}$  between 0.005 and 0.08 since we were interested only in a regime where significant network contraction appears without F-actin severing in Fig. 2.2c.

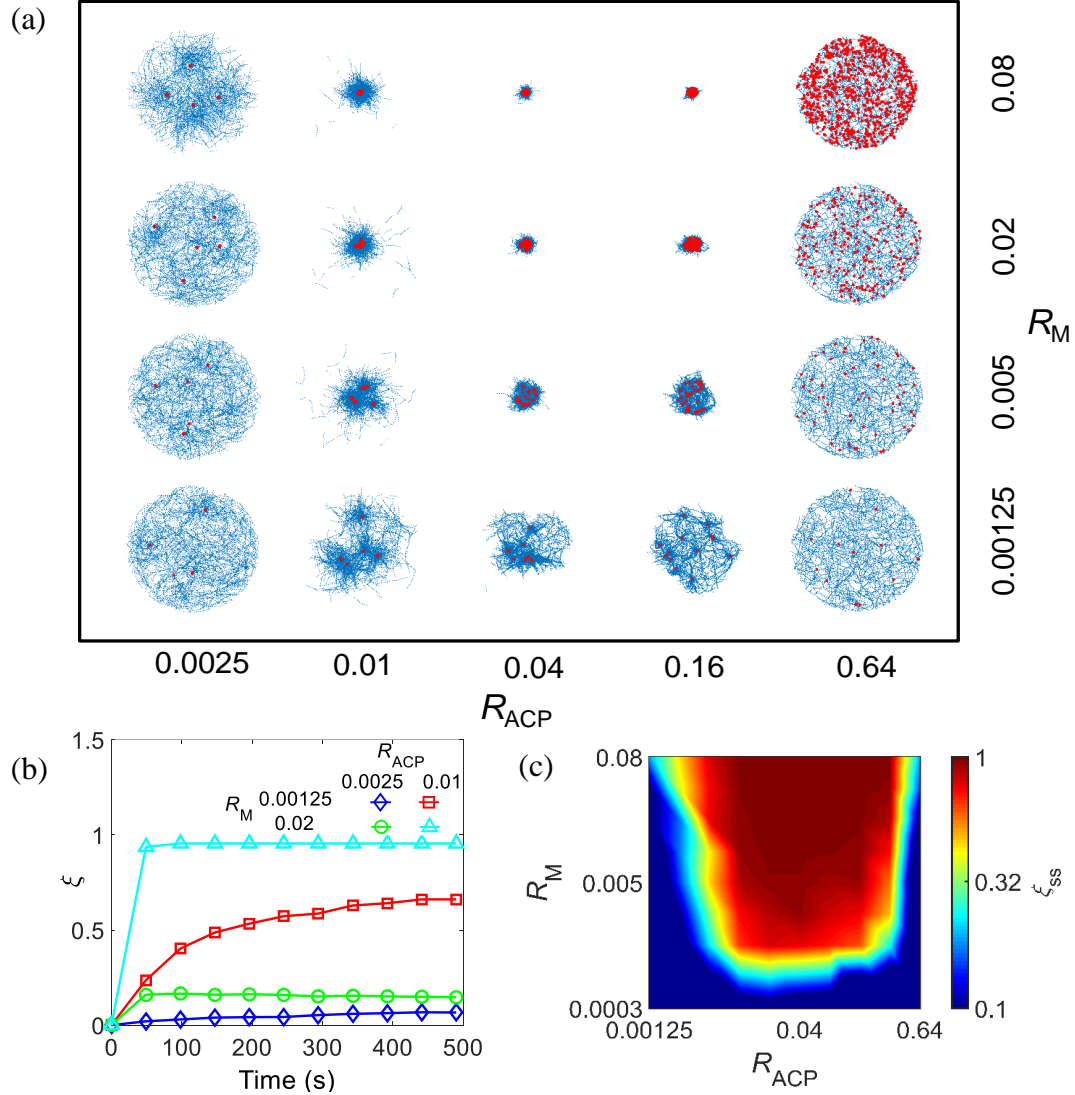


Fig. 2.2 Network contraction is regulated by densities of motors ( $R_M$ ) and ACPs ( $R_{ACP}$ ). Contraction was evaluated under various  $R_M$  and  $R_{ACP}$ . (a) Network morphology with actins and motors represented by blue and red, respectively. Note that motors can aggregate very tightly due to the absence of a volume-exclusion effect between them. (b) Time evolution of the extent of contraction ( $\xi$ ) for four different cases. (c)  $\xi$  measured at a steady state ( $\xi_{ss}$ ). Large network contraction occurs above critical  $R_M$  with intermediate  $R_{ACP}$ .

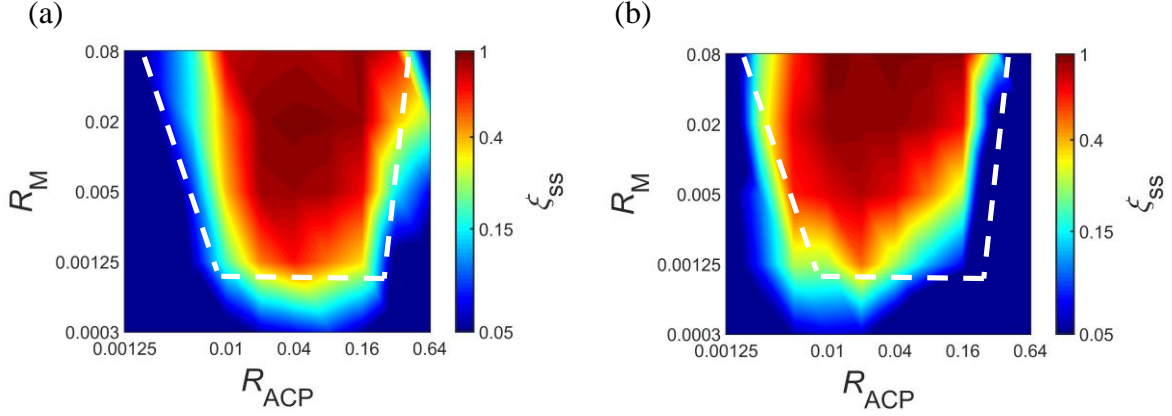


Fig. 2.3 Bending stiffness ( $\kappa_{b,A}$ ) and length ( $\langle L_f \rangle$ ) of actin filaments modulate network contraction. (a) When  $\langle L_f \rangle$  is reduced from  $2.53 \mu\text{m}$  to  $1.74 \mu\text{m}$ , critical levels of  $R_{ACP}$  above which large contraction occurs are higher (c.f. Fig. 2.2c) because more ACPs are needed for the minimal network connectivity if the network has lower connectivity due to shorter actin filaments. (b) When  $\kappa_{b,A}$  is increased 16-fold, the transition of contraction on the left still occurs at  $R_{ACP} \sim 0.0025\text{-}0.005$ . By contrast, the transition on the right takes place at lower  $R_{ACP}$  (c.f. Fig. 2.2c) because buckling of actin filaments requires a larger amount of forces (i.e. higher  $R_M$ ) at each  $R_{ACP}$ . In (a-b), for comparison, red dashed lines indicate a regime where large network contraction emerges in Fig. 2.2c.

### ***Buckling-induced severing controls optimal level of contraction***

Recent *in vitro* experiments have demonstrated that F-actins can be severed spontaneously due to an increase in their bending angle caused by thermal fluctuation, and the probability of severing is significantly enhanced by binding of cofilin [128, 129]. Since buckling also increases bending angle of F-actins, it can mediate severing of F-actins. We recently showed that external shear strain applied to passive cross-linked actin networks can facilitate severing by making a portion of F-actins buckled, and that the severing induces a very distinct stress relaxation in the passive networks [114]. Considering that buckling also takes place during the active contraction driven by motors, F-actin severing induced by the buckling has potential to play an important role in the network contraction [123]. By incorporating the severing model implemented in our previous study [114], we evaluated effects of the severing on contractile behaviors. Specifically, we measured contraction at wide ranges of a zero-angle severing rate constant ( $k_{s,A}^0$ ) and  $\kappa_{b,A}$  (Fig. 2.4), with  $R_M = 0.08$  and  $R_{ACP} = 0.02$  where very large contraction to a single focus occurs in the absence of severing. As expected, networks show smaller contraction with 64-fold higher  $\kappa_{b,A}$

since F-actin buckling is suppressed (Fig. 2.4d). However, motors form aggregation in various fashions, leaving aster-like F-actin structures (Fig. 2.4a), which is reminiscent of contraction of microtubule networks observed in several experiments [130, 131]. This contraction is mediated by polarity sorting, meaning that barbed ends of F-actins are brought to the center of the aster-like structures by motors [125]. With higher  $k_{s,A}^0$  and lower  $\kappa_{b,A}$ , F-actins are severed more frequently during contraction (Fig. 2.4b). Interestingly, under the condition resulting in numerous severing events, a network is transformed to multiple foci with small contraction because F-actins are fragmented into short filaments during contraction, leading to severe deterioration of network connectivity (Figs. 2.4a, c). Thus, in the presence of F-actin severing, the network contraction can be maximal at intermediate levels of  $\kappa_{b,A}$ , not the smallest level. Time required for reaching a steady state ( $\tau_{ss}$ ) is proportional to  $\kappa_{b,A}$  but is almost independent of  $k_{s,A}^0$ , indicating that a network comprised of stiffer filaments resists myosin-driven contraction more. An average contraction rate shows dependence on  $k_{s,A}^0$  and  $\kappa_{b,A}$  similar to dependence of the final contraction ( $\xi_{ss}$ ) on  $k_{s,A}^0$  and  $\kappa_{b,A}$  although it shows stronger dependence on  $\kappa_{b,A}$ .

It is not feasible to change bending rigidity of F-actins in experiments over the range tested in this study although it is curvature (i.e. large local bending angle), facilitating numerous severing events. Note that the highest  $R_{ACP}$  tested here is 0.08 which is much lower than the critical  $R_{ACP}$  in Fig. 2.2c above which it is known that the bending rigidity is slightly varied by binding of actin-associated proteins, such as phalloidin, calponin, and tropomyosin [115, 132, 133]. However, cases with 64-fold higher  $\kappa_{b,A}$  (corresponding to the persistence length of 0.58 mm) may be compared with networks of microtubules whose persistence length is  $\sim 5$  mm [22]. As mentioned earlier, in those cases, we observed formation of structures similar to microtubule networks contracted by motors. By contrast, it is viable to modulate the F-actin severing rate by including a different amount of cofilin [134]. It will be interesting to test our predictions using reconstituted actomyosin networks with various concentrations of cofilin.

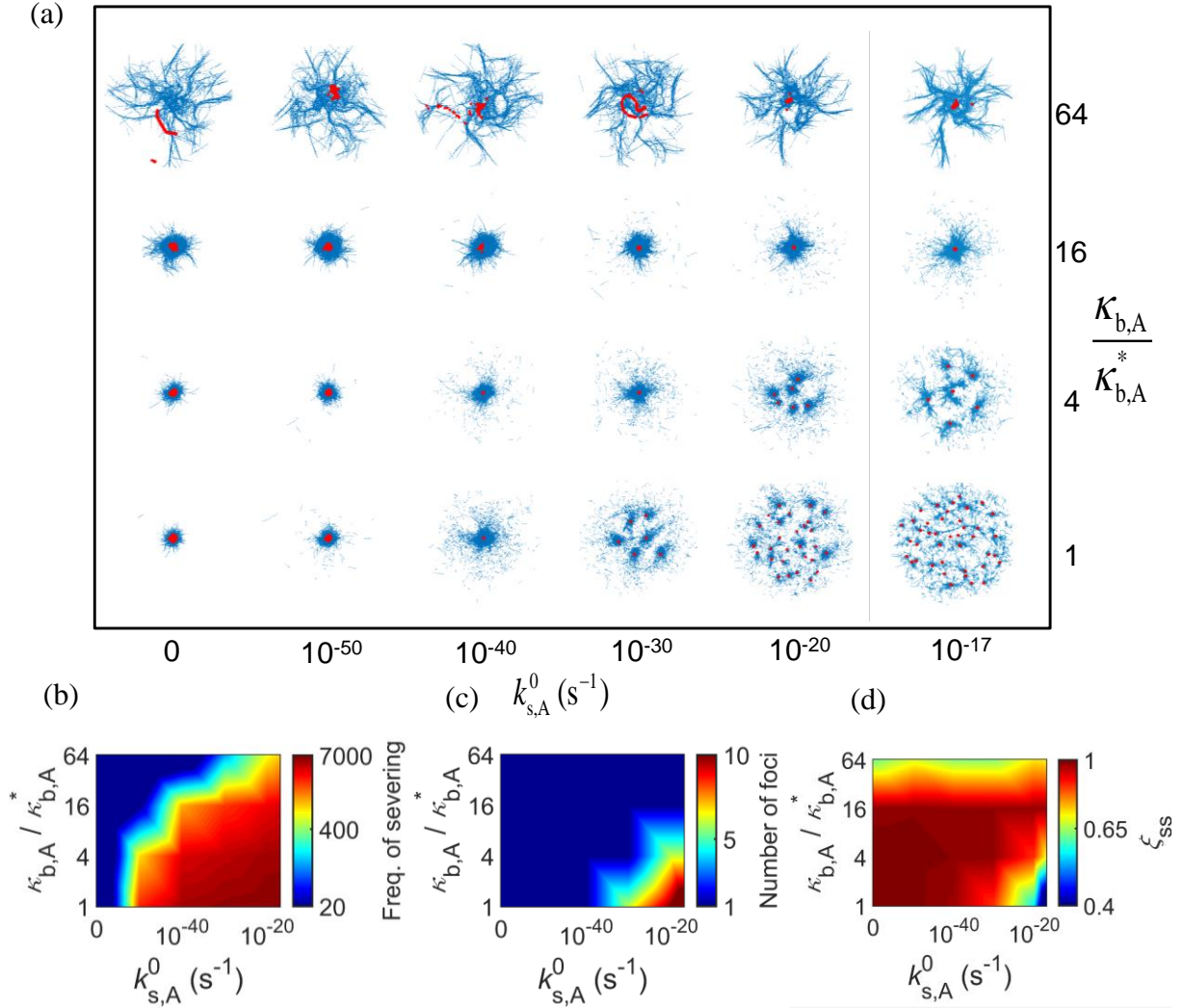


Fig. 2.4 If filaments can be severed due to buckling, intermediate bending rigidity can lead to the largest network contraction. We evaluated network contraction with diverse bending stiffness of filaments ( $\kappa_{b,A}$ ) and zero-angle severing rate constant ( $k_{s,A}^0$ ) at  $R_M = 0.08$  and  $R_{ACP} = 0.02$ . (a) Morphology of networks with actins and motors represented by blue and red, respectively. (b) Frequency of filament severing. (c) Number of foci measured at a steady state. (d)  $\zeta_{ss}$  evaluated at a steady state. If  $\kappa_{b,A}$  is very high, buckling is inhibited, leading to small contraction and formation of motor foci and aster-like actin structures. Higher  $k_{s,A}^0$  and lower  $\kappa_{b,A}$  result in formation of multiple foci with small contraction because filament severing occurs very frequently under such conditions, severely deteriorating network connectivity. Thus, optimal intermediate  $\kappa_{b,A}$  exists at high  $k_{s,A}^0$ .



### *Networks containing more motors and fewer ACPs show optimal $\kappa_{b,A}$ more apparently*

We further investigated conditions under which the optimal intermediate  $\kappa_{b,A}$  exists (Figs. 2.5, 2.6).  $k_{s,A}^0$  is fixed at  $10^{-30} \text{ s}^{-1}$  while  $R_{ACP}$  is varied significantly from the reference value, 0.02, and  $\kappa_{b,A}$  is increased up to a 64-fold higher value as before (Fig. 2.5). F-actin buckling occurs more frequently at higher  $R_{ACP}$  (Fig. 2.5b), which is consistent with our previous study [114]. Buckling of F-actins highly confined by many cross-linking points results in sharp curvature (i.e. large local bending angle), facilitating numerous severing events. Note that the highest  $R_{ACP}$  tested here is 0.08 which is much lower than the critical  $R_{ACP}$  in Fig. 2.2c above which buckling is inhibited,  $\sim 0.32$ . By contrast, if F-actins are loosely confined, buckling with mild curvature is not always followed by severing. It was observed the existence of the optimal intermediate  $\kappa_{b,A}$  is more conspicuous at lower  $R_{ACP}$  (Fig. 2.5d). Interestingly, at high  $R_{ACP}$ , the contraction is very large and leads to a single focus despite numerous severing events since enhancement of network connectivity via more ACPs is superior to deterioration of connectivity induced by F-actin severing during contraction (Figs. 2.5a, c). Since severing takes place in conjunction with an increase in effective actin concentration during contraction, ACPs can cross-link fragmented short F-actins. This is not identical to a situation where very short F-actins are cross-linked by numerous ACPs before contraction. If initial actin concentration is not very high, ACPs cannot cross-link very short F-actins into a percolated network regardless of their density. We also observe that  $\tau_{ss}$  is greater with higher  $R_{ACP}$  because networks become much stiffer and thus resist contraction to a much higher degree under such conditions.  $\tau_{ss}$  is still proportional to  $\kappa_{b,A}$  as seen in Fig. 2.7. As a result, the average contraction rate is greater with higher  $R_{ACP}$  and lower  $\kappa_{b,A}$  (Fig. 2.8).

We also varied  $R_M$  from a reference value, 0.08, with  $R_{ACP}$  fixed at 0.02 in order to probe the importance of an amount of motors for network contraction (Fig. 2.6). With higher  $R_M$ , frequency of F-actin severing and the number of foci after full contraction tend to be greater because stronger forces exerted by more motors make more filaments buckled and thus severed (Figs. 2.6b, c). Since  $R_{ACP}$  is constant, this leads to significant reduction of network connectivity. As a result, networks show more apparent optimal intermediate  $\kappa_{b,A}$  with higher  $R_M$  (Fig. 2.6d). Interestingly, this is opposite to the outcome obtained by an increase in  $R_{ACP}$  (Fig. 2.5d). Since larger forces can contract networks faster,  $\tau_{ss}$  is smaller with greater  $R_M$  (Fig. 2.9). As a result, the average contraction rate is greater with higher  $R_M$  and lower  $\kappa_{b,A}$  (Fig. 2.9).

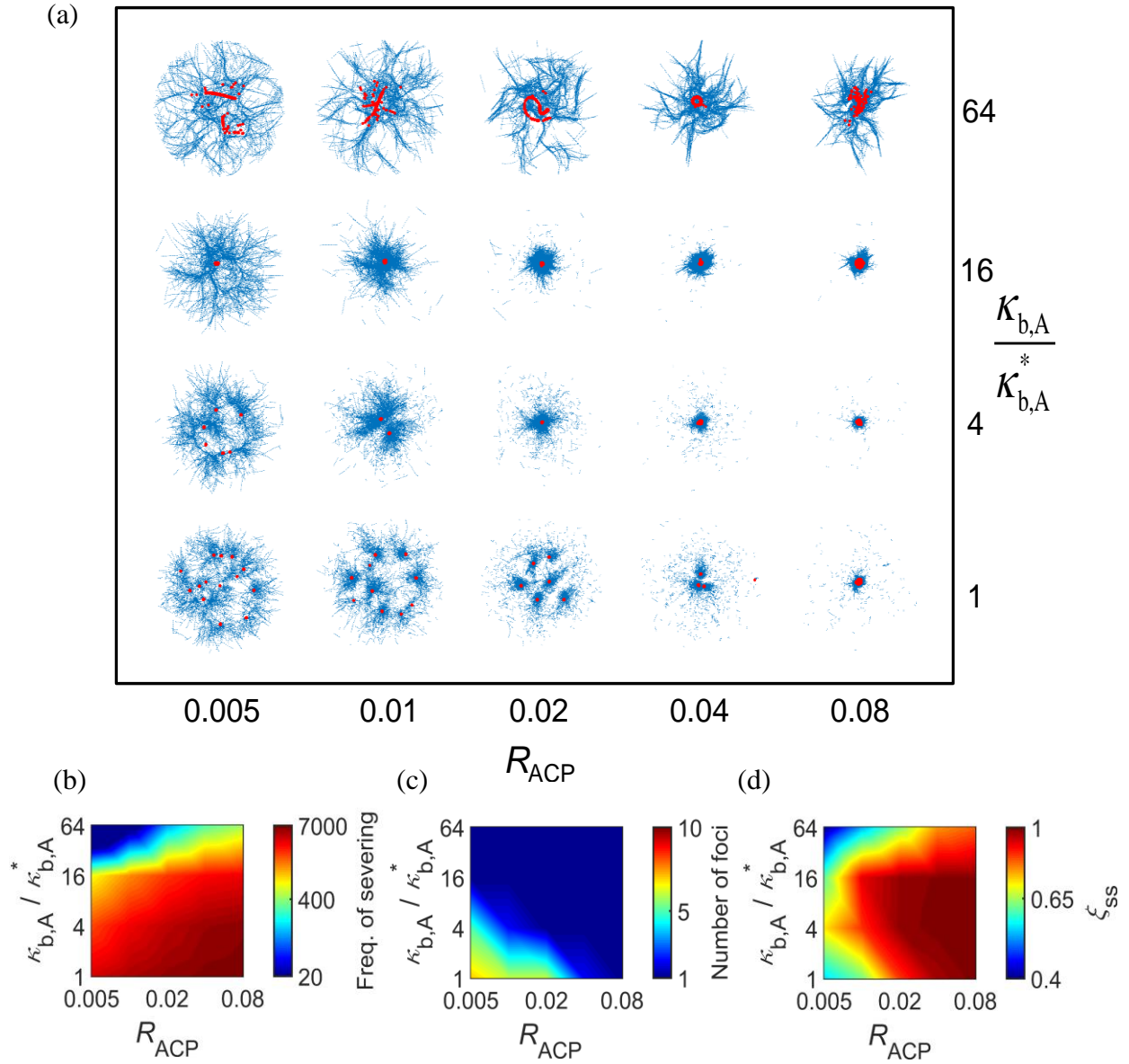


Fig. 2.5 The optimal intermediate bending rigidity is more apparent in loosely cross-linked networks. We probed network contraction over a wide range of  $R_{ACP}$  and  $\kappa_{b,A}$  with  $\kappa_{s,A}^0 = 10^{-30} \text{ s}^{-1}$  and  $R_M = 0.08$ . Here, the range of  $R_{ACP}$  is narrowed to 0.005-0.08 to consider only a regime where significant network contraction appears without F-actin severing in Fig. 2c. (a) Network morphology showing actins (blue) and motors (red). (b) Frequency of filament severing. (c) Number of foci evaluated at a steady state. (d)  $\zeta_{ss}$  measured at a steady state. If  $R_{ACP}$  is smaller, the range of  $\kappa_{b,A}$  leading to large contraction becomes narrower. By contrast, if  $R_{ACP}$  is sufficiently high, networks contract to a single focus regardless of  $\kappa_{b,A}$  despite much more frequent severing events because enhancement of network connectivity resulting from more ACPs is superior to deterioration of connectivity induced by F-actin severing during contraction.

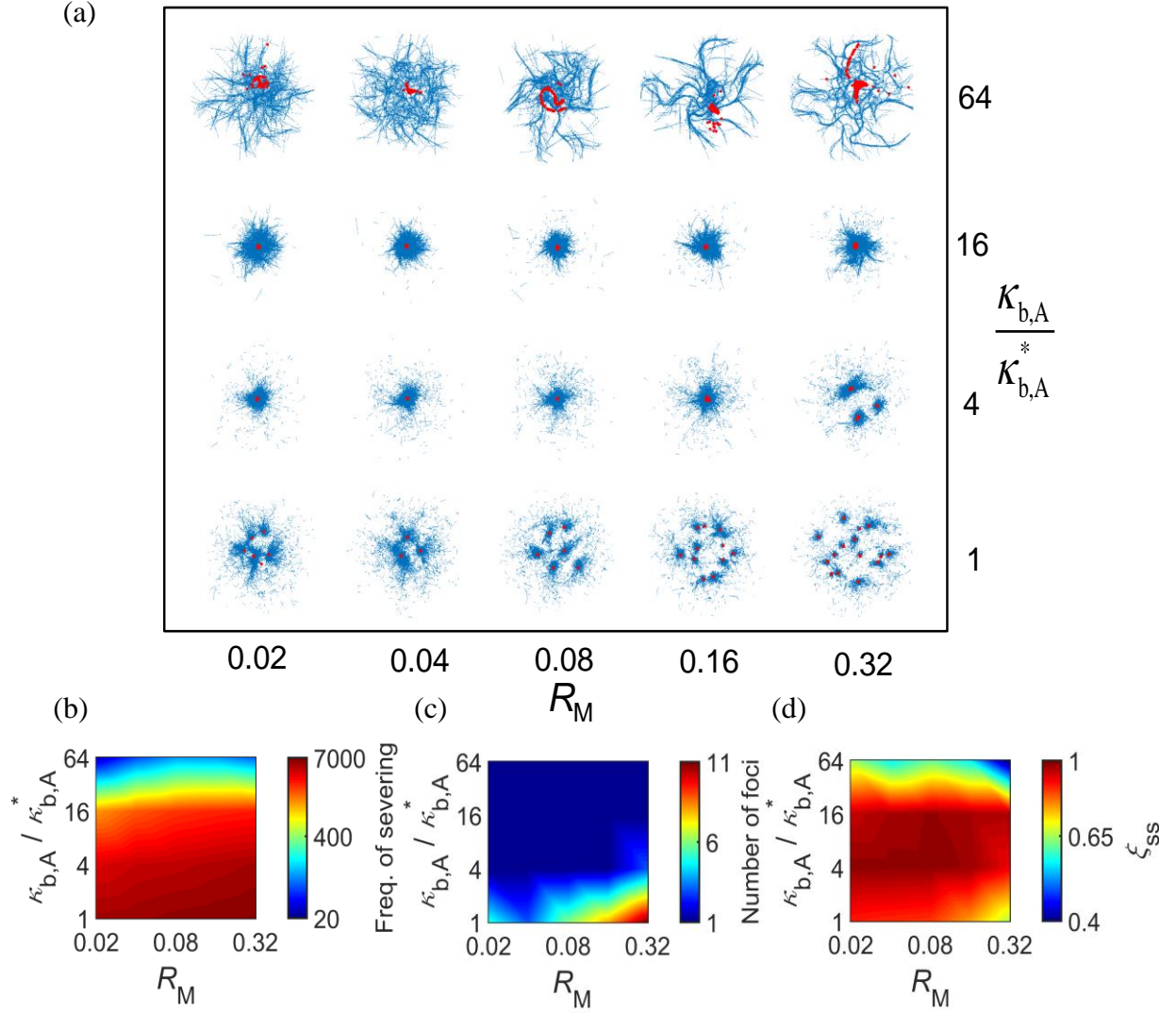


Fig. 2.6 With more motors, the optimal intermediate bending rigidity is more conspicuous. Network contraction was measured over a wide range of  $R_M$  and  $\kappa_{b,A}$  with  $k_{s,A}^0 = 10^{-30} \text{ s}^{-1}$  and  $R_{ACP} = 0.02$ . (a) Morphology of networks with actins (blue) and motors (red). (b) Frequency of filament severing. (c) Number of foci measured at a steady state. (d)  $\xi_{ss}$  at a steady state. If there are a larger number of motors, more filaments are buckled and severed during contraction because larger compressive forces are exerted on filaments. Since  $R_{ACP}$  is constant in all cases, networks experiencing more severing events have poorer connectivity. Thus, an increase in  $R_M$  leads to formation of multiple foci and small contraction at low  $\kappa_{b,A}$  and low contraction at high  $\kappa_{b,A}$ , making the optimal intermediate  $\kappa_{b,A}$  more apparent.

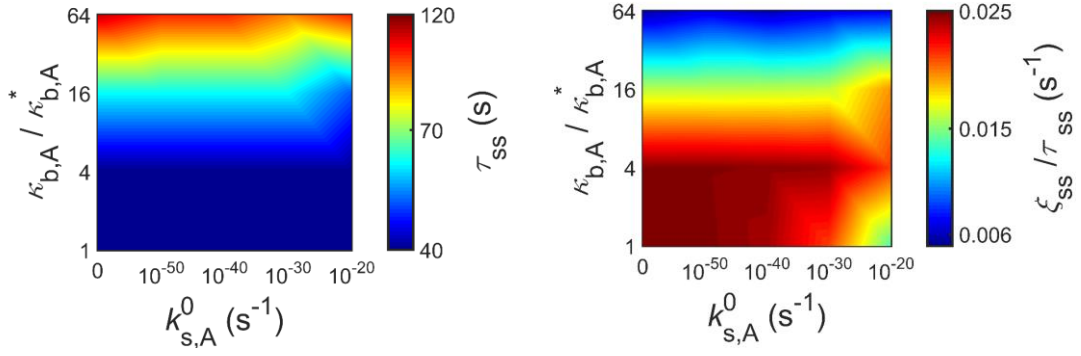


Fig. 2.7 Time required for reaching the steady state of contraction ( $\tau_{ss}$ ) and average contraction rate which corresponds to  $\xi_{ss} / \tau_{ss}$ , at various  $k_{s,A}^0$  and  $\kappa_{b,A}^*$ .

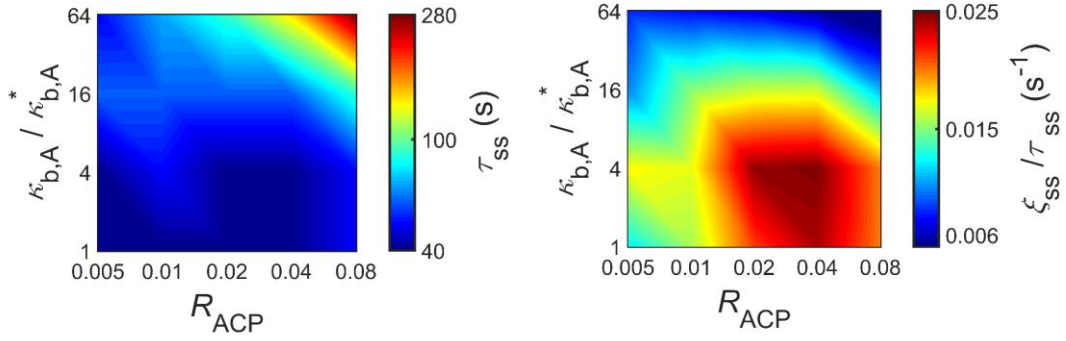


Fig. 2.8  $\tau_{ss}$  and average contraction rate over a wide range of  $R_{ACP}$  and  $\kappa_{b,A}^*$ .

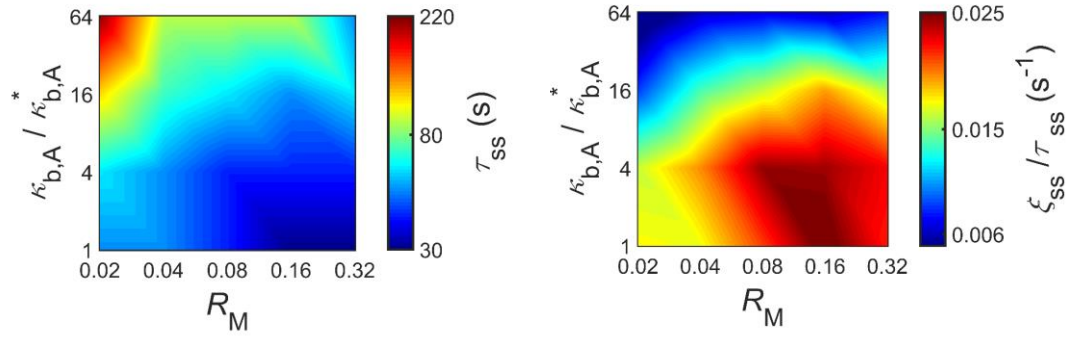


Fig. 2.9  $\tau_{ss}$  and average contraction rate at various  $R_M$  and  $\kappa_{b,A}^*$ .

### 2.3.4 Conclusion and discussion

Based on results from this study, we conclude that actomyosin networks consisting of severable filaments can be in three different states after contraction: i) a single focus with large contraction, ii) a single focus with negligible contraction due to inhibition of F-actin buckling, iii) multiple foci with small contraction due to severe F-actin severing (Fig. 2.10a). Through further exploration of parametric spaces, we created a three-dimensional phase diagram involved with four factors: motor density ( $R_M$ ), ACP density ( $R_{ACP}$ ), zero-angle severing rate constant ( $k_{s,A}^0$ ), and bending stiffness of F-actin ( $\kappa_{b,A}$ ) (Fig. 2.10b).

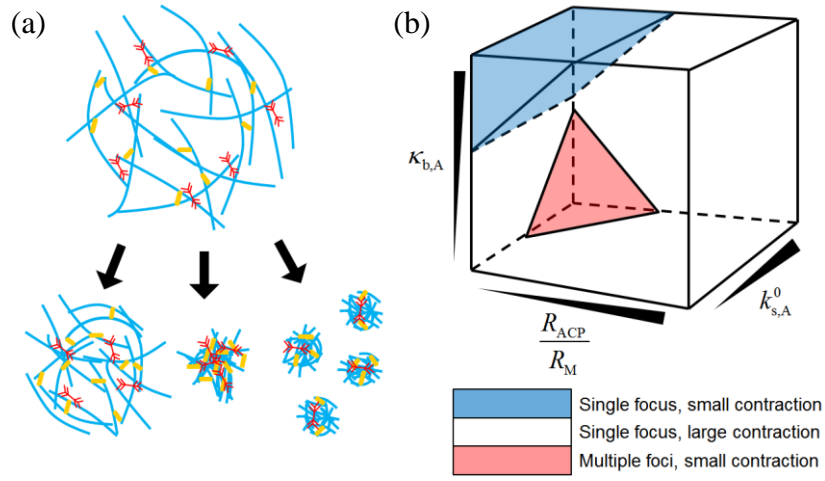


Fig. 2.10 Actomyosin networks contract to either of three possible states depending on bending stiffness of F-actin ( $\kappa_{b,A}$ ), zero-angle severing rate constant ( $k_{s,A}^0$ ), ACP density ( $R_{ACP}$ ), and motor density ( $R_M$ ). (a) The three possible states are i) small contraction with a single focus (left), ii) large contraction with a single focus (middle), and iii) small contraction with multiple foci (right). (b) Three-dimensional phase diagram showing regimes for the three states.

Under most conditions, networks exhibit large contraction into a single focus. However, if the ratio of  $R_{ACP}$  to  $R_M$  is low, two other regimes emerge. With sufficiently high  $\kappa_{b,A}$ , networks do not show large contraction because most of F-actins are not buckled. The critical  $\kappa_{b,A}$  above which contraction becomes substantially small is proportional to  $R_{ACP}/R_M$ . Since F-actins are hardly buckled, the critical  $\kappa_{b,A}$  is not dependent on  $k_{s,A}^0$ . By contrast, at small  $\kappa_{b,A}$ , F-actins are severed frequently if  $k_{s,A}^0$  is high. These severing events can be critical for network contraction if  $R_{ACP}/R_M$  is low since an insufficient number of ACPs cannot provide enough network connectivity to rescue

a network from the deterioration of connectivity induced by severing. Thus, multiple foci appear as a result of contraction. Due to these two regimes with small contractions, an optimal level of  $\kappa_{b,A}$  leading to the largest contraction exists above a certain level of  $k_{s,A}^0$ , which has not been identified in any previous study. Recent theoretical studies predicted that network contraction will always be suppressed with higher  $\kappa_{b,A}$  because they did not consider the possibility of F-actin severing induced by buckling. This novel finding provides a more comprehensive, realistic view about the contraction of actomyosin networks. We will extend our study by incorporating actin turnover dynamics, such as polymerization, depolymerization, and capping to capture and study network contraction under more physiologically relevant conditions.

## 2.4 Pulsatile contraction of actomyosin network

### 2.4.1 Background

Forces produced from actomyosin contractility facilitate a wide variety of morphogenetic phenomena at cell and tissue scales [109]. For example, contractility induces cortical flows of the cortex for formation of cytokinetic furrow and drives polarization in the one-cell stage *C. elegans* embryo [135, 136]. In addition, during invagination of *Drosophila* mesoderm cells, anisotropic generation of forces from actomyosin cortex drives apical constriction [10]. Interestingly, in these morphogenetic events, the actomyosin cortex exhibits pulsed contraction; F-actin and myosin II proteins show transient accumulation followed by scattering at various length scales, rather than irreversible accumulation [136, 137]. It has been suggested that the local accumulation of F-actin and myosin originates from contractile instability which inevitably exists in highly contractile actomyosin cortex [121, 138]. The contractile instability is controlled by a spatiotemporal oscillator of RhoA that regulates myosin motor activity, which enables cells to use an intrinsically unstable contractile cortex for driving morphogenetic processes. As a result of the instability control, pulsed contraction emerges in the cortex. To understand how actomyosin contractility facilitates these morphogenetic phenomena, various methods have been applied for perturbing the constituents of actomyosin machinery in cells. However, there are limitations on the extent of perturbation, and results obtained from perturbation are often too unclear to understand how the actomyosin contractility works in cells.

Thus, alternatively, contractile behaviors driven by the actomyosin contractility have been extensively studied in recent works using computational and theoretical models as well as reconstituted actomyosin systems. It was demonstrated that the architecture and connectivity of actomyosin networks can significantly affect pattern formation [121, 125, 139]. In addition, it was shown that force-dependent unbinding of ACPs from F-actin plays a critical role for a change in force generation and morphology of actomyosin networks [127, 140]. Recently, buckling of F-actin was found to be crucial for large contraction of networks into small clusters [123, 125], consistent with a theoretical prediction [124]. We recently suggested that buckling-induced severing of F-actin can also be very important for contraction of actomyosin networks [141]. Several recent studies demonstrated that actin turnover stabilizes stress generated by actomyosin networks and helps maintain homogeneous network morphology by counteracting motor activity [82, 142, 143]. Although these previous studies have provided insights into understanding of contractile behaviors of actomyosin networks in general, most of them could not recapitulate the pulsed contraction observed during morphogenetic events. They showed only existence of two different states: irreversible aggregation without disassembly of clusters after formation or negligible contraction which represents a homogeneous network. One study showed coalescence and breakage of actomyosin clusters observed in their *in vitro* experiments. However, it used an artificial assumption for the phenomenological model that the unbinding rate of motors highly increases within clusters in order to enforce clusters to spontaneously break into two or three pieces. In addition, their observation on the coalescence and breakage of clusters is intrinsically different from the pulsed contraction that occurs via gradual growth and shrinkage of clusters. A recent computational study claimed that pulsed contraction can appear when F-actins turn over [144]. However, they simulated the actin turnover by removing and adding entire F-actins at a fixed rate, which may not be physiologically relevant. In addition, the size of clusters emerging in their simulation showed fluctuation without complete disassembly of clusters. The lack of observations on the pulsed contraction in these previous computational, theoretical, and *in vitro* studies raises the question of whether the spatiotemporal biochemical control is indispensable for pulsed contraction of actomyosin networks.

To address this question and identify the necessary conditions for the emergence of pulsed contraction, we employed a well-established agent-based model for simulating a very thin actomyosin network consisting of F-actin, motor, and ACP [80, 82, 127, 141]. First, we explored

parametric spaces consisting of the turnover rate and length of F-actin and the density of ACPs to identify the regimes in which pulsed contraction occurs. Via quantitative analysis of dynamic changes in network morphology, we found the pulsed contraction can appear without the spatiotemporal biochemical control if force generation from motors is in the balance with force relaxation induced by F-actin treadmilling. However, we observed that average size of clusters formed during pulsed contraction is much smaller than that observed during the morphogenetic events. If cluster size increases beyond a critical level, the clusters either continuously grow or shrink slowly. We found that inclusion of buckling-induced severing of F-actin enables larger clusters to be disassembled quickly, leading to strong pulsed contraction with much larger clusters. However, if there is only severing without treadmilling, F-actins are shortened over time and thus unable to form large, pulsed clusters consistently. We concluded that both local force relaxation via F-actin severing and turnover of F-actin via treadmilling are necessary for strong pulsed contraction in actomyosin networks.

## 2.4.2 Additional method

### *F-actin turnover and severing*

Formation of F-actin begins from a nucleation event with appearance of one cylindrical segment with polarity in a random direction perpendicular to the  $z$  direction. Polymerization and depolymerization of actins are simulated by addition and removal of one cylindrical segment, respectively, as in our previous studies [82]. Via spatiotemporal control of rate constants governing the nucleation, polymerization, and depolymerization, we can simulate various types of actin turnover facilitated by actin binding proteins, such as cofilin, formin, and capping proteins. However, to avoid unnecessary complexity and uncertainty, we employed the simplest form of actin turnover, treadmilling [82]. In order to mimic the F-actin treadmilling, we assumed that polymerization and depolymerization occur only at barbed ends and pointed ends, respectively. It was further assumed that a rate constant governing polymerization ( $k_{+,A}$ ) has the same value as that governing depolymerization ( $k_{-,A}$ ), which results in a dynamic equilibrium at actin concentration of  $1 \mu\text{M}$ . We define a turnover rate ( $k_{t,A}$ ) to indicate the rate of actin treadmilling, and the value and unit of  $k_{t,A}$  are identical to those of  $k_{-,A}$ . By adjusting the ratio of the nucleation rate constant ( $k_{n,A}$ ) to  $k_{t,A}$ , average length of F-actin ( $\langle L_f \rangle$ ) is varied between  $0.7 \mu\text{m}$  and  $5.0 \mu\text{m}$ . This range of



$\langle L_f \rangle$  is smaller than that used in typical reconstituted actomyosin networks without control of F-actin length ( $\sim 20 \mu\text{m}$ ) [145, 146]. However, the range is very comparable to that estimated in the cell cortex [147, 148]. In addition, for some of the simulations, we employed angle-dependent F-actin severing as in our recent work [141]. F-actin severing is mimicked in a simulation by eliminating one actin segment on F-actin. To determine a segment to eliminate, the sum of bending angles at two ends of each actin segment ( $\theta_{s,A}$ ) is calculated. Then, the severing rate is calculated from Eq. 2.9. The relationship in Eq. 2.9 was found empirically by comparing with *in vitro* experiments [129] as explained and justified in Appendix B. Although we devised Eq. 2.9 without a rigorous physical basis, it reflects an experimental observation that severing takes places only at a large bending angle (i.e. a small radius curvature). Our results are insensitive to the choice of a specific model for F-actin severing.

### ***Quantification of network heterogeneity***

We evaluate the heterogeneity of network morphology by measuring spatial distributions of F-actins in the computational domain. For measurement, the domain is divided into  $N_G \times N_G$  grids in x and y directions, where  $N_G$  indicates the number of grids in each direction. Each grid has its coordinate,  $(i, j)$ . We measure the number of actin segments located in each grid,  $\rho_A^{i,j}$ , in order to create the 3D histogram representing their density map. Then, standard deviation of  $\rho_A^{i,j}$  calculated over all grids is considered as an indicator for the heterogeneity of network morphology,  $Q_A$ . Since the heterogeneity calculated in this method depends on the choice of  $N_G$ , we carefully determined the optimal range of  $N_G = 10\text{-}20$ .

As an additional measure for heterogeneity, we employ an analysis method used in a previous study [149]. First, we randomly choose 1% of actin segments and calculate distances between them. We calculate a radial distribution function,  $g(r)$ , as a histogram with a bin size  $\delta r$ :

$$g(r) = P(r) / (2\pi r \delta r \rho_a) \quad (2.11)$$

where  $\rho_a$  represents the density of selected actin segments calculated over a whole network, and  $P(r)$  is the probability of actin segments with a separate distance between  $r$  and  $r + \delta r$ .  $r$  is varied from 50 nm to 1  $\mu\text{m}$  with an increment of  $\delta r = 50$  nm. Smaller  $\delta r$  enables smoother radial distribution curve and transition. Higher peaks at low  $r$  indicate that a network is highly heterogeneous. By contrast, a very homogeneous network leads to  $g(r) \sim 1$  for all  $r$  values.

### *Quantitative analysis of motor motions and clustering*

To evaluate how fast motors move at each time point, we quantify their average speed. We track the center position of each motor over time,  $\mathbf{r}_{i,M}$ , where  $i$  is an index of a motor. Since the domain is very thin in the  $z$  direction, we assumed that  $\mathbf{r}_{i,M}$  has only  $x$  and  $y$  components. Then, ensemble average of speed of motors is calculated every 1 sec:

$$\langle v_M(t) \rangle = \frac{1}{N_M} \sum_{i=1}^{N_M} v_{i,M}(t) = \frac{1}{N_M} \sum_{i=1}^{N_M} \frac{|\mathbf{r}_{i,M}(t) - \mathbf{r}_{i,M}(t-1)|}{1 \text{ s}} \quad (2.12)$$

where  $N_M$  is the total number of motors. For a certain time range, we calculate time average of the ensemble average:

$$\langle v_M \rangle_{t_1 \rightarrow t_2} = \frac{1}{t_2 - t_1} \sum_{t=t_1}^{t_2} \langle v_M(t) \rangle \quad (2.13)$$

where  $t_1$  and  $t_2$  are lower and upper limits of the time range of interest. If the time interval is shorter than 1 s, the calculated speed becomes noisier because influences of thermal fluctuation on motor motions are not averaged out sufficiently. If the time interval is too long, the number of data points is not enough to calculate  $\langle v_M \rangle_{t_1 \rightarrow t_2}$ . We therefore used the time interval of 1 s for the best analysis of motor motions.

We probed the onset and emergence of pulsed contraction in an actomyosin network. In the density map of actin segments explained above, all adjacent grids whose density and duration are above threshold values are grouped and considered to be a single cluster. Since results of quantification can significantly vary depending on the threshold value, we carefully chose the threshold values of density and duration. Then, we calculate the center position of each cluster and the number of actin segments that belong to each cluster. This analysis is repeated for all data recorded every 1 s. We then correlated clusters at one time point to those at a next time point. Two clusters in consecutive time points will be regarded as the same cluster if two primary criteria are met. First, the distance between centers of two clusters should not be larger than a chosen threshold. The threshold value is assumed to be proportional to size of clusters. Second, the difference in the number of actin segments in the two clusters should not be larger than half of the number of actin segments in the cluster at a later time point. When two or more clusters are merged, one of the clusters at a previous time point will share the same identity of a merged cluster at a

next time point. Only the cluster with the longest history will be kept. For instance, if two clusters that are merged later started emerging from different time points, one formed earlier would be kept and linked to the merged cluster while the other formed later would be ignored for the analysis. In addition, we ignore clusters that last for less than 20 s to avoid counting trivial small structures. The threshold value for the minimum duration was also chosen carefully as explained in Supporting Information.

Formation of clusters requires persistent movement of motors toward a specific point. We probed how persistently motors move over time. First, we calculate the ensemble average of velocities of all motors located in each grid,  $\mathbf{v}_M^{i,j}(t)$ , and then analyze the autocorrelation of  $\mathbf{v}_M^{i,j}$  as a measure for persistency of the velocities over time:

$$\langle \cos \phi(t) \rangle = \frac{1}{N_G^2} \sum_{i=1}^{N_G} \sum_{j=1}^{N_G} \cos \phi_{i,j}(t) = \frac{1}{N_G^2} \sum_{i=1}^{N_G} \sum_{j=1}^{N_G} \frac{\mathbf{v}_M^{i,j}(t) \cdot \mathbf{v}_M^{i,j}(t+\tau)}{|\mathbf{v}_M^{i,j}(t)| |\mathbf{v}_M^{i,j}(t+\tau)|} \quad (2.14)$$

where  $\tau$  is 1 s. Values of  $\langle \cos \phi \rangle$  are averaged between 10 s and 20 s, representing dynamics of the motors at early time points when a network exhibits very active aggregating behaviors in all cases. Note that the average value of  $\langle \cos \phi \rangle$  close to 1 is indicative of very persistent motions of motors which are the signature of clustering.

### 2.4.3 Results

In this study, we performed simulations under various conditions in order to study the contractile behaviors of 2D actomyosin networks. We varied the turnover rate ( $k_{l,A}$ ), severing rate ( $k_{s,A}$ ), and average length ( $\langle L_f \rangle$ ) of F-actin and cross-linking density ( $R_{ACP}$ ) in the simulations, whereas we fixed actin concentration ( $C_A$ ) at 60  $\mu\text{M}$  and motor density ( $R_M$ ) at 0.04.

#### *Turnover of F-actin suppresses cluster formation*

In recent computational studies [142-144, 150-152], it was shown that actin turnover prevents motors from forming aggregation in 2D and 3D actomyosin networks as well as stabilizes stress generated from the networks by relaxing forces produced from motor activities. As in our previous study [82], we implemented the simplest form of turnover, treadmilling of F-actin, by imposing identical rate constants for polymerization at a barbed end and depolymerization at a

pointed end. Despite its simplicity, the treadmilling is more realistic turnover dynamics than abrupt disappearance and appearance of F-actins employed in recent computational studies [142-144].

We imposed  $k_{t,A}$ , which represents a treadmilling rate, between  $15 \text{ s}^{-1}$  and  $240 \text{ s}^{-1}$  with  $R_{ACP} = 0.02$  and  $\langle L_f \rangle = 1.6 \text{ } \mu\text{m}$ . With the lowest  $k_{t,A} = 15 \text{ s}^{-1}$ , a large portion of a network aggregates into a large cluster, resulting in very heterogeneous F-actin distribution (Figs. 2.11). However, as  $k_{t,A}$  increases, networks tend to be more homogeneous with less distinct, smaller clusters as force relaxation is elevated. We also analyzed motor activities in a quantitative manner. With lower  $k_{t,A}$ , motors move persistently toward centers of the clusters and move much slower after formation of clusters (Figs. 2.11b, c). With higher  $k_{t,A}$ , motors exhibit less persistent movements since motors cannot stably walk on F-actins that turn over rapidly via treadmilling (Fig. 2.11b). In addition, since a network does not aggregate significantly, the average speed of motors does not change much over time (Fig. 2.11c).

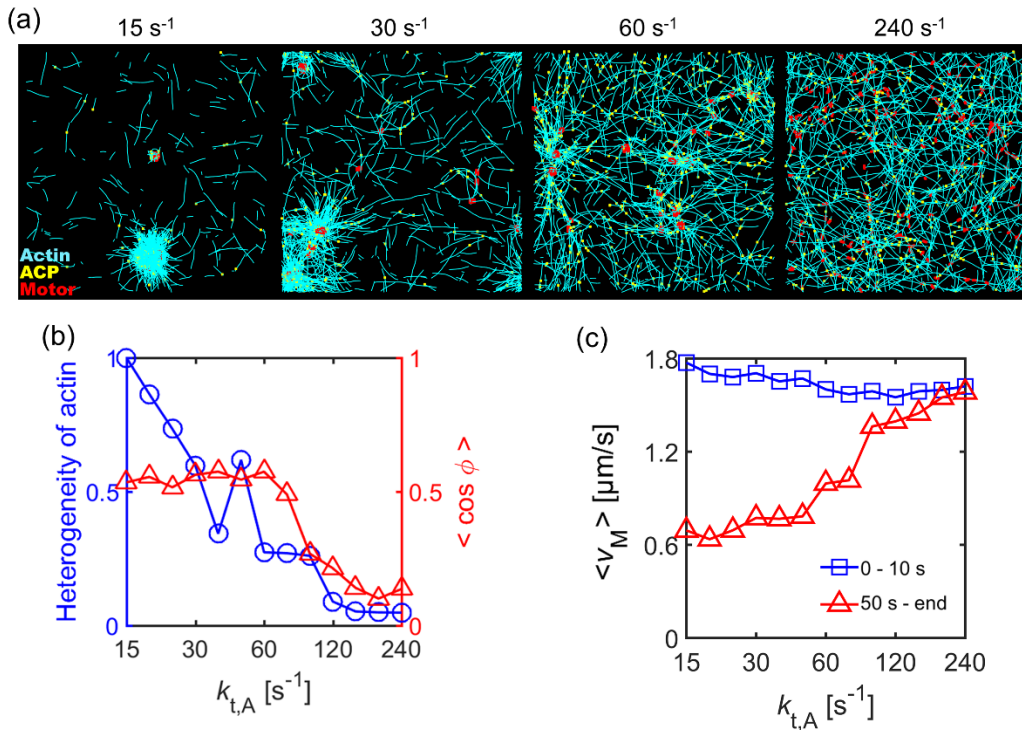


Fig. 2.11 Network contraction is regulated by F-actin turnover. We varied actin turnover rate ( $k_{t,A}$ ) between  $15 \text{ s}^{-1}$  and  $240 \text{ s}^{-1}$  at  $R_M = 0.04$ ,  $R_{ACP} = 0.02$ , and  $\langle L_f \rangle = 1.6 \text{ } \mu\text{m}$ . (a) Morphology of networks at 65 s with four different  $k_{t,A}$ . (b) Heterogeneity of F-actin distribution (blue circle) and  $\langle \cos \phi \rangle$  indicating persistency of motor velocities between 10 s and 20 s (red triangle) depending on  $k_{t,A}$ . The heterogeneity monotonically decreases as  $k_{t,A}$  increases. At low  $k_{t,A}$ , motors tend to move persistently over time, but as  $k_{t,A}$  increases, motors exhibit less persistent motions because F-actins undergo rapid turnover without formation of large clusters. (c)

Average speed of motors at early times (0-10 s, blue square) and late times (from 50 s till end, red triangle) as a function of  $k_{t,A}$ . While the average speed hardly changes at high  $k_{t,A}$ , it is significantly reduced over time at low  $k_{t,A}$ .

### ***Network connectivity critically affects contraction***

It has been shown that network connectivity plays a critical role for contractile behaviors of actomyosin networks [125]. We recently demonstrated that a cross-linked actomyosin network in the absence of actin turnover shows maximal contraction at intermediate level of  $R_{ACP}$  because poor connectivity prevents motors from stably generating forces between pairs of F-actins, whereas too high connectivity leads to strong resistance of the network to contraction due to high network elasticity [141]. This is consistent with previous experimental results [73], and reproduced in other computational study later [144].

In the presence of slow actin turnover ( $k_{t,A} = 30 \text{ s}^{-1}$ ), we systematically tested influences of  $R_{ACP}$  and  $\langle L_f \rangle$  that are likely to govern network connectivity. It was observed that a change in  $R_{ACP}$  and  $\langle L_f \rangle$  has similar effects on network contraction. With very poor network connectivity due to low  $R_{ACP}$  or  $\langle L_f \rangle$ , a network hardly contracts or contracts into multiple small clusters, but as connectivity increases, a single, large cluster is formed from aggregation of F-actins (Figs. 2.12a, 2.13a). A further increase in connectivity suppresses formation of disconnected clusters, resulting in a network consisting of interconnected bundles. Thus, at intermediate connectivity, spatial distribution of F-actins is the most heterogeneous, and motors exhibit the most persistent movements toward centers of large clusters (Figs. 2.12b, 2.13b). In addition, the average speed of motors at early times is the highest at intermediate connectivity due to large contraction into a single cluster (Figs. 2.12c, 2.13c). The average speed becomes much lower at late times in most cases where networks show large contraction into clusters or bundle networks. However, at very low  $R_{ACP}$ , a decrease in the average speed of motors is less significant because the network does not form distinct clusters.

### ***Force generation and relaxation leads to weak pulsed contraction***

By analyzing morphological changes in networks, we probed the existence of pulsed contraction.

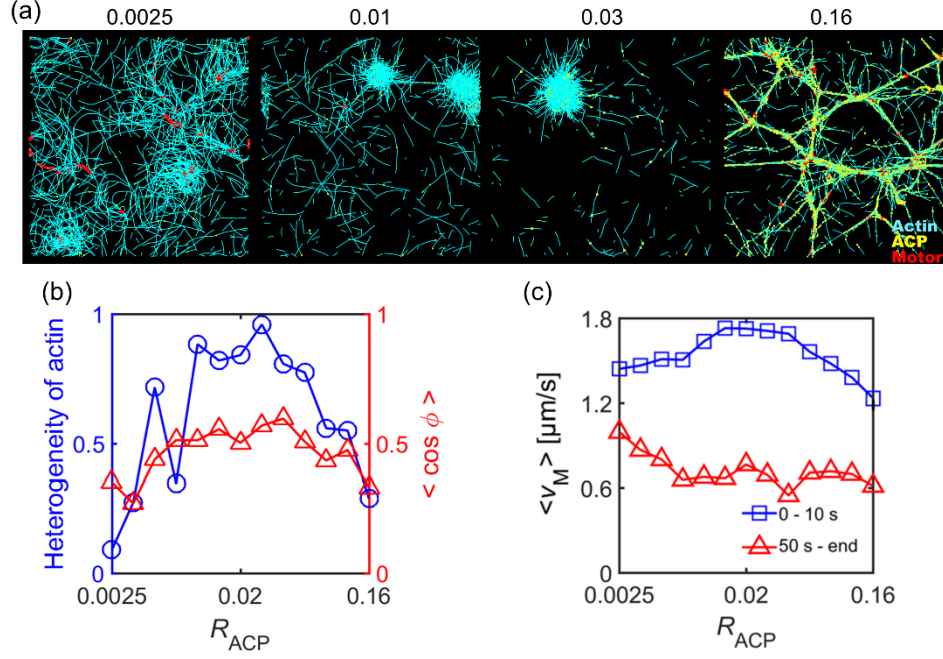


Fig. 2.12 ACPs regulate contractile behaviors of networks. We changed ACP density ( $R_{ACP}$ ) between 0.0025 and 0.16 at  $R_M = 0.04$ ,  $\langle L_f \rangle = 1.6 \mu\text{m}$ , and  $k_{tA} = 30 \text{ s}^{-1}$ . (a) Morphology of networks at 65 s depending on  $R_{ACP}$ . (b) Heterogeneity and persistency of motor velocities. (c) Average speed of motors at early and late times.

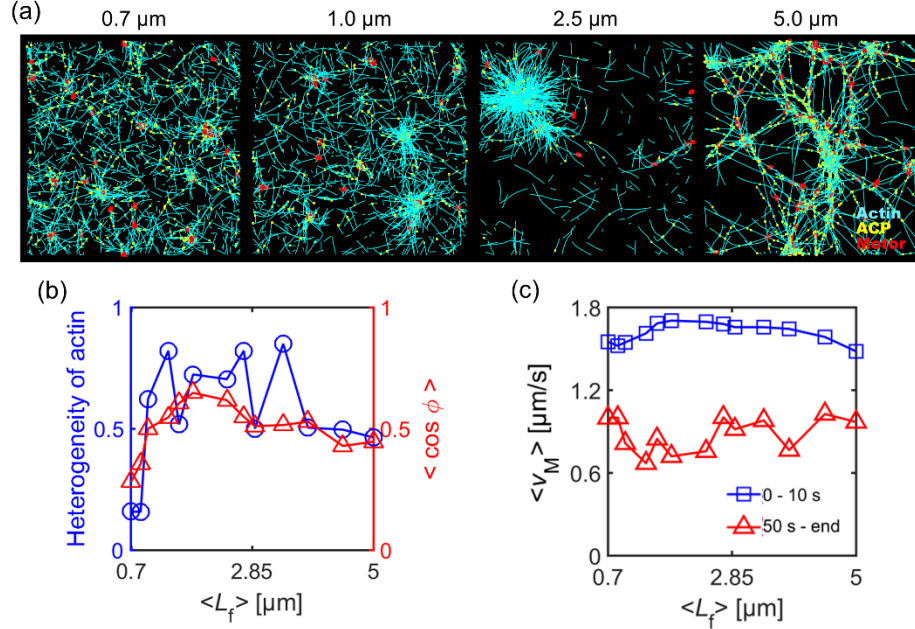


Fig. 2.13 Average length of F-actins ( $\langle L_f \rangle$ ) highly affects network contraction in a similar fashion to  $R_{ACP}$ . We varied  $\langle L_f \rangle$  between 0.7  $\mu\text{m}$  and 5.0  $\mu\text{m}$  at  $R_M = 0.04$ ,  $R_{ACP} = 0.02$ , and  $k_{tA} = 30 \text{ s}^{-1}$ . (a) Morphology of networks at 65 s depending on  $\langle L_f \rangle$ . (b) Heterogeneity and persistency of motor velocities. (c) Average speed of motors at early and late times.

Under specific conditions, we observed weak pulsed contraction with very small clusters. F-actins and motors aggregate toward a focal point, but nascent small clusters are disassembled before growing their size (Figs. 2.14a, b), indicating pulsed contraction. This weak pulsed contraction originates from subtle balance between force generation from motor activities and force relaxation induced by actin turnover. To identify types of clusters based on size and duration, we traced individual clusters and measured the percentage of actin segments that belong to each cluster over time. These small pulsed clusters appear by themselves at higher  $k_{t,A}$ . However, at lower  $k_{t,A}$ , they appear with some small clusters that fluctuate in their size till the end of simulations (Figs. 2.14a, c, d). An apparent difference between the nascent pulsed clusters and fluctuating clusters is whether or not complete disassembly occurs soon after formation. Fluctuating clusters form since force relaxation is not fast enough to relax forces generated by actomyosin components. We evaluated the size and duration of nascent clusters during the weak pulsed contraction (Figs. 2.14e, f). The clusters are quite small and do not last for long time with lifetime shorter than 50 s. Note that pulsed clusters observed in cells are typically  $\sim 2\text{-}4\ \mu\text{m}$  in diameter and  $\sim 40$  to  $100$  s in duration [110] .

A previous computational study which demonstrated pulsed contraction with larger clusters employed a different way to account for actin turnover [144]. In their model, a whole F-actin is randomly removed in a domain, and a new F-actin appears in a different location as other studies [142]. Such turnover of entire F-actins can break down multiple connections in clusters at once, enabling large clusters to be disassembled. Although this is an efficient way to induce local, strong force relaxation for pulsed contraction, it is much less physiological than our turnover model. Indeed, pulsed contraction observed in the recent study is more similar to the behavior of fluctuating clusters in our study because sizes of their clusters showed consistent fluctuation without complete disassembly [144].

If we lower  $k_{t,A}$  further, most of the clusters either grow consistently for longer than 100 s until the end of simulation or show relatively fast growth followed by very slow decay although some small nascent clusters still form at early times. None of these clusters is analogous to pulsed clusters observed in cells in terms of size and duration [110]. Thus, it is expected that an additional mechanism of force relaxation is necessary for enabling larger clusters to be disassembled completely within a reasonable time range. Note that in all these simulations, the average length of F-actins remains relatively constant ( $\sim 1\ \mu\text{m}$ ) over time and is independent of  $k_{t,A}$ .

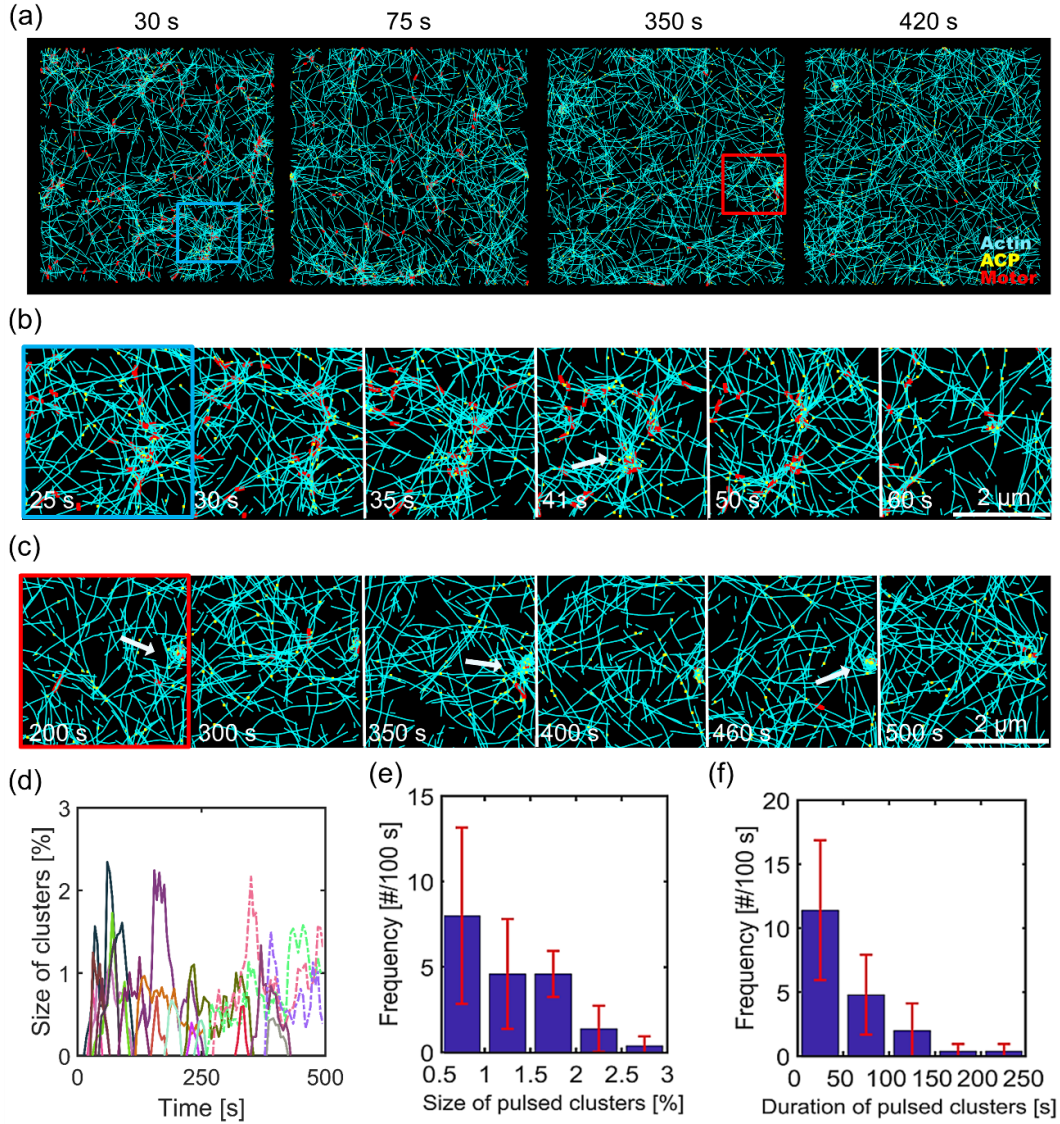


Fig. 2.14 Balance between force generation and relaxation causes weak pulsatile contraction with formation of very small clusters. Conditions used in a case shown here are  $R_M = 0.04$ ,  $R_{ACP} = 0.01$ ,  $\langle L_f \rangle = 1 \mu\text{m}$ , and  $k_{tA} = 70 \text{ s}^{-1}$ . (a) Morphology of networks showing cluster formation taken at different time points. (b) Time evolution of a small pulsed cluster indicated by a blue box in (a). This cluster appears from  $\sim 30 \text{ s}$  and then becomes the largest at  $41 \text{ s}$  as indicated by a white arrow. Then, it disassembles gradually over time. (c) Time evolution of a fluctuating cluster highlighted by a red box in (a). (d) Time evolution of the percentage of actin segments located within clusters. Random colors are assigned to curves to distinguish each cluster. Nascent pulsed clusters are shown in solid lines, whereas fluctuating clusters are shown in dot-dashed lines. (e, f) Frequency of appearance of pulsed clusters per 100 s depending on their size (e) and duration (f). Most clusters are very small and do not last for long time periods.



In addition, we quantified cluster dynamics in a wide parametric space consisting of  $\langle L_f \rangle$ ,  $k_{t,A}$ , and  $R_{ACP}$ . It was observed that the small nascent pulsed clusters appear only in a very narrow regime with short  $\langle L_f \rangle$  ( $\sim 1 \mu\text{m}$ ), intermediate actin turnover rate ( $\sim 70 \text{ s}^{-1}$ ), and low/intermediate network connectivity. It is likely that most of the previous computational studies investigating contractile behaviors of actomyosin networks neglected the appearance of the nascent pulsed clusters since they appear in such a narrow regime.

### ***Angle-dependent severing facilitates strong pulsed contraction***

A recent *in vitro* experiment clearly demonstrated that F-actins undergo severe fragmentation during contraction of actomyosin networks [123]. This fragmentation is likely to originate from angle-dependent severing of F-actin induced by buckling. Our recent computational study also showed that frequent severing events of F-actin can inhibit network contraction [141]. Since F-actin is prone to buckling and more severing at the location where contraction takes place, the severing may relax forces locally within contracting clusters and thus help disassembly of larger clusters for more distinct pulsed contraction. We employed the model of angle-dependent F-actin severing used in our previous study to check influences of severing on the pulsed contraction [141]. We incorporated F-actin severing in a case that showed formation of relatively large clusters without pulsed contraction and varied the zero-angle severing rate constant ( $k_{s,A}^0$ ) between  $10^{-60} \text{ s}^{-1}$  and  $10^{-10} \text{ s}^{-1}$ . It was observed that average length of F-actins remains close to an initial value ( $\sim 1 \mu\text{m}$ ) in all simulations except a case with  $k_{s,A}^0 = 10^{-10} \text{ s}^{-1}$ . When  $k_{s,A}^0$  is very low ( $=10^{-60} \text{ s}^{-1}$ ), severing events hardly occur, so large irreversible clusters are formed. With intermediate values of  $k_{s,A}^0$  ( $10^{-50}$ - $10^{-30} \text{ s}^{-1}$ ), large clusters are still formed, but many of them are disassembled much faster than decaying clusters, indicative of strong pulsed contraction (Figs. 2.15a, 5b). The size and duration of these clusters are very comparable to those of pulsed clusters observed *in vivo*. It was found that more than half of the severing events take place within clusters at these  $k_{s,A}^0$  values (Fig. 2.15c), which implies that buckling arising from contraction of clusters induces F-actin severing and thus relaxation of forces generated by motors within clusters. Note that at  $10^{-50} \text{ s}^{-1} \leq k_{s,A}^0 \leq 10^{-20} \text{ s}^{-1}$ , a greater number of smaller clusters with shorter lifetime ( $< 50 \text{ s}$ ) emerged with higher  $k_{s,A}^0$  (Figs. 2.15c-e). In addition, the percentage of severing events occurring

within clusters decreases, meaning that severing takes place in a less selective manner. If  $k_{s,A}^0$  increases more to  $10^{-10} \text{ s}^{-1}$ , only a few small, pulsed clusters are formed (Figs. 2.15a, c-e). If  $k_{s,A}^0$  is very high, network connectivity is deteriorated, so contraction is impeded.

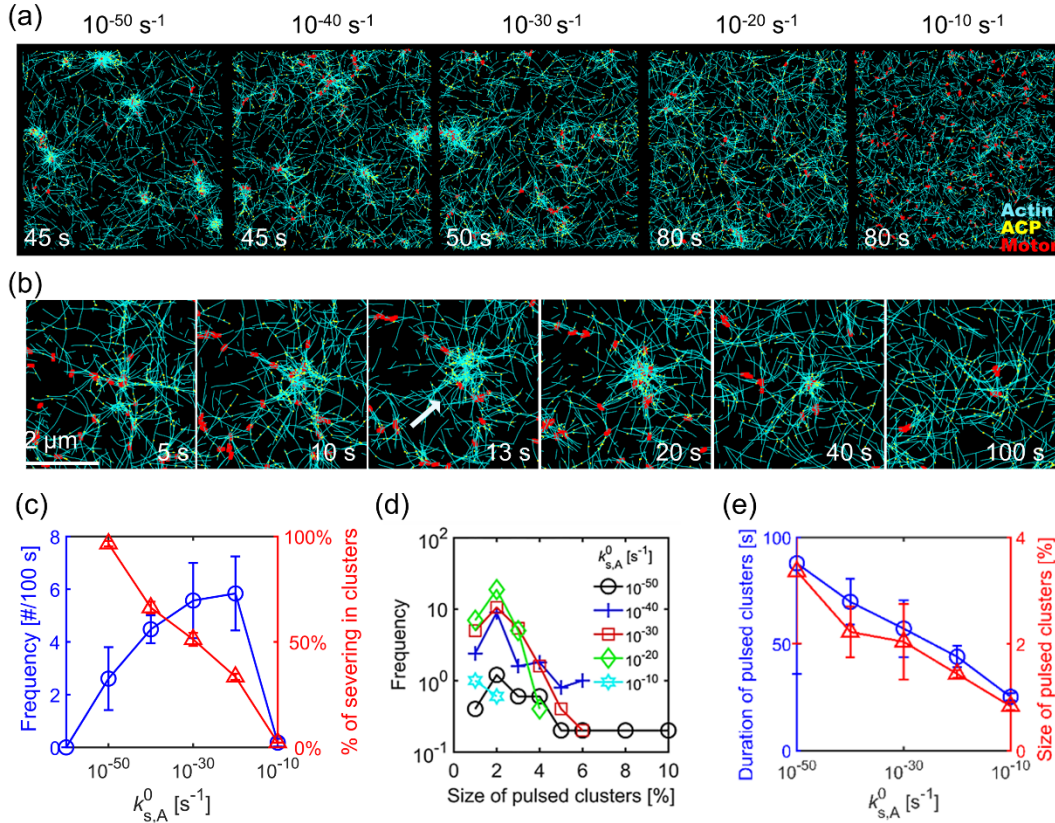


Fig. 2.15 Severing of F-actin facilitates strong pulsed contraction via selective force relaxation within clusters. We varied the zero-angle severing rate constant ( $k_{s,A}^0$ ) between  $10^{-60} \text{ s}^{-1}$  and  $10^{-10} \text{ s}^{-1}$  at  $R_M = 0.04$ ,  $R_{ACP} = 0.02$ ,  $\langle L_f \rangle = 1 \mu\text{m}$ ,  $k_{t,A} = 30 \text{ s}^{-1}$ , and  $\lambda_{s,A} = 1.6 \text{ deg}$ . (a) Morphology of networks with various  $k_{s,A}^0$ . As  $k_{s,A}^0$  increases, clusters become apparently smaller. (b) Time evolution of a relatively large pulsed cluster. The cluster appears at ~5 s and becomes the largest at 13 s as marked by a white arrow. Then, it disassembles completely at ~100 s. (c) Frequency of appearance of pulsed clusters per 100 s (blue circle) and percentage of severing events occurring within pulsed clusters (red triangle) depending on  $k_{s,A}^0$ . As  $k_{s,A}^0$  increases, more pulsed clusters appear, and more severing events take place outside the pulsed clusters. However, few pulsed clusters are formed if  $k_{s,A}^0$  is too high. (d) Distribution of size of pulsed clusters depending on  $k_{s,A}^0$ . With lower  $k_{s,A}^0$ , larger pulsed clusters are more likely to emerge. (e) Average duration (blue circle) and size (red triangle) of the largest pulsed clusters found from each of 5 simulations with different  $k_{s,A}^0$ . With lower  $k_{s,A}^0$ , more larger clusters appear and last longer before complete disassembly.

We also tested the effects of the insensitivity of F-actin severing to a bending angle ( $\lambda_{s,A}$ ). As explained in the method section, with higher  $\lambda_{s,A}$ , severing occurs at larger bending angles. At the range of  $\lambda_{s,A}$  tested in this study, the average length of F-actins does not show strong dependence on  $\lambda_{s,A}$ . The total number of pulsed clusters is not affected much by  $\lambda_{s,A}$  (Fig. 2.16b), but more large clusters appear with higher  $\lambda_{s,A}$  (Figs. 2.16c). The size and duration of the largest cluster in each simulation are proportional to  $\lambda_{s,A}$  (Fig. 2.16d). If severing is very sensitive to bending angles due to small  $\lambda_{s,A}$ , a large portion of F-actins within clusters are severed before substantial growth of the clusters, resulting in small pulsed clusters with short lifetime. By contrast, with large  $\lambda_{s,A}$ , the severing is delayed till F-actins are subject to greater bending angles within larger clusters, leading to formation of large pulsed clusters with relatively long lifetime. In addition, the F-actin severing is more likely to occur within clusters if  $\lambda_{s,A}$  is higher (Fig. 2.16b).

As shown above, both an increase in  $\lambda_{s,A}$  and a decrease in  $k_{s,A}^0$  lead to formation of more large pulsed clusters. However, their impacts on small pulsed clusters are quite different. Since an increase in  $\lambda_{s,A}$  hardly affects the frequency of emergence of small pulsed clusters (Fig. 2.16c), large pulsed clusters coexist with small ones at high  $\lambda_{s,A}$  (Fig. 2.16a). By contrast, a decrease in  $k_{s,A}^0$  drastically reduces emergence of small pulsed clusters (Fig. 2.15d), so large pulsed clusters appear without many small pulsed clusters (Fig. 2.15a). Thus, to finely tune populations of small and large pulsed clusters, regulation of both  $k_{s,A}^0$  and  $\lambda_{s,A}$  is necessary.

All of these results imply that in addition to F-actin turnover (i.e. treadmilling), severing results in local force relaxation that helps disassembly of otherwise irreversible large clusters. However, only with severing, strong pulsed contraction cannot last for long time because F-actins are gradually fragmented into shorter filaments over time. Actin turnover based on treadmilling helps remove the shorter filaments and recycle actin monomers to form another F-actin in a different location, resulting in relatively constant average length of F-actins over time. Thus, with the presence of both actin treadmilling and severing, the strong pulsed contraction with large clusters with long lifetime can appear.

#### 2.4.4 Conclusion and discussion

The actomyosin cortex facilitates various morphogenetic events by spatiotemporally regulating its cortical tension. The cortex usually shows homogeneous morphology and bears

tensile forces. In our previous studies, we showed that an actomyosin network cross-linked by transient ACPs can maintain homogeneous morphology and generate sustainable tensile forces in two ways. If there is no F-actin turnover, the number of active motors generating forces should be small enough to result in only a small load on each ACP. If F-actin undergoes relatively fast turnover, a network with a large number of active motors can be stable because the F-actin turnover prevents motors from developing large forces. Based on observations in previous experiments [82, 125, 153-155], it is likely that the actomyosin cortex in cells can be stable due to F-actin turnover. For example, when F-actin turnover was perturbed by drugs, the actomyosin cortex formed aggregates and lost most of traction forces.

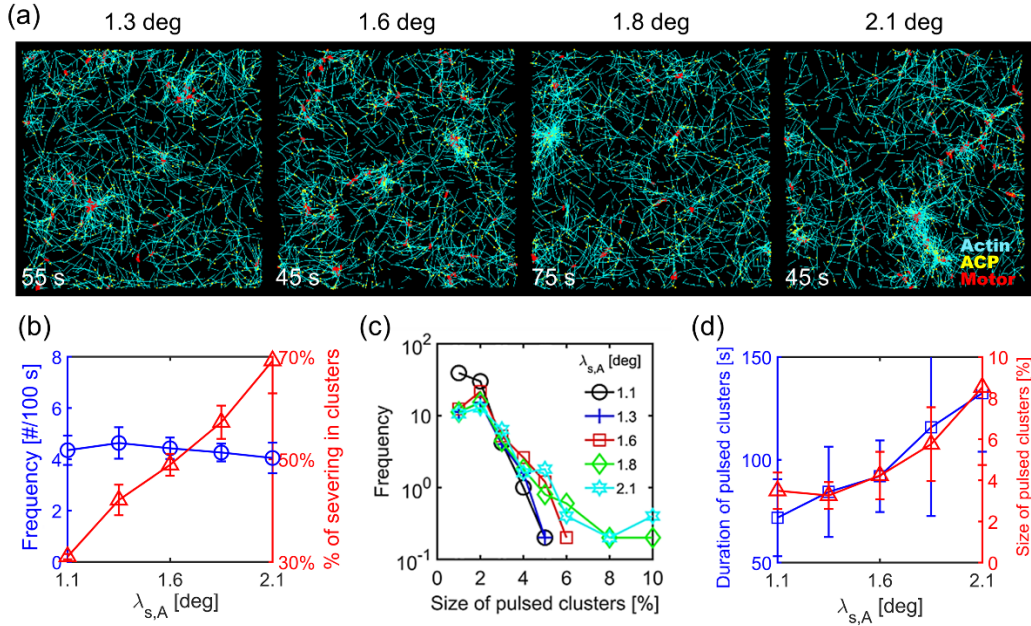


Fig. 2.16 Dependence of the severing rate on a bending angle regulates the pulsed contraction. We modulated insensitivity of the severing rate to a bending angle ( $\lambda_{s,A}$ ) at  $R_M = 0.04$ ,  $R_{ACP} = 0.02$ ,  $\langle L_f \rangle = 1 \mu\text{m}$ ,  $k_{t,A} = 30 \text{ s}^{-1}$ , and  $k_{s,A}^0 = 10^{-30} \text{ s}^{-1}$ . Severing takes place at larger bending angles if  $\lambda_{s,A}$  is larger. (a) Morphology of networks with various  $\lambda_{s,A}$ . With higher  $\lambda_{s,A}$ , more large pulsed clusters emerge. (b) Frequency of appearance of pulsed clusters per 100 s (blue circle) and percentage of severing events occurring within pulsed clusters (red triangle) depending on  $\lambda_{s,A}$ . Although relatively the same number of clusters are formed regardless of  $\lambda_{s,A}$ , more severing events take place within clusters as  $\lambda_{s,A}$  increases. (c) Distribution of size of pulsed clusters with different  $\lambda_{s,A}$ . With larger  $\lambda_{s,A}$ , there are a greater number of large pulsed clusters although small pulsed clusters appear at a similar frequency. (d) Average duration (blue circle) and size (red triangle) of the largest pulsed clusters found from each of 5 simulations depending on  $\lambda_{s,A}$ . With larger  $\lambda_{s,A}$ , there are more larger clusters, and they last longer.

In recent experiments [137, 156, 157], it has been observed that the actomyosin cortex exhibits pulsed contraction during certain morphogenetic events. Despite efforts made by a myriad of theoretical, computational, and *in vitro* experimental studies, critical regulators of the pulsed contraction emerging in the actomyosin cortex remain elusive. Considering that stability of actomyosin cortex is maintained by F-actin turnover, it is likely that pulsed contraction is involved with competition and balance between force generation from motors and force relaxation induced by F-actin dynamics. In this study, we employed a computational model to illuminate the origins of pulsed contraction.

First, we demonstrated that actin turnover highly affects the contractile behaviors of a network. As F-actin turns over slower, a network becomes more heterogeneous with larger irreversible clusters. This is consistent with several computational studies showing the effects of F-actin turnover on contractile behaviors of networks [142-144]. In order to correlate motor activities with a variation in network morphology, we quantified the speed and persistency of motor movements. We found that when a network forms large clusters, motors move towards the center of the clusters in a persistent manner and then slow down after reaching the center. By contrast, when cluster formation is inhibited by fast actin turnover, motors keep moving fast and less persistently. Because treadmilling occurs toward the barbed end of F-actin, it can prevent motors from stably walking for long time, causing less persistent motions.

In addition, it has been suggested that connectivity between F-actins also plays an important role for contractile behaviors of actomyosin networks. For example, an *in vitro* experiment using cell extracts from *Xenopus* egg cells showed that a change in the amount of one type of ACPs,  $\alpha$ -actinin, can result in distinct morphologies in the presence of actin turnover by modulating network connectivity [158]. Without actin turnover, effects of network connectivity on contractile behaviors of actomyosin networks are shown to be significant [121, 125, 141]. We probed effects of connectivity between F-actins on network morphology and motor movements by changing either F-actin length or ACP density at relatively low actin turnover rate. At low network connectivity, the network minimally contracts or shows formation of small clusters, leading to less persistent movements of motors. An increase in network connectivity results in formation of large clusters with very persistent motor movements. Emergence of the large clusters is related to increased ranges over which forces generated by motors are transmitted [158]. A further increase in network connectivity suppresses formation of separated clusters, resulting in bundled networks

with less persistent motor movements. However, the entire network will contract into a single cluster at such high connectivity in the absence of the periodic boundary condition as demonstrated in a previous study [121] since the effective size of the network becomes finite without the periodic boundary condition. It is expected that the ACP density at which the network transitions between the three states (small clusters, large clusters, and bundle network) is proportional to the actin turnover rate as shown in our previous study [82]. For example, if F-actin turns over faster, the transitions will occur at higher ACP density to achieve the same degree of network connectivity.

Interestingly, we found that weak pulsed contraction with nascent clusters occurs when there is subtle balance between force generation by myosin motors and force relaxation by actin turnover. These short-lived small clusters appear by themselves or in conjunction with clusters with size fluctuating over time in a very narrow parametric regime comprised of ACP density and the turnover rate and average length of F-actin. Outside the regime, most of the clusters irreversibly grow or decay very slowly after growth. None of these clusters resemble large pulsed clusters observed in cells [136, 137, 159]. While duration of the short-lived clusters is similar to that of the *in vivo* pulsed clusters (~1 min), they are much smaller in size. The fluctuating clusters show pulsed growth and shrinkage but do not disassemble completely. The decaying clusters exhibit reversibility, but they are disassembled too slowly. As mentioned earlier, using turnover of entire F-actins, a recent computational study demonstrated emergence of clusters showing pulsed behaviors [144], but they are close to fluctuating clusters rather than the *in vivo* pulsed clusters. All of these imply that force relaxation only via F-actin turnover is not enough to form the large distinct pulsed clusters. As size of clusters increases, more F-actins are entangled and cross-linked heavily with each other within the clusters. Then, it becomes very hard to disassemble the clusters due to very high connectivity between F-actins, resulting in very slow decay or irreversible growth. If actin turnover is very fast, disassembly of large clusters might be possible, but such large clusters are not formed since force relaxation by actin turnover dominates force generation by motors. Therefore, formation of the distinct large, pulsed clusters requires an additional mechanism for locally reducing F-actin connectivity within clusters and thus relaxing forces generated by motors.

We found that angle-dependent severing of F-actin can be the additional mechanism. Buckling-induced F-actin severing has been observed during myosin-driven contraction of actin networks [123] and membrane-bound F-actins [160]. Severing of F-actin can decrease network connectivity by breaking F-actin into two fragments, which may facilitate force relaxation and

cluster disassembly. We demonstrated that F-actin severing enables large clusters to be disassembled quickly, resulting in a significant increase in the size and duration of the pulsed clusters. If F-actin severing tends to occur slower or at larger bending angles, a larger portion of severing events take place within the clusters, leading to appearance of larger pulsed clusters. This indicates that F-actin severing can induce local force relaxation selectively in large clusters. However, if F-actin severing hardly occurs due to either a very low base rate or very low insensitivity to bending angles, clusters become irreversible or decay very slowly. By contrast, if severing occurs too frequently, a significant reduction in filament length prevents F-actins from forming large clusters. In addition, we found that formation of large pulsed clusters requires both F-actin severing and actin turnover via treadmilling. If treadmilling does not occur (i.e. without actin polymerization or depolymerization), fragmented filaments resulting from severing cannot be completely depolymerized or elongated. As a result, F-actin length is reduced significantly, so cluster formation does not occur.

Cells have various ways to regulate the severing rate of F-actins. Activity of gelsolin which severs F-actin by destabilizing interactions between actins and then binds to a new barbed end is regulated by  $\text{Ca}^{2+}$  [161]. In addition, previous studies have shown that binding of cofilin to F-actin promotes severing [129, 162]. Depending on cofilin concentration, severing events occur with quite distinct rates and different angle insensitivities. Association of cofilin to F-actin can be enhanced significantly by diverse actin-binding proteins, such as coronin and Aip 1 [163, 164]. Therefore, variations in parameters for the F-actin severing rate in this study may be related to physiological functions of cells.

## **2.5 Contraction regulated by motility of molecular motors**

### **2.5.1 Background**

Cells require mechanical forces for their physiological functions, such as cell migration, cytokinesis, wound healing, and morphogenesis [165]. The forces originate primarily from interactions between F-actin, ACP, and molecular motors in the actin cytoskeleton [109]. In cells, F-actins are known to bear tensile forces due to activities of myosin motor proteins on F-actins. Dimers of myosin II self-assemble into a thick filament, and the heads walk toward the barbed end of F-actin by consuming chemical energy stored in ATP molecules [166]. Myosin II is involved

with a myriad of cellular processes, such as force generation, morphogenesis, and cell migration [109]. By contrast, myosin I motors have only one head with their tails bound to a cell membrane, and their single heads walk on F-actins. Myosin I is known to facilitate diverse cellular behaviors, including endocytosis, exocytosis, vesicle shedding, and membrane-cytoskeleton adhesion [167]. Walking of myosin motors is often explained by the cross-bridge cycle with multiple states, and transitions between the states are described by mechanochemical rates [168]. It has been observed that the mechanochemical rates are regulated in various ways. For example, it is known that interactions between myosin I and F-actin are governed by calcium [167, 169]; if calcium binds directly to calmodulin which is a calcium-binding protein with affinity to the IQ motif within the light chain-binding domain of myosin I, actin-activated ATPase activities of myosin I motors are modulated. In addition, depending on types of myosin motors and environments around the motors, myosin motors may undergo different resistance to their movement. For example, myosin thick filaments in non-muscle cells are mostly free to move against small viscous drag force originating from surrounding cytosol. By contrast, myosin II molecules in cytokinetic nodes are linked to a cell membrane that exhibits higher effective viscosity than cytosol [170], so they are less free to move. Myosin I is less mobile because it is also bound to the cell membrane and other membrane-associated proteins [166, 167].

Myosin motility assays have been used to understand the interactions between F-actin and immobilized myosin *in vitro*. In the motility assay, motions of F-actins gliding on a surface coated densely with myosin heads were analyzed [171]. With severe crowding effects and high F-actin density, synchronized oriented motions of F-actins were observed due to volume-exclusion effects between F-actins [172-176]. For example, above a critical density, F-actins move collectively as clusters, swirls, and inter-connected bands. In the presence of ACPs, F-actin motions became more or less oriented [177-179]. For example, fascin leads to either polar structures, rings, or elongated fibers depending on conditions, whereas  $\alpha$ -actinin results in formation of contractile patches, but filamin A tends to form a stable network. It was also shown that other types of ACPs, including  $\alpha$ -EPLIN, cortexillin, and anillin, result in the distinct structures and dynamics of actomyosin networks. Overall, these studies have demonstrated how molecular interactions between F-actin, ACP, and myosin motors lead to collective behaviors at filament and network levels. However, the fixation of motors on a surface in the motility assay is not physiologically relevant. In any



event, a large portion of motors in cells are mobile unlike those in the motility assay [166], so results obtained from the motility assay do not fully represent what happens in cells.

The other extreme condition for mobility of motors has been tested in models or experiments using reconstituted actin gels consisting of F-actin, ACP, and myosin motor in solution [73, 75, 120, 146, 180]. Since motors were not fixed in space in these experiments, they often aggregated into either a single or multiple clusters. In addition, these studies suggested various mechanisms for contractile behaviors of actomyosin networks. For example, it was shown that contraction of actin networks occurs above percolation level by driving initially well-connected networks to a critical state [121, 181]. In addition, it was found that buckling caused by compressive forces arising from myosin activity is crucial for contraction of actin networks [123], consistent with theoretical predictions [74, 124]. Recent models have indeed showed that suppression of F-actin buckling can substantially reduce contraction [125, 141]. Furthermore, these studies have identified two key determining factors for the final state of networks: the network connectivity regulated by F-actin length and ACP density and the force-induced destabilization of ACPs [121, 125-127].

Since only two extreme conditions (i.e. free or fixed) have been used to date, the importance of mobility of motors for network behaviors has remained elusive although motors in cells are likely to have different mobility. To uncover the impacts of motor mobility, we used a well-established agent-based computational model based on Brownian dynamics with the Langevin equation [83, 127, 141, 182]. By allowing motors to move against distinct level of resistance controlled by their drag forces, we investigated how motor mobility affects the contractile behaviors of actomyosin networks. We found that the motor mobility plays a very different role depending on how many F-actins motors can bind to.

### **2.5.2 Additional method**

We used an agent-based computational model based on Brownian dynamics as in our previous studies [83, 127, 141, 182]. In this model, F-actin, motor, and ACP are coarse-grained by cylindrical segments. Motions of the cylindrical segments are governed by the Langevin equation. Extensional and bending forces maintain equilibrium distances and angles formed by the cylindrical segments, respectively, and repulsive force accounts for volume-exclusion effects between overlapping actin segments. Each segment moves against a drag force which is directly

proportional to its velocity and drag coefficient. While the drag coefficients of segments for F-actins and ACPs are fixed at constant values in all simulations, the drag coefficient of motors ( $\zeta_M$ ) is varied over a wide range to modulate the mobility of motors. Motors with higher  $\zeta_M$  can move less at each time step than motors with lower  $\zeta_M$  if forces applied to those motors are the same. Actin undergoes nucleation and polymerization events to form F-actin. ACPs bind to F-actin at a constant rate but unbind from F-actin in a force-dependent manner following Bell's law [116].

### *Dynamic behaviors of motors*

Each motor in the model has one or two arms. It is assumed that a motor arm represents collective behaviors of a small number of myosin heads in terms of kinetic behaviors. One-arm motors represent myosin motors that can bind to only one F-actin, whereas two-arm motors represent those that can bind to two F-actins. Thus, connectivity to F-actins is a key difference between the two types of motors rather than the number of myosin heads. To avoid confusion, we name two types of motors one-arm motors and two-arm motors rather than one-headed motors and two-headed motors. Each motor arm can bind only to one binding site on actin segments at a rate of  $40N_h \text{ s}^{-1}$ , where  $N_h$  is the number of myosin heads represented by each motor arm. This means that two-arm motors can bind to a pair of F-actins while one-arm motors can bind to only one F-actin. Walking ( $k_{w,M}$ ) and unbinding rates ( $k_{u,M}$ ) of the motor arms are determined by the parallel cluster model (PCM) to capture the mechanochemical cycle of myosin motors [118, 119]. In the PCM, three mechanochemical states are defined, and there are 5 mechanochemical rates between the states (Table B.2). Details of implementation and benchmarking of the PCM in our model were explained in detail in our previous study [127]. We assumed  $N_h = 8$  for one-arm motors but  $N_h = 4$  for two-arm motors to maintain maximum force generated by one motor ( $= N_h \times \text{stall force} \times \text{the number of arms}$ ) at relatively the same level since the maximum amount of forces that motors can generate is expected to be a very important factor for contractile behaviors. These values of  $N_h$  result in slightly more processive motors and higher stall forces than one myosin head in general, but a variation in  $N_h$  does not change force-dependent behaviors of motors drastically. In this study, we varied one of the mechanochemical rates, ATP-dependent unbinding rate of myosin heads ( $k_{20}$ ), to probe its influences. Fig. 2.17 shows  $k_{w,M}$  and  $k_{u,M}$  with various values of  $k_{20}$  with  $N_h = 4$  or 8. Note that  $k_{w,M}$  and  $k_{u,M}$  generated by PCM are lower with higher applied force, regardless of  $N_h$  and  $k_{20}$ , to describe the catch-bond behavior of myosin motors [183, 184], and also they are

proportional to  $k_{20}$ . The stall force is inversely proportional to  $k_{20}$ . Although we used the value of  $N_h$  higher than 1, the wide ranges of  $k_{w,M}$ ,  $k_{u,M}$ , and stall force explored in this study enable us to account for more and less processive motors. With the reference value of  $k_{20}$  ( $k_{20}^* = 20 \text{ s}^{-1}$ ), the unloaded walking velocity of motors is 140 nm/s, which is similar to non-muscle myosin II [185, 186], whereas it is  $\sim 2 \text{ }\mu\text{m/s}$  with the highest value of  $k_{20}$ , which is larger than the walking velocity of smooth muscle myosin II [185, 187].

### ***Initial simulation setup***

We used a very thin computational domain ( $10 \times 10 \times 0.1 \text{ }\mu\text{m}$ ) with a periodic boundary condition in only x and y directions. In the z direction, repulsive forces are applied to segments that cross either of the two boundaries in order to keep them within the domain. F-actins are formed by self-assembly of actin segments. In a set of the simulations, ACPs are included, binding to F-actin to form functional cross-links between pairs of F-actins. Motors with one or two arms are allocated in random x, y, and z coordinates within the thin computational domain. In the motility assay experiments, myosin motors are located in relatively the same z position because they are fixed on a surface. Thus, with a plenty of crowding agents, F-actins pushed strongly toward the surface may show ordered behaviors due to a severe volume-exclusion effect between F-actins. However, myosin I motors bound to a cell membrane may not be located in a planar manner because of the curvature and active fluctuation of the membrane. Myosin II motors in the actomyosin cortex beneath the membrane are distributed uniformly. In addition, since the cortex is not very thin (100-200 nm) [13], F-actins in the cortex would not undergo a severe volume-exclusion effect. Thus, allocation of motors in our model is not far from the physiological circumstance.

A fraction of the motor arms bind to F-actin without walking motion. Although motors have different z positions, they can interact with F-actins if their x and y positions are similar to those of F-actins because of very small width of the domain in z direction. After a network is formed, motors start walking on F-actin.

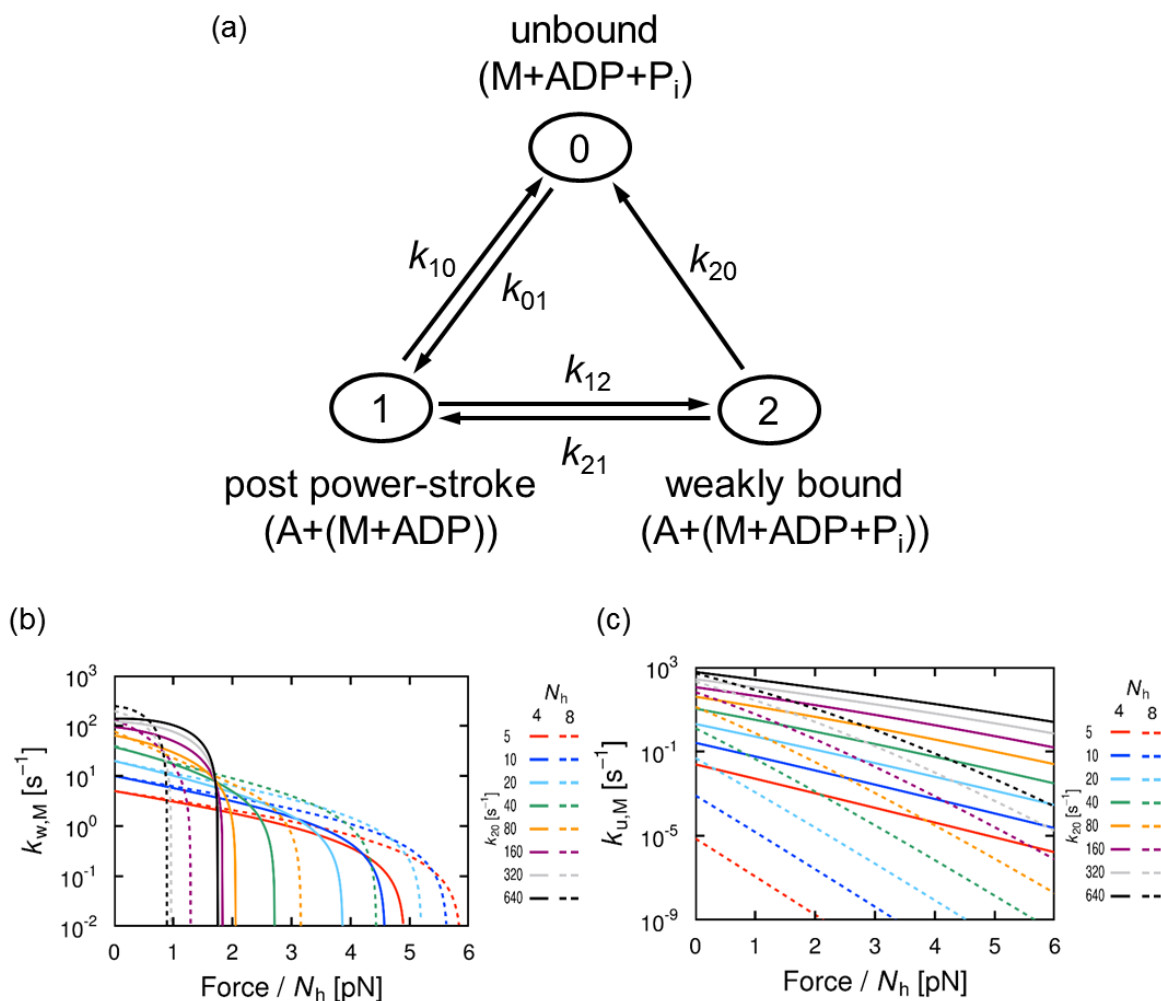


Fig. 2.17 The parallel cluster model (PCM). (a) Myosin motor cycle assumed in the PCM. Three mechanochemical rates were defined, and there are 5 transition rates between the states. In this study, we varied only the value of  $k_{20}$ . (b, c) Force-dependent walking ( $k_{w,M}$ ) and unbinding rate ( $k_{u,M}$ ) of a motor arm calculated by the PCM for various ATP-dependent unbinding rates ( $k_{20}$ ) and two different numbers of myosin heads represented by one motor arm ( $N_h$ ).

### ***Evaluation of network morphology***

We evaluate how heterogeneous network morphology is, by measuring spatial distribution of F-actins in the domain. For the measurement, the domain is divided into  $N_G \times N_G$  grids in x and y directions, where  $N_G$  indicates the number of grids in each direction. Each grid has its coordinate,  $(i, j)$ . We measure the number of actin segments located in each grid,  $\rho_A^{i,j}$ . Then, standard deviation of  $\rho_A^{i,j}$  is calculated over grids with the same  $i$  or  $j$  (i.e. in x or y direction). By averaging all the standard deviations, heterogeneity of F-actin,  $Q_A$ , is calculated like the following:

$$Q_A = \frac{1}{2N_G} \left[ \sum_{i=1}^{N_G} \text{std}(\rho_A^{i,j} |_{j=1..N}) + \sum_{j=1}^{N_G} \text{std}(\rho_A^{i,j} |_{i=1..N}) \right] \quad (2.15)$$

Since the heterogeneity calculated in this method depends on the choice of  $N_G$ , we carefully determined the optimal value of  $N_G$  at 20.

### **Measurement of average speed of F-actin**

We analyzed motions of F-actins. First, velocities of endpoints of all actin segments,  $v_{i,A}(t)$ , are calculated every 2 s. We quantified the distribution of  $|v_{i,A}|$  measured at all time points to show speed distribution of all F-actins. Also, to evaluate how fast F-actins are displaced by motors in average, the average speed of F-actin for each simulation is obtained by averaging  $|v_{i,A}|$  over all endpoints and all time points.

### ***Analysis of forces exerted by motors***

Forces exerted by motor arms that are engaged with F-actins are monitored. Average of the forces is calculated over time to estimate how much force motors generate at each time point on average.

### ***Analysis of network stress***

We calculated the distribution of tensile stress on network. A domain is divided into  $20 \times 20$  grids in the x and y directions. In each grid, forces acting on all F-actins, ACPs, and motors located within the grid are added, and the sum is divided by the area of the grid to calculate stress for the grid. Since F-actins are prone to be buckled in response to compressive forces, stress measured on

the network is always tensile. The distribution of network stress is visualized using heat maps with linear color scaling to better show a correlation between the local stress and morphology of networks and to avoid showing noisy small stress.

### 2.5.3 Results

As mentioned earlier, effects of motor activities on a system consisting of F-actins have been studied only under two extreme conditions of motor mobility. However, various types of motor behaviors exist in the cell cytoskeleton, depending on their specific location and mechanochemical state. We investigated contractile behaviors of networks with mobile motors that have distinct mobility and different connectivity to F-actin. We ran most of the simulations up to 100 s, but some simulations did not reach 100 s because of a significant increase in the computational cost induced by severe aggregation of networks. For the reference condition of simulations, we employed bending stiffness of F-actin ( $\kappa_{b,A}$ ) corresponding to 9  $\mu\text{m}$ , average length of F-actin ( $\langle L_f \rangle$ ) is  $\sim 1.5 \mu\text{m}$ , motor density ( $R_M$ ) is 0.8, ACP density ( $R_{ACP}$ ) is 0.1, and ATP-dependent unbinding rate ( $k_{20}$ ) is 20  $\text{s}^{-1}$ .

#### *Influences of the mobility of one-arm motors*

First, we evaluated effects of the drag coefficient ( $\zeta_M$ ) and ATP-dependent unbinding rate ( $k_{20}$ ) of one-arm motors. The drag coefficient directly controls mobility of the motors; with a smaller drag coefficient, mobility of motors is higher. With higher mobility, the average tensile force exerted by motors tends to be lower (Fig. 2.18a). Motors used in these simulations can bind to only one F-actin like myosin I, so motors can displace F-actins well only if drag force exerted on motors is high enough. Thus, if motor mobility is high, motors are displaced along F-actins rather than pulling F-actins toward them, resulting in development of low forces on motor arms. However, more motors can bind to F-actin with higher mobility because they can change their positions more easily (Fig. 2.18b). Interestingly, it was observed that force exerted by motors is the highest at intermediate levels of  $k_{20}$ . With very small  $k_{20}$ , motors unbind from F-actins very infrequently, so most of them generate forces in locations close to their initial positions without the opportunity to search other locations where they can produce larger forces closer to their stall force. By contrast, motors with too high  $k_{20}$  cannot stably walk on F-actins for long time due to

their high unbinding rate, so they cannot generate large force close to their stall force level. In addition, higher  $k_{20}$  leads to a smaller number of motors bound to each F-actin at equilibrium. Unlike motors with very high and very low  $k_{20}$ , motors with intermediate  $k_{20}$  keep unbinding from and binding to F-actins until they find locations where they can generate force large enough to be stalled with a negligible unbinding rate. Thus, these motors are able to generate the largest forces.

The average speed of F-actins shows a similar dependence on  $\zeta_M$  and  $k_{20}$  to the dependence of motor forces on  $\zeta_M$  and  $k_{20}$  since forces exerted by motors are used to pull F-actins (Fig. 2.18c). However, there are some differences between them because  $k_{20}$  also changes the unbinding rate of motors substantially. Particularly, with lower mobility, motors generate similar forces at low ( $k_{20}/k_{20}^* \leq 1$ ) and high  $k_{20}$  ( $8 \leq k_{20}/k_{20}^* \leq 16$ ), where  $k_{20}^* = 20 \text{ s}^{-1}$  is the reference value of  $k_{20}$ . However, the average speed at high  $k_{20}$  is much smaller because motors unbind from F-actins much more frequently as seen in the lower fraction of bound motors at dynamic equilibrium (Fig. 2.18b).

Interestingly, the heterogeneity of F-actin spatial distribution is the largest at intermediate levels of  $\zeta_M$  and  $k_{20}$  (Figs. 2.18d, 2.19). If mobility is low, each one-arm motor is capable of generating relatively large force (Fig. 2.18a). However, because motors are not able to move easily, they pull F-actins toward their invariant positions, resulting in formation of many small clusters. By contrast, if mobility is high, each motor can generate smaller forces, but F-actins are allowed to aggregate to a few large clustering structures because motors pulling F-actins can move along with F-actins. Because of these two effects of a change in motor mobility, heterogeneity of F-actin spatial distribution is maximal at optimal level of  $\zeta_M$ . The optimal level is smaller with larger  $k_{20}$  because stall force of each motor is smaller, so aggregation of F-actins is a more important factor than a decrease in force generated by each motor. The dependence of the heterogeneity of F-actin spatial distribution on  $k_{20}$  is attributed to forces exerted by motors shown earlier (Fig. 2.18a).

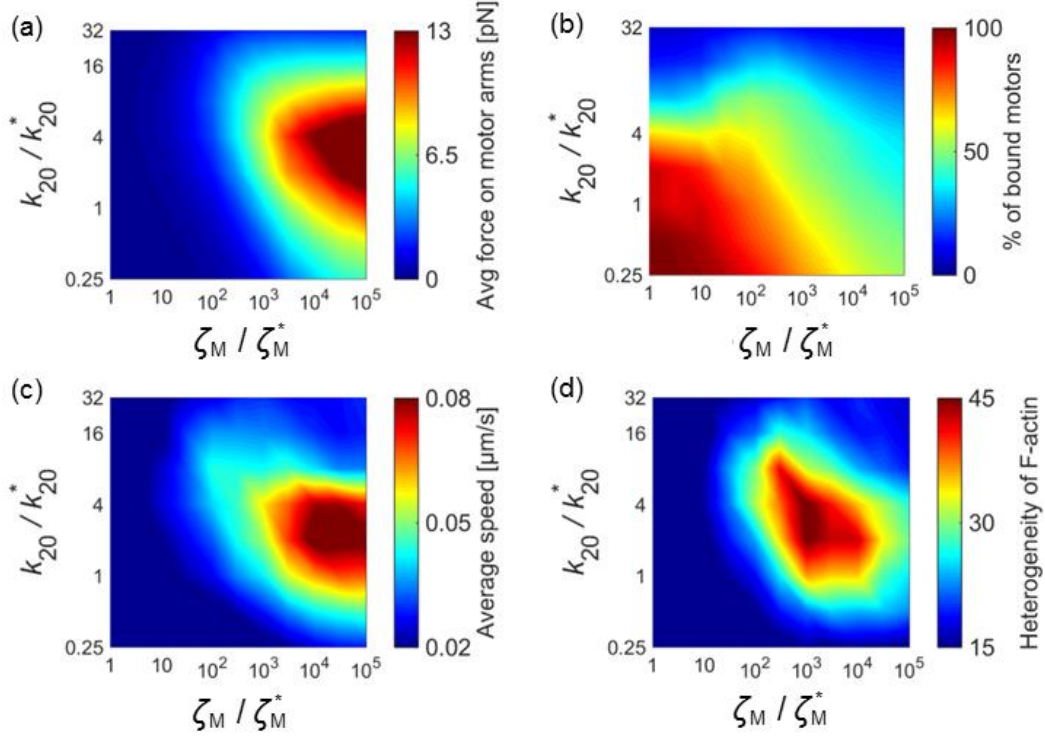


Fig. 2.18 Effects of mobility of motors and mechanochemical rate with one-arm motors. (a) Average tensile force exerted by motor arms, (b) fraction of motors bound to F-actins, (c) average speed of F-actins, and (d) heterogeneity of F-actin spatial distribution. ATP-dependent unbinding rate of myosin heads ( $k_{20}$ ) and motor mobility modulated by the drag coefficient of motors ( $\zeta_M$ ). Forces exerted by motor arms and the average speed of F-actins are larger at higher  $\zeta_M$  and intermediate levels of  $k_{20}$ . More motors are bound to F-actins with smaller  $\zeta_M$  and  $k_{20}$ . Distribution of F-actins is the most heterogeneous at intermediate levels of  $\zeta_M$  and  $k_{20}$ .  $\zeta_M^* = 8.10 \times 10^{-8} \text{ kg/s}$  and  $k_{20}^* = 20 \text{ s}^{-1}$  are reference values of  $\zeta_M$  and  $k_{20}$ , respectively.

With high mobility or large  $k_{20}$ , we observed the formation of bundles in a network (Fig. 2.19). Since we used high  $R_{\text{ACP}} (= 0.1)$ , F-actins spontaneously form bundles if there is no motor. If mobility is low, or if  $k_{20}$  is small, motors prevent F-actins from aligning in parallel with other F-actins for formation of bundles. By contrast, with low mobility or large  $k_{20}$ , F-actins can move relatively easily, so they can form bundles with many cross-linking points as if there were no motor. In addition, we observed that the spatial distribution of motors is heterogeneous with intermediate mobility and  $k_{20}$  (Fig. 2.19). In the networks with heterogeneous motor distribution, the density of motors is high in regions where F-actins do not exist. We found that with higher mobility, motors bound to F-actin show a greater propensity to walk toward the barbed end of F-actin and then slide off from the barbed end. If mobility is very high, free motors can easily bind to F-actins again since spatial density of F-actins is quite homogeneous. By contrast, with intermediate mobility,



free motors are more likely to remain in a free state due to the heterogeneous F-actin distribution, resulting in such heterogeneous motor distribution at the end of simulations. Dependence of the motor distribution on  $k_{20}$  can be explained in a similar manner.

It is worthwhile noting that heterogeneity of spatial distribution of F-actins and motors keep evolving over time till the end of simulations ( $t = 100$  s) in cases with severe network aggregation into clusters, whereas, other measured quantities, such as average force exerted by motors, the percent of bound motors, and average speed of F-actin, do not change significantly after  $t = 20$ . This implies that it takes time for motors to contract networks into small clusters because of resistance originating from network elasticity and repulsive forces between F-actins.

The level of stress acting on networks tends to be proportional to average forces exerted by motors shown in (Fig. 2.18a); with high mobility and intermediate  $k_{20}$ , the stress is the highest and concentrated on the clusters. By contrast, with high mobility or high  $k_{20}$ , stress level is very low because one-arm motors cannot generate large forces under such conditions as explained above. These cases show quite homogeneous network morphology. It implies that the level of stress exerted on networks cannot always be predicted by how the networks look.

### ***Effects of mobility of two-arm motors***

We found that effects of  $\zeta_M$  on measured quantities are drastically different if motors can bind to a pair of F-actins. Over the same range of  $k_{20}$ , we ran simulations with two-arm motors with various values of  $\zeta_M$ . Note that we used a 4-fold smaller time step in these simulations to maintain numerical stability. Unlike one-arm motors, forces generated by motors bound to two F-actins are substantial even at high mobility (Fig. 2.20a). Motors bound to two F-actins oriented in relatively opposite (i.e. anti-parallel) directions do not need to rely much on resistance from viscous drag forces for displacing F-actins. Motors bound to relatively parallel F-actins generate smaller forces. With low mobility, all motors bound to two F-actins generate relatively large forces by either pulling relatively parallel F-actins using resistance from strong drag forces or pulling relatively anti-parallel F-actins. Forces generated by motors bound to only a single F-actin show similar dependence on  $\zeta_M$  shown in Fig. 2.18a. Regardless of where they are bound, forces exerted by all two-arm motors are the highest at intermediate values of  $k_{20}$  due to the same reason explained earlier for one-arm motors; higher  $k_{20}$  decreases the stall force of motors, whereas too low  $k_{20}$  prevents motors from finding ideal locations to exert large forces.

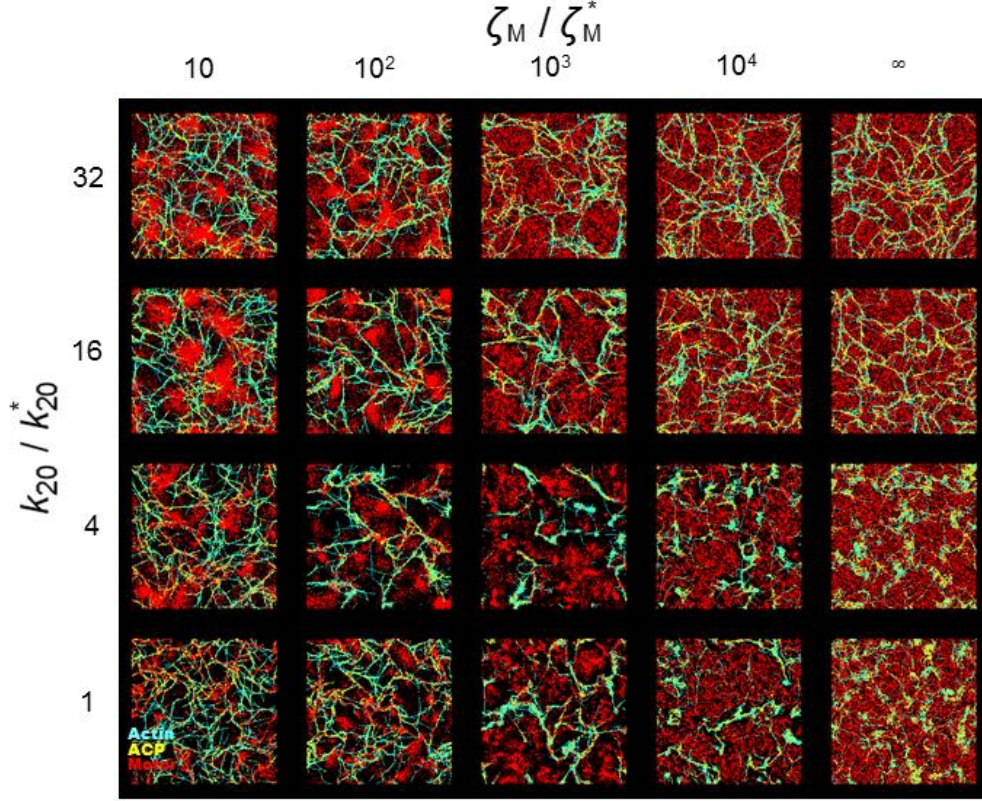


Fig. 2.19 Morphology of networks with one-arm motors depend on mobility of motors and mechanochemical rate. Network morphology measured in all cases at a last time point where steady state is reached,  $t = 100$  s, with various ATP-dependent unbinding rate of myosin heads ( $k_{20}$ ) and motor mobility modulated by the drag coefficient of motors ( $\zeta_M$ ). F-actins, ACPs, and motors are visualized by cyan, yellow, and red, respectively.  $\zeta_M^* = 8.10 \times 10^{-8}$  kg/s and  $k_{20}^* = 20$  s $^{-1}$  are reference values of  $\zeta_M$  and  $k_{20}$ , respectively.

An increase in mobility substantially increases the number of two-arm motors interacting with pairs of F-actins (Fig. 2.20b). As a result, the number of motors interacting with a single F-actin slightly decreases with increasing mobility. Smaller  $k_{20}$  tends to result in a larger amount of motors bound to F-actins because each motor arm unbinds from F-actin less frequently. However, at  $k_{20}/k_{20}^* \leq 1$ , the number of motors bound to anti-parallel F-actins does not depend on  $k_{20}$  because the motors already unbind very rarely from F-actins at the range of  $k_{20}$ .

Total forces generated by motors cannot be calculated simply by multiplying average force exerted by motors to the number of motors interacting with F-actins because the direction of individual force vectors would be different. In addition, cooperativity of motors makes prediction of the total forces even harder. However, to relate the total forces generated by motors with network morphology and F-actin speed, we assume that the total forces would be approximately

proportional to forces generated by motors and the number of motors interacting with F-actins. Since two-arm motors bound to pairs of F-actins still exert substantial forces with high mobility unlike one-arm motors, a large increase in the number of bound motors can result in much higher total forces with high mobility. By contrast, as shown earlier, each of one-arm motors exerts much lower force with higher mobility, so the total forces exerted collectively by one-arm motors are smaller despite an increase in the number of bound motors. The total forces generated by two-arm motors are likely to be the largest at around  $k_{20}/k_{20}^* = 1$  among conditions that we tested because the average force generated by two-arm motors bound to anti-parallel F-actins is reduced if  $k_{20}$  decreases further below  $k_{20}^*$ , whereas the number of bound motors does not change significantly at  $k_{20}/k_{20}^* < 1$ .

Due to enhanced total forces, average speed and heterogeneity of F-actins with two-arm motors are higher with higher mobility at the intermediate values of  $k_{20}$  (Figs. 2.20c-d, 2.21). These results in different dependence of average speed and heterogeneity of F-actins on  $\zeta_M$  compared to those shown in Figs. 2.18c-d. Interestingly, heterogeneity of spatial distribution of motors is much higher in cases with two-arm motors although the fraction of bound motors is not very different (Fig. 2.20b). The significant difference in heterogeneity of motor distribution is mainly attributed to the heterogeneity of F-actin distribution; if a network becomes very heterogeneous due to motor activities, motors bound to F-actins are also distributed in a very heterogeneous manner. Note that all quantities measured here tend to change over time more dynamically in cases with formation of large clusters. Many F-actin bundles are formed at high  $k_{20}$  since motors are not processive enough to contract networks, but the bundles do not appear at small  $\zeta_M$  because two-arm motors can contract a network into a few small clusters unlike one-arm motors. Stress is higher and more concentrated on clusters if network morphology is more heterogeneous.

Note that results from simulations with  $\zeta_M / \zeta_M^* < 10$  are not shown here because some of the simulations with very high mobility underwent severe network aggregation and thus did not reach sufficiently long time points for comparison with other cases due to exponentially increased computational costs.

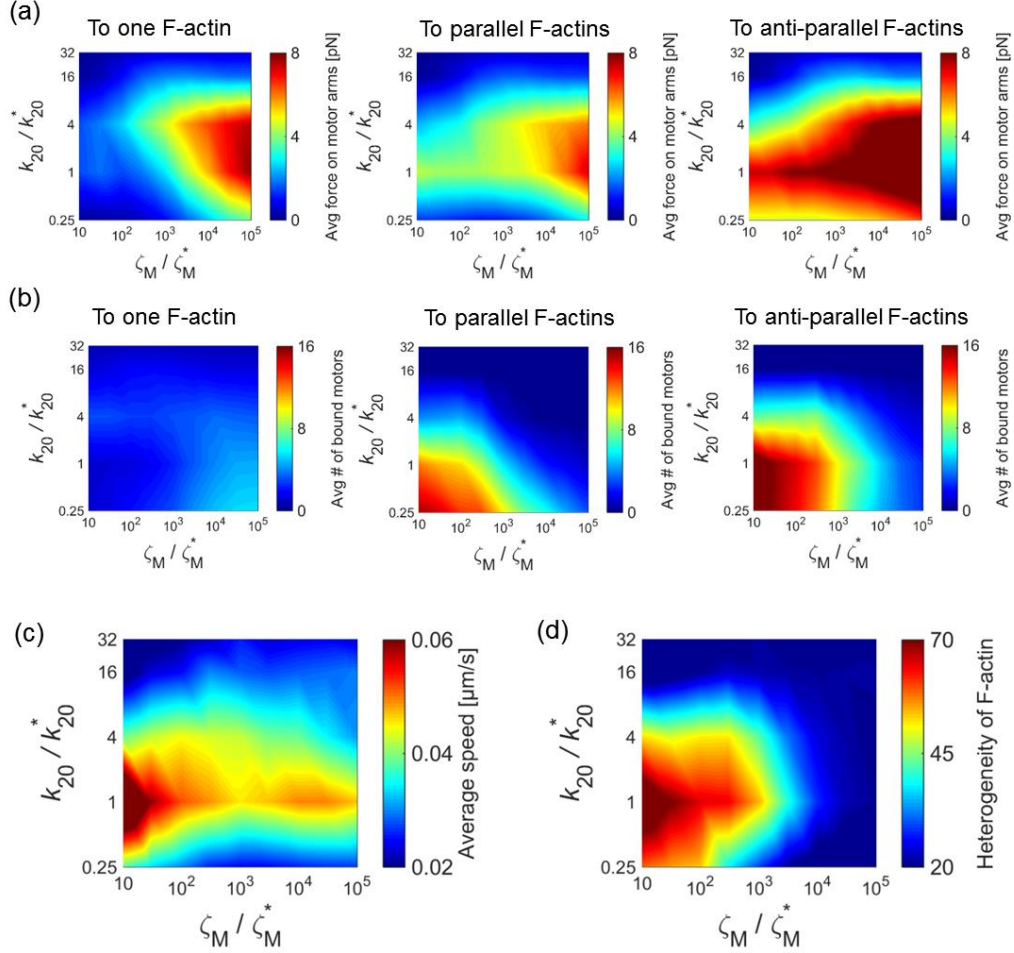


Fig. 2.20 Impacts of motor mobility and mechanochemical rate on network contraction with two-arm motors. (a) Average tensile force exerted by motor arms, (b) fraction of motors bound to F-actins, (c) Average speed of F-actin, and (d) heterogeneity of F-actin spatial distribution, with various ATP-dependent unbinding rate of myosin heads ( $k_{20}$ ) and motor mobility modulated by the drag coefficient of motors ( $\zeta_M$ ). In (a-b), the left, center, and right plots correspond to motors bound to one F-actin, motors bound to relatively parallel F-actins, and motors bound to relatively anti-parallel F-actins, respectively. Average force exerted by two-arm motors bound to parallel F-actins shows weak dependence on  $\zeta_M$ , and the number of those motors increases as  $\zeta_M$  decreases. Thus, the total forces exerted by all motors are higher with lower  $\zeta_M$ . F-actins move faster, and the distribution of F-actins is much more heterogeneous with lower  $\zeta_M$ .  $\zeta_M = 8.10 \times 10^{-8}$  kg/s and  $k_{20}^* = 20$  s $^{-1}$  are reference values of  $\zeta_M$  and  $k_{20}$ , respectively.

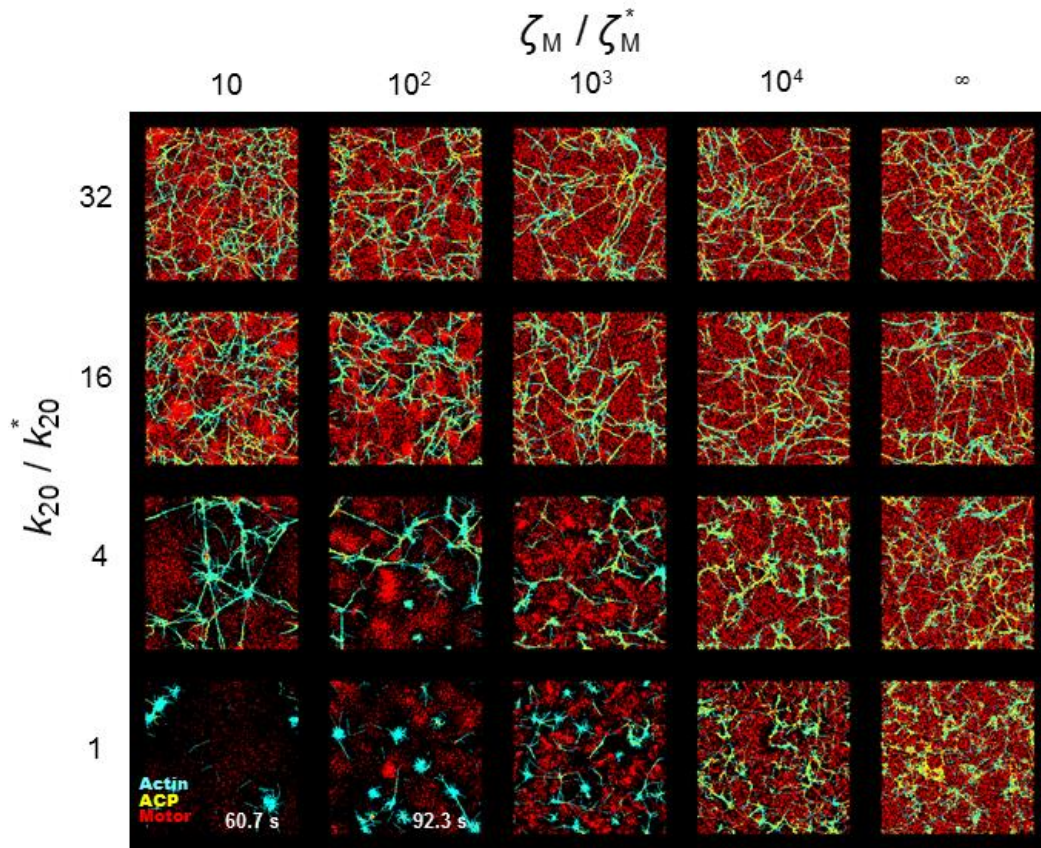


Fig. 2.21 Morphology of networks with two-arm motors depending on the mobility and mechanochemical rate of motors. Network morphology measured in all cases at a last time point where steady state is reached,  $t = 100$  s, at wide ranges of ATP-dependent unbinding rate of myosin heads ( $k_{20}$ ) and motor mobility modulated by the drag coefficient ( $\zeta_M$ ). F-actins, ACPs, and motors are visualized by cyan, yellow, and red, respectively.  $\zeta_M^* = 8.10 \times 10^{-8}$  kg/s and  $k_{20}^* = 20$  s $^{-1}$  are reference values of  $\zeta_M$  and  $k_{20}$ , respectively.



#### 2.5.4 Conclusion and discussion

It is well known that interactions between F-actin and myosin motors lead to the formation of distinct actomyosin structures and the generation of contractile forces [171]. During recent decades, a myriad of *in vitro* experiments and computational models have been employed for understanding the contractile behaviors of actomyosin networks. However, those studies were conducted with either immobile or highly mobile motors although the mobility of myosin motors in cells is likely to vary at a wide range, depending on their types and conditions. Thus, current understanding of the impacts of motor mobility is limited significantly. In this study, we used an agent-based model to illuminate the role of motor mobility for contractile behaviors of the actomyosin networks.

First, we used immobile motors to find reference values of parameters including the bending stiffness and length of F-actin, the density and mechanochemical rate of motors, and the density and unbinding rate of ACPs. Although we observed aggregation of F-actins into clusters in the presence of ACPs, the size of clusters was not large because motors cannot move freely; immobile motors pull F-actins toward their invariant locations. Therefore, several small clusters are formed rather than a few large clusters, but much larger contraction into bundles or clusters has been observed in cells [136, 188, 189]. A key difference between motors in cells and motors in these simulations and the motility assay experiments is the ability of motors to move. Motors in the cells show different mobility, depending on their type and where they are bound. Particularly, myosin I with only one head is linked to F-actin as well as phospholipid or proteins embedded in the cell membrane, such as  $\text{Na}^+$  channel [190] and amino acid transporters [191], so myosin I is likely to exhibit various mobility depending on where it is bound [167, 169]. Myosin I can pull F-actin strongly if it can resist reaction force from F-actin as one can pull a rope better on a rough surface than on a slippery surface (Fig. 2.22a). By contrast, if myosin I motors move relatively freely, force generated by the mobile motors would be smaller. However, global contraction into bundles or clusters may occur because formation of such large structures requires aggregation of motors. Thus, higher mobility of motors has both positive (motor aggregation) and negative (smaller force) effects on enhancement of network contraction, so it is not clear how an increase in motor mobility affects network morphology.

To check whether mobile motors enhance or reduce network heterogeneity, we allowed motors to move with different mobility by varying their drag coefficient (Figs. 2.18, 2.19). We

found that networks with one-arm motors yield the most heterogeneity at intermediate motor mobility. If mobility of motors is too high, motors walk along F-actins rather than pulling and exerting force on F-actins (Fig. 2.22c). However, if motors can move to some extent as well as pull F-actins, F-actins can severely aggregate to a few large clusters. We also found that the optimal motor mobility inducing the most heterogeneous network morphology depends on stall force and affinity of motors; motors with lower stall force and higher unbinding rate resulting from larger ATP-dependent unbinding rate are not able to pull F-actins strongly and stably. Thus, even when these motors are immobile, a network is not very heterogeneous. For these weak motors, their mobility allowing many F-actins to aggregate into a cluster becomes more important, which yields larger optimal motor mobility for the highest network heterogeneity. Indeed, it is known that cells actively regulate affinity of myosin I. For example, binding of calcium to calmodulin which binds to myosin I is known to directly affect mechanochemical rates of myosin I motors [167, 169]. Our results obtained with a wide range of a mechanochemical rate and mobility of one-arm motors can provide insights into understanding how myosin I in different states regulates actin structures for various cellular functions.

The biphasic dependence of network heterogeneity on mobility of one-arm motors may be verified using *in vitro* experiments. If myosin I motors are linked directly to a rigid surface, they will have negligible mobility. By contrast, if myosin I motors are bound to a lipid bilayer as in [192], they will move against drag forces originating from the effective viscosity of the lipid bilayer. It is possible to alter the effective viscosity by using phospholipids with irregular shapes or cholesterol. In addition, via mutation [193], it might be feasible to change the number of phospholipids to which each myosin I motor binds; as myosin I binds to more phospholipids, its mobility would substantially decrease. By comparing contractile behaviors of a network induced by myosin I motors under such various conditions, our observation could be verified qualitatively.

Interestingly, we found that effects of motor mobility on network morphology with two-arm motors that can bind to a pair of F-actins are drastically different (Figs. 2.20, 2.21); as motors can move more freely, networks become more heterogeneous. Unlike one-arm motors, two-arm motors bound to a pair of F-actins aligned in relatively anti-parallel orientations do not need to rely on resistance originating from drag forces as we can pull two ropes with both hands in opposite directions even on a very slippery surface (Fig. 2.22b). The fraction of such motors bound to anti-

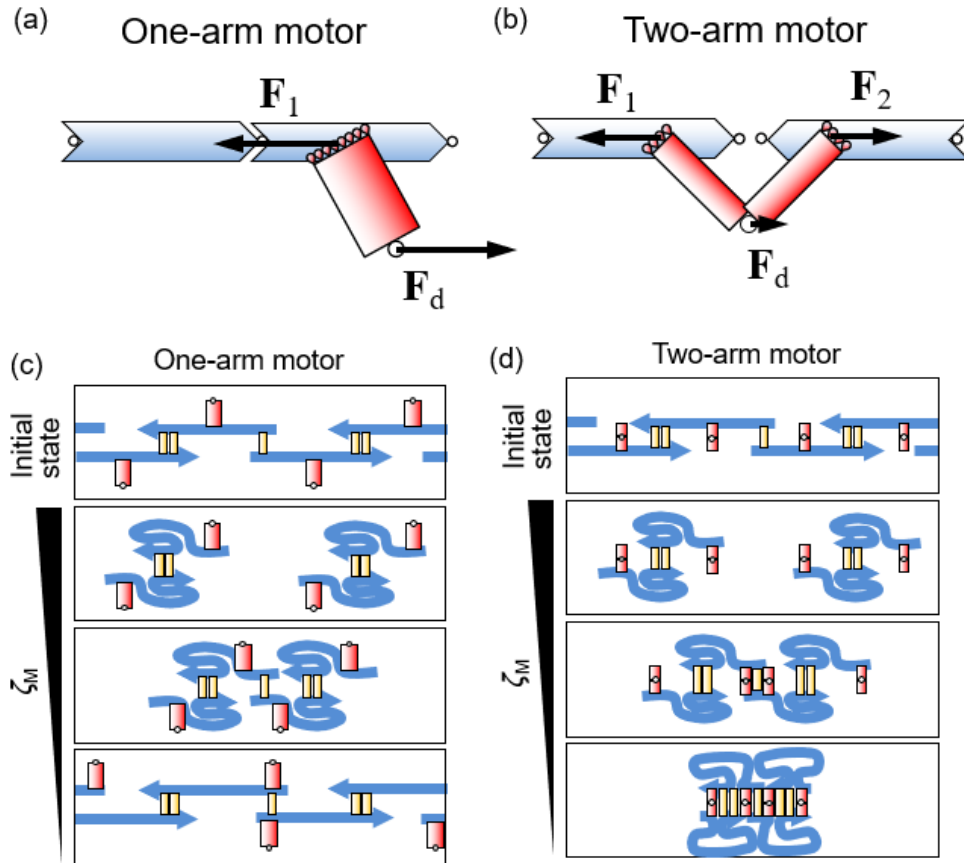


Fig. 2.22 Schematic diagrams summarizing results. (a, b) Comparison between one-arm motor and two-arm motor. Since one-arm motors can bind to only one F-actin, they rely much on resistance originating from drag force ( $F_d$ ) when they pull F-actin. For example, one-arm motors with a higher drag coefficient ( $\zeta_M$ ) feel a larger drag force when they try to move. Thus, they have less mobility, enabling them to exert a larger force on F-actin. If two-arm motors pull two F-actins in relatively opposite directions, they do not need to rely on  $F_d$ . (c, d) Initial state (top) and final states of networks (the rest) with one-arm motors or two-arm motors with different  $\zeta_M$ . Note that all two-arm motors in the diagram are initially located in anti-parallel F-actins to show a case opposite to that with one-arm motors. In (c, d), it is assumed that a periodic boundary condition exists on the left and right boundaries.



parallel F-actins becomes quite large as motors are freer to move. Therefore, as more motors exert substantial forces on F-actins, network morphology is more heterogeneous (Fig. 2.22d). Depending on the affinity and stall force of motors regulated by the ATP-dependent unbinding rate of myosin heads, the extent of network contraction varies, but the contraction is always maximal with the highest motor mobility. Two-arm motors in our model resemble most types of myosin motors that can bind to more than one F-actin like myosin II, V, VI, VIII, XI [166]. Our results imply that an increase in mobility of motors that can bind to more than one F-actin always enhances contractile behaviors of actomyosin networks. It is expected that thick filaments formed by self-assembly of myosin II molecules also induce larger network contraction with higher mobility because their ability to connect to multiple F-actins enables them to find relatively anti-parallel F-actins more easily. Indeed, global contraction has been observed in previous *in vitro* studies using two-headed myosins [125] and myosin thick filaments [73, 120, 121, 123, 146, 181] without any constraint on motor movement. Like myosin I, myosin II molecules can have different mobility. During cytokinesis of fission yeast cells, anillin and other proteins form cytokinesis nodes that anchor the ends of myosin II tails to a cell membrane [170]. Several myosin II heads bound to each cytokinesis node extend into the cytoplasm and interact with F-actins to form and contact a contractile ring. The nodes are known to move bidirectionally during constriction. Due to multiple myosin heads, each cytokinesis node behaves as a thick filament, but its mobility is much smaller because it is bound to the membrane via a complicated protein complex, and movement of the nodes is suppressed by physical contacts between the plasma membrane and the cortical endoplasmic reticulum [194]. Nevertheless, the nodes are able to facilitate the ring constriction due to their connectivity to multiple F-actins. It was demonstrated that an increase in mobility of the cytokinesis nodes inhibits normal assembly of a cytokinetic ring because it results in clustering of actin filaments even before the assembly.

As mentioned before, only two extreme conditions for motors have been considered in previous *in vitro* studies: immobile motors and highly mobile motors. Thus, systematic comparison between our results with various motor mobility and previous literature is hard. However, in previous studies using *in vitro* experiments and simulations, it is obvious that networks with immobile motors tend to form small clusters [177, 178], whereas networks with highly mobile motors can aggregate into a few, large clusters [73, 120, 121, 181, 195], which is consistent with our simulation results. In addition, results in experiments with different ATP concentration can be

compared with our results with distinct ATP-dependent unbinding rates ( $k_{20}$ ); higher ATP concentration leads to a larger  $k_{20}$  value in our simulations. One study demonstrated that contractile behaviors of reconstituted actin networks with mobile motors and fascin are maximal at intermediate ATP concentration [196]. We also observed such biphasic dependence of heterogeneity of network morphology on  $k_{20}$ . Another study showed that actin networks with immobile motors and  $\alpha$ -actinin form small clusters and bundles at low and high ATP concentrations [177], respectively, which is consistent with our results with immobile motors.

Care should be taken when our results are compared with the cell cortex interacting with diverse myosin motors. It is not easy to estimate drag coefficients of myosins in a cell with highly crowded, heterogeneous environments. The viscosity of cytoplasm reported in previous studies is quite different depending on measurement methods and conditions [197, 198]. The surface viscosity of giant vesicle membranes was measured before [199], but this viscosity does not necessarily represent the effective surface viscosity of a real cell membrane because of existence of other membrane-associated proteins and variations in the conditions of the lipid bilayer. Due to these uncertainties, quantitative comparison between drag coefficients of motors in our model and those in the cell is quite challenging. In addition, our model does not account for all aspects of environments of the cell cortex. For example, it is assumed that F-actins in the model do not undergo F-actin turnover after polymerization. By contrast, F-actins in cells experience a wide variety of dynamic behaviors, such as severing, capping, and branching. We also assumed that molecular motors are positioned in a relatively planar manner although myosins in cells can be bound to the cell membrane with much more complex geometry. These differences between the real cell cortex and our model may limit direct comparisons between experimental observation and our simulation results. However, such assumptions in our model were made for using a minimal system so that we can avoid a significant increase in the number of parameters and uncertainties, as other researchers have employed *in vitro* actomyosin gels and myosin motility assays due to the same reason.

### 3. A DISCRETE MODEL OF CORTICAL MICROTUBULE ARRAY

#### 3.1 Introduction

##### 3.1.1 Cortical microtubule patterning in plant cells

Microtubules are highly dynamic polymers in the cell, with individual microtubules and the entire microtubule network turning over on the time scale of minutes [87, 200]. The underlying biochemical and biomechanical dynamic instability of microtubules generates these unpredictable behaviors [87, 104, 200]. Microtubules are cytoskeletal polymers comprised of  $\alpha$  and  $\beta$  tubulins with polarity defined by plus and minus ends. The nucleation of microtubules in the plant cortex can occur de novo or by branching from pre-existing microtubules [201-203]. Although both ends of microtubules exhibit a frequent switch between growth, shrinkage, and pause states [16] (three-state dynamics), the plus end is far more unstable than the minus end. When microtubules grow from the plus end with the dynamic instability in the plant cortex, they often encounter other microtubules. Since they are tightly coupled to the cell wall, the microtubules collide with each other, which can lead to different consequences. When the plus end of a microtubule makes contact to other microtubule with a small angle below  $\sim 40^\circ$ , it is reoriented in a direction parallel to the other microtubule, which is called zippering. By contrast, the collision with a contact angle greater than  $\sim 40^\circ$  lead to either crossover or a transition from growth to shrinkage called catastrophe. The microtubule undergoing rapid shrinkage can transition to a growth state, which is called rescue. These dynamic behaviors of microtubules result in various patterns. Most importantly, the encounter-based catastrophe and zippering is the main driving force for ordered cortical microtubule array. Dixit et al. showed that the balance between steep-angle catastrophe and shallow-angle zippering are necessary and sufficient to promote parallel configuration during self-organization of microtubules [104], as these encounter events provide directional guidance to the plus end [204]. Other geometrical features regulating microtubule organization such as microtubule-templated nucleation, polarity and length are reviewed comprehensively in [204].

Recent studies showed distinct morphologies of microtubule patterns in leaf epidermal cells of *Arabidopsis thaliana*. The leaf epidermal consist mainly of three classes: trichome, pavement cells, and stomatal guard cells [205, 206]. Trichome is a single cell with a long stalk, serving as epidermal hair. The trichome initially appears as a small bulge and then elongates predominantly

in one direction, whereas its expansion in the transverse direction is restricted. In small young trichomes ( $\sim 20\text{-}30\ \mu\text{m}$ ), cortical microtubules are mostly aligned in the transverse direction [9, 207, 208], spanning the flank region. These microtubules contribute to the restriction of the cell growth in the transverse direction. This growth pattern characterized by unidirectional elongation and transverse microtubule orientation is called “diffusive growth” [3]. In the apical region of the trichome, microtubules are commonly absent, forming a microtubule depletion zone [9]. Considering that the apical region has more isotropic cell wall properties than the flank region, mechanical anisotropy of the cell wall is likely to be correlated with distribution and orientation of cortical microtubules. As leaf trichome elongates through the diffusive growth, tip refinement progressively occurs, and the microtubule depletion zone lasts until the trichome reaches threshold length. As the trichome matures and grows longer, microtubules are reoriented from the transverse direction to the oblique direction with appearance of spiral tracks along the long stalk in either clockwise or counterclockwise directions [171]. As maturation proceeds, microtubules are eventually reoriented to the longitudinal direction [208]. The dynamic orientation of microtubules has been observed in multicellular trichomes as well [209].

### **3.1.2 Patterning of microtubule in response to mechanical stress**

Microtubules are positioned in a way that they can be coupled to tensile force machineries that are linked to the cell wall. Growing cells are highly vacuolated and in most instance, microtubules are restricted to the cortex by default. Further, microtubules do not laterally diffuse [16], and are tightly anchored to the plasma membrane [17]. Therefore, morphological changes in the microtubule patterns are likely to be attributed to mechanical loads that they sense. In a number of recent plant-focused studies, a relationship between mechanical stress and the self-organization of cortical microtubule array has been extensively investigated. At the multicellular level, microtubules can be oriented in alignment with the supra-cellular stress pattern [42, 210-212]. Additionally, microtubule alignments can be correlated with both tensile and compressive stress. For instance, epidermal cells such as stomata are under tension with an elevated position and the surrounding microtubules are observed to be predominantly aligned in the circumferential direction where the stress peaks [211]. Compressive stress leads to hyper alignment of microtubules in pavement cells [210]. In response to a mechanical perturbation induced by external

pressure, microtubules are remodeled gradually and continuously with intrinsic dynamic instability [42, 213-216]. Interestingly, the microtubule anisotropy upon mechanical perturbation is dependent on the change in stress intensity. A multicellular ablation, compared with a single-cell one, leads to stress perturbation at a larger scale and a stronger corresponding response of microtubules in the circumferential direction [210]. The key molecular players underlying the response of cortical microtubules to mechanical stress is still a hot matter of debate. Williamson has proposed that a potential sensor could be a protein complex or single protein targeting cell wall growth substances [217]. The sensor should be responsive to cell growth rate and direction, which correspondingly updates the stress or strain patterns [213, 217]. It has been proposed that katanin-mediated severing activity is strongly correlated with the mechanical response of microtubules, especially at local sites of mechanical perturbation [211, 218]. In pavement cells, mechanical perturbation led to up-regulation of katanin-mediated severing at microtubule crossover sites [211]. In shoot apical meristem cells, the growth anisotropy is significantly reduced in the absence of katanin. The response of microtubule to local stress pattern during growth is also attenuated without katanin at multicellular scales [218, 219].

Besides katanin, a few other microtubule-associated proteins responsible for reorientation of microtubules have been suggested. Augmin and  $\gamma$ -tubulin might play a role in repairing stress-induced microtubule defects and promoting rescue [220, 221]. The cellulose synthase-microtubule uncoupling protein could provide microtubules with the ability to withstand forces and prevent lateral movement during cellulose synthesis [222]. However, it remains elusive how the microtubules in the plant cortex sense external stimuli. To understand it, a few computational works simulated the responses of microtubules to stress or geometrical cues by incorporating two-state (growth and shrinkage) or three-state microtubule dynamics (growth, pause and shrinkage) [91, 97, 100, 104, 105, 223, 224]. Dixit and Cyr introduced a Monte Carlo simulation for cortical microtubule array and highlighted the importance of zippering and collision-induced catastrophe in network ordering [104]. They speculated that steeper contact angle between microtubules lead to larger axial force along microtubule and thereby increase the probability of catastrophe. Allard et al. proposed the first three-state model that systematically examined the parameterization of plus and minus end dynamics [91]. The two-dimensional model with a square domain showed biased alignment of microtubule in the transverse direction when two edges act as catastrophe-inducing boundaries. Such boundary effect was further confirmed in a three-dimensional model where the

end walls (top and bottom boundaries) in a cylindrical domain act as either catastrophe-inducing or reflective boundaries [223]. Both types of boundary condition induced transverse alignment even if collision-induced catastrophe between microtubules was disabled. However, microtubule organization was disrupted and became homogeneous in the absence of zippering, regardless of the boundary conditions [223]. In microtubule models inside epithelia cells, the catastrophe-inducing boundary is also a key determinant in the length distribution of microtubules as it helps the microtubules ‘sense’ the shape and geometric scale of the cell [225]. More interestingly, microtubule catastrophe near cell boundaries has shown angle dependence *in vivo* [226]. On the other hand, boundary-induced catastrophe can be mitigated by proteins like CLASP near the cell edges. To explore effect by the cell edges, Ambrose et al. developed a model that accounts for microtubule’s ability to bypass the cell edges between different cell faces [97]. In simulations with CLASP-facilitated growth around the transverse edges of cells, microtubules tended to form a mixed array with bundles in both longitudinal and transverse directions [97]. However, in trichome, the apex exceeds the radius of curvature threshold of 2.5  $\mu\text{m}$  [8], below which CLASP-dependent stabilization of transfacial microtubules operates [97]. The radius of curvature of a trichome tip is likely involved in later stages of tapering and may mediate longitudinal alignment of microtubules as the branch elongates. Thus, curvature induced catastrophe can play a role but does not fully explain microtubule ordering in some cell types that exceed the threshold such as pavement cells and leaf trichomes.

The differential patterning has been further investigated in 3D computational domains. Mirabet et al. simulated various shapes of interphase cells with different curvatures and found that microtubule array anisotropy is strongly influenced by cell curvature instead of shape [100]. With a very high aspect ratio of the cell geometry, a long cell could direct the microtubule array to be deposited along the longest axis. This has been observed in both hypocotyl and trichome cells where microtubules predominantly align in the longitudinal direction along with cell maturation [208, 227, 228]. A recent model by Chakraborty et al. pioneered in the integration of microtubule dynamics and realistic cell geometry [105]. With a rectangular domain, they concluded that edge-induced catastrophe and cell face stability both contribute to the selective mechanism for a dominant angle during microtubule self-organization. These effects can enhance or even override the geometrical cues that influence the global array patterning. The model framework was further extended to a single pavement cell domain and the results recapitulated the microtubule bands

around the necks [105]. All of the aforementioned models only address interplay between microtubule self-organization [91, 104, 223, 224], cell shape changes [100, 105], and edge-induced effects [97]. The existing models with a mechanical feedback loop between stress and growth anisotropy lack detailed descriptions about discrete-level microtubule dynamics [211, 215, 229-231]. Yet stress is a crucial patterning element as it not only couples with geometries of the cells and tissues but also reflects compositional properties of the cell wall [8]. Using experiments, it is hitherto hard to illuminate a relationship between cell-wall stress and intrinsic dynamic parameters governing microtubule self-organization. In Chapter 3, we implemented a discrete model with transient behaviors of microtubules influenced by local mechanical stress in order to probe stress-induced self-reorganization of cortical microtubules. By exploring a wide parametric space and imposing physiologically relevant stress patterns, we defined a constitutive relationship between local stress and microtubule dynamics. We found that a stress gradient mimicking stress distribution on cell walls leads to the formation of transverse bands commonly observed near the cell apex. Results in Chapters 3.3 provide a more systematic understanding of how microtubules are self-organized by responding to physiologically relevant mechanical stimuli. In Chapter 3.4, we studied the combinative effect by branched nucleation and severing of microtubules in absence of stress pattern, which would be further discussed.

## 3.2 Method

### 3.2.1 Model overview

Each microtubule is represented by serially connected individual segments with lengths of 100 nm. The nucleation of new microtubules takes place at the rate of  $10 \cdot \mu\text{m}^{-2} \cdot \text{min}^{-1}$  at a random location without dependence on existing microtubules, which lead to the formation of a homogeneous network at the beginning of simulations. Following approaches in a previous study [91], it is assumed that the plus end can switch between growth, shrinkage and pause state (three-state dynamics), whereas the minus end always undergoes slow shrinkage at a constant rate (Fig. 3.1a).

Based on experimental observations, it is assumed that a collision between two microtubules with a contact angle smaller than  $40^\circ$  results in zippering meaning that one of the microtubules changes its orientation to align with the other microtubule (Fig. 3.1b). A spacing between

microtubules is set to 25-50 nm which is close to observation in animal and plant cells [232, 233]. A collision with an angle greater than  $40^\circ$  leads to either crossover or catastrophe (Fig. 3.1b). The probability of catastrophe after a collision is between 0.2 and 0.8 [91]. The simulation parameter set is summarized in Table 3.1 and Table B.3.

Stochastic dynamic events of microtubules were updated once per 0.001 min, collisions between microtubules were considered once per 0.05 min (Fig. 3.2), which is consistent with a previous model [91].

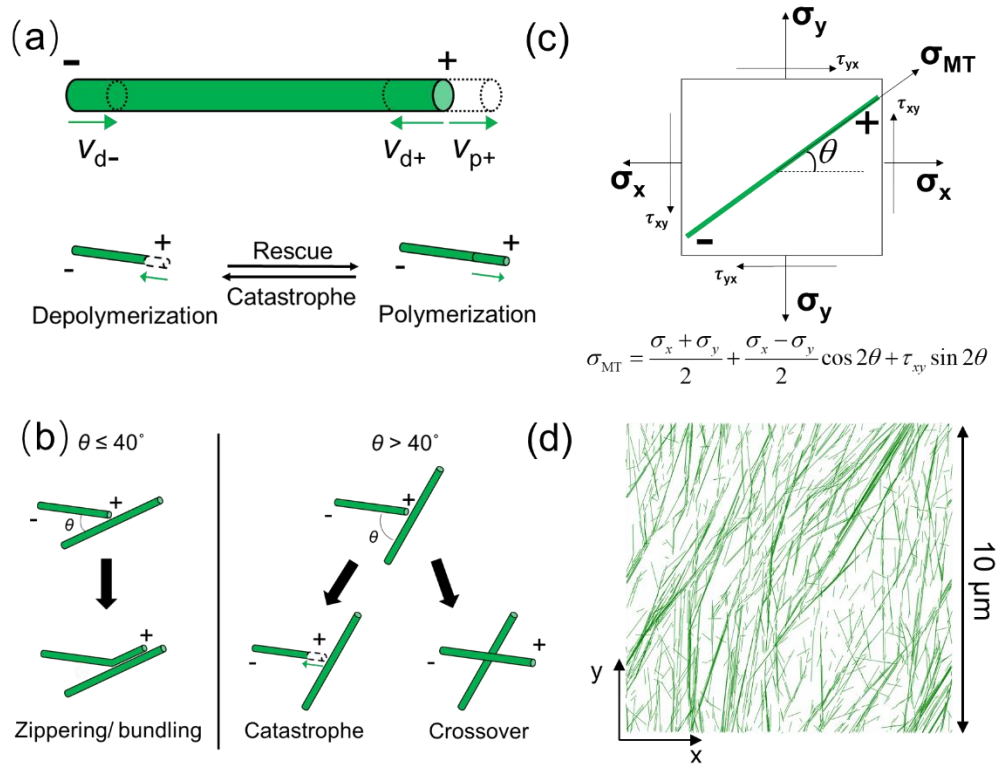


Fig. 3.1 Model schematic and microtubule dynamics. (a and b) Schematic of MT dynamics, including stochastic events and angle-dependent collision/deterministic events. (a) Stochastic events include polymerization ( $v_{p+}$ ) and depolymerization ( $v_{d+}$ ) at the plus end and constant slow depolymerization ( $v_{d-}$ ) at the minus end, rescue and catastrophe. (b) Angle-dependent collision-based events of MTs include zippering at a shallow angle ( $<40^\circ$ ) and catastrophe or crossover beyond a critical angle ( $>40^\circ$ ). (c) Mathematical relationship between local principal stress and stress acting on individual microtubules depending on their angle of orientation. (d) MT simulation domain is a  $10 \times 10 \mu m$  (initial domain size) square network with periodic boundary conditions in both  $x$  and  $y$  directions. MTs in the simulation domain are composed of serially connected small segments representing tubulin monomers, as shown in green.



### 3.2.2 Constitutive equation for stress sensing

To investigate the effects of local cell wall stress on microtubules, we map various stress patterns onto a computational domain. For a square domain of  $10 \times 10 \mu\text{m}$  in size and the periodic boundary condition in  $x$  and  $y$  directions (Fig. 3.1d). When we repeated simulations with a larger domain of  $20 \times 20 \mu\text{m}$ , there was no significant difference in results.

For the static stress pattern, stress components remain constant throughout the simulation for  $\sim 100$ - $200$  min. For implementing a dynamic stress pattern, an initial stress pattern is maintained for  $\sim 100$  min. Then, the predominant direction of the stress pattern is rotated by  $90^\circ$ . The change in the stress pattern takes place either instantaneously or gradually. For the gradual change, stress components are varied linearly. For instance, if the stress pattern is initially predominant in  $y$  direction, the  $y$  component of stress is linearly reduced over time, whereas the  $x$  component is linearly increased. At the mid of the gradual change, stress becomes isotropic. At the end of the change, the extent of the stress anisotropy becomes identical to the initial anisotropy. It takes  $50$ - $150$  min to complete the gradual change in the stress pattern, which is comparable to time taken for the dynamic pattern of cortical microtubules to be reoriented [234, 235], in the scales of tens of minutes or a few hours.

We use a rectangular computational domain with  $30 \times 10 \mu\text{m}$  in size for the stress gradient simulation. The longer direction ( $x$ ) is parallel with the cell long axis, and the shorter direction ( $y$ ) is parallel to the transverse direction. In this stress pattern, the extent of stress anisotropy is relatively constant along the cell long axis, whereas the magnitude of stresses decreases from left (the cell apex) to right (the cell base), indicating the existence of a stress gradient. The periodic boundary condition is imposed in the  $y$  direction to avoid size effects. In the  $x$  direction, there is no periodic boundary condition, unless otherwise specified, to avoid an abrupt change in the stress across the boundaries. Instead, three different types of boundary conditions are imposed; the catastrophe-inducing boundary enforce growing microtubules to switch to a shrinkage state, whereas the reflective boundary causes microtubules growing toward the boundary to change the direction, and the repulsive boundary pauses a growing microtubule as soon as it hits the boundary. These types of boundary conditions have been used in previous modeling studies [91, 223].

### 3.2.3 Simulation algorithm

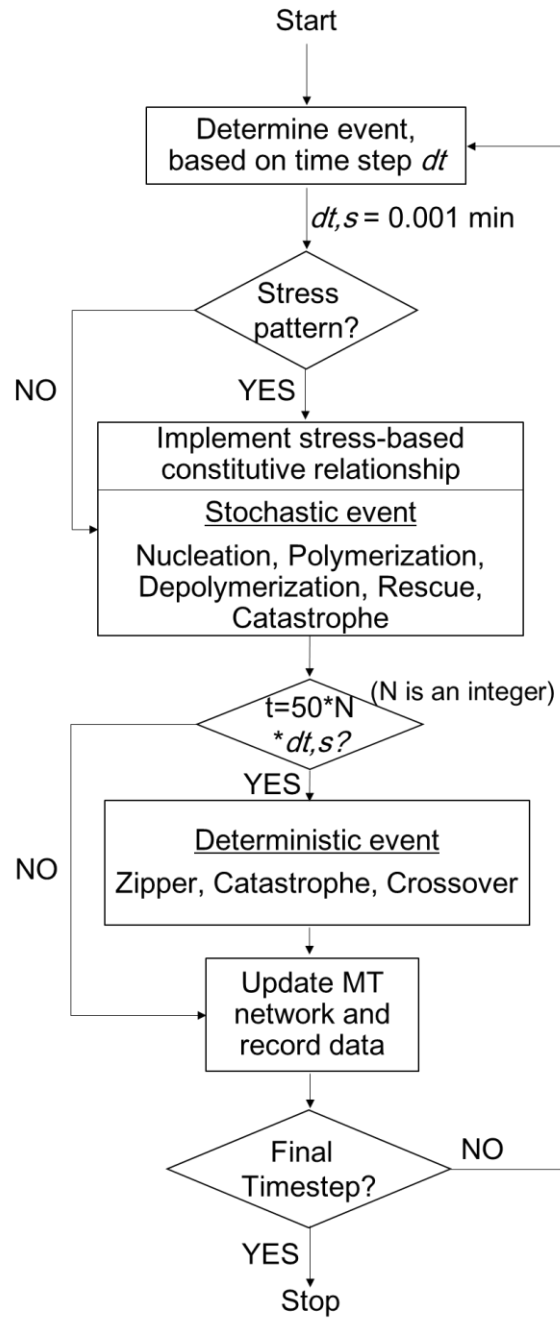


Fig. 3.2 Simulation flowchart. Stochastic and deterministic event with separate timesteps.

### 3.2.4 Quantification of self-organization

The order parameter ( $S_p$ ) is calculated to evaluate the extent of the alignment of microtubules:

$$S_p = \frac{\sum_{i=1}^{N_{MT}} l_i [\cos^2(\theta_i - \theta_p) - \sin^2(\theta_i - \theta_p)]}{\sum_{i=1}^{N_{MT}} l_i} \quad (3.1)$$

where  $N_{MT}$  is the number of microtubules,  $\theta_p$  is the dominant angle parallel to direction of principal stress, and  $\theta_i$  and  $l_i$  are the angle and length of each microtubule segment, respectively. We quantify a time constant to indicate the rate of a change in the order parameter. The first time constant ( $\tau_p$ ) represents time at which  $S_p$  reaches half of its steady-state value. The second ( $\tau_{p,2}$ ) and third ( $\tau_{p,3}$ ) time constants indicate time at which  $S_p$  reaches 75% and 87.5% of the steady-state value, respectively. In addition, we calculate the instantaneous rate of a change in  $S_p$ .

### 3.2.5 Microscopic imaging

We performed live cell imaging in the stages 2-4 trichome tips where two to three short branches are formed. *Arabidopsis thaliana* seedlings were grown in Murashige and Skoog medium under continuous illumination. Single channel images were performed and collected with mCherry:MBD seedlings. Arabidopsis trichomes are imaged 10-12 DAG, where confocal fluorescence microscopy was performed using a Yokogawa spinning disk CSU-10 head mounted on a Zeiss Observer.Z1 inverted microscope. Stages 2-4 trichomes were imaged using a 100X PlanApo 1.46 oil-immersion objective while mCherry was excited by 561 nm laser lines. Minute-scale images were acquired by Evolve 52 camera (Photometrics) through band-pass filters (482.35 and 617/73; Semrock). The collected z-stacks were analyzed in ImageJ.

### 3.3 Stress pattern is potent to reorganize cortical microtubules

Our goal was to create a computational framework to determine if tensile force patterns in the wall could act as cellular-scale cue to influence microtubule array organization. Microtubules were simulated as unstable linear polymers with polarity and dynamic properties based on live cell imaging data [16, 98]. As plant microtubules bind closely to the plasma membrane [17], our two-dimensional model is sufficient and rigorous enough accounting for the stochastic behaviors of microtubules and interactions between microtubules as well as stress patterns (Figs. 3.1a-c). The parameters used to depict the stochastic properties of dynamic microtubules and deterministic

behaviors of microtubule-microtubule interactions are listed in Tables 3.1. The simulation domain is a 10  $\mu\text{m}$  x 10  $\mu\text{m}$  array with periodic boundary conditions in both x and y directions (Fig. 3.1d).

Table 3.1 List of microtubule dynamic parameters in the simulation for three-state models.

Parameter	WT[16]	Description
$f_{gp}$	0.47 [ $\text{min}^{-1}$ ]	Freq. growth to pause
$f_{gs}$	0.97 [ $\text{min}^{-1}$ ]	Freq. growth to shorten
$f_{pg}$	0.51 [ $\text{min}^{-1}$ ]	Freq. pause to growth
$f_{ps}$	0.24 [ $\text{min}^{-1}$ ]	Freq. pause to shorten
$f_{sg}$	0.87 [ $\text{min}^{-1}$ ]	Freq. shorten to growth
$f_{sp}$	0.23 [ $\text{min}^{-1}$ ]	Freq. shorten to pause
$v_g^p$	3.69 [ $\mu\text{m}/\text{min}$ ]	Growth rate (+ end)
$v_s^p$	5.80 [ $\mu\text{m}/\text{min}$ ]	Shorten rate (+ end)
$v_s^m$	0.53* [ $\mu\text{m}/\text{min}$ ]	Shorten rate (- end)

### 3.3.1 Sensitivity of stochastic parameter to mechanical cues

Following the simulation flow chart (Fig. 3.2), we implemented stress patterns with various levels and anisotropy and analyzed diverse constitutive relationships between stress and microtubule dynamics. We analyzed how the morphology of microtubule arrays changes depending on how tensile force is coupled to the microtubule system. Recent experiments found that a tensile force increasing up to  $\sim 10$  pN increases the polymerization rate and the rescue frequency but decreases the depolymerization rate and the catastrophe frequency [236]. We assume that microtubule dynamics is dependent on local maximal principal stress acting on the cell wall, based on these experimental measurements. The range of stress on the cell wall that we estimated from the previous FE model is 3-15 MPa [9]. If microtubules are assumed to be coupled to this large stress directly, the magnitude of forces from the stress is far beyond a the level that microtubules can sustain without rupturing [237]. Thus, it is expected that microtubules are partially or indirectly coupled to the cell wall stress to sense its magnitude and direction [8, 213, 215], although it still remains unknown exactly how stress tensors are couple to microtubules. Because microtubules align according to the magnitude and direction of a tensile force [211, 213, 218], it is assumed that the magnitude of stress that a microtubule with a certain orientation experiences affects one of the dynamics behaviors of microtubules (Fig. 3.1c). Using the stress

transformation equation in continuum mechanics, we calculate the orientation-dependent local stress,  $\sigma_{MT}$ :

$$\sigma_{MT} = \frac{\sigma_x + \sigma_y}{2} + \frac{\sigma_x - \sigma_y}{2} \cos 2\theta \quad (3.2)$$

where  $\sigma_x$  and  $\sigma_y$  are normal stresses, and  $\theta$  is the orientation of microtubules measured relative to the +x direction in the simulation space. Note that shear stress is assumed to be negligible in this equation. A constitutive relationship was defined between  $\sigma'$  and either the grow rate, the shrinkage rate, the catastrophe frequency, or the rescue frequency is defined based on *in vitro* measurements [236]. The relationship is assumed to be in a linear, concave, or convex form.

We tested if stress patterns obtained from a validated FE model of a polarized plant cell [9] could bias the cellular scale organization of the microtubule array. If the network stress is isotropic, microtubule bundles align in random directions because microtubules are subjected to the same level of stress regardless of their orientations (Figs. 3.3a-b). Consequently, the order parameter measured at a steady state is very similar to that in a case without any stress ( $\sim 0.4$ - $0.5$ ) and is not dependent highly on which dynamic parameter was affected by stress (Figs. 3.3d). As another metric to analyze the sensitivity of different microtubule parameters to stress, the half-time to reach steady state in  $S_p$  was defined ( $\tau_p$ ) (Fig. 3.3c).  $\tau_p$  did not vary between different conditions when the four parameters were varied in response to an isotropic stress (Fig. 3.3e). The lifetime and length of microtubules were not enhanced by isotropic stress, compared to the case without stress (Table 3.2). When anisotropic stress with a 10:1 ratio ( $\sigma_x < \sigma_y$ ) was imposed, microtubules were aligned in the principal direction of stress to different extents depending on which parameter was modulated by stress (Figs. 3.3a, b). To evaluate the extent of microtubule alignment, the order parameter was calculated (Fig. 3.3c). In all cases, the order parameter increased fast at early time points and slowed down later. Oriented stress increased the order parameter for all of the +end variables compared to the isotropic stress control; however, the largest increase in  $S_p$  was observed when stress enhanced the polymerization rate or reduced the catastrophe frequency (Fig. 3.3d). Stress-dependent modulation of depolymerization rate was the least potent in terms of affecting  $S_p$ , and rescue frequency was intermediate.  $\tau_p$  did not differ significantly when depolymerization and rescue frequency were modulated by stress (Figs. 3.3e). However,  $\tau_p$  was significantly reduced in both cases with the polymerization rate and the catastrophe frequency varied by stress. The average length and lifetime of microtubules were also enhanced more in those cases (Table 3.2).

Larger changes in steady-state order parameter, time constants, and the length and lifetime of microtubules predict that the polymerization rate and the catastrophe frequency were more efficient stress-sensitive regulators of microtubule alignment.

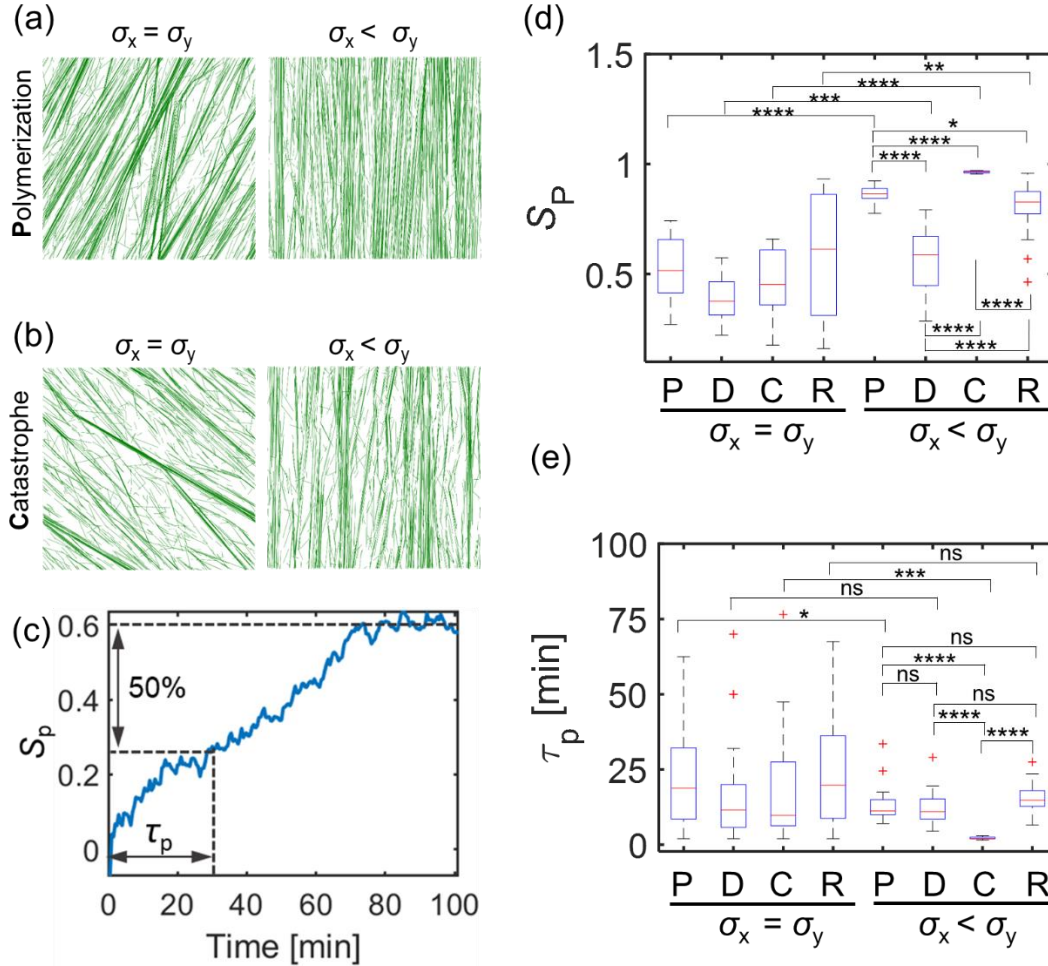


Fig. 3.3 Anisotropic stress affects self-organization of microtubules and correlates with global orientation. (A and B) Steady state MT network morphology. All snapshots are taken at 100 min. MTs are subject to network stress predominant in y direction (right), isotropic (left). In A and B, polymerization rate is enhanced, and catastrophe frequency is reduced in alignment with principal stress, respectively. (C) A representative case with the time evolution of the network order parameter  $S_p$ . The first time constant is calculated as the time required to reach half of the  $S_p$  value at steady state. (D) Summary of the network order parameter  $S_p$  at 100 min for all different conditions with isotropic vs. anisotropic stress in which principal stress influences individual stochastic parameter independently. (E) Boxplot of the time constants acquired from cases with isotropic vs. anisotropic stress in all conditions. Data for each condition are averaged over 20 simulations in each case. P: polymerization, D: depolymerization, C: catastrophe, R: rescue; ns  $p > 0.05$ , \*  $p < 0.05$ , \*\*  $p < 0.01$ , \*\*\*  $p < 0.001$ , \*\*\*\*  $p < 0.0001$ .

Table 3.2 Average microtubule lifetime and length under various stress conditions.

$\tau_{\text{life}}$ [min] $\langle L_{\text{MT}} \rangle$ [ $\mu\text{m}$ ]		P Polymerization	D Depolymerization	C Catastrophe	R Rescue
Stress free control	$\tau_{\text{life}}$	2.2 min			
	$\langle L_{\text{MT}} \rangle$	2.0 $\mu\text{m}$			
Isotropic stress $\sigma_x = \sigma_y$	$\tau_{\text{life}}$	2.3 min	2.3 min	2.3 min	2.3 min
	$\langle L_{\text{MT}} \rangle$	2.6 $\mu\text{m}$	2.0 $\mu\text{m}$	2.5 $\mu\text{m}$	2.2 $\mu\text{m}$
Anisotropic stress $\sigma_x < \sigma_y$ or $\sigma_x > \sigma_y$	$\tau_{\text{life}}$	2.9 min	2.4 min	3.0 min	2.4 min
	$\langle L_{\text{MT}} \rangle$	2.8 $\mu\text{m}$	2.2 $\mu\text{m}$	2.9 $\mu\text{m}$	2.3 $\mu\text{m}$

We next wanted to determine the threshold of stress anisotropy that is sufficient to increase microtubule order. By testing different levels of stress anisotropy ( $\sigma_y/\sigma_x$ ), we found that the minimal ratio of 1.5:1 was required to induce microtubule alignment in the direction of principal stress (Fig. 3.4). In response to stress anisotropy with the minimal ratio, both the  $S_p$  and  $\tau_p$  exhibited a substantial increase or decrease, respectively ( $p < 0.001$ ,  $n = 10$ ). Based on a validated FE model of a growing trichome branch, its anisotropy has been estimated to be  $\sim 2:1$  [9]. This implies that the physiological level of the stress anisotropy is large enough to result in microtubule alignment, which is also confirmed by our simulations.

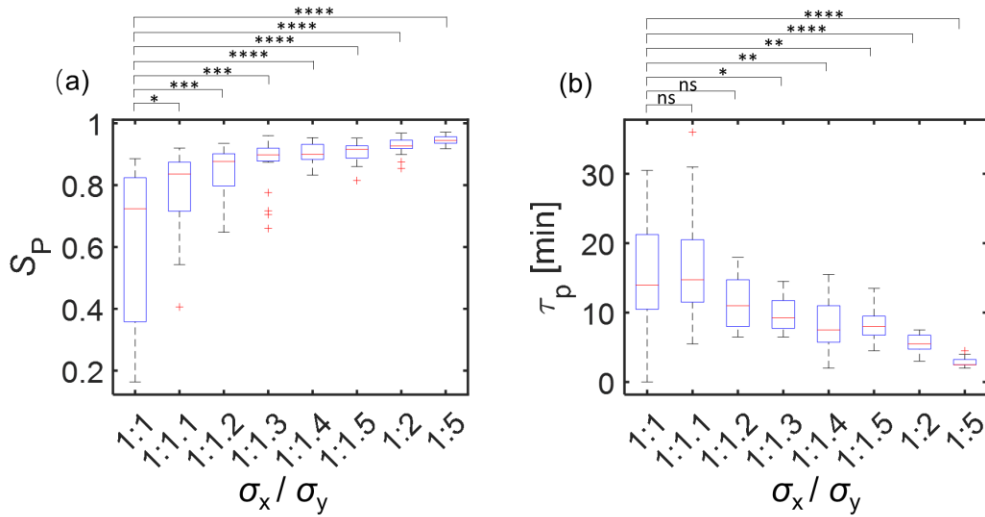


Fig. 3.4 Order parameter and first time constant with different stress anisotropy ratios.

### 3.3.2 Stress reorientation leads to CMT reorganization

Stress patterns are not static features but can change at differing time scales. As such, dynamic stress patterns can lead to corresponding reorientation of cortical microtubule array [9, 42]. To determine whether an established ordered microtubule array can be reoriented by a change in stress anisotropy, we imposed a dynamic stress pattern that is dominant in y direction at the beginning for 100 min and undergoes a directional shift near the middle of the simulation. We chose the catastrophe frequency to integrate stress dynamics because it was the most efficient stress-sensitive parameter for microtubule alignment. The transition in the stress pattern occurred either instantaneously or gradually to reflect the slow shape change of plant cells that occurs on time scales of 10s of minutes (Figs. 3.5a, b). The ratio of stress was 2:1 at the beginning and at end of the transition. When the principal direction of stress was rotated by 90 deg instantaneously at ~100 min, well-aligned microtubules were quickly depolymerized due to a reduction in their average lifetime compared to the value before 100 min, and newly nucleated microtubules were polymerized more persistently and then stabilized in the direction parallel to the new principal stress. This is due to the abrupt change in the differentiated catastrophe frequency by the rotation of stress pattern. It took ~5 min for aligned microtubules to be transformed into randomly oriented microtubules. 50 min after the abrupt stress reorientation, most of microtubules were reoriented in the perpendicular direction (Fig. 3.5c), followed by stabilization and thickening of bundles due to a decrease in collision-induced catastrophe events. We next imposed a more gradual change in the stress pattern. As in the case with the rapid stress change, microtubules were initially aligned in the y direction perpendicular to the new stress (Fig. 3.5d). As stress anisotropy  $\sigma_x/\sigma_y$  was enhanced over time (150 min), more short microtubule segments emerged in the x direction. At ~215 min, the microtubule array became relatively homogeneous with randomly oriented microtubules (Figs. 3.5b, d). At 350 min, most of the microtubules were reoriented to the x direction, and bundles looked quite similar to those observed at the end of simulations run with the rapid stress change (Figs. 3.5a, b). The results are similar in the cases with 100 min and 50 min time window for gradual change in stress pattern. Regardless of the time window, the order parameter measured with respect to the x direction showed an increase and reached similar level at the end (Fig. 3.5e). The complete reorientation, in all cases, took about 50 min. It was also indicated that it took about 20 min for the network to become homogeneous (order parameter near zero), which was in alignment with the timepoint where stress became isotropic (Fig. 3.5e). These values are similar



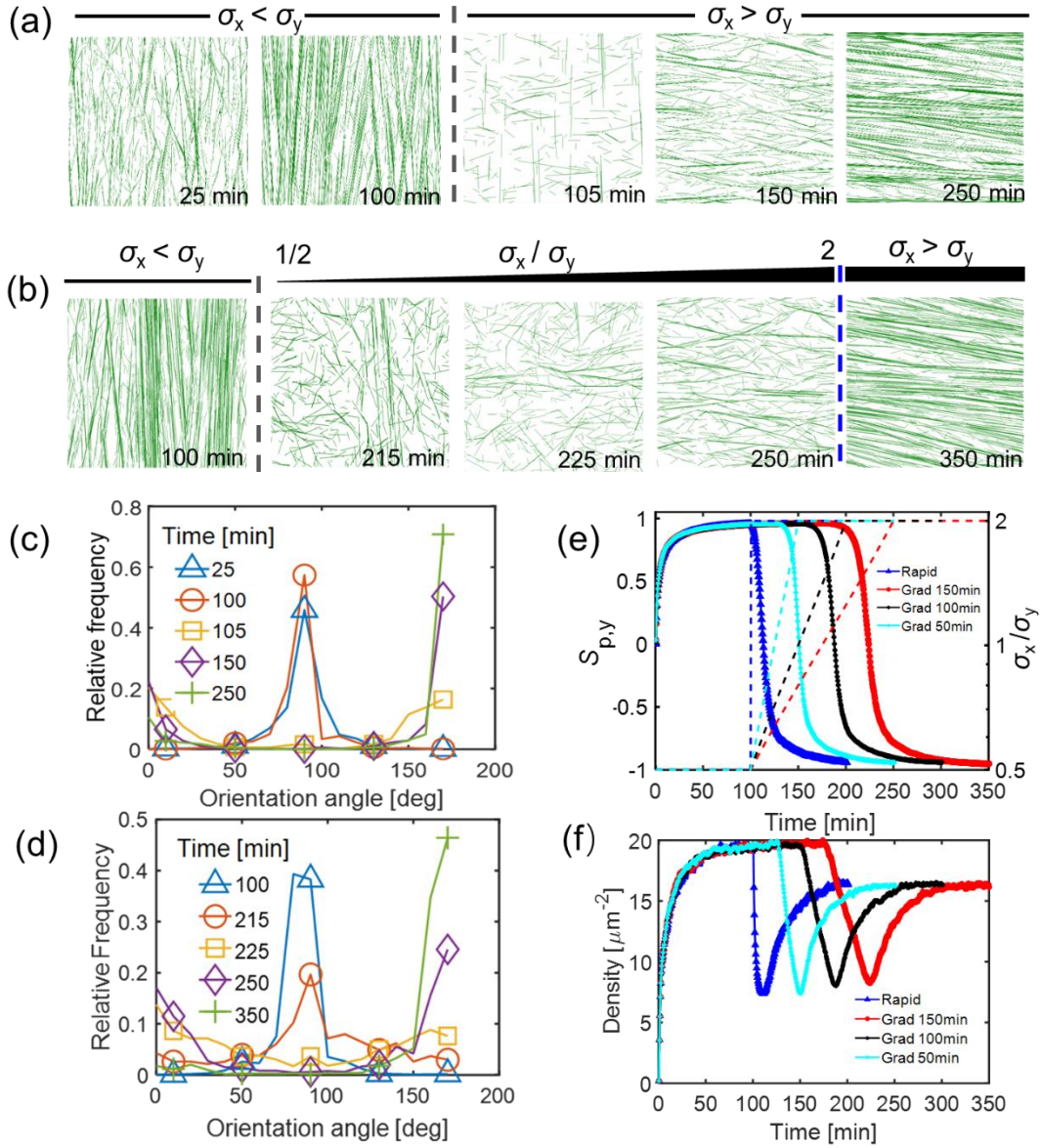


Fig. 3.5 Dynamic stress pattern reorientation leads to remodeling of the microtubule network. (A and B) Time evolution of the MT network morphology (at various timepoints including 25, 100, 105, 150, 250 min for a rapid transition and 100, 215, 225, 250, 350 min for a gradual transition). Grey dashed line indicates the timepoint (100 min) after which reorientation of anisotropic stress takes place. The blue dash line indicates the timepoint after which anisotropic stress is stabilized. Initial network stress pattern is predominant in y direction. In A, stress pattern reorients instantaneously and becomes predominant in x direction after 100 min. In B, stress pattern gradually reorients until 250 min and becomes steady afterwards. (C and D) Relative frequency showing the distribution of microtubule orientation angle at various timepoints during stress pattern reorientation in A and B respectively. 90 degree is equivalent to the direction parallel to y axis, and 0 or 180 degree is equivalent to the direction parallel to x axis. A flat curve indicates homogeneous distribution of MT orientation angles. (E, F) Time evolution of the network order parameter  $S_{p,y}$  (E) and network microtubule segment densities (F) in four cases: rapid transition (as indicated in A, blue), gradual transition of stress (150 min, as indicated in B, red; 100 min, black; 50 min, cyan).

to the values of 10 min to 2 hours for experimentally determined rate of reorientation [218, 238, 239]. The average lifetime of microtubules aligned in various directions do not show much difference between cases with a rapid change of stress pattern and those of a gradual stress pattern reorientation. Local heterogeneity of microtubule orientations positively correlated with the stress pattern transition. Interestingly, during microtubule orientation, we noticed microtubule density was almost halved when network became homogeneous, followed by a rescue when the new bundles formed (Fig. 3.5f).

### **3.3.3 Stress gradient potentially generate organized microtubule arrays**

In young trichoblast cells an apical collar of highly ordered microtubules are needed to program anisotropic expansion and tip tapering [9]. Cell wall stress is not constant along a cell surface, and we next wanted to determine if spatially variant stress could be sufficient to generate cellular scale patterns in the microtubule network. Tensile force cannot be measured directly and, in most cell types, the stress patterns are completely unknown. However, realistic wall stress patterns have been predicted for elongating leaf trichoblasts (Fig. 3.6a) based on a known cell wall thickness gradient and a validated FE model [9]. In young branches of this cell type, the microtubule array is highly organized, forming an apical microtubule depletion zone and an extended collar of transverse microtubules that become progressively less dense toward the branch base (Fig. 3.6b) [9]. We adapted the stress pattern of the curved FE model of the branch to a rectangular MT simulation space of  $30\ \mu\text{m} \times 10\ \mu\text{m}$  in size (Fig. 3.6a). The stress pattern reflects principal stress decreasing from the apical flanks of the tapered to the base. The stress pattern is due to a combination of a tapered morphology and an increasingly thick cell wall at the base [9]. To analyze boundary effects, we also applied four different types of conditions to two boundaries normal to the longitudinal cell orientation: catastrophe-inducing, reflective, repulsive, and a periodic boundary as a control (Fig. 3.7).

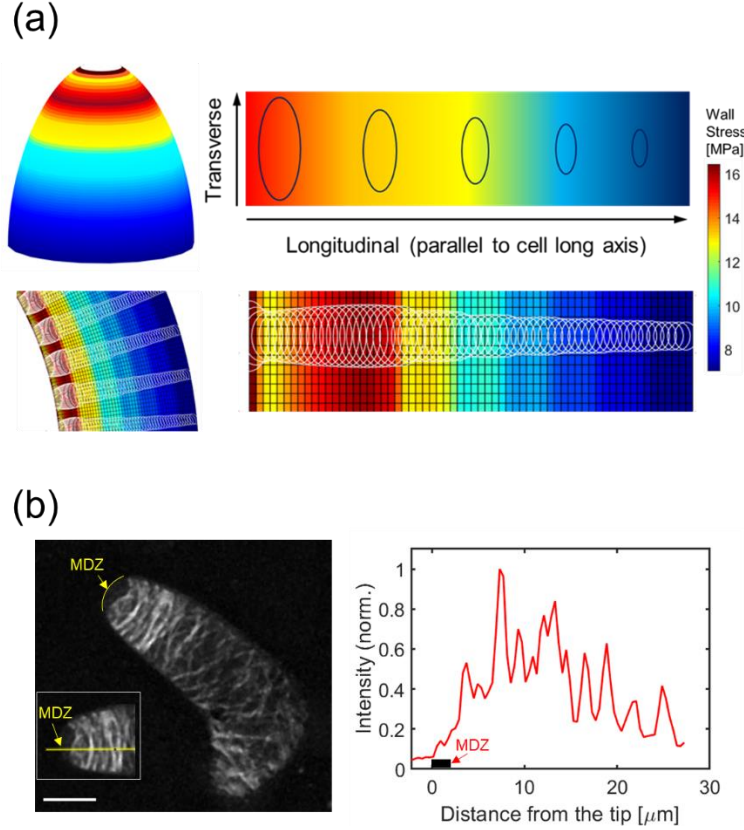


Fig. 3.6 (a) Schematic of the stress pattern gradient pertinent to a finite element model of trichome morphogenesis. Magnitude of stress decreases from left to right, along the direction parallel to cell long axis while the stress is highly anisotropic and predominant in the transverse direction, indicated by the ellipses. The lower panels show an unfolded stress pattern based on the model results. The unfolded meshed stress pattern is mapped onto the simulation domain. (b) Representative confocal image showing microtubule localization in stage 4 young trichome branches (left panel). Transverse band is prominent near the cell apex. The microtubule depleted zone (MDZ) is highlighted and marked in yellow. Scale bar: 10  $\mu\text{m}$ . Right panel shows the intensity profile from the apex to the base in the image shown in the left panel along the yellow line.

We first tested control cases with a global isotropic or stress-free condition along with a periodic boundary or catastrophe-inducing boundary condition. We first tested control cases with a global isotropic or stress-free condition along with a periodic boundary or catastrophe-inducing boundary condition. Under stress-free condition when all boundaries are periodic, the network was homogeneous with small bundles, leading to uniform local order parameter and density when both parameters were measured at transverse sectors along the longitudinal axis of the cell (Figs. 3.8). When two catastrophe-inducing boundaries were employed, more aligned bundles aggregated near

the regions in close proximity to the boundaries, characterized by a sharp local increase in the order parameter and increased local densities of microtubules (Figs. 3.9a-d, 3.8). Under isotropic stress condition, the local order parameter had similar distribution. However, isotropic stress significantly enhanced the order parameter globally by  $\sim 0.3$  due to enhanced average length of lifetime of microtubules (Table 3.2). These results indicated that catastrophe-inducing boundary alone could only increase local heterogeneity without affecting global alignment. Next, we implemented a stress gradient. We observed apical microtubule clustering with each type of the imposed boundary conditions (Fig. 3.10). With catastrophe-inducing, reflective and repulsive boundaries, bundles were formed in the direction parallel to principal stress (i.e., perpendicular to the cell axis) in regions with large stress (Figs. 3.9e-h). The local order parameter of microtubules did show a clear difference from the control (Figs. 3.9c, g). Regions with higher stress showed  $S_p > 0.6$  within  $20\ \mu\text{m}$  from the distal boundary. By contrast, in proximal regions near the base regions with lower stress, microtubules were noticeably less dense and more homogenous in all cases. This is attributed to a local fraction of disordered microtubules that turnover quickly due to encounter based catastrophe. To test whether *in vivo* stress patterns at the cell apex could generate a microtubule depletion zone, we included a small apical zone of  $2\ \mu\text{m}$  at the leftmost boundary to represent a region with isotropic stress ( $\sigma_x/\sigma_y=1$ ). Isotropic stress is present in the FE model of apex (Figs. 3.11). Interestingly, an apical isotropic stress zone resulted in a very localized sparse, disordered population of short microtubules similar to the base (Figs. 3.9i-l), with a sharp decrease in the order parameter in the tip zone. The rest of network showed similar pattern where the stress gradient was intact. The relative intensity of microtubule segments showed consistent results with the microtubule morphology. Thus, the combination of spatially defined gradients of stress magnitude and anisotropy could generate a microtubule pattern that closely resembled the functional cortical array in living cells (Fig. 3.6b).

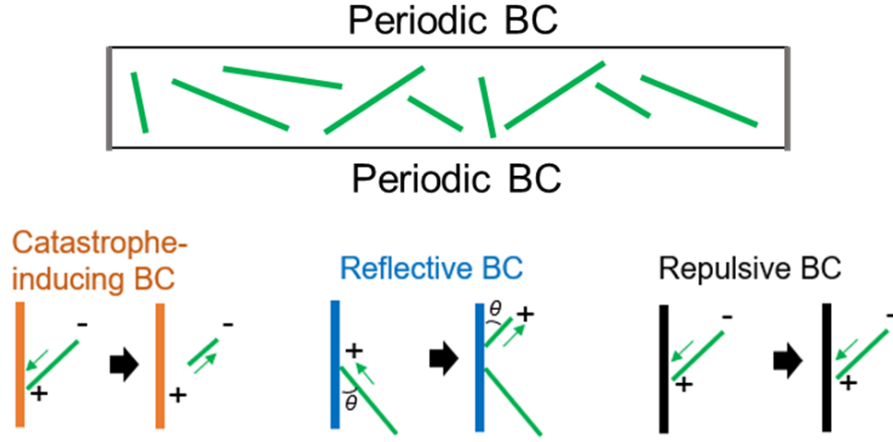


Fig. 3.7 Different types of boundary conditions imposed in the simulation.

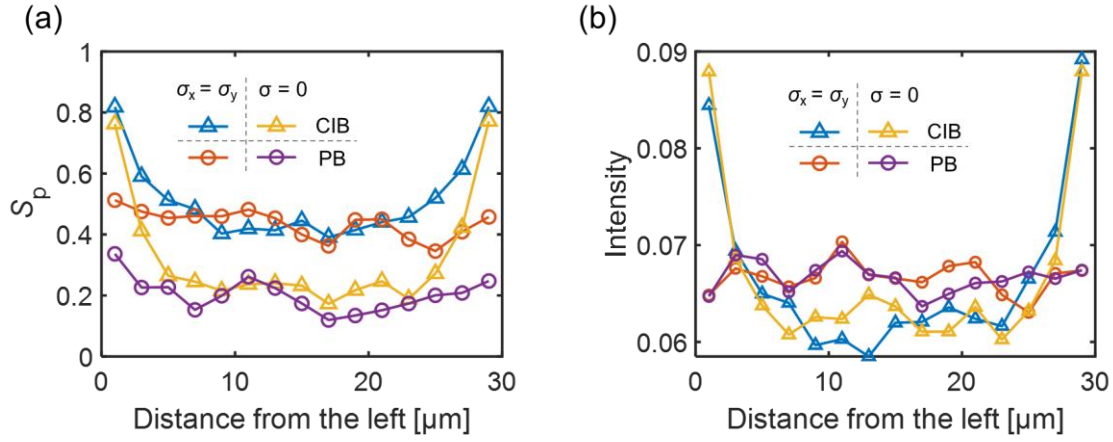


Fig. 3.8 Order parameter (a) and local intensity (b) of the network under various conditions: stress free control and isotropic stress. Boundary conditions include catastrophe inducing boundary (CIB) and periodic boundary (PB).

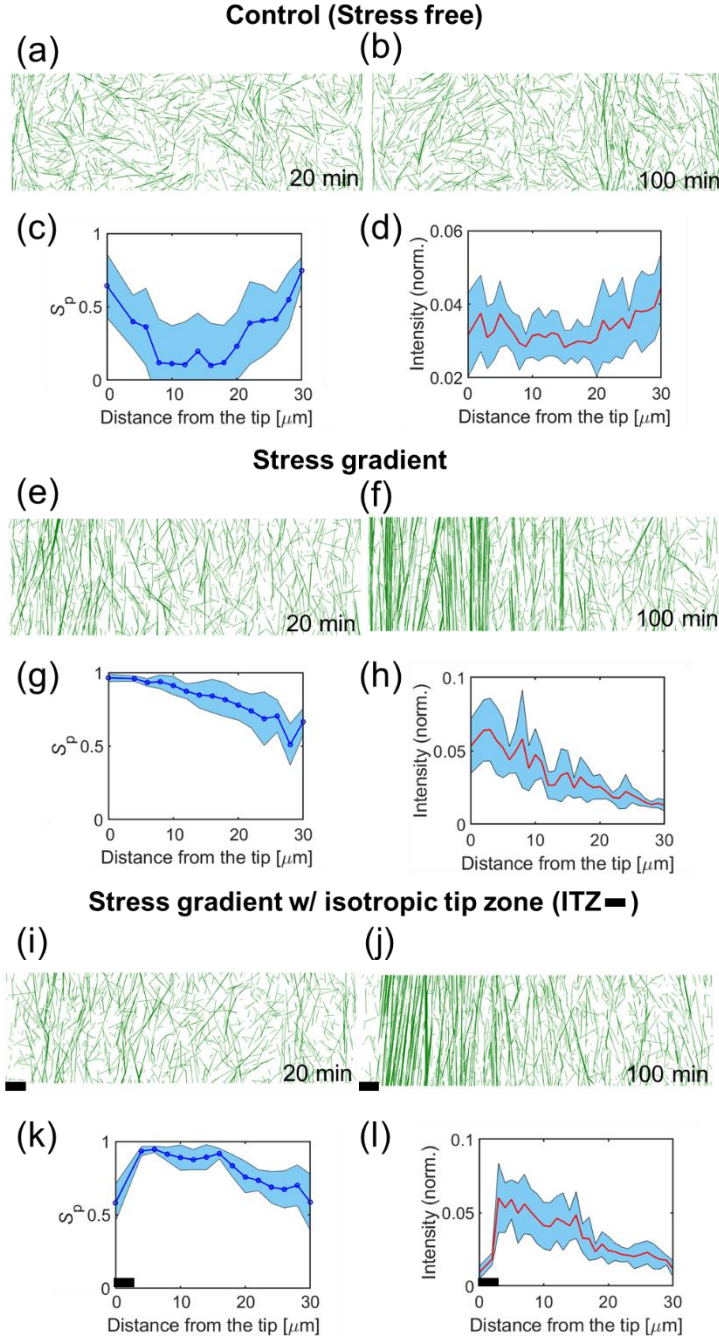


Fig. 3.9 A catastrophe-inducing boundary condition is implemented on the two short edges of the simulation domain ( $30\ \mu\text{m} \times 10\ \mu\text{m}$ ). (a, e, i) Early-time (20 min) and (b, f, j) steady-state (100 min) morphology of network in stress free (a, b), stress gradient (e, f), and stress gradient with isotropic stress in the tip zone (i, j,  $2\ \mu\text{m}$  tip zone marked by black bar). (c, g, k) Local order parameter of microtubules in subregions of cases in b, f, j respectively. For this, the network was divided into fifteen subregions, incrementally separated by  $2\ \mu\text{m}$  along the x direction. Blue curve indicates and shaded region represents standard deviation ( $n=10$ ). (d, h, l) Normalized intensity of MT segments (tubulin dimers) as a function of the distance from the tip (left boundary), which is nearest to apex of a real cell.



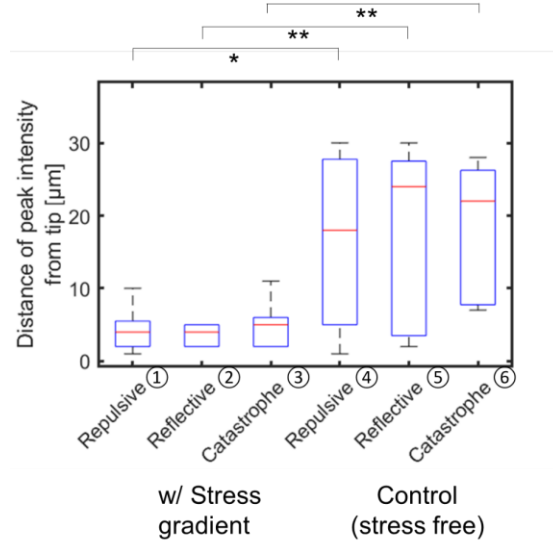


Fig. 3.10 Distance of peak microtubule dimer intensity from the tip under various conditions.

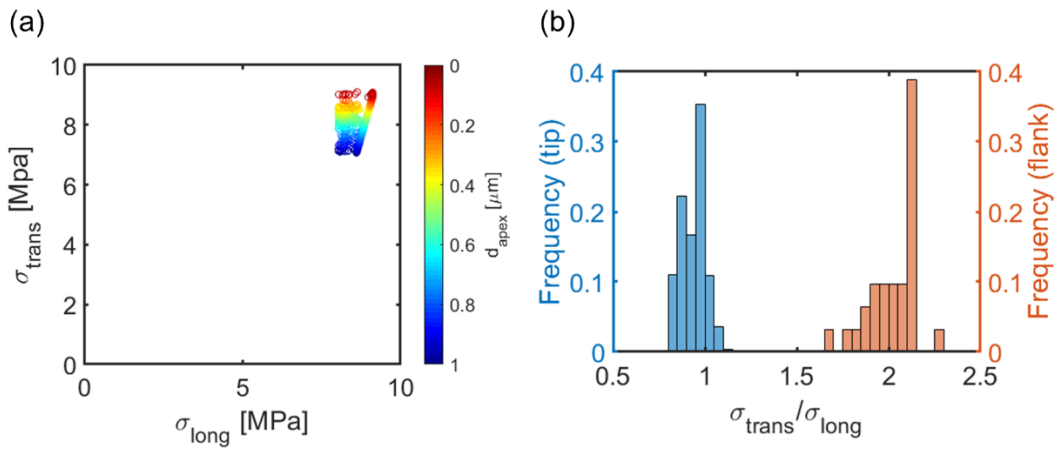


Fig. 3.11 Stress profile from the FEM model. (a) Paired values of longitudinal and transverse stress in the apex of trichome model. Color indicates the distance from apex. (b) Distribution of the stress anisotropy ratio in the tip zone (blue) and flank region (orange). Stress is isotropic in the tip zone while anisotropic in the flank region, as implemented in our simulations.

### 3.4 Branched nucleation determines CMT array bundling

#### 3.4.1 Background

*In vivo* and *in vitro*, nucleation is initiated and facilitated by recruitment of  $\gamma$ -tubulin complex to the lattice of pre-existing microtubules. This can occur in two ways: branch or parallel form. In the branch form, nucleated microtubules form from a specific angle in a typical range from  $20^\circ$  to  $60^\circ$  [240], with an average of  $\sim 40^\circ$ , towards the plus ends of existing microtubules. In the parallel form, fresh microtubules nucleate predominantly with a degree of  $180^\circ$  to the existing microtubule, leading to antiparallel or parallel bundles [240]. Microtubule nucleation is also crucial for cortical array patterning. Mutation in subunit of  $\gamma$ -tubulin complex resulted in significant disruption in normal microtubule nucleation and caused a much wider nucleation angle distribution [241]. This perturbation consequently led to spiral patterning of microtubules in hypocotyls instead of longitudinal alignment in wild type. Interestingly, it was found that katanin is not a determinant of the nucleation angle of nascent microtubules. However, experimental evidence has shown that katanin activity is actively involved in the detachment of branched or daughter microtubules from the nucleation site of a mother microtubule [242]. It is plausible that severing facilitates the freeing of minus end from the nucleation site, contributing to the full release of a daughter microtubule via depolymerization. A recent model implemented both nucleation and severing to study differentiated band formation [243]. It is crystal clear that stochastic nucleation does not lead to any separation of bands across of the network. Complete branched nucleation led to highly heterogenous band morphology. However, the model is limited to a confined cylindrical space, which narrows down the scope of the cell system. Furthermore, it does not fully explain the mutual interaction between severing and branched nucleation. Therefore, in Chapter 3.4, we used the discrete model with implementation of branched nucleation and severing to study bundle formation in the cortical array. First, our results suggested that the bundle skewness is sensitive to both nucleation angle which is tightly coupled to the zippering angle. Second, the model showed that different severing modes have distinguishable impact on the network bundle configuration.

#### 3.4.2 Additional method: Nucleation and severing dynamics

We employed branched nucleation in addition to the stochastic nucleation in section 3.2 (Figs. 3.12a,b). Stochastic nucleation takes place independent of existing microtubules dimers and



can occur at random locations across the network. In contrast, branched nucleation is fully dependent on existing microtubules. To be consistent with experiments, we implemented a wide parametric space for the specific angle of branched nucleation  $\theta_b$  as well as probability of branched nucleation  $P_n$ , where  $\theta_b$  is between  $10^\circ$  to  $60^\circ$  for branch form;  $0^\circ$  for parallel nucleation and  $180^\circ$  for antiparallel nucleation.  $P_n$  is defined as the percentage of branched nucleation events over the total number of nucleation events at each time step. The total number nucleation events is the sum of branched nucleation and stochastic nucleation events.  $P_n$  is varied from 0, 0.2, 0.4, 0.6, 0.8 to 1, where 0 indicates completely stochastic nucleation and 1 represents a condition with only branched nucleation. Branched nucleation takes places with equal probability in terms of the relative direction to an existing microtubule: it can branch off from either left or right side of a template, regardless of initial configuration or direction of pre-existing microtubules. The total frequency of nucleation is the same as in section 3.2,  $1000 \text{ min}^{-1}$ .

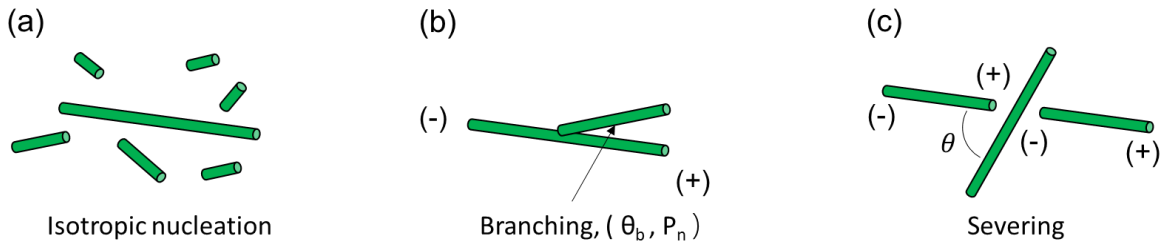


Fig. 3.12 Schematic for (a) isotropic nucleation (stochastic), (b) branched nucleation and (c) severing at crossover sites of MTs.

For actin severing, we employed two different modes: stochastic severing and severing at the crossover sites of microtubules (Fig. 3.12c). These two modes are commonly observed in experiments and implemented in a previous model [93]. In the stochastic mode, severing events are randomly selected to occur on existing microtubules. The uniform severing rate is 10 per unit length per minute. Therefore, the severing frequency is dependent on the total length density of microtubules in the network. In the crossover mode, severing occurs at the intersection of microtubules at a constant rate of 10 per minute. We also employed a lifetime dependency to vary the severing frequency. It was previously shown that as crossover site's lifetime increases, the severing frequency linearly increases until an equilibrium threshold at remains constant afterwards. In the simulations, we set a threshold of 3 min. Based on *in vitro* observations, the severing event takes place at the crossing microtubules instead of crossed microtubules. Therefore, we assume

severing at the crossover sites occur at the microtubules that encountered existing microtubules during the crossing events. In both severing modes, the newly formed plus end is directly assigned to be in a depolymerization state, and the new minus end starts slow shrinkage instantaneously.

### 3.4.3 Additional method: Quantitative analysis of bundling

For quantification of the bundling orientation, we plotted the distribution of the microtubules using a rose plot. For thickness of bundle quantification, we implemented a method based on the method by Higaki et al. for imaging analysis of the microtubule bundles in stomata cells [244]. For that, we evaluate the skewness of bundle morphology by measuring spatial distributions of microtubule dimers in the computational domain. For measurement, the domain is divided into  $N_G \times N_G$  grids in x and y directions, where  $N_G$  indicates the number of grids in each direction. We measure the number of microtubule segments located in each grid,  $\rho_{M,i}$ , in order to create the 3D histogram representing their density map. Then, standard deviation of  $\rho_{M,i}$  is calculated over all grids to further quantify skewness,  $Q_M$ :

$$Q_M = \frac{1}{N} \sum_{i=1}^N \left( \frac{\rho_{M,i} - \overline{\rho_M}}{\sigma} \right)^3 \quad (3.3)$$

where  $\overline{\rho_M}$  is the average density of microtubule segments in all grids and N is equal to  $N_G^2$ , the total number of grids in the domain.  $\sigma$  is the standard deviation of  $\rho_{M,i}$ :

$$\sigma = \frac{1}{N} \sum_{i=1}^N \left( \rho_{M,i} - \overline{\rho_M} \right)^2 \quad (3.4)$$

Since the skewness calculated in this method depends on the choice of  $N_G$ , we carefully determined the optimal range of  $N_G = 20$  for better consistency with [244]. The skewness is a direct measure of how the grid-based distribution of the density of microtubule segments deviates from normal distribution. The larger the skewness, the more heterogeneous and thicker the bundle is. A homogeneous network would have a skewness  $Q_M$  smaller than 1.

### 3.4.4 Branched and parallel nucleation lead to differentiated bundle morphology

Stochastic and deterministic events, the major constituents of the intrinsic dynamics of microtubules, are sufficient to drive ordering of cortical microtubule arrays. However, the effect

by angle-dependent nucleation still cannot be neglected. The tight control of nucleation angle is a necessary and sufficient condition for precise alignment of daughter microtubules from an existing template, reminiscent of the spatial heterogeneity and flexibility of branched microtubule networks. As aforementioned, nucleation of microtubules in plant cortical array is categorized into various modes depending on the cell type and developmental stages. While parallel and antiparallel nucleation enable daughter microtubules to sense and follow the polarity of mother microtubules, branched nucleation usually leads to more dispersed arrays. The balance between parallel, antiparallel, and branched nucleation might contribute to dynamic reorganization of cortical microtubule array as well as its response to mechanical or developmental cues. We explored a wide parametric space for the probability of branched nucleation  $P_n$  and nucleation angle  $\theta_n$  (Fig. 3.13). For a reference state, we choose the parameter set from Shaw et al. [16] which leads to a randomly ordered array without branched nucleation. Since nucleation occurs in an isotropic manner, the skewness of microtubules is relatively low  $\sim 0.1$ , indicating very thin bundles. The network order parameter at the reference conditions is between 0.7-0.8. When we slightly increase the  $P_n$  (0.2 – 0.4), thicker bundles form with an increase in the bundle skewness to  $\sim 1$ . The skewness slightly decreases with increasing branched angle when the angle is shallow ( $<30^\circ$ ). When the branched angle is further increased to  $40^\circ$  or above, the skewness is significantly reduced as the network bundles become much thinner and comparable to the reference conditions with isotropic nucleation. The average lifetime of microtubules is not significantly enhanced (Fig. 3.15). However, the average length of microtubules is increased by  $\sim 0.5 \mu\text{m}$  (Fig. 3.15). As  $P_n$  is increased to (0.6 – 0.8), The bundles become much thicker, with a skewness between 1 to 5. The dependence of skewness on the branching angle is still obvious at a given  $P_n$  (Fig. 3.14). The average length of microtubules is similar to that in the low  $P_n$  cases, with an 0.5 – 1 min increase in the average lifetime (Fig. 3.15). When  $P_n=1$ , all nucleation occurs in the branched mode which leads to a higher skewness value which still decreases with increasing branching angle (Fig. 3.14). Beyond a branching angle threshold  $40^\circ$ , the network remains homogeneous with short evenly distributed microtubule segments. At shallow branching angles, the skewness is higher than 10. This also corresponds well to a 1 – 2 min increase in the average lifetime of microtubules, with a doubled average length (Fig. 3.15). Interestingly, we observed an increase in the microtubule polarity when branched nucleation becomes more predominant ( $P_n \geq 0.8$ ) with a shallow angle ( $10^\circ - 40^\circ$ ). When  $P_n=1$ , the networks are mostly composed of parallel bundles, as branched nucleation occurs toward

the plus end of the mother microtubules. In terms of the network order parameter, both the order parameter at steady state and the efficiency of network ordering increases with increasing  $P_n$  when branching angle is shallow ( $<30^\circ$ ) (Fig. 3.15). This is mainly attributed to a decrease in the zippering angle and increase in the frequency of zippering events during self-organization of microtubules and network evolution. In the parallel and antiparallel nucleation mode, the skewness is enhanced in comparison with the reference condition regardless of the probability of bundle nucleation  $P_n$ . Although the increase in zippering events and decrease in zippering angle is very pronounced, the enhancement of order parameter and the efficiency of the global alignment is nearly the same in all cases regardless of  $P_n$ . However, the lifetime and average length of microtubules are further enhanced, indicating more stability compared to the cases with branched nucleation (Fig. 3.15).

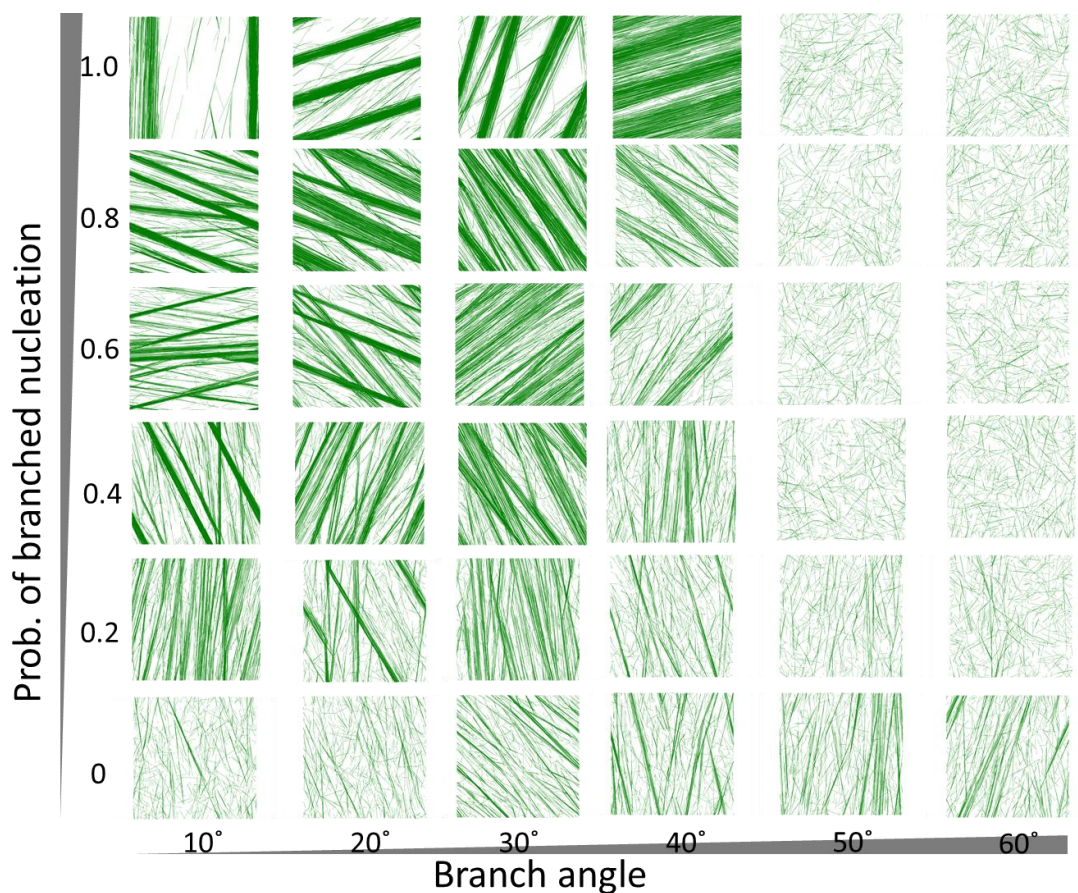


Fig. 3.13 Steady state network morphology at various combinations of probability of branched nucleation and branching nucleation angle.

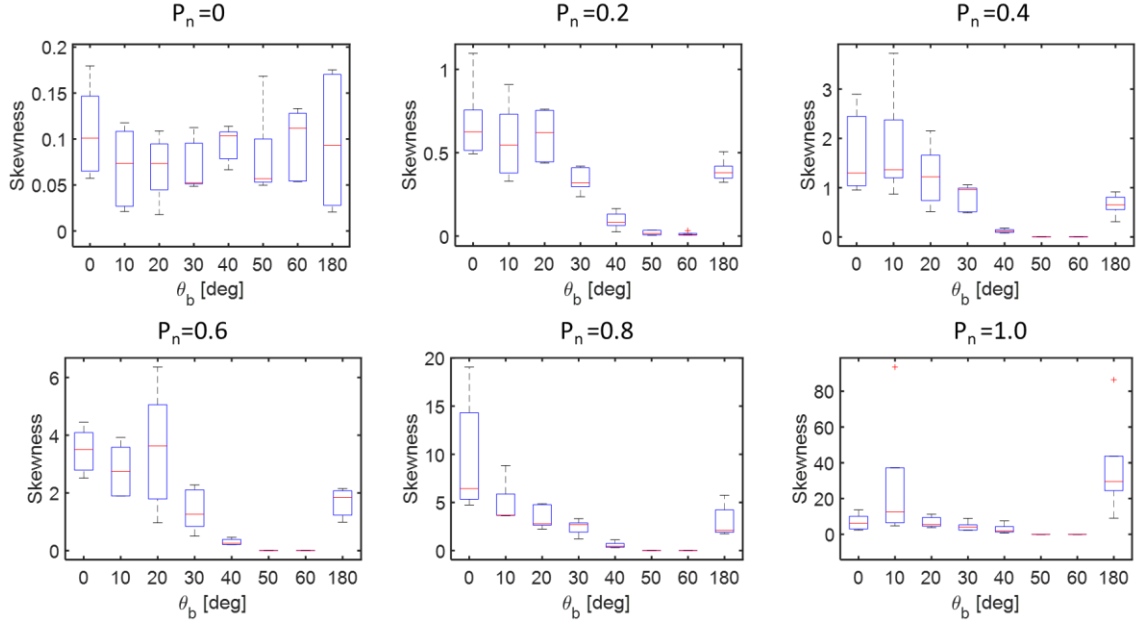


Fig. 3.14 Skewness of microtubule bundles as a function of branched nucleation angle under cases with various probabilities of branched nucleation.

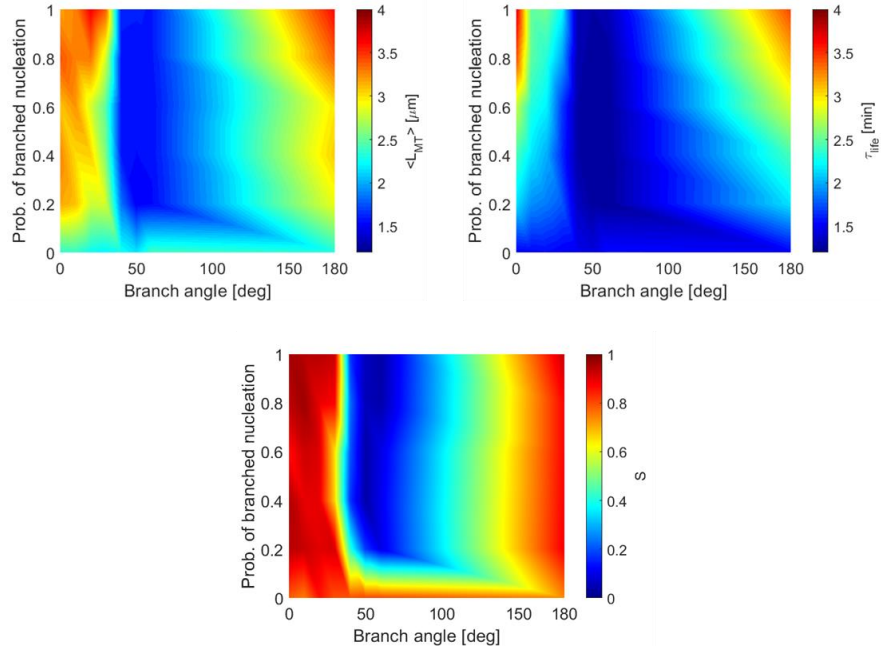


Fig. 3.15 Heatmaps showing the average length, lifetime of microtubules and steady state order parameter of the cortical array, under various combination of probability of branched nucleation and branched nucleation angle.

### 3.4.5 Nucleation angle couples with zippering angle for bundle formation

Since we noticed the dependence of network bundle morphology on the branching angle and the critical threshold  $\sim 40^\circ$  might be tightly correlated with the zippering angle threshold, we explored the cooperative mechanism within the two parametric spaces. The reference angle for zippering was initially set at  $40^\circ$ . At a fixed percentage of branched nucleation ( $P_n = 0.4$ ), we varied both the zippering angle and branch angle from  $20^\circ$  to  $60^\circ$ . At a shallow zipper angle ( $< 30^\circ$ ), the network remains homogeneous in all cases, independent of the branch angle. This is expected since zippering is the main driving force for bundle formation. In these cases, the average lifetime and length of microtubules are significantly reduced compared with those in the reference condition (Fig. 3.16). The order parameter is therefore very small ( $0 \sim 0.2$ ). When the zippering threshold angle is increase above  $40^\circ$ , the network could always evolve into intertwined bundle morphology as long as the branching angle does not exceed the zippering threshold angle. The enhanced lifetime and average length led to much larger network order parameter at steady state ( $0.7 \sim 0.8$ ) regardless of the branching angle. However, it could not reach 1 as in the case in Section 3.3 due to the lack of directional bias (Fig. 3.16). Formation of stable interconnected bundle endures over the time course of simulation, increasing the local spatial heterogeneity. In addition, the dominant angle of local heterogeneous bundles remains stochastic. Therefore, it is rare to observe a network with a single dominant angle. The existence of the combinative effect by the branching angle and zippering threshold angle could be explained by a simple principle of geometry. If we consider an ideal case with two perfectly parallel microtubule bundles positioned next to each other, we could derive a possible combinative mechanism for intra-bundle dynamics and morphological enhancement. The angle of branched nucleation and the angle of zippering would be considered as two internal staggered angles. If the two angles are identical, newly branched daughter microtubule could easily zipper with the neighbor in parallel configuration; If the branching angle is smaller than zippering threshold, all new daughter microtubules could bridge the two parallel microtubules by zippering; If the branching angle is greater than the zippering threshold, the branched microtubules would end up in catastrophe or crossover event upon collision with the parallel neighbor. Thus, the bundle formation in cortical array is precisely controlled by the subtle balance between the nucleation branching angle and the zippering threshold angle, both of which directly impact the deterministic event upon collision. The ideal parallel configuration of two

existing microtubules is practical since a non-parallel configuration would diminish the probability of intra-bundle zippering and worsen the network ordering.

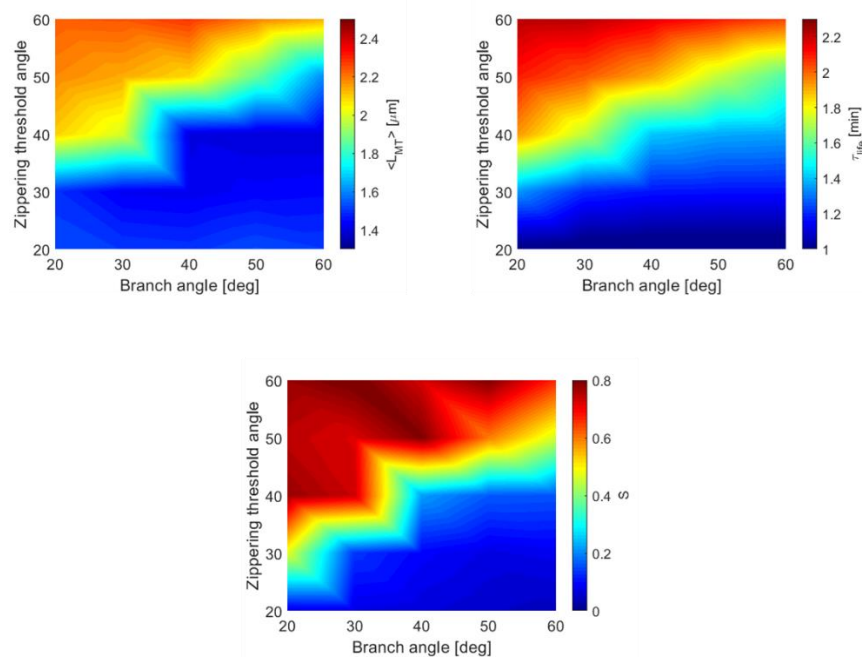


Fig. 3.16 Heatmaps showing the average length, lifetime of microtubules and steady state order parameter of the cortical array, under various combination of branched nucleation angle and zippering threshold angle.

### 3.4.6 Severing act as a potential mechanism to facilitate bundle morphology

In this section, the results for different severing modes are presented. We kept the parametric space for branched nucleation angle and probability of branched nucleation. Under all conditions, the transition and dependence of bundle skewness closely resembles the heatmap for network order parameter (Fig. 3.17). When the network is free from severing, the cutoff value for branched nucleation probability is  $\sim 0.2$ . Above this threshold, we see a monotonic trend of decreasing skewness with increasing branched nucleation. The critical value for bundle vanishing increases with increasing probability of branched nucleation. In the case of stochastic, isotropic severing, the threshold for branching probability is elevated to  $\sim 0.6$ , largely due to the high turnover of short microtubules after severing. The bundle could not be sustained long enough unless branched nucleation angle is much smaller ( $< 20^\circ$ ) than the reference value. To overcome the unrealistic phenomenon, we incorporated crossover site severing. With this inclusion, the bundle skewness more closely aligned with network ordering under the cases with various combination of zippering



and severing angle. This indicates that severing at crossover site, has a very similar role in controlling the deterministic events during self-organization and bundle dynamics of microtubules.

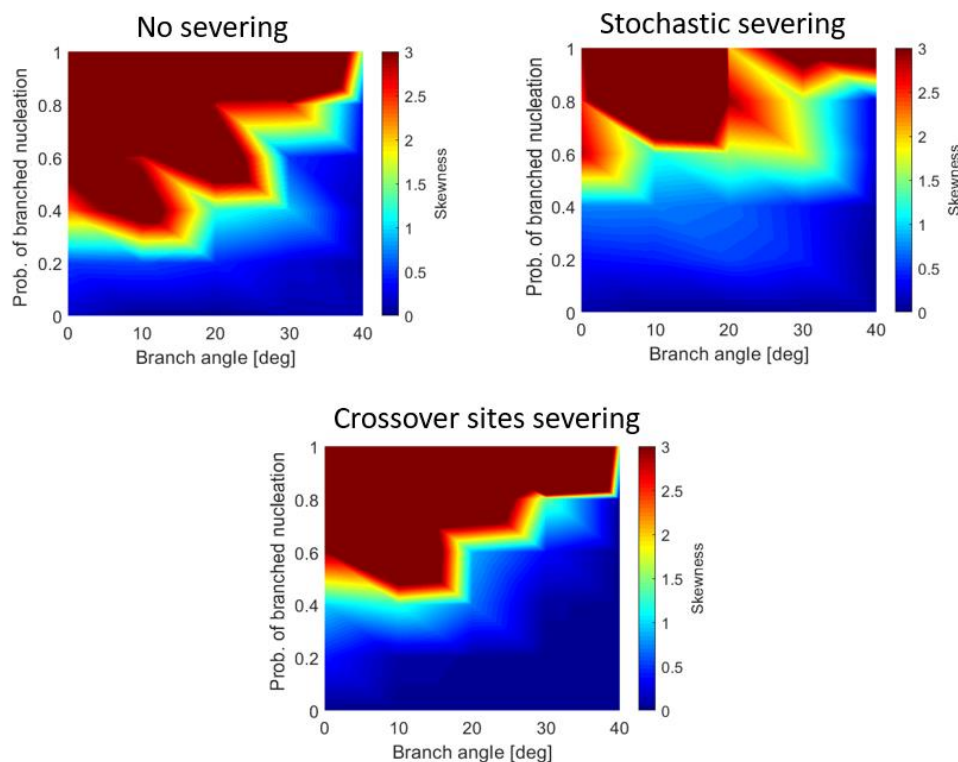


Fig. 3.17 Skewness of microtubule bundles in severing free condition, with stochastic and crossover site severing conditions. The heatmap shows dependence on the parametric space of probability of branched nucleation and branched nucleation angle.

### 3.5 Conclusion and Discussion

Microtubules must sense the magnitude and direction of stress, and in the simulation strategy here direction-dependent stress sensing was coupled to different stochastic properties of microtubules. By mapping a simple stress pattern onto the square domain with  $10 \times 10 \mu\text{m}$  in size and relating stress with one of four dynamic parameters, we were able to find the most efficient stress-sensitive parameter that can lead to better microtubule alignment. These sensitivity analyses indicated that modulation of the polymerization rate and catastrophe frequency were the most potent means to rapidly establish a cell-geometry-aligned microtubule array. The temporal component of the model is based on experimentally determined stochastic properties (Table 3.1) and the time to establish an order array were typically  $\sim 100$  min. These timescales are consistent with the rates of stress-dependent reorientation that have been measured using live cell imaging



[239]. We predict that polymerization rate and catastrophe frequency are more sensitive to stress pattern due to the following reason: the plus ends of microtubules switch between growth, pause, and shrinkage states with dynamic instability, so a large fraction of short microtubules can disappear very easily. If stress increases the polymerization rate or reduces the catastrophe frequency of microtubules oriented in a certain direction, the aligned subpopulation of short new microtubules can grow fast by making polymerization more dominant. Suppression of the catastrophe events can break symmetry between polymerization and depolymerization better so that microtubules are aligned faster and to a greater extent.

Cell wall stresses serve as useful multiscale patterning elements to modulate microtubule arrays because the stresses are nonuniform on a cell surface and depend on both geometric and cell wall compositional. For example, in an intact tensile forces are locally concentrated and aligned at the interface where unpaired outer periclinal walls pull upward on anticlinal walls, and microtubules at this location are highly co-aligned [8, 102]. The magnitude of cell wall stress is also inversely proportional to cell autonomous parameters like wall thickness. In isolated leaf trichoblasts subcellular cell wall thickness gradients exist [9], and we show here that the spatial information in stress direction and magnitude can be decoded to generate an ordered microtubule array with a tip to base density gradient that mirrors that of living cells. Living trichoblasts have an apical microtubule depletion zone that may reflect an additional gradient in stress anisotropy. In cells that grow in the absence of tightly adhered and pressurized neighboring cells, gradients in stress anisotropy will also occur based on cell geometry. In domed, cylindrically shaped trichoblasts, root hairs, pollen tubes, and moss protonema stress will be more isotropic at the apex compared to the cell flanks. Based on geometry alone the flanks of cylindrically shaped cell are expected to have anisotropy ratios of  $\sim 2:1$ . This value exceeds the threshold of  $1.5:1$  that was needed to order the microtubule network in simulations (Fig. 3.4). The apex dome is often an important site of signal transduction and cytoskeletal patterning, and in leaf and cotton fiber trichoblasts that taper while employing a MT-MF-dependent diffuse growth mechanism, the extreme apex contains a clearly-defined microtubule depletion zone [9]. In *Arabidopsis* the trichoblast apex is a site of localized Rho-of-plants (ROP) activation and signaling to the cytoskeleton [238], and it was hypothesized that ROP-dependent microtubule destabilization generated the microtubule depletion zone. However, the dome is also predicted to have isotropic wall stress and define a spatial domain with a clear gradient of stress anisotropy. The computational

simulations here showed that a combination of spatially defined gradients of stress anisotropy and magnitude can pattern a microtubule array with the basic alignment and density features of the cortical array of early stage trichoblasts. Using the same rectangular domain with boundary conditions that were either periodic or catastrophe-inducing, we observed that microtubule density and alignment patterns were not similar to the experimental observations. These results are important because they suggest that stress-dependent alignment of the microtubule array is a plausible and sufficient feedback control mechanism to persistently integrate cell geometry and the MT-MF systems during morphogenesis. In the context of a tissue, the interface of the outer periclinal and anticlinal walls of mechanically coupled cells is another locale where gradients of stress magnitude and anisotropy are likely to influence the MT-MF system and morphogenesis.

In growing cells and tissues the wall stress fields are constantly remodeled (albeit slowly) as the geometry and wall material properties change. Tensile forces and microtubule alignment can also change as a function of the growth dynamics of underlying tissues [245]. The microtubule network simulations conducted as a function of changing stress patterns reflect the robustness of the system. The more stable states in the microtubule simulations were not predestined and fixed outcomes defined by the input variables. We observed that during microtubule reorientation, bundles with different orientations could coexist with rather homogeneous morphology. This was previously observed in experiments where mechanical perturbation was employed to alter microtubule patterns [210, 211]. Our simulation approach captures the behaviors of an unstable system that uses tensile force coupling to dynamic instability variables of microtubules to rearrange the array. Our preliminary results for branched nucleation and severing highlighted the significance of the angle-dependent deterministic events. In alignment with previous studies [241, 242], although severing is not responsible for branched nucleation events, it actively sorts out the discordant microtubules and contributes to the determination of the critical threshold angle for bundling. Consequently, the combinative mechanism might suppress local bundle heterogeneity.

In this chapter, we recapitulated the alignment and reorientation of microtubules in response to local stress pattern with anisotropy on the plant cell wall as well as physiologically relevant transverse band formation. Our results shed light on the potential key players of a mechanical feedback between cell wall mechanics and cortical microtubules. It also provides guidance for future experiments to identify stress-sensing proteins at subcellular level.

## 4. CONCLUSION AND OUTLOOK

### 4.1 Summary

Active remodeling of the cytoskeleton system is the prerequisite for a multitude of cellular processes including morphogenesis, migration, adhesion, growth, and development. The cortex is a thin layer beneath the plasma membrane as plays a crucial role during cell morphogenesis. The cortex in animal cells is mainly composed of actomyosin and the plant cortex is reinforced by microtubule cytoskeleton. In the actomyosin cortex, the active pulling force generated by myosin motors on the F-actin is the main driving force for the remodeling and contractility, leading to multiple structure including bundles and clusters. In Chapter 2, we implemented a well-established agent-based model consisting of F-actin, myosin motors, and ACPs to study the actomyosin contractility. The modeling results in Chapter 2.3 first showed that network contraction is regulated by the ACP density which controls the network connectivity. Second, buckling-induced severing of the F-actin was sufficient to drive the network into multiple contractile morphologies. When F-actin bending stiffness was high, the network contracted into highly bent single network; when F-actin bending stiffness was low, the contractile network shifted from a single cluster to multiple clusters with increasing F-actin severing frequencies. Third, we varied the motor density and ACP density to show the dependence of optimal bending stiffness of F-actin that leads to various clustering behavior. We summarized the results with a 3D phase diagram for network clustering behavior depending on the bending stiffness of F-actin, relative ratio between ACPs and motors, and severing frequency of F-actins. The wide parametric space of these three parameters led to three distinctive networks: i) a single cluster with minimal contraction ii) a single cluster with large contraction iii) multiple clusters with minimal contraction.

To recapitulate the pulsatile contraction as observed *in vivo*, we finetuned the model by varying the F-actin turnover rate and F-actin severing. In Chapter 2.4, we found the optimal level of network connectivity that led to large network contraction. With the addition of F-actin turnover only, we observed the emergence of small nascent pulsatile clusters. Further, we showed that the balance between force generation and force generation is the prerequisite for large pulsatile cluster formation, under the condition of both F-actin turnover and F-actin severing. In Chapter 2.5, the main contribution of our agent-based model focused on understanding the actomyosin contraction

depending on different motor types and mobilities. We showed that one-arm motor led to most heterogeneous network at intermediate mobility. The biphasic behavior of network heterogeneity is attributed to the dependence of motor motility on viscous drags. Since two-arm motors do not have such dependence, they can freely contract the network with increasing mobility.

The main contribution of the results in Chapter 3 is to help understand the mechanical feedback between cortical microtubules and cell wall mechanics, underlying plant cell morphogenesis. We developed a coarse-grained model for cortical microtubule dynamics by event-driven simulations. Deterministic angle-dependent dynamics are sufficient to drive self-organization into ordered array with random orientations. However, directional bias by cellular scale tensile stress could override the geometry-based boundary effects to induce dynamic orientation of the cortical array. We showed that plus-end polymerization and catastrophe are the two parameters potent to provide microtubules the “sensitivity” to external mechanical stimuli. We implemented a cell-based stress gradient derived from a FEM trichome model and simulated a global cortical array pattern that is alignment with microtubule distribution and organization in young trichomes. Further, in a network without stress-based directional cues, branched nucleation and microtubule severing at crossover sites are the key determinants of network bundling during cortical array remodeling.

## **4.2 Future directions**

### **4.2.1 Actomyosin contractility**

Recent experiments have demonstrated that pulsed contraction results from contractile instability regulated by spatiotemporal expression of RhoA [110, 156, 157, 159]. During morphogenetic events and in one-cell stage *C. elegans* embryo, myosin and RhoA co-localize with the pulsed clusters. Although results from those experiments have suggested that the pulsed contraction is a direct consequence of RhoA cycling activity [156], a recent study suggested that RhoA might act as a pacemaker [110]. During one pulse, RhoA locally enhances activities of myosin motors to form clusters and then deactivate the motors later. However, after deactivation of motor activities, it is not likely that numerous connections between F-actins within clusters are broken simultaneously for disassembly of the clusters. Based on results in our study, it is

anticipated that the turnover and severing of F-actin still play a very crucial role for cluster disassembly and pulsed contraction by locally reducing connectivity within the clusters.

In Chapter 2.4, our study provides insights into understanding of a role of F-actin severing for the distinct pulsed contraction observed during various physiological events. In our future studies, we will incorporate the spatiotemporal expression of RhoA and then relate the RhoA activity with motor activities in order to recapitulate and study more physiological pulsed contraction. Additionally, other mechanisms such as capping of F-actin plus end could be employed in our future work to provide more systematic behavior.

In Chapter 2.5, we showed different clustering behavior depending on motor mobility. Despite the limitations of the model, our study not only verifies contemporary hypotheses but also provides new insights into the critical role of motor mobility for the contraction of actomyosin networks. Results from our study clearly demonstrated that impacts of motor mobility on networks can be quite different depending on mechanochemical rates of motors and connectivity between F-actins and motors. Our study sheds light on how cells regulate and use activities of different types of myosin motors to form structurally distinct cytoskeletal structures and generate mechanical forces for cellular functions. In our future studies, we will investigate effects of elastic or viscous interactions between mobile motors on contractile behaviors of actomyosin networks since motors in cells may undergo such interactions via the cell membrane or the backbones of thick filaments.

#### **4.2.2 Cortical microtubule patterning**

The discrete model introduced in Chapter 3 showed that tensile stress at cellular scale is potent to induce directional self-organization by influencing the plus-end dynamics. Although we identified the two most sensitive parameters in response to anisotropic stress pattern, we need to examine the *in vitro* models to understand the real mechanism underlying the differentiated growth rates and catastrophe frequencies at different stages of growth. In these stages, the dynamic reorientation and time evolution of stress pattern directly coupled to the cortical array microtubules should be further confirmed along with the corresponding changes in the stochastic dynamics of microtubules in live cells. Another important question is how the flexibility of cortical array pattern is integrated with the complexity of local cell curvature with various global shapes. The model could be extended to be integrated with finite element model which updates time-dependent stress

pattern in a more realistic manner. The reinforcement fiber built in the FEMs generally determines the local mechanical properties of the cell wall. We need to update the direction of the fiber corresponding to the dynamic reorientation of the discrete microtubule array. In this way, we would have a successful coupling between microtubule (in the discrete model) and cellulose microfibrils (fiber in FEM). Such extension of the model would be extremely beneficial for understanding the real-time feedback between mechanical stress and cortical cytoskeletal dynamics. The way how microtubules adapt to growth pattern of various plants remains a topic of debate for a few decades. Recent evidence from experiments and models primarily focuses on the geometry-based, light-induced morphogenetic cues and overlooked the significance of mechanical stress. The fact that shape-derived stress coincides with the cortical microtubule array pattern at specific growth stages is intriguing and requires further validation from the model. Should our discrete model be improved, it needs to be adaptable and fully versatile under various cell geometries to address both static condition and dynamic analysis. For instance, a question about how cortical microtubules emerge from transverse alignment and switch to oblique and longitudinal orientation as trichome matures can be answered by our model in the future. In addition, we also need to implement stress-based severing at crossover sites in combination with branched nucleation. The fact that branched nucleation protects the microtubule from helical pattern in the long-term is nontrivial. Additionally, katanin-mediated severing is believed to play a crucial role in the propagation of supracellular stress pattern. Therefore, we need to take a step further and build a domain for multicellular interactions. The prominent goal is to build a multi-scale model that could address the sensing mechanism behind microtubule self-organization in response to cellular, supracellular or even tissue-level stress. The major contribution of the improved model would shed light on the mechanotransduction embedded in and spanning across the microtubule-membrane-wall continuum.

## A. MATRIX-CELL REMODELING

In this section Appendix A of the thesis, we simulate ECM remodeling induced a single contractile cell. During various physiological processes, such as wound healing and cell migration, cells continuously interact mechanically with a surrounding extracellular matrix (ECM). Contractile forces generated by the actin cytoskeleton are transmitted to a surrounding ECM, resulting in structural remodeling of the ECM. To better understand how matrix remodeling takes place, a myriad of *in vitro* experiments and simulations have been performed during recent decades. However, physiological ECMs are viscoelastic, exhibiting stress relaxation or creep over time. The time-dependent nature of matrix remodeling induced by cells remains poorly understood. Here, we employed a discrete model to investigate how the viscoelastic nature of ECMs affects matrix remodeling and stress profiles. In particular, we used explicit transient cross-linkers with varied density and unbinding kinetics to capture viscoelasticity unlike most of the previous models. Using this model, we quantified the time evolution of generation, propagation, and relaxation of stresses induced by a contracting cell in an ECM. It was found that matrix connectivity, regulated by fiber concentration and cross-linking density, significantly affects the magnitude and propagation of stress and subsequent matrix remodeling, as characterized by fiber displacements and local net deformation. In addition, we demonstrated how the base rate and force sensitivity of cross-linker unbinding regulate stress profiles and matrix remodeling. We verified simulation results using *in vitro* experiments performed with fibroblasts encapsulated in a three-dimensional collagen matrix. Our study in Appendix A provides key insights into the dynamics of physiologically relevant mechanical interactions between cells and a viscoelastic ECM.

### Method

#### *Model overview*

In this study, we employed an agent-based model for studying the matrix remodeling and force transmission induced by a contracting cell. Supplementary Text and Table S1 describe the details of the model and all parameter values used in the model.

In the model, a cell is located at the center of a circular matrix in a computational domain with a cylindrical solid shape whose radius and height are 100  $\mu\text{m}$  and 1  $\mu\text{m}$ , respectively (Figs. A.1a, b). The initial radii of the cell and the matrix are 10  $\mu\text{m}$  and 100  $\mu\text{m}$ , respectively, and their thickness is 1  $\mu\text{m}$ . The cell is simplified into a structure with a membrane and actomyosin cortex coarse-grained by serially connected rectangular solid elements whose height is 1  $\mu\text{m}$ . The matrix is comprised of fibers interconnected by transient cross-linkers. Each fiber consists of serially connected cylindrical elements, and the average length of fibers is  $\sim 10$   $\mu\text{m}$ . Cross-linkers consisting of two cylindrical arms represent weak bonds formed between collagen fibers. Nodes connecting two membrane elements are defined by only x and y positions, whereas nodes constituting fibers and cross-linkers have x, y, and z positions.

The displacements of the cylindrical elements are updated by the Langevin equation and the Euler integration scheme. In the Langevin equation with inertia neglected, deterministic, drag, and stochastic forces determine the velocity of elements at each time step. For deterministic forces of matrix fibers, cross-linkers, membrane, and cortex, bending and extensional forces are considered. In addition, membrane and cortex elements located adjacently attract each other to maintain proximity. Repulsive forces between membrane elements and the elements representing matrix fibers and cross-linkers prevent the matrix elements from entering the inner space of the membrane.

At the beginning of a simulation, membrane and cortex are created with a circular shape. Then, within the first 200 s, matrix fibers are formed via nucleation and polymerization events. The nucleation event corresponds to the appearance of one cylindrical element, and the polymerization event occurs via the addition of elements on both ends of existing fibers. It is assumed that either end of matrix fibers can form a permanent link to nodes on the cortex. During the assembly of matrix fibers, cross-linkers connect pairs of fibers in a transient manner. After the first 200 s, a cell starts contracting radially and circumferentially, resulting in force development and structural remodeling of the matrix (Fig. A.1c).

### ***Links between matrix fibers and cortex***

The permanent links between matrix fibers and nodes on the cortex represent FAs formed between the actin cytoskeleton and ECM ligands, mediated by integrins and a myriad of FA-associated proteins (Fig. A.1a). The length of the links ( $r_{fc}$ ) is maintained near their equilibrium length ( $r_{0,fc}$ ) via the following harmonic potential ( $U_{s,fc}$ ):



$$U_{s,fc} = \frac{1}{2} \kappa_{s,fc} (r_{fc} - r_{0,fc})^2 \quad (\text{A.1})$$

where  $\kappa_{s,fc}$  is extensional stiffness. Note that the links are not affected by repulsive forces acting between the membrane and matrix constituents, considering  $r_{0,fc}$  is longer than membrane thickness.

### ***Cell contraction***

The cortex in the model always behaves as a contractile element because it is consistently subjected to a spring force with zero equilibrium length. This leads to the development of tensile forces along the cell surface, mimicking cortical contraction that regulates cell mitosis and morphogenesis in cells. In some of the simulations, the strength of this contractility is varied to probe its effects on the force transmission and remodeling in a surrounding matrix.

### ***Evaluation of the orientations of tensed and buckled fibers***

We analyze the orientations of two types of matrix fibers at the end of simulation: tensed and buckled fibers. We measured the end-to-end distance of all fibers at both the final and initial timesteps. Dividing the end-to-end distance at the final timestep by that of the initial timestep gives a ratio indicating the extension/tensile or curved/buckled states of the fiber. If the ratio is 1, it means the fiber overall length or geometry remains unchanged. If the ratio is greater than 1, the fiber is likely to be under tension therefore identified as tensed fiber. In the case with a ratio less than 1, the fiber is most likely bent and curved, and we identify them as buckled. The orientations of tensed and buckled fibers are calculated as follows. First, all points on fiber segments are projected onto the x-y plane. Then, we connect the two ends of each fiber segment by a linear segment. We calculate a difference between the orientation of the linear segment and that of a line connecting the cell center and the midpoint of the segment. Then, orientation angles of all segments are averaged for the angle of each individual fiber. The orientation is further averaged over all tensed and buckled fibers for each range of radial distances from the cell center. If the difference is close to zero, it means that most of the fibers are aligned in radial directions. If the difference is close to 90°, it indicates that fibers are oriented mainly in circumferential directions.

### ***Measurement of stress and matrix deformation***

Local stress acting on the matrix is calculated as follows. For measuring stress as a function of a radial distance, we identify all chains of fibers and cross-linkers that cross the lateral surface of a cylindrical solid whose radius is a multiple of 10  $\mu\text{m}$  (i.e.,  $r = 10, 20, \dots, 90 \mu\text{m}$ ). Then, the radial component of spring forces acting on those identified chains is summed and divided by the area of the lateral surface, which gives the stress in radial directions.

To calculate the displacement of matrix fibers due to cell contraction, we employ a vector between the initial and final positions for each matrix fiber. Then, the vector is projected onto the radial direction corresponding to the direction of a line connecting the cell center and the initial position of the matrix fiber. The length of this projection is considered to be the fiber displacement.

Local matrix deformation is calculated using fiber displacements. First, the matrix is divided into annulus regions with 10  $\mu\text{m}$  intervals in radial directions. Next, the average of fiber displacements is calculated for each annulus section. Then, the deformation is defined as a difference in the average displacement between two adjacent annulus regions. For example, deformation at  $r = 20\text{-}30 \mu\text{m}$  is equal to a difference between the average displacements at  $r = 20\text{-}30 \mu\text{m}$  and  $r = 30\text{-}40 \mu\text{m}$ . We also quantify how anisotropic matrix deformation is. First, the matrix is divided into annulus regions. The mean and standard deviation of the fiber displacement for each region are determined. Then, the uniformity in each region is defined as the standard deviation of fiber displacements normalized by the mean.

### **Results**

we employed explicit transient cross-linkers to connect pairs of matrix fibers to capture the viscoelastic properties of ECMs, which were modulated by tuning the density and unbinding kinetics of cross-linkers. We focused on time-dependent matrix remodeling and force transmission induced by uniform cell contraction. In the following sections, we varied the strength of cortical contraction, cross-linking density, fiber concentration, and two parameters governing the unbinding behaviors of cross-linkers (i.e., zero-force unbinding rate constant and force sensitivity) in order to show their effects on matrix remodeling and force transmission.

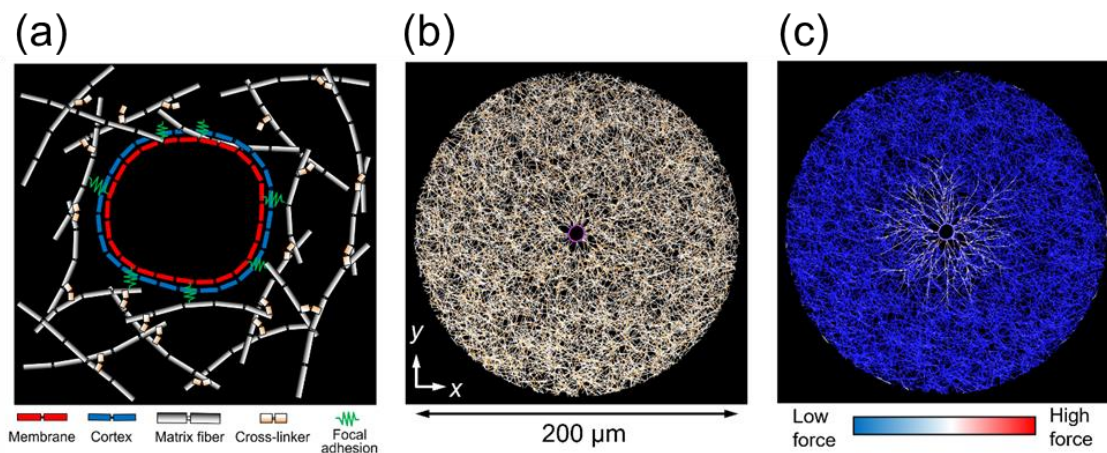


Fig. A.1 Computational model for interactions between a cell and an extracellular matrix. (a) Schematic of the network components. Matrix fibers are represented by serially connected white segments. Cross-linkers shown as short orange cylindrical segments connect pairs of matrix fibers. Red and blue segments indicate elements constituting cell cortex and membrane, respectively. The cell cortex is physically connected to the matrix fibers via green springs for exerting forces during contraction. (b) Snapshot of the model showing the cell contraction in the matrix. All components are visualized using the same colors as those used in (a). The initial radii of the matrix and the cell are 100  $\mu\text{m}$  and 10  $\mu\text{m}$ , respectively. (c) Snapshot of the matrix showing the development of tensile forces during contraction via color scaling.

### ***Stronger cell contraction results in greater deformation and longer-range stress transmission***

Different cell types exert different levels of contractile forces. For example, fibroblasts exhibit stronger contraction than other types of cells in general. In addition, cell contractility can be varied by inhibiting or enhancing myosin activity using small molecule inhibitors or promoters. To investigate the effects of cell contraction, we varied the strength of cortical contraction over a wide range. We found that the strength of the cortical contraction ( $\kappa_{s,c}$ ) can significantly affect matrix deformation and the magnitude and relaxation of stress.

We measured stress over time at various distances from the cell center. In all cases, stress near the membrane ( $r \sim 20 \mu\text{m}$ ) rapidly increased right after contraction was initiated, and then relaxed gradually over time after reaching peak level (Figs. A.2a-c). The peak stress was almost directly proportional to  $\kappa_{s,c}$ . The time evolution of stress normalized by the peak stress showed that two cases with lower  $\kappa_{s,c}$  exhibited relatively slow stress relaxation to a similar extent, whereas two cases with higher  $\kappa_{s,c}$  showed enhanced stress relaxation (Fig. A.2c inset). Our previous study reported that this enhanced stress relaxation can emerge in a collagen gel if shear strain applied to the gel is large enough [246]. We suggested that this is attributed to force-dependent unbinding of weak cross-links formed between collagen fibers. This implies that enhanced stress relaxation

observed in the two cases with stronger cell contraction could be caused fully or partially by faster unbinding events of cross-linkers that support large forces. To include the contribution of cross-linker unbinding to the viscoelastic responses of the matrix, we employed the largest value of  $\kappa_{s,c}$  for further simulations. For regions far from the cell, stress tends to increase over time, implying that it took significant time for stress to be transmitted through the matrix with a viscoelastic nature (Figs. A.2a, b inset).

If stress propagates throughout the matrix and reaches a steady state, the stress is supposed to decay as a function of  $r^{-1}$  unlike 3D models where it decays as a function of  $r^{-2}$ , as shown in the previous study [247]. This is attributed to a difference in the geometry of the simulation domain; in our cylindrical domain, the lateral surface area for a specific  $r$  value is directly proportional to  $r$ , whereas the surface area for a specific  $r$  value in the 3D domain is proportional to  $r^2$ . If the sum of tensile forces measured along the lateral surface area is very close to cell contraction forces regardless of  $r$ , stress becomes inversely proportional to  $r$ . Stress in the case with higher  $\kappa_{s,c}$  showed a good match with  $r^{-1}$ , indicating that stress could be transmitted to the boundary of the matrix (Fig. A.2b inset). However, stress in two other cases did not match  $r^{-1}$  even after 1 h, meaning that stress propagated either much slower or only over shorter distances (Fig. A.2a inset). In either case, it is apparent that stronger cortical contraction resulted in better stress transmission through the viscoelastic matrix.

In addition, we measured the displacements of all matrix fibers. Overall, fibers located closer to the membrane tended to be displaced more (Figs. A.2d, e). This implies that a large fraction of the matrix underwent local deformation (Fig. A.2f); if the matrix fibers merely move inward without local deformation, the displacements would be very similar, regardless of distance from the cell center. Three cases with higher  $\kappa_{s,c}$  showed similar local deformation at the end, but the matrix with lower  $\kappa_{s,c}$  showed slower development of deformation. Considering that the cell became negligibly small after full contraction in these cases, the deformation curves seem to represent the maximum deformation that can occur in the simulation. This is consistent with observation that stress reached similar plateau level at late times. In addition, it was also observed that the deformation was more isotropic near the cell membrane (Fig. A.2g); the uniformity of deformation tended to be higher in regions farther from the cell center. However, in regions of the matrix where stress was not transmitted, deformation became isotropic again. Interestingly, deformation was more anisotropic with the highest  $\kappa_{s,c}$  than the two other cases showing similar

deformation and stress (Figs. A.2e, g). This is attributed to the unbinding events of cross-linkers enhanced by strong contractile forces. When the cell exerted large stress on the surrounding matrix, a fraction of matrix fibers lost connections to other fibers due to the unbinding events of cross-linkers bearing large tensile forces. This resulted in slightly smaller plateau stress near the membrane (Fig. A.2c). It has been also shown that fibers bearing high tensile forces are aligned in radial directions, whereas buckled fibers are aligned in circumferential directions. We observed similar orientations for two types of matrix fibers.

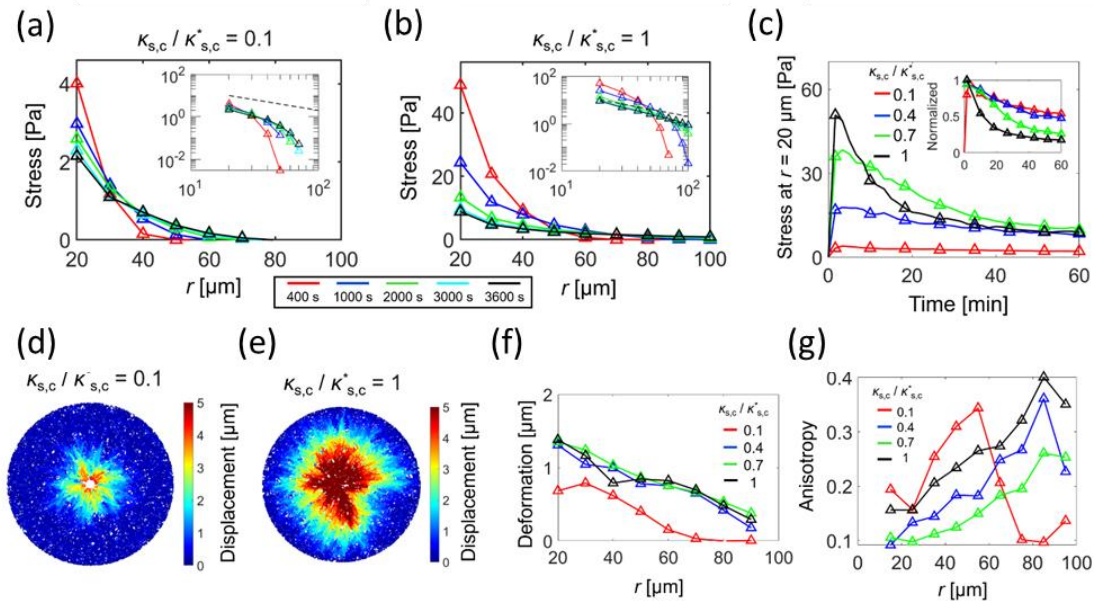


Fig. A.2 Matrix deformation and stress generation, propagation, and relaxation depend on the strength of cell cortical contraction,  $\kappa_{s,c}$ . (a, b) Stress acting on a matrix in radial directions at five different time points (legend), as a function of a distance from the cell center,  $r$ , with two different values of  $\kappa_{s,c}$ . Insets: the same curves in the log-log scale. Dashed lines indicate  $r^{-1}$ . Initially, stress is concentrated on regions near the cell membrane and then propagates to the outer regions of the matrix over time. (c) Time evolution of the stress measured at  $r = 20$  μm with different levels of  $\kappa_{s,c}$ . Inset: stress normalized by peak level. Over time, the stress decreases gradually, indicating stress relaxation. Higher  $\kappa_{s,c}$  tends to lead to faster, more pronounced stress relaxation. (d, e) Fiber displacements at the end of simulations with different  $\kappa_{s,c}$ . (f) Net matrix deformation and (g) the uniformity of matrix deformation, depending on  $r$  and  $\kappa_{s,c}$ . Note that  $\kappa_{s,c}^*$  is the reference value of  $\kappa_{s,c}$ .

***Lower fiber concentrations lead to more anisotropic deformations, shorter-range stress transmission, and rapid stress relaxation***

Extracellular matrices show various fiber concentrations depending on their locations. To understand the effects of fiber concentration, several *in-vitro* experiments using collagen gels have been performed with or without cells [248]. We also probed the influences of 2-fold lower and 2-fold higher fiber concentrations on matrix remodeling and stress generation. We found that the fiber density ( $C_f$ ) highly affects the degree of force transmission, anisotropic deformation, and stress relaxation.

Peak stress measured near the membrane ( $r \sim 20 \mu\text{m}$ ) was significantly lower in a case with the lowest  $C_f$ , whereas it was quite similar in two other cases (Figs. A.3a-c). Stress relaxation was noticeably faster in cases with lower  $C_f$ . For example, stress in the case with 2-fold lower  $C_f$  was reduced by  $\sim 80\%$  after 10 min, whereas it was decreased in the case with 2-fold higher  $C_f$  only by  $\sim 20\%$  after 1 hour. With higher  $C_f$ , stress was transmitted over a longer distance, matching well the prediction with  $r^{-1}$ . This implies that stress relaxation and transmission are highly dependent on matrix connectivity. If  $C_f$  is higher with the same molar ratio of cross-linkers to fibers, there are more cross-linking points per volume. Since more cross-linkers share loads, their unbinding events are enhanced to a lesser extent. With such higher, stable connectivity, the cell was able to generate and transmit larger stress through a matrix better. By contrast, if connectivity is low, fibers that the cell pulls may not be connected well to the rest of the matrix, so the generation and transmission of large stress would not be easy.

The case with larger  $C_f$  showed very isotropic fiber displacements and local deformation (Figs. A.3d, g). In addition, local deformation in the case also exhibited the maximum level like the case with the reference value of  $C_f$  (Fig. A.3f). However, it took more time for stress to reach the maximum level. By contrast, lower  $C_f$  caused large fiber displacements mostly near the membrane in a highly anisotropic fashion (Figs. A.3e-g). These differences can be explained by matrix connectivity mentioned above. With larger  $C_f$ , connectivity is higher and more stable, so a greater portion of the matrix can be deformed in a more isotropic manner. We also found that the orientations of tensed and buckled fibers with larger  $C_f$  exhibited a clearer contrast than those with the reference value of  $C_f$ .

Note that the case with larger  $C_f$  showed the same extents of fiber displacement and local deformation as those in the case with the reference value of  $C_f$  because the contraction strength

used in these simulations was large enough to induce deformation throughout an entire matrix even with higher  $C_f$ . Indeed, when we reduced the contraction strength 10-fold, fiber displacements and local deformation were apparently lower with higher  $C_f$ ; if the cell generates low forces, a stiffer matrix with more fibers would be deformed less. However, overall dependences of peak stress, stress relaxation, and deformation uniformity on  $C_f$  were maintained.

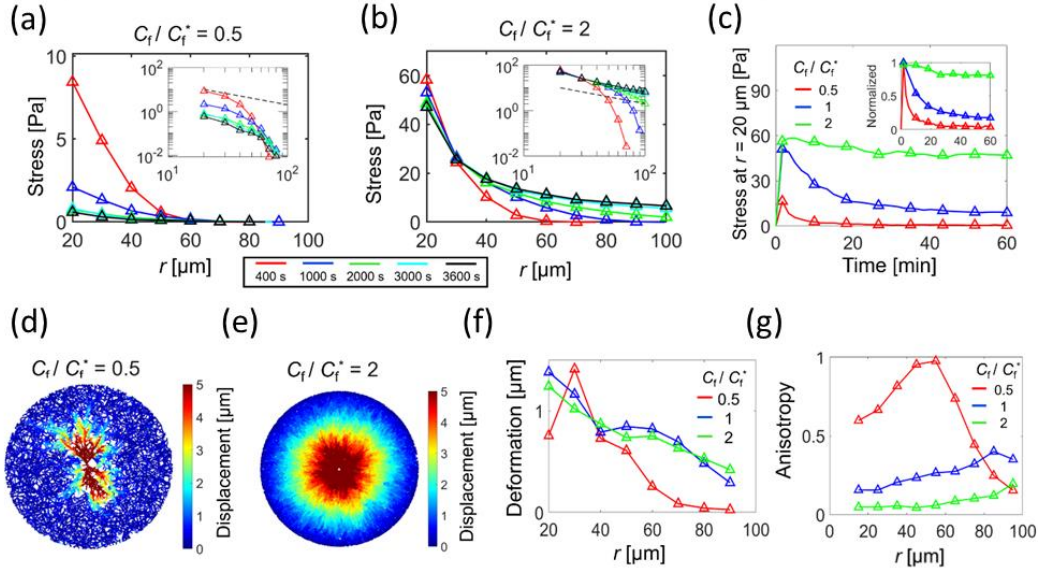


Fig. A.3 Fiber density,  $C_f$ , influences stress profiles and matrix deformation by altering matrix connectivity. (a, b) Tensile stress exerted on a matrix in radial directions at different time points (legend), as a function of a distance from the cell center,  $r$ , with two values of  $C_f$ . Insets: the same stress curves in the log-log scale. Dashed lines indicate the prediction of  $r^{-1}$ . (c) Relaxation of the stress calculated at  $r = 20$  μm with different  $C_f$ . Inset: stress normalized by peak level. (d, e) Spatial distribution of fiber displacements at the end of simulations with two values of  $C_f$ . (f) Net local matrix deformation and (g) the uniformity of the matrix deformation as a function of  $r$  and  $C_f$ . Note that  $C_f^*$  is the reference value of  $C_f$ .

### ***Denser cross-linkers lead to slower stress relaxation and more isotropic matrix deformation***

The formation of cross-links between fibers can increase matrix connectivity. Previous studies suggested that collagen fibrils in a matrix can form weak cross-links via fibril-fibril interactions [249]. In addition, covalent cross-linkers that permanently connect collagen fibers have been used in several studies [250]. To probe how the amounts of cross-linkers affect matrix remodeling and stress generation, we varied the density of the cross-linkers ( $R_{xl}$ ) over a wide range.

We found that the inclusion of more cross-linkers in the matrix resulted in slower stress relaxation and long-range stress propagation (Figs. A.4a-c). Peak stress tends to be proportional to



$R_{xl}$ , but the rate of stress relaxation is inversely proportional to  $R_{xl}$ . For example, with  $R_{xl}/R_{xl}^* = 0.5$ , stress measured at  $r \sim 20 \mu\text{m}$  decreased by more than 90 percent at 1 h after reaching the peak value. In addition, the stress failed to reach the prediction of  $r^{-1}$ . However, as  $R_{xl}$  increased, the rate of decrease in stress became much smaller, and the stress followed the prediction of  $r^{-1}$  better. This implies that a large number of cross-linkers enhance stress generation and transmission by sharing loads without a significant increase in their unbinding rate. In cases with  $R_{xl}/R_{xl}^* \geq 0.5$ , fiber displacements reached their maximal level, but it took more time for them to reach the level when  $R_{xl}$  was higher (Figs. A.4d, e). Interestingly, local deformation near the membrane is the highest in the case with  $R_{xl}/R_{xl}^* = 0.25$ . This is possible because too low connectivity can prevent the cell from pulling many fibers, whereas high connectivity leads to greater resistance to the pulling forces generated by the cell. The local deformation of the matrix was more isotropic with higher  $R_{xl}$  (Fig. A.4g). These observations are comparable to those observed in the cases with a variation in fiber concentration, which is reasonable considering increases in both fiber concentration and cross-linking density can enhance matrix connectivity.

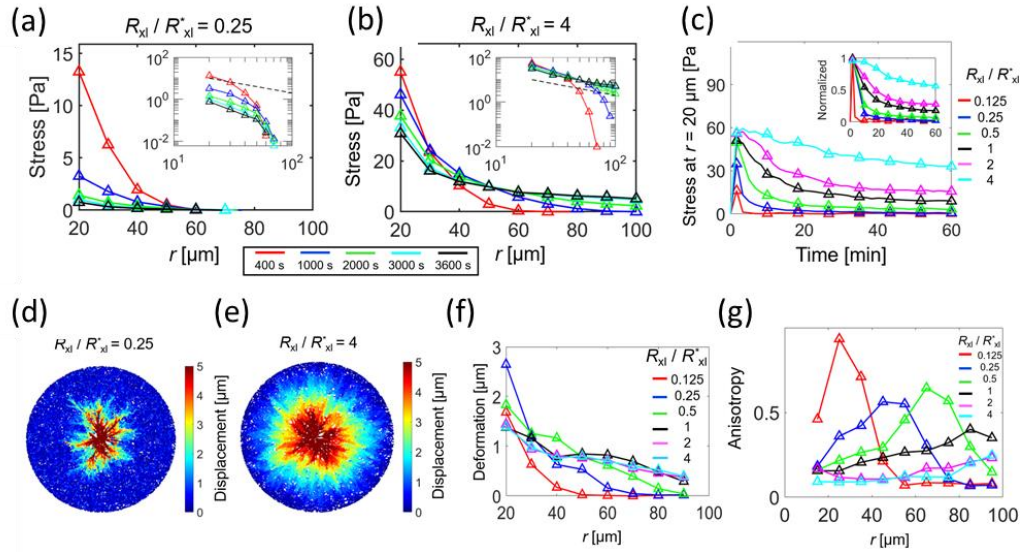


Fig. A.4 Cross-linking density,  $R_{xl}$ , affects how stress and deformation develop over time in a matrix. (a, b) Stress acting on the matrix in radial directions at different time points (legend), as a function of a distance from the cell center,  $r$ , with two different values of  $R_{xl}$ . Insets: stress in the log-log scale. Dashed lines represent  $r^{-1}$ . (c) Relaxation of the stress measured at  $r = 20 \mu\text{m}$  with various values of  $R_{xl}$ . Inset: stress normalized by peak level. (d, e) Visualization of fiber displacements via color scaling at the end of simulations. (f) Matrix deformation and (g) the uniformity of the deformation, depending on  $r$  and  $R_{xl}$ . Note that  $R_{xl}^*$  is the reference value of  $R_{xl}$ .



### ***Cross-linker unbinding enhances stress relaxation and reduces stress propagation and matrix deformation***

In our previous studies, we suggested that the force-dependent unbinding of cross-linkers contributes to matrix remodeling induced by cells [251]. In this study, we assumed that cross-linker unbinding behaves as a slip bond whose unbinding rate increases when it supports a larger force. We varied two parameters in Bell's law that governs the slip-bond behavior: zero-force unbinding rate constant ( $k_{ub,0}$ ) and force sensitivity ( $x_{ub}$ ).

Peak stress did not vary depending on  $k_{ub,0}$  because there was not enough time for many cross-linkers to unbind before the stress quickly reached the peak level (Figs. A.5a-c). However, with higher  $k_{ub,0}$ , stress relaxed faster and propagated over a shorter distance. Interestingly, without any unbinding ( $k_{ub,0} = 0$ ), stress still relaxed by more than 50%, which implies that there is an additional way to relax stress in the matrix. We used the strongest contraction strength, so contraction quickly occurred locally around the cell to a large extent at the beginning of simulations, which led to a sharp increase in the stress at  $r \sim 20 \mu\text{m}$ . The stress could originate from elastic and viscous resistances. Given fiber concentration and cross-linking density, the matrix could not sustain such high stress in only an elastic manner even without cross-linker unbinding. Thus, the stress near the membrane decreased over time, reaching plateau level that is what the matrix can sustain for long time. Note that we showed earlier that stress relaxation could be reduced by increasing either fiber concentration or cross-linking density, and that a difference between peak level and plateau level is smaller if the contraction strength is low. Despite this additional way of stress relaxation, the dependence of plateau stress on  $k_{ub,0}$  still indicates that cross-linking unbinding contributes to stress relaxation. With higher  $k_{ub,0}$ , fibers were displaced less, and local deformation were smaller and more anisotropic (Figs. A.5d-g).

An increase in  $x_{ub}$  affected matrix deformation and the generation and transmission of stress in similar ways to an increase in  $k_{ub,0}$ . As  $x_{ub}$  increases, cross-linkers underwent more frequent unbinding events. Therefore, stress relaxed faster and was transmitted over a shorter distance, and local deformation became smaller and more anisotropic.

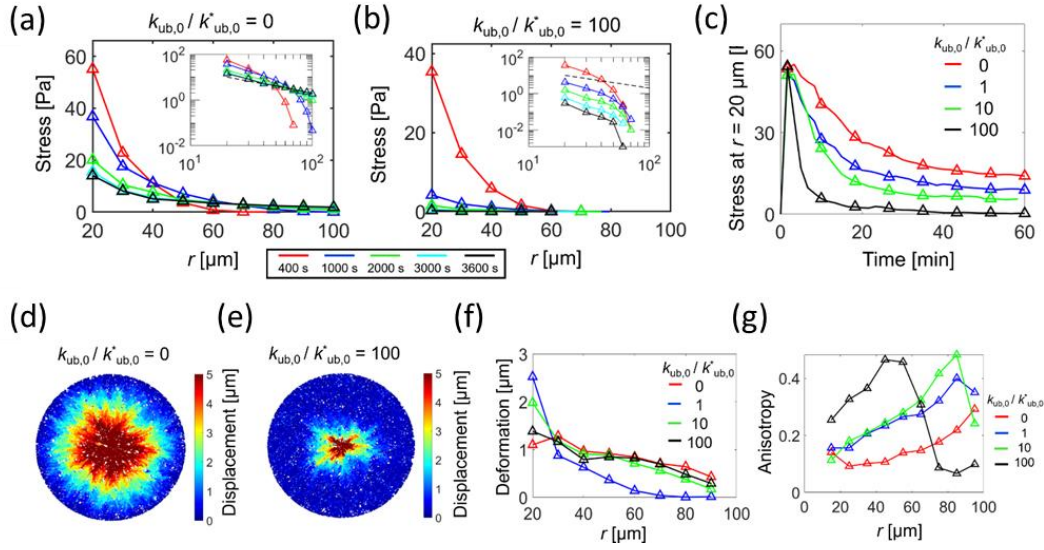


Fig. A.5 Cross-linker unbinding enhances stress relaxation and inhibits uniform and isotropic deformation. The zero-force unbinding rate constant,  $k_{ub,0}$ , was varied. (a, b) Stress exerted on the matrix in radial directions at different time points (legend), depending on a distance from the cell center,  $r$ , with two values of  $k_{ub,0}$ . Insets: the same stress curves in the log-log scale. Dashed lines represent the prediction of  $r^{-1}$ . (c) Time evolution of the stress calculated at  $r = 20 \mu\text{m}$  with four values of  $k_{ub,0}$ . (d, e) Fiber displacements measured at the end of simulations with two values of  $k_{ub,0}$ . (f) Net local matrix deformation and (g) the uniformity of the deformation, depending on  $r$  and  $k_{ub,0}$ . Note that  $k_{ub,0}^*$  is the reference value of  $k_{ub,0}$ .

## B. SEVERING AND MODEL PARAMETER

### *Determination of parameters for the F-actin severing model*

In our previous study, we determined the values of zero-angle severing rate constant ( $k_{s,A}^0$ ) and sensitivity to bending angles ( $\lambda_{s,A}$ ) in Eq. 2.9 by comparing with an *in vitro* experiment. In the experiment, they measured distribution of angles where thermally fluctuating F-actin was spontaneously severed. We ran a simulation with thermally fluctuating F-actins and found the values of  $k_{s,A}^0$  and  $\lambda_{s,A}$  resulting in similar distribution of severing angles. In the simulation, we observed severing angles only up to  $68^\circ$  since frequency of very large bending angles was very small partially due to the discretization of F-actin into cylindrical segments. However, large bending angles above  $68^\circ$  can easily occur if F-actin experiences buckling events in response to external mechanical stimuli or as a result of motor activity. Considering that the local accumulation of stress is known to be a molecular origin of the filament severing, an exponential increase in the severing rate due to an increase in a bending angle seems valid for bending angles above  $68^\circ$ . Note that Eq. 1 allows F-actin without any bending to be severed. However, a severing rate for  $0^\circ$  is negligibly small, so it is not likely that F-actin is severed without bending during simulations or within physiologically relevant time scales.

Table B.1 List of parameters employed in the model. For some of the parameters, references are provided if the parameters were determined based on specific previous studies.

Symbol	Definition	Value
$r_{0,A}$	Length of an actin segment	$1.4 \times 10^{-7}$ [m]
$r_{c,A}$	Diameter of an actin segment	$7.0 \times 10^{-9}$ [m] [252]
$\theta_{0,A}$	Bending angle formed by adjacent actin segments	0 [rad]
$\kappa_{s,A}$	Extensional stiffness of F-actin	$1.69 \times 10^{-2}$ [N/m]
$\kappa_{b,A}^*$	Reference bending stiffness of F-actin	$2.64 \times 10^{-19}$ [N·m] [115]
$r_{0,ACP}$	Length of an ACP arm	$2.35 \times 10^{-8}$ [m] [253]
$r_{c,ACP}$	Diameter of an ACP arm	$1.0 \times 10^{-8}$ [m]
$\theta_{0,ACP}$	Bending angle formed by two ACP arms	0 [rad]
$\kappa_{s,ACP}$	Extensional stiffness of ACP	$2.0 \times 10^{-3}$ [N/m]
$\kappa_{b,ACP}$	Bending stiffness of ACP	$1.04 \times 10^{-19}$ [N·m]
$r_{0,M}$	Length of a motor arm	$1.35 \times 10^{-8}$ [m]
$r_{c,M}$	Diameter of a motor arm	$1.0 \times 10^{-8}$ [m]
$\kappa_{s,M}$	Extensional stiffness of a motor arm	$1.0 \times 10^{-3}$ [N/m]
$k_{20}^*$	Reference ATP-dependent unbinding rate of myosin heads	20 [s <sup>-1</sup> ]
$N_h$	Number of heads represented by a motor arm	4 or 8
$N_a$	Number of arms in a motor	1 or 2
$k_{n,A}$	Nucleation rate of actin	$0.000125 - 1$ [ $\mu\text{M}^{-1}\text{s}^{-1}$ ]
$k_{+,A}$	Polymerization rate of actin at the barbed end	60 [ $\mu\text{M}^{-1}\text{s}^{-1}$ ]
$k_{u,ACP}^{0*}$	Reference zero-force unbinding rate constant of ACP	0.115 [s <sup>-1</sup> ] [117]
$\lambda_{u,ACP}$	Sensitivity of ACP unbinding to applied force	$1.04 \times 10^{-10}$ [m] [117]
$\kappa_r$	Strength of repulsive force	$1.69 \times 10^{-3}$ [N/m]
$\Delta t$	Time step	$1.15 \times 10^{-5}$ [s] or $2.875 \times 10^{-6}$ [s]
$\mu$	Viscosity of surrounding medium	$8.6 \times 10^{-1}$ [kg/m·s]
$k_B T$	Thermal energy	$4.142 \times 10^{-21}$ [J]
$\zeta_M^*$	Reference drag coefficient of a motor	$8.10 \times 10^{-8}$ [kg/s]
$C_A$	Actin concentration	60 [ $\mu\text{M}$ ]
$R_M$	Ratio of motor concentration to $C_A$	0.008 – 0.8
$R_{ACP}$	Ratio of ACP concentration to $C_A$	0 – 0.1
$\langle L_f \rangle$	Average length of F-actins	0.69 – 3.02 [ $\mu\text{m}$ ]

Table B.2 List of parameter values used for adopting “parallel cluster model” [118, 119]. Note that we used slightly different values for  $F_0$ ,  $d$ , and  $k_m$  from those in the literature.

Symbol	Definition	Value
$k_{01}$	A rate from unbound to weakly bound state	40 [s <sup>-1</sup> ]
$k_{10}$	A rate from weakly bound to unbound state	2 [s <sup>-1</sup> ]
$k_{12}$	A rate from weakly bound to post-power-stroke state	1000 [s <sup>-1</sup> ]
$k_{21}$	A rate from post-power-stroke to weakly bound state	1000 [s <sup>-1</sup> ]
$k_{20}$	A rate from post-power-stroke to unbound state	5-640 [s <sup>-1</sup> ]
$F_0$	Constant for force dependence	$5.04 \times 10^{-12}$ [N]
$E_{pp}$	Free energy bias toward the post-power-stroke state	$-60 \times 10^{-21}$ [J]
$E_{ext}$	External energy contribution	0 [J]
$d$	Step size	$7 \times 10^{-9}$ [m]
$k_m$	Spring constant of the neck linkers	$1.0 \times 10^{-3}$ [N/m] ( $= \kappa_{s,M}$ )

Table B.3 Stochastic and deterministic event parameters in addition to dynamic instability

Notation	Value	Description
$\theta_Z$	40° [98, 104]	Entrainment angle upon collision
$f_{nuc}$	100 [ $\mu\text{m}^{-2} \text{min}^{-1}$ ]	Nucleation rate
$p_{cat}$	0.2 - 0.8	Probability of catastrophe upon collision
$p_{zip}$	1.0 [104]	Probability of zippering
$\delta$	0 – 50 nm	Spacing between bundled MTs
$p_g$	0.65 [16]	Phase of growth %
$p_p$	0.10 [16]	Phase of pause %
$p_s$	0.25 [16]	Phase of shorten %
$\delta_{seg}$	0.1 [ $\mu\text{m}$ ]	MT segment length

## C. EFFECT OF ENCOUNTER BASED CATASTROPHE

### *Stress anisotropy and collision-induced catastrophe coregulate microtubule ordering*

We showed earlier that microtubule can form bundles without stress anisotropy. Such stress-free alignment is mainly attributed to collision-induced catastrophe. Although zippering, the alignment of two microtubules after collision with small contact angles, can help microtubules align, the reorientation of microtubule bundles can be facilitated only by the collision-induced catastrophe. Microtubules can turn over more frequently in the presence of the collision-induced catastrophe, which helps microtubules align with each other. The collision-induced catastrophe could be more or less important if there is stress anisotropy that can also lead to microtubule ordering. To understand how these two different mechanisms facilitate microtubule alignment in a cooperative or antagonistic manner, we ran simulations with different probabilities for the collision-induced catastrophe and different levels of stress anisotropy. The probability of the catastrophe ( $P_{\text{cat}}$ ) was varied between 0.2 and 0.8 to be consistent with the previous literature [91]. In cases with a stress-dependent variation in three parameters – the polymerization rate, the depolymerization rate, and the rescue frequency – the low probability of collision-induced catastrophe resulted in nearly randomly oriented microtubules due to substantial increases in cross-over events. As  $P_{\text{cat}}$  increases, the dependence of microtubule ordering on the degree of stress anisotropy became stronger in cases with all the three parameters (polymerization, depolymerization rates and rescue frequency) varied by stress (Fig. C.1). The cases with the polymerization rate and the rescue frequency as a stress-sensitive parameter showed almost equal dependence of microtubule ordering on  $P_{\text{cat}}$  and stress anisotropy level (Figs. C.1a, d). By contrast, the case with the depolymerization rate varied by stress showed that microtubule ordering is more sensitivity to  $P_{\text{cat}}$  than stress anisotropy (Fig. C.1b). At small stress anisotropy level, the order parameter in the case with the depolymerization rate varied by stress significantly increased when  $P_{\text{cat}}$  was changed from 0.6 to 0.8. However, it remained at very small values when  $P_{\text{cat}}$  was below this range, unlike order parameter in the cases of the polymerization rate and the rescue frequency varied by stress showing a consistent increase with an increase in  $P_{\text{cat}}$ .

In the case with the catastrophe frequency modulated by stress, microtubules were aligned well even at low  $P_{\text{cat}}$  when intermediate stress anisotropy level was imposed (Fig. C.1c). Both

stochastic catastrophe and collision-induced catastrophe contribute to the turnover of microtubules. By decreasing the stochastic catastrophe frequency, microtubule ordering became less dependent on stress anisotropy level since the turnover of microtubules are predominantly regulated by collision-induced catastrophe. By contrast, when stochastic catastrophe events take place frequently, microtubule ordering depends more on stress anisotropy because microtubule turnover became more dependent on free catastrophe (Figs. C.1e-f).

In sum, the combinative effects of stress anisotropy and collision-induced catastrophe result in microtubule alignment and ordering. Stress anisotropy directly impacts the efficiency of the alignment of microtubules with the direction of principal stress, whereas collision-induced catastrophe controls the portion and turnover of misaligned microtubules.

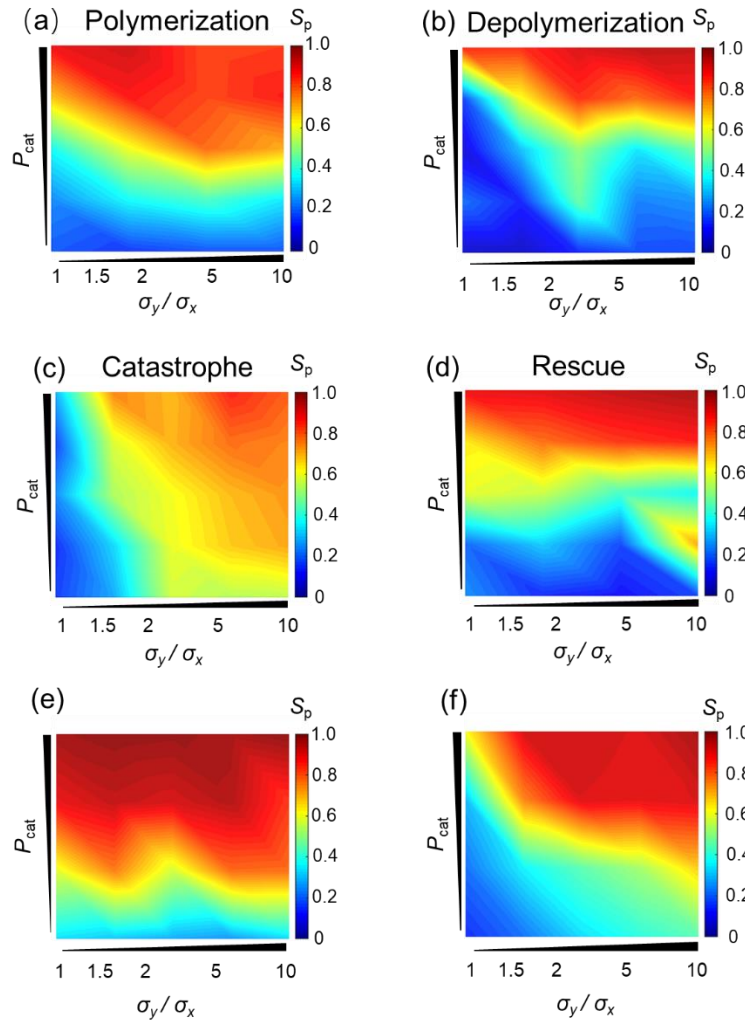


Fig. C.1 Steady state order parameter as a function of stress anisotropy and probability of encounter-based catastrophe.

## REFERENCES

1. Goryachev, A.B., and Mallo, M. (2020). Patterning and Morphogenesis From Cells to Organisms: Progress, Common Principles and New Challenges. *Frontiers in cell and developmental biology* 8, 602483.
2. Howard, J., Grill, S.W., and Bois, J.S. (2011). Turing's next steps: the mechanochemical basis of morphogenesis. *Nature reviews. Molecular cell biology* 12, 392-398.
3. Cosgrove, D.J. (2018). Diffuse Growth of Plant Cell Walls. *Plant physiology* 176, 16-27.
4. Conlon, I., and Raff, M. (1999). Size control in animal development. *Cell* 96, 235-244.
5. Foard, D.E., and Haber, A.H. (1961). Anatomic Studies of Gamma-Irradiated Wheat Growing without Cell Division. *American Journal of Botany* 48, 438-446.
6. Tzur, A., Kafri, R., LeBleu, V.S., Lahav, G., and Kirschner, M.W. (2009). Cell growth and size homeostasis in proliferating animal cells. *Science* 325, 167-171.
7. Yang, C., Czech, L., Gerboth, S., Kojima, S., Scita, G., and Svitkina, T. (2007). Novel roles of formin mDia2 in lamellipodia and filopodia formation in motile cells. *PLoS biology* 5, e317.
8. Belteton, S.A., Li, W., Yanagisawa, M., Hatam, F.A., Quinn, M.I., Szymanski, M.K., Marley, M.W., Turner, J.A., and Szymanski, D.B. (2021). Real-time conversion of tissue-scale mechanical forces into an interdigitated growth pattern. *Nature plants* 7, 826-841.
9. Yanagisawa, M., Desyatova, A.S., Belteton, S.A., Mallery, E.L., Turner, J.A., and Szymanski, D.B. (2015). Patterning mechanisms of cytoskeletal and cell wall systems during leaf trichome morphogenesis. *Nature plants* 1, 15014.
10. Leptin, M. (2005). Gastrulation movements: the logic and the nuts and bolts. *Developmental cell* 8, 305-320.
11. Xu, K., Zhong, G., and Zhuang, X. (2013). Actin, spectrin, and associated proteins form a periodic cytoskeletal structure in axons. *Science* 339, 452-456.
12. Esau, K. (1977). Anatomy of seed plants.
13. Salbreux, G., Charras, G., and Paluch, E. (2012). Actin cortex mechanics and cellular morphogenesis. *Trends in cell biology* 22, 536-545.
14. Clark, A.G., Wartlick, O., Salbreux, G., and Paluch, E.K. (2014). Stresses at the cell surface during animal cell morphogenesis. *Current biology : CB* 24, R484-494.



15. Gunning, P.W., Ghoshdastider, U., Whitaker, S., Popp, D., and Robinson, R.C. (2015). The evolution of compositionally and functionally distinct actin filaments. *Journal of cell science* 128, 2009-2019.
16. Shaw, S.L., Kamyar, R., and Ehrhardt, D.W. (2003). Sustained microtubule treadmilling in Arabidopsis cortical arrays. *Science* 300, 1715-1718.
17. Wasteney, G.O., and Ambrose, J.C. (2009). Spatial organization of plant cortical microtubules: close encounters of the 2D kind. *Trends in cell biology* 19, 62-71.
18. Yamauchi, T., Abe, F., Tsutsumi, N., and Nakazono, M. (2019). Root Cortex Provides a Venue for Gas-Space Formation and Is Essential for Plant Adaptation to Waterlogging. *Frontiers in plant science* 10, 259.
19. Kelkar, M., Bohec, P., and Charras, G. (2020). Mechanics of the cellular actin cortex: From signalling to shape change. *Current opinion in cell biology* 66, 69-78.
20. Yanagida, T., Nakase, M., Nishiyama, K., and Oosawa, F. (1984). Direct observation of motion of single F-actin filaments in the presence of myosin. *Nature* 307, 58-60.
21. Wang, J.A., Meyer, T.F., and Rudel, T. (2008). Cytoskeleton and motor proteins are required for the transcytosis of Neisseria gonorrhoeae through polarized epithelial cells. *International journal of medical microbiology : IJMM* 298, 209-221.
22. Gittes, F., Mickey, B., Nettleton, J., and Howard, J. (1993). Flexural rigidity of microtubules and actin filaments measured from thermal fluctuations in shape. *The Journal of cell biology* 120, 923-934.
23. Wiggins, C.H., Riveline, D., Ott, A., and Goldstein, R.E. (1998). Trapping and wiggling: elastohydrodynamics of driven microfilaments. *Biophysical journal* 74, 1043-1060.
24. Tsuda, Y., Yasutake, H., Ishijima, A., and Yanagida, T. (1996). Torsional rigidity of single actin filaments and actin-actin bond breaking force under torsion measured directly by in vitro micromanipulation. *Proceedings of the National Academy of Sciences of the United States of America* 93, 12937-12942.
25. Esue, O., Tseng, Y., and Wirtz, D. (2009). Alpha-actinin and filamin cooperatively enhance the stiffness of actin filament networks. *PloS one* 4, e4411.
26. Schneider, R., and Persson, S. (2015). Connecting two arrays: the emerging role of actin-microtubule cross-linking motor proteins. *Frontiers in plant science* 6, 415.
27. Kikumoto, M., Kurachi, M., Tosa, V., and Tashiro, H. (2006). Flexural rigidity of individual microtubules measured by a buckling force with optical traps. *Biophysical journal* 90, 1687-1696.
28. Mickey, B., and Howard, J. (1995). Rigidity of microtubules is increased by stabilizing agents. *The Journal of cell biology* 130, 909-917.

29. Chelminiak, P., Dixon, J.M., and Tuszynski, J.A. (2010). Torsional elastic deformations of microtubules within continuous sheet model. *The European physical journal. E, Soft matter* 31, 215-227.
30. Torisawa, T., Taniguchi, D., Ishihara, S., and Oiwa, K. (2016). Spontaneous Formation of a Globally Connected Contractile Network in a Microtubule-Motor System. *Biophysical journal* 111, 373-385.
31. C. Probine, M., and D. Preston, R. (1962). Cell growth and the structure and mechanical properties of the wall in internodal cells of *Nitella opaca*: II. Mechanical properties of the walls, Volume 13.
32. Wolf, S., Mravec, J., Greiner, S., Mouille, G., and Hofte, H. (2012). Plant cell wall homeostasis is mediated by brassinosteroid feedback signaling. *Current biology : CB* 22, 1732-1737.
33. Wolf, S., van der Does, D., Ladwig, F., Sticht, C., Kolbeck, A., Schurholz, A.K., Augustin, S., Keinath, N., Rausch, T., Greiner, S., et al. (2014). A receptor-like protein mediates the response to pectin modification by activating brassinosteroid signaling. *Proceedings of the National Academy of Sciences of the United States of America* 111, 15261-15266.
34. ZhiMing, Y., Bo, K., XiaoWei, H., ShaoLei, L., YouHuang, B., WoNa, D., Ming, C., Hyung-Taeg, C., and Ping, W. (2011). Root hair-specific expansins modulate root hair elongation in rice. *The Plant journal : for cell and molecular biology* 66, 725-734.
35. Cosgrove, D.J. (2016). Catalysts of plant cell wall loosening. *F1000Research* 5.
36. Chan, J., Eder, M., Crowell, E.F., Hampson, J., Calder, G., and Lloyd, C. (2011). Microtubules and CESA tracks at the inner epidermal wall align independently of those on the outer wall of light-grown *Arabidopsis* hypocotyls. *Journal of cell science* 124, 1088-1094.
37. Paredez, A.R., Somerville, C.R., and Ehrhardt, D.W. (2006). Visualization of cellulose synthase demonstrates functional association with microtubules. *Science* 312, 1491-1495.
38. Somerville, C. (2006). Cellulose synthesis in higher plants. *Annual review of cell and developmental biology* 22, 53-78.
39. Gutierrez, R., Lindeboom, J.J., Paredez, A.R., Emons, A.M., and Ehrhardt, D.W. (2009). *Arabidopsis* cortical microtubules position cellulose synthase delivery to the plasma membrane and interact with cellulose synthase trafficking compartments. *Nature cell biology* 11, 797-806.
40. Paredez, A.R., Persson, S., Ehrhardt, D.W., and Somerville, C.R. (2008). Genetic evidence that cellulose synthase activity influences microtubule cortical array organization. *Plant physiology* 147, 1723-1734.

41. Xiao, C., Zhang, T., Zheng, Y., Cosgrove, D.J., and Anderson, C.T. (2016). Xyloglucan Deficiency Disrupts Microtubule Stability and Cellulose Biosynthesis in Arabidopsis, Altering Cell Growth and Morphogenesis. *Plant physiology* 170, 234-249.
42. Hamant, O., Heisler, M.G., Jonsson, H., Krupinski, P., Uyttewaal, M., Bokov, P., Corson, F., Sahlin, P., Boudaoud, A., Meyerowitz, E.M., et al. (2008). Developmental patterning by mechanical signals in Arabidopsis. *Science* 322, 1650-1655.
43. Lindeboom, J.J., Nakamura, M., Hibbel, A., Shundyak, K., Gutierrez, R., Ketelaar, T., Emons, A.M., Mulder, B.M., Kirik, V., and Ehrhardt, D.W. (2013). A mechanism for reorientation of cortical microtubule arrays driven by microtubule severing. *Science* 342, 1245533.
44. Benoit, B., and Pous, C. (2019). Microtubule reorientation in the blue spotlight: Cutting and CLASping at dynamic hot spots. *The Journal of cell biology* 218, 8-9.
45. Sambade, A., Pratap, A., Buschmann, H., Morris, R.J., and Lloyd, C. (2012). The influence of light on microtubule dynamics and alignment in the Arabidopsis hypocotyl. *The Plant cell* 24, 192-201.
46. Kesten, C., Menna, A., and Sanchez-Rodriguez, C. (2017). Regulation of cellulose synthesis in response to stress. *Current opinion in plant biology* 40, 106-113.
47. Chan, J., Crowell, E., Eder, M., Calder, G., Bunnewell, S., Findlay, K., Vernhettes, S., Hofte, H., and Lloyd, C. (2010). The rotation of cellulose synthase trajectories is microtubule dependent and influences the texture of epidermal cell walls in Arabidopsis hypocotyls. *Journal of cell science* 123, 3490-3495.
48. Cosgrove, D.J. (2005). Growth of the plant cell wall. *Nature reviews. Molecular cell biology* 6, 850-861.
49. Elliott, A., and Shaw, S.L. (2018). Update: Plant Cortical Microtubule Arrays. *Plant physiology* 176, 94-105.
50. Lei, L., Singh, A., Bashline, L., Li, S., Yingling, Y.G., and Gu, Y. (2015). CELLULOSE SYNTHASE INTERACTIVE1 Is Required for Fast Recycling of Cellulose Synthase Complexes to the Plasma Membrane in Arabidopsis. *The Plant cell* 27, 2926-2940.
51. Li, S., Lei, L., Somerville, C.R., and Gu, Y. (2012). Cellulose synthase interactive protein 1 (CS11) links microtubules and cellulose synthase complexes. *Proceedings of the National Academy of Sciences of the United States of America* 109, 185-190.
52. Holmes, K.C., Popp, D., Gebhard, W., and Kabsch, W. (1990). Atomic model of the actin filament. *Nature* 347, 44-49.
53. Bindschadler, M., Osborn, E.A., Dewey, C.F., Jr., and McGrath, J.L. (2004). A mechanistic model of the actin cycle. *Biophysical journal* 86, 2720-2739.

54. Splettstoesser, T., Holmes, K.C., Noe, F., and Smith, J.C. (2011). Structural modeling and molecular dynamics simulation of the actin filament. *Proteins* 79, 2033-2043.
55. Chapin, L.M., Edgar, L.T., Blankman, E., Beckerle, M.C., and Shiu, Y.T. (2014). Mathematical modeling of the dynamic mechanical behavior of neighboring sarcomeres in actin stress fibers. *Cellular and molecular bioengineering* 7, 73-85.
56. Pierleoni, C., Ciccotti, G., and Ryckaert, J.P. (2015). A semi-flexible model prediction for the polymerization force exerted by a living F-actin filament on a fixed wall. *The Journal of chemical physics* 143, 145101.
57. Abhilash, A.S., Zhang, L., Stiefel, J., Purohit, P.K., and Joshi, S.P. (2014). Predictive maps for stochastic nonaffine stiffening and damage in fibrous networks. *Physical review. E, Statistical, nonlinear, and soft matter physics* 89, 022607.
58. Chandran, P.L., and Mofrad, M.R. (2009). Rods-on-string idealization captures semiflexible filament dynamics. *Physical review. E, Statistical, nonlinear, and soft matter physics* 79, 011906.
59. Andrews, S.S. (2014). Methods for modeling cytoskeletal and DNA filaments. *Physical biology* 11, 011001.
60. Fan, J., Saunders, M.G., Haddadian, E.J., Freed, K.F., De La Cruz, E.M., and Voth, G.A. (2013). Molecular origins of cofilin-linked changes in actin filament mechanics. *Journal of molecular biology* 425, 1225-1240.
61. Prochniewicz, E., Pierre, A., McCullough, B.R., Chin, H.F., Cao, W., Saunders, L.P., Thomas, D.D., and De La Cruz, E.M. (2011). Actin filament dynamics in the actomyosin VI complex is regulated allosterically by calcium-calmodulin light chain. *Journal of molecular biology* 413, 584-592.
62. Shimada, Y., Adachi, T., Inoue, Y., and Hojo, M. (2009). Coarse-grained modeling and simulation of actin filament behavior based on Brownian dynamics method. *Molecular & cellular biomechanics : MCB* 6, 161-173.
63. Carlsson, A.E. (2006). Stimulation of actin polymerization by filament severing. *Biophysical journal* 90, 413-422.
64. Wilhelm, J., and Frey, E. (2003). Elasticity of stiff polymer networks. *Physical review letters* 91, 108103.
65. Head, D.A., Levine, A.J., and MacKintosh, F.C. (2003). Distinct regimes of elastic response and deformation modes of cross-linked cytoskeletal and semiflexible polymer networks. *Physical review. E, Statistical, nonlinear, and soft matter physics* 68, 061907.
66. Onck, P.R., Koeman, T., van Dillen, T., and van der Giessen, E. (2005). Alternative explanation of stiffening in cross-linked semiflexible networks. *Physical review letters* 95, 178102.

67. Heussinger, C., Schaefer, B., and Frey, E. (2007). Nonaffine rubber elasticity for stiff polymer networks. *Physical review. E, Statistical, nonlinear, and soft matter physics* 76, 031906.
68. Heussinger, C., and Frey, E. (2006). Floppy modes and nonaffine deformations in random fiber networks. *Physical review letters* 97, 105501.
69. Heussinger, C., and Frey, E. (2007). Role of architecture in the elastic response of semiflexible polymer and fiber networks. *Physical review. E, Statistical, nonlinear, and soft matter physics* 75, 011917.
70. Heussinger, C., and Frey, E. (2007). Force distributions and force chains in random stiff fiber networks. *The European physical journal. E, Soft matter* 24, 47-53.
71. Missel, A.R., Bai, M., Klug, W.S., and Levine, A.J. (2010). Affine-nonaffine transition in networks of nematically ordered semiflexible polymers. *Physical review. E, Statistical, nonlinear, and soft matter physics* 82, 041907.
72. Bischofs, I.B., Klein, F., Lehnert, D., Bastmeyer, M., and Schwarz, U.S. (2008). Filamentous network mechanics and active contractility determine cell and tissue shape. *Biophysical journal* 95, 3488-3496.
73. Bendix, P.M., Koenderink, G.H., Cuvelier, D., Dogic, Z., Koeleman, B.N., Briehner, W.M., Field, C.M., Mahadevan, L., and Weitz, D.A. (2008). A quantitative analysis of contractility in active cytoskeletal protein networks. *Biophysical journal* 94, 3126-3136.
74. Lenz, M. (2014). Geometrical Origins of Contractility in Disordered Actomyosin Networks. *Physical Review X* 4, 041002.
75. Wang, S., and Wolynes, P.G. (2012). Active contractility in actomyosin networks. *Proceedings of the National Academy of Sciences of the United States of America* 109, 6446-6451.
76. Huisman, E.M., van Dillen, T., Onck, P.R., and Van der Giessen, E. (2007). Three-dimensional cross-linked F-actin networks: relation between network architecture and mechanical behavior. *Physical review letters* 99, 208103.
77. Huisman, E.M., Storm, C., and Barkema, G.T. (2010). Frequency-dependent stiffening of semiflexible networks: a dynamical nonaffine to affine transition. *Physical review. E, Statistical, nonlinear, and soft matter physics* 82, 061902.
78. Huisman, E.M., Storm, C., and Barkema, G.T. (2008). Monte Carlo study of multiply crosslinked semiflexible polymer networks. *Physical review. E, Statistical, nonlinear, and soft matter physics* 78, 051801.
79. Inoue, Y., Deji, T., Shimada, Y., Hojo, M., and Adachi, T. (2010). Simulations of dynamics of actin filaments by remodeling them in shear flows. *Computers in biology and medicine* 40, 876-882.

80. Kim, T., Hwang, W., Lee, H., and Kamm, R.D. (2009). Computational analysis of viscoelastic properties of crosslinked actin networks. *PLoS computational biology* 5, e1000439.
81. Kim, T., Hwang, W., and Kamm, R.D. (2011). Dynamic role of cross-linking proteins in actin rheology. *Biophysical journal* 101, 1597-1603.
82. Mak, M., Zaman, M.H., Kamm, R.D., and Kim, T. (2016). Interplay of active processes modulates tension and drives phase transition in self-renewing, motor-driven cytoskeletal networks. *Nature communications* 7, 10323.
83. Kim, T. (2015). Determinants of contractile forces generated in disorganized actomyosin bundles. *Biomechanics and modeling in mechanobiology* 14, 345-355.
84. Borau, C., Kim, T., Bidone, T., Garcia-Aznar, J.M., and Kamm, R.D. (2012). Dynamic mechanisms of cell rigidity sensing: insights from a computational model of actomyosin networks. *PloS one* 7, e49174.
85. Tian, J., and Kong, Z. (2019). The Role of the Augmin Complex in Establishing Microtubule Arrays. *Journal of experimental botany*.
86. Shi, X.Q., and Ma, Y.Q. (2010). Understanding phase behavior of plant cell cortex microtubule organization. *Proceedings of the National Academy of Sciences of the United States of America* 107, 11709-11714.
87. Dixit, R., and Cyr, R. (2004). The cortical microtubule array: from dynamics to organization. *The Plant cell* 16, 2546-2552.
88. Tulin, A., McClerklin, S., Huang, Y., and Dixit, R. (2012). Single-molecule analysis of the microtubule cross-linking protein MAP65-1 reveals a molecular mechanism for contact-angle-dependent microtubule bundling. *Biophysical journal* 102, 802-809.
89. Baulin, V.A., Marques, C.M., and Thalmann, F. (2007). Collision induced spatial organization of microtubules. *Biophysical chemistry* 128, 231-244.
90. Allard, J.F., Ambrose, J.C., Wasteneys, G.O., and Cytrynbaum, E.N. (2010). A mechanochemical model explains interactions between cortical microtubules in plants. *Biophysical journal* 99, 1082-1090.
91. Allard, J.F., Wasteneys, G.O., and Cytrynbaum, E.N. (2010). Mechanisms of self-organization of cortical microtubules in plants revealed by computational simulations. *Molecular biology of the cell* 21, 278-286.
92. Mace, A., and Wang, W. (2015). Modelling the role of catastrophe, crossover and katanin-mediated severing in the self-organisation of plant cortical microtubules. *IET systems biology* 9, 277-284.

93. Deinum, E.E., Tindemans, S.H., Lindeboom, J.J., and Mulder, B.M. (2017). How selective severing by katanin promotes order in the plant cortical microtubule array. *Proceedings of the National Academy of Sciences of the United States of America* 114, 6942-6947.
94. Deinum, E.E., Tindemans, S.H., and Mulder, B.M. (2011). Taking directions: the role of microtubule-bound nucleation in the self-organization of the plant cortical array. *Physical biology* 8, 056002.
95. Chan, J., Sambade, A., Calder, G., and Lloyd, C. (2009). Arabidopsis cortical microtubules are initiated along, as well as branching from, existing microtubules. *The Plant cell* 21, 2298-2306.
96. Atkinson, S., Kirik, A., and Kirik, V. (2014). Microtubule array reorientation in response to hormones does not involve changes in microtubule nucleation modes at the periclinal cell surface. *Journal of experimental botany* 65, 5867-5875.
97. Ambrose, C., Allard, J.F., Cytrynbaum, E.N., and Wasteneys, G.O. (2011). A CLASP-modulated cell edge barrier mechanism drives cell-wide cortical microtubule organization in Arabidopsis. *Nature communications* 2, 430.
98. Ambrose, J.C., and Wasteneys, G.O. (2008). CLASP modulates microtubule-cortex interaction during self-organization of acentrosomal microtubules. *Molecular biology of the cell* 19, 4730-4737.
99. Chakraborty, B., Willemsen, V., de Zeeuw, T., Liao, C.Y., Weijers, D., Mulder, B., and Scheres, B. (2018). A Plausible Microtubule-Based Mechanism for Cell Division Orientation in Plant Embryogenesis. *Current biology : CB* 28, 3031-3043 e3032.
100. Mirabet, V., Krupinski, P., Hamant, O., Meyerowitz, E.M., Jonsson, H., and Boudaoud, A. (2018). The self-organization of plant microtubules inside the cell volume yields their cortical localization, stable alignment, and sensitivity to external cues. *PLoS computational biology* 14, e1006011.
101. Armour, W.J., Barton, D.A., Law, A.M., and Overall, R.L. (2015). Differential Growth in Periclinal and Anticlinal Walls during Lobe Formation in Arabidopsis Cotyledon Pavement Cells. *The Plant cell* 27, 2484-2500.
102. Belteton, S.A., Sawchuk, M.G., Donohoe, B.S., Scarpella, E., and Szymanski, D.B. (2018). Reassessing the Roles of PIN Proteins and Anticlinal Microtubules during Pavement Cell Morphogenesis. *Plant physiology* 176, 432-449.
103. Zhang, C., Halsey, L.E., and Szymanski, D.B. (2011). The development and geometry of shape change in Arabidopsis thaliana cotyledon pavement cells. *BMC plant biology* 11, 27.
104. Dixit, R., and Cyr, R. (2004). Encounters between dynamic cortical microtubules promote ordering of the cortical array through angle-dependent modifications of microtubule behavior. *The Plant cell* 16, 3274-3284.

105. Chakraborty, B., Blilou, I., Scheres, B., and Mulder, B.M. (2018). A computational framework for cortical microtubule dynamics in realistically shaped plant cells. *PLoS computational biology* 14, e1005959.
106. Durand-Smet, P., Spelman, T.A., Meyerowitz, E.M., and Jonsson, H. (2020). Cytoskeletal organization in isolated plant cells under geometry control. *Proceedings of the National Academy of Sciences of the United States of America* 117, 17399-17408.
107. Colin, L., Chevallier, A., Tsugawa, S., Gacon, F., Godin, C., Viasnoff, V., Saunders, T.E., and Hamant, O. (2020). Cortical tension overrides geometrical cues to orient microtubules in confined protoplasts. *Proceedings of the National Academy of Sciences of the United States of America* 117, 32731-32738.
108. Lim, C.T., Zhou, E.H., and Quek, S.T. (2006). Mechanical models for living cells--a review. *Journal of biomechanics* 39, 195-216.
109. Murrell, M., Oakes, P.W., Lenz, M., and Gardel, M.L. (2015). Forcing cells into shape: the mechanics of actomyosin contractility. *Nature reviews. Molecular cell biology* 16, 486-498.
110. Nishikawa, M., Naganathan, S.R., Julicher, F., and Grill, S.W. (2017). Controlling contractile instabilities in the actomyosin cortex. *eLife* 6.
111. Murrell, M., Thoresen, T., and Gardel, M. (2014). Reconstitution of contractile actomyosin arrays. *Methods in enzymology* 540, 265-282.
112. Underhill, P., and Doyle, P. (2004). On the coarse-graining of polymers into bead-spring chains. *J. Non-Newtonian Fluid Mech* 122, 3-31.
113. Clift, R., Grace, J.R., and Weber, M.E. (2013). Bubbles, Drops, and Particles, (Dover Publications, Incorporated).
114. Jung, W., Murrell, M.P., and Kim, T. (2016). F-Actin Fragmentation Induces Distinct Mechanisms of Stress Relaxation in the Actin Cytoskeleton. *ACS Macro Letters* 5, 641-645.
115. Isambert, H., Venier, P., Maggs, A.C., Fattoum, A., Kassab, R., Pantaloni, D., and Carlier, M.F. (1995). Flexibility of actin filaments derived from thermal fluctuations. Effect of bound nucleotide, phalloidin, and muscle regulatory proteins. *The Journal of biological chemistry* 270, 11437-11444.
116. Bell, G.I. (1978). Models for the specific adhesion of cells to cells. *Science* 200, 618-627.
117. Ferrer, J.M., Lee, H., Chen, J., Pelz, B., Nakamura, F., Kamm, R.D., and Lang, M.J. (2008). Measuring molecular rupture forces between single actin filaments and actin-binding proteins. *Proceedings of the National Academy of Sciences of the United States of America* 105, 9221-9226.



118. Erdmann, T., Albert, P.J., and Schwarz, U.S. (2013). Stochastic dynamics of small ensembles of non-processive molecular motors: The parallel cluster model. *The Journal of chemical physics* 139, 175104.
119. Erdmann, T., and Schwarz, U.S. (2012). Stochastic force generation by small ensembles of myosin II motors. *Physical review letters* 108, 188101.
120. Soares e Silva, M., Depken, M., Stuhmann, B., Korsten, M., MacKintosh, F.C., and Koenderink, G.H. (2011). Active multistage coarsening of actin networks driven by myosin motors. *Proceedings of the National Academy of Sciences of the United States of America* 108, 9408-9413.
121. Alvarado, J., Sheinman, M., Sharma, A., MacKintosh, F.C., and Koenderink, G.H. (2013). Molecular motors robustly drive active gels to a critically connected state. *Nat Phys* 9, 591-597.
122. Linsmeier, I., Banerjee, S., Oakes, P.W., Jung, W., Kim, T., and Murrell, M.P. (2016). Disordered actomyosin networks are sufficient to produce cooperative and telescopic contractility. *Nature communications* 7, 12615.
123. Murrell, M.P., and Gardel, M.L. (2012). F-actin buckling coordinates contractility and severing in a biomimetic actomyosin cortex. *Proceedings of the National Academy of Sciences of the United States of America* 109, 20820-20825.
124. Lenz, M., Thoresen, T., Gardel, M.L., and Dinner, A.R. (2012). Contractile units in disordered actomyosin bundles arise from F-actin buckling. *Physical review letters* 108, 238107.
125. Ennomani, H., Letort, G., Guerin, C., Martiel, J.L., Cao, W., Nedelec, F., De La Cruz, E.M., Thery, M., and Blanchoin, L. (2016). Architecture and Connectivity Govern Actin Network Contractility. *Current biology : CB* 26, 616-626.
126. Astrom, J.A., Kumar, P.B.S., and Karttunen, M. (2009). Aster formation and rupture transition in semi-flexible fiber networks with mobile cross-linkers. *Soft Matter* 5, 2869-2874.
127. Jung, W., Murrell, M.P., and Kim, T. (2015). F-actin cross-linking enhances the stability of force generation in disordered actomyosin networks. *Computational Particle Mechanics* 2, 317-327.
128. Schmoller, K.M., Niedermayer, T., Zensen, C., Wurm, C., and Bausch, A.R. (2011). Fragmentation is crucial for the steady-state dynamics of actin filaments. *Biophysical journal* 101, 803-808.
129. McCullough, B.R., Grintsevich, E.E., Chen, C.K., Kang, H., Hutchison, A.L., Henn, A., Cao, W., Suarez, C., Martiel, J.L., Blanchoin, L., et al. (2011). Cofilin-linked changes in actin filament flexibility promote severing. *Biophysical journal* 101, 151-159.

130. Foster, P.J., Furthauer, S., Shelley, M.J., and Needleman, D.J. (2015). Active contraction of microtubule networks. *eLife* 4.
131. Belmonte, J.M., and Nedelec, F. (2016). Large-scale microtubule networks contract quite well. *eLife* 5.
132. Jensen, M.H., Watt, J., Hodgkinson, J.L., Gallant, C., Appel, S., El-Mezgueldi, M., Angelini, T.E., Morgan, K.G., Lehman, W., and Moore, J.R. (2012). Effects of basic calponin on the flexural mechanics and stability of F-actin. *Cytoskeleton* 69, 49-58.
133. Goldmann, W.H. (2000). Binding of tropomyosin-troponin to actin increases filament bending stiffness. *Biochemical and biophysical research communications* 276, 1225-1228.
134. (!!! INVALID CITATION !!!).
135. Eggert, U.S., Mitchison, T.J., and Field, C.M. (2006). Animal cytokinesis: from parts list to mechanisms. *Annual review of biochemistry* 75, 543-566.
136. Munro, E., Nance, J., and Priess, J.R. (2004). Cortical flows powered by asymmetrical contraction transport PAR proteins to establish and maintain anterior-posterior polarity in the early *C. elegans* embryo. *Developmental cell* 7, 413-424.
137. Martin, A.C., Kaschube, M., and Wieschaus, E.F. (2009). Pulsed contractions of an actin-myosin network drive apical constriction. *Nature* 457, 495-499.
138. Bois, J.S., Julicher, F., and Grill, S.W. (2011). Pattern formation in active fluids. *Physical review letters* 106, 028103.
139. Reymann, A.C., Boujemaa-Paterski, R., Martiel, J.L., Guerin, C., Cao, W., Chin, H.F., De La Cruz, E.M., Thery, M., and Blanchoin, L. (2012). Actin network architecture can determine myosin motor activity. *Science* 336, 1310-1314.
140. Oelz, D. (2014). A viscous two-phase model for contractile actomyosin bundles. *Journal of mathematical biology* 68, 1653-1676.
141. Li, J., Biel, T., Lomada, P., Yu, Q., and Kim, T. (2017). Buckling-induced F-actin fragmentation modulates the contraction of active cytoskeletal networks. *Soft Matter* 13, 3213-3220.
142. Hiraiwa, T., and Salbreux, G. (2016). Role of turnover in active stress generation in a filament network. *Physical review letters* 116, 188101.
143. McFadden, W.M., McCall, P.M., Gardel, M.L., and Munro, E.M. (2017). Filament turnover tunes both force generation and dissipation to control long-range flows in a model actomyosin cortex. *PLoS computational biology* 13, e1005811.
144. Belmonte, J.M., Leptin, M., and Nedelec, F. (2017). A theory that predicts behaviors of disordered cytoskeletal networks. *Molecular systems biology* 13, 941.

145. Kasza, K.E., Broedersz, C.P., Koenderink, G.H., Lin, Y.C., Messner, W., Millman, E.A., Nakamura, F., Stossel, T.P., Mackintosh, F.C., and Weitz, D.A. (2010). Actin filament length tunes elasticity of flexibly cross-linked actin networks. *Biophysical journal* 99, 1091-1100.
146. Koenderink, G.H., Dogic, Z., Nakamura, F., Bendix, P.M., MacKintosh, F.C., Hartwig, J.H., Stossel, T.P., and Weitz, D.A. (2009). An active biopolymer network controlled by molecular motors. *Proceedings of the National Academy of Sciences of the United States of America* 106, 15192-15197.
147. Chugh, P., Clark, A.G., Smith, M.B., Cassani, D.A.D., Dierkes, K., Ragab, A., Roux, P.P., Charras, G., Salbreux, G., and Paluch, E.K. (2017). Actin cortex architecture regulates cell surface tension. *Nature cell biology* 19, 689-697.
148. Erlenkamper, C., and Kruse, K. (2013). Treadmilling and length distributions of active polar filaments. *The Journal of chemical physics* 139, 164907.
149. Freedman, S.L., Banerjee, S., Hocky, G.M., and Dinner, A.R. (2017). A Versatile Framework for Simulating the Dynamic Mechanical Structure of Cytoskeletal Networks. *Biophysical journal* 113, 448-460.
150. Dierkes, K., Sumi, A., Solon, J., and Salbreux, G. (2014). Spontaneous oscillations of elastic contractile materials with turnover. *Physical review letters* 113, 148102.
151. Machado, P.F., Blanchard, G.B., Duque, J., and Gorfinkiel, N. (2014). Cytoskeletal turnover and Myosin contractility drive cell autonomous oscillations in a model of Drosophila Dorsal Closure. *The European Physical Journal Special Topics* 223, 1391-1402.
152. Hannezo, E., Dong, B., Recho, P., Joanny, J.F., and Hayashi, S. (2015). Cortical instability drives periodic supracellular actin pattern formation in epithelial tubes. *Proceedings of the National Academy of Sciences of the United States of America* 112, 8620-8625.
153. Cooper, J.A. (1987). Effects of cytochalasin and phalloidin on actin. *The Journal of cell biology* 105, 1473-1478.
154. Wakatsuki, T., Schwab, B., Thompson, N.C., and Elson, E.L. (2001). Effects of cytochalasin D and latrunculin B on mechanical properties of cells. *Journal of cell science* 114, 1025-1036.
155. Kraning-Rush, C.M., Carey, S.P., Califano, J.P., Smith, B.N., and Reinhart-King, C.A. (2011). The role of the cytoskeleton in cellular force generation in 2D and 3D environments. *Physical biology* 8, 015009.
156. Mason, F.M., Xie, S., Vasquez, C.G., Tworoger, M., and Martin, A.C. (2016). RhoA GTPase inhibition organizes contraction during epithelial morphogenesis. *The Journal of cell biology* 214, 603-617.

157. Vasquez, C.G., Tworoger, M., and Martin, A.C. (2014). Dynamic myosin phosphorylation regulates contractile pulses and tissue integrity during epithelial morphogenesis. *The Journal of cell biology* 206, 435-450.
158. Tan, T.H., Malik-Garbi, M., Abu-Shah, E., Li, J., Sharma, A., MacKintosh, F.C., Keren, K., Schmidt, C.F., and Fakhri, N. (2018). Self-organized stress patterns drive state transitions in actin cortices. *Science Advances* 4.
159. Baird, M.A., Billington, N., Wang, A., Adelstein, R.S., Sellers, J.R., Fischer, R.S., and Waterman, C.M. (2017). Local pulsatile contractions are an intrinsic property of the myosin 2A motor in the cortical cytoskeleton of adherent cells. *Molecular biology of the cell* 28, 240-251.
160. Vogel, S.K., Petrasek, Z., Heinemann, F., and Schwille, P. (2013). Myosin motors fragment and compact membrane-bound actin filaments. *eLife* 2, e00116.
161. Yin, H.L. (1987). Gelsolin: calcium- and polyphosphoinositide-regulated actin-modulating protein. *BioEssays : news and reviews in molecular, cellular and developmental biology* 7, 176-179.
162. Elam, W.A., Kang, H., and De la Cruz, E.M. (2013). Biophysics of actin filament severing by cofilin. *FEBS letters* 587, 1215-1219.
163. Chen, Q., Courtemanche, N., and Pollard, T.D. (2015). Aip1 promotes actin filament severing by cofilin and regulates constriction of the cytokinetic contractile ring. *The Journal of biological chemistry* 290, 2289-2300.
164. Mikati, M.A., Breitsprecher, D., Jansen, S., Reisler, E., and Goode, B.L. (2015). Coronin enhances actin filament severing by recruiting cofilin to filament sides and altering F-actin conformation. *Journal of molecular biology* 427, 3137-3147.
165. Gardel, M.L., Kasza, K.E., Brangwynne, C.P., Liu, J., and Weitz, D.A. (2008). Chapter 19: Mechanical response of cytoskeletal networks. *Methods in cell biology* 89, 487-519.
166. Schliwa, M., and Woehlke, G. (2003). Molecular motors. *Nature* 422, 759-765.
167. McConnell, R.E., and Tyska, M.J. (2010). Leveraging the membrane - cytoskeleton interface with myosin-1. *Trends in cell biology* 20, 418-426.
168. Spudich, J.A. (2001). The myosin swinging cross-bridge model. *Nature reviews. Molecular cell biology* 2, 387-392.
169. Greenberg, M.J., and Ostap, E.M. (2013). Regulation and control of myosin-I by the motor and light chain-binding domains. *Trends in cell biology* 23, 81-89.
170. Laplante, C., Huang, F., Tebbs, I.R., Bewersdorf, J., and Pollard, T.D. (2016). Molecular organization of cytokinesis nodes and contractile rings by super-resolution fluorescence

- microscopy of live fission yeast. *Proceedings of the National Academy of Sciences of the United States of America* 113, E5876-E5885.
171. Butt, T., Mufti, T., Humayun, A., Rosenthal, P.B., Khan, S., and Molloy, J.E. (2010). Myosin motors drive long range alignment of actin filaments. *The Journal of biological chemistry* 285, 4964-4974.
  172. Schaller, V., and Bausch, A.R. (2013). Topological defects and density fluctuations in collectively moving systems. *Proceedings of the National Academy of Sciences of the United States of America* 110, 4488-4493.
  173. Schaller, V., Weber, C., Frey, E., and Bausch, A.R. (2011). Polar pattern formation: hydrodynamic coupling of driven filaments. *Soft Matter* 7, 3213-3218.
  174. Schaller, V., Weber, C., Semmrich, C., Frey, E., and Bausch, A.R. (2010). Polar patterns of driven filaments. *Nature* 467, 73-77.
  175. Suzuki, R., and Bausch, A.R. (2017). The emergence and transient behaviour of collective motion in active filament systems. *Nature communications* 8, 41.
  176. Suzuki, R., Weber, C.A., Frey, E., and Bausch, A.R. (2015). Polar pattern formation in driven filament systems require non-binary particle collisions. *Nat Phys* 11, 839-843.
  177. Schaller, V., Hammerich, B., and Bausch, A.R. (2012). Active compaction of crosslinked driven filament networks. *The European physical journal. E, Soft matter* 35, 81.
  178. Schaller, V., Schmoller, K.M., Karakose, E., Hammerich, B., Maier, M., and Bausch, A.R. (2013). Crosslinking proteins modulate the self-organization of driven systems. *Soft Matter* 9, 7229-7233.
  179. Schaller, V., Weber, C.A., Hammerich, B., Frey, E., and Bausch, A.R. (2011). Frozen steady states in active systems. *Proceedings of the National Academy of Sciences of the United States of America* 108, 19183-19188.
  180. Mizuno, D., Tardin, C., Schmidt, C.F., and Mackintosh, F.C. (2007). Nonequilibrium mechanics of active cytoskeletal networks. *Science* 315, 370-373.
  181. Alvarado, J., Sheinman, M., Sharma, A., MacKintosh, F.C., and Koenderink, G.H. (2017). Force percolation of contractile active gels. *Soft Matter* 13, 5624-5644.
  182. Bidone, T.C., Jung, W., Maruri, D., Borau, C., Kamm, R.D., and Kim, T. (2017). Morphological transformation and force generation of active cytoskeletal networks. *PLoS computational biology* 13, e1005277.
  183. Guo, B., and Guilford, W.H. (2006). Mechanics of actomyosin bonds in different nucleotide states are tuned to muscle contraction. *Proceedings of the National Academy of Sciences of the United States of America* 103, 9844-9849.

184. Thomas, W.E., Vogel, V., and Sokurenko, E. (2008). Biophysics of catch bonds. *Annual review of biophysics* 37, 399-416.
185. Cuda, G., Pate, E., Cooke, R., and Sellers, J.R. (1997). In vitro actin filament sliding velocities produced by mixtures of different types of myosin. *Biophysical journal* 72, 1767-1779.
186. Umemoto, S., and Sellers, J.R. (1990). Characterization of in vitro motility assays using smooth muscle and cytoplasmic myosins. *The Journal of biological chemistry* 265, 14864-14869.
187. Harris, D.E., and Warshaw, D.M. (1993). Smooth and skeletal muscle myosin both exhibit low duty cycles at zero load in vitro. *The Journal of biological chemistry* 268, 14764-14768.
188. Burnette, D.T., Manley, S., Sengupta, P., Sougrat, R., Davidson, M.W., Kachar, B., and Lippincott-Schwartz, J. (2011). A role for actin arcs in the leading-edge advance of migrating cells. *Nature cell biology* 13, 371-381.
189. Stanhope, K.T., Yadav, V., Santangelo, C.D., and Ross, J.L. (2017). Contractility in an extensile system. *Soft Matter* 13, 4268-4277.
190. Komaba, S., and Coluccio, L.M. (2015). Myosin 1b Regulates Amino Acid Transport by Associating Transporters with the Apical Plasma Membrane of Kidney Cells. *PloS one* 10, e0138012.
191. Wagner, M.C., Blazer-Yost, B.L., Boyd-White, J., Srirangam, A., Pennington, J., and Bennett, S. (2005). Expression of the unconventional myosin Myo1c alters sodium transport in M1 collecting duct cells. *American journal of physiology. Cell physiology* 289, C120-129.
192. Pyrpassopoulos, S., Arpag, G., Feeser, E.A., Shuman, H., Tuzel, E., and Ostap, E.M. (2016). Force generation by membrane-associated myosin-I. *Scientific reports* 6, 25524.
193. Chen, C.L., Wang, Y., Sesaki, H., and Iijima, M. (2012). Myosin I links PIP3 signaling to remodeling of the actin cytoskeleton in chemotaxis. *Science signaling* 5, ra10.
194. Zhang, D., Bidone, T.C., and Vavylonis, D. (2016). ER-PM Contacts Define Actomyosin Kinetics for Proper Contractile Ring Assembly. *Current biology : CB* 26, 647-653.
195. Freedman, S.L., Hocky, G.M., Banerjee, S., and Dinner, A.R. (2018). Nonequilibrium phase diagrams for actomyosin networks. *Soft Matter* 14, 7740-7747.
196. Kohler, S., Schaller, V., and Bausch, A.R. (2011). Collective dynamics of active cytoskeletal networks. *PloS one* 6, e23798.
197. Luby-Phelps, K. (2000). Cytoarchitecture and physical properties of cytoplasm: volume, viscosity, diffusion, intracellular surface area. *International review of cytology* 192, 189-221.

198. Kuimova, M.K., Yahioglu, G., Levitt, J.A., and Suhling, K. (2008). Molecular rotor measures viscosity of live cells via fluorescence lifetime imaging. *Journal of the American Chemical Society* 130, 6672-6673.
199. Honerkamp-Smith, A.R., Woodhouse, F.G., Kantsler, V., and Goldstein, R.E. (2013). Membrane viscosity determined from shear-driven flow in giant vesicles. *Physical review letters* 111, 038103.
200. Ehrhardt, D.W., and Shaw, S.L. (2006). Microtubule dynamics and organization in the plant cortical array. *Annu Rev Plant Biol* 57, 859-875.
201. Alfaro-Aco, R., Thawani, A., and Petry, S. (2020). Biochemical reconstitution of branching microtubule nucleation. *eLife* 9.
202. Murata, T., and Hasebe, M. (2007). Microtubule-dependent microtubule nucleation in plant cells. *Journal of plant research* 120, 73-78.
203. Murata, T., Sonobe, S., Baskin, T.I., Hyodo, S., Hasezawa, S., Nagata, T., Horio, T., and Hasebe, M. (2005). Microtubule-dependent microtubule nucleation based on recruitment of gamma-tubulin in higher plants. *Nature cell biology* 7, 961-968.
204. Mani, N., Wijeratne, S.S., and Subramanian, R. (2021). Micron-scale geometrical features of microtubules as regulators of microtubule organization. *eLife* 10.
205. Glover, B.J. (2000). Differentiation in plant epidermal cells. *Journal of experimental botany* 51, 497-505.
206. Bird, S.M., and Gray, J.E. (2003). Signals from the cuticle affect epidermal cell differentiation. *New Phytologist* 157, 9-23.
207. Tian, J., Han, L., Feng, Z., Wang, G., Liu, W., Ma, Y., Yu, Y., and Kong, Z. (2015). Orchestration of microtubules and the actin cytoskeleton in trichome cell shape determination by a plant-unique kinesin. *eLife* 4.
208. Mathur, J., and Chua, N.H. (2000). Microtubule stabilization leads to growth reorientation in Arabidopsis trichomes. *The Plant cell* 12, 465-477.
209. Chang, J., Xu, Z., Li, M., Yang, M., Qin, H., Yang, J., and Wu, S. (2019). Spatiotemporal cytoskeleton organizations determine morphogenesis of multicellular trichomes in tomato. *PLoS genetics* 15, e1008438.
210. Jacques, E., Verbelen, J.P., and Vissenberg, K. (2013). Mechanical stress in Arabidopsis leaves orients microtubules in a 'continuous' supracellular pattern. *BMC plant biology* 13, 163.
211. Sampathkumar, A., Krupinski, P., Wightman, R., Milani, P., Berquand, A., Boudaoud, A., Hamant, O., Jonsson, H., and Meyerowitz, E.M. (2014). Subcellular and supracellular

- mechanical stress prescribes cytoskeleton behavior in Arabidopsis cotyledon pavement cells. *eLife* 3, e01967.
212. Oda, Y. (2015). Cortical microtubule rearrangements and cell wall patterning. *Frontiers in plant science* 6, 236.
  213. Hamant, O., Inoue, D., Bouchez, D., Dumais, J., and Mjolsness, E. (2019). Are microtubules tension sensors? *Nature communications* 10, 2360.
  214. Louveaux, M., Rochette, S., Beauzamy, L., Boudaoud, A., and Hamant, O. (2016). The impact of mechanical compression on cortical microtubules in Arabidopsis: a quantitative pipeline. *The Plant journal : for cell and molecular biology* 88, 328-342.
  215. Sampathkumar, A. (2020). Mechanical feedback-loop regulation of morphogenesis in plants. *Development* 147.
  216. Landrein, B., and Hamant, O. (2013). How mechanical stress controls microtubule behavior and morphogenesis in plants: history, experiments and revisited theories. *The Plant journal : for cell and molecular biology* 75, 324-338.
  217. Williamson, R.E. (1990). Alignment of Cortical Microtubules by Anisotropic Wall Stresses, Volume 17.
  218. Uyttewaal, M., Burian, A., Alim, K., Landrein, B., Borowska-Wykret, D., Dedieu, A., Peaucelle, A., Ludynia, M., Traas, J., Boudaoud, A., et al. (2012). Mechanical stress acts via katanin to amplify differences in growth rate between adjacent cells in Arabidopsis. *Cell* 149, 439-451.
  219. Burk, D.H., and Ye, Z.H. (2002). Alteration of oriented deposition of cellulose microfibrils by mutation of a katanin-like microtubule-severing protein. *The Plant cell* 14, 2145-2160.
  220. Aumeier, C., Schaedel, L., Gaillard, J., John, K., Blanchoin, L., and Thery, M. (2016). Self-repair promotes microtubule rescue. *Nature cell biology* 18, 1054-1064.
  221. Wang, G., Wang, C., Liu, W., Ma, Y., Dong, L., Tian, J., Yu, Y., and Kong, Z. (2018). Augmin Antagonizes Katanin at Microtubule Crossovers to Control the Dynamic Organization of Plant Cortical Arrays. *Current biology : CB* 28, 1311-1317 e1313.
  222. Liu, Z., Schneider, R., Kesten, C., Zhang, Y., Somssich, M., Zhang, Y., Fernie, A.R., and Persson, S. (2016). Cellulose-Microtubule Uncoupling Proteins Prevent Lateral Displacement of Microtubules during Cellulose Synthesis in Arabidopsis. *Developmental cell* 38, 305-315.
  223. Eren, E.C., Dixit, R., and Gautam, N. (2010). A three-dimensional computer simulation model reveals the mechanisms for self-organization of plant cortical microtubules into oblique arrays. *Molecular biology of the cell* 21, 2674-2684.



224. Hawkins, R.J., Tindemans, S.H., and Mulder, B.M. (2010). Model for the orientational ordering of the plant microtubule cortical array. *Physical review. E, Statistical, nonlinear, and soft matter physics* 82, 011911.
225. Plochocka, A.Z., Ramirez Moreno, M., Davie, A.M., Bulgakova, N.A., and Chumakova, L. (2021). Robustness of the microtubule network self-organization in epithelia. *eLife* 10.
226. Gomez, J.M., Chumakova, L., Bulgakova, N.A., and Brown, N.H. (2016). Microtubule organization is determined by the shape of epithelial cells. *Nature communications* 7, 13172.
227. Baskin, T.I. (2005). Anisotropic expansion of the plant cell wall. *Annual review of cell and developmental biology* 21, 203-222.
228. Crowell, E.F., Timpano, H., Desprez, T., Franssen-Verheijen, T., Emons, A.M., Hofte, H., and Vernhettes, S. (2011). Differential regulation of cellulose orientation at the inner and outer face of epidermal cells in the Arabidopsis hypocotyl. *The Plant cell* 23, 2592-2605.
229. Hervieux, N., Dumond, M., Sapala, A., Routier-Kierzkowska, A.L., Kierzkowski, D., Roeder, A.H., Smith, R.S., Boudaoud, A., and Hamant, O. (2016). A Mechanical Feedback Restricts Sepal Growth and Shape in Arabidopsis. *Current biology : CB*.
230. Zhao, F., Du, F., Oliveri, H., Zhou, L., Ali, O., Chen, W., Feng, S., Wang, Q., Lu, S., Long, M., et al. (2020). Microtubule-Mediated Wall Anisotropy Contributes to Leaf Blade Flattening. *Current biology : CB* 30, 3972-3985 e3976.
231. Oliveri, H., Traas, J., Godin, C., and Ali, O. (2019). Regulation of plant cell wall stiffness by mechanical stress: a mesoscale physical model. *Journal of mathematical biology* 78, 625-653.
232. Chen, J., Kanai, Y., Cowan, N.J., and Hirokawa, N. (1992). Projection domains of MAP2 and tau determine spacings between microtubules in dendrites and axons. *Nature* 360, 674-677.
233. Chan, J., Jensen, C.G., Jensen, L.C., Bush, M., and Lloyd, C.W. (1999). The 65-kDa carrot microtubule-associated protein forms regularly arranged filamentous cross-bridges between microtubules. *Proceedings of the National Academy of Sciences of the United States of America* 96, 14931-14936.
234. Adamowski, M., Li, L., and Friml, J. (2019). Reorientation of Cortical Microtubule Arrays in the Hypocotyl of Arabidopsis thaliana Is Induced by the Cell Growth Process and Independent of Auxin Signaling. *International journal of molecular sciences* 20.
235. Yuan, M., Shaw, P.J., Warn, R.M., and Lloyd, C.W. (1994). Dynamic reorientation of cortical microtubules, from transverse to longitudinal, in living plant cells. *Proceedings of the National Academy of Sciences of the United States of America* 91, 6050-6053.

236. Akiyoshi, B., Sarangapani, K.K., Powers, A.F., Nelson, C.R., Reichow, S.L., Arellano-Santoyo, H., Gonen, T., Ranish, J.A., Asbury, C.L., and Biggins, S. (2010). Tension directly stabilizes reconstituted kinetochore-microtubule attachments. *Nature* 468, 576-579.
237. Endow, S.A., and Marszalek, P.E. (2019). An estimate to the first approximation of microtubule rupture force. *European biophysics journal : EBJ* 48, 569-577.
238. Yanagisawa, M., Alonso, J.M., and Szymanski, D.B. (2018). Microtubule-Dependent Confinement of a Cell Signaling and Actin Polymerization Control Module Regulates Polarized Cell Growth. *Current biology : CB* 28, 2459-2466 e2454.
239. Cleary, A.L., and Hardham, A.R. (1993). Pressure Induced Reorientation of Cortical Microtubules in Epidermal Cells of *Lolium rigidum* Leaves. *Plant and Cell Physiology* 34, 1003-1008.
240. Yagi, N., Matsunaga, S., and Hashimoto, T. (2018). Insights into cortical microtubule nucleation and dynamics in Arabidopsis leaf cells. *Journal of cell science* 131.
241. Nakamura, M., and Hashimoto, T. (2009). A mutation in the Arabidopsis gamma-tubulin-containing complex causes helical growth and abnormal microtubule branching. *Journal of cell science* 122, 2208-2217.
242. Nakamura, M., Ehrhardt, D.W., and Hashimoto, T. (2010). Microtubule and katanin-dependent dynamics of microtubule nucleation complexes in theacentrosomal Arabidopsis cortical array. *Nature cell biology* 12, 1064-1070.
243. Schneider, R., Klooster, K.V., Picard, K.L., van der Gucht, J., Demura, T., Janson, M., Sampathkumar, A., Deinum, E.E., Ketelaar, T., and Persson, S. (2021). Long-term single-cell imaging and simulations of microtubules reveal principles behind wall patterning during proto-xylem development. *Nature communications* 12, 669.
244. Higaki, T., Kutsuna, N., Sano, T., Kondo, N., and Hasezawa, S. (2010). Quantification and cluster analysis of actin cytoskeletal structures in plant cells: role of actin bundling in stomatal movement during diurnal cycles in Arabidopsis guard cells. *The Plant journal : for cell and molecular biology* 61, 156-165.
245. Hejnowicz, Z., Rusin, A., and Rusin, T. (2000). Tensile Tissue Stress Affects the Orientation of Cortical Microtubules in the Epidermis of Sunflower Hypocotyl. *Journal of plant growth regulation* 19, 31-44.
246. Nam, S., Lee, J., Brownfield, D.G., and Chaudhuri, O. (2016). Viscoplasticity Enables Mechanical Remodeling of Matrix by Cells. *Biophysical journal* 111, 2296-2308.
247. Ronceray, P., Broedersz, C.P., and Lenz, M. (2016). Fiber networks amplify active stress. *Proceedings of the National Academy of Sciences of the United States of America* 113, 2827-2832.

- 248. Chieh, H.F., Sun, Y., Liao, J.D., Su, F.C., Zhao, C., Amadio, P.C., and An, K.N. (2010). Effects of cell concentration and collagen concentration on contraction kinetics and mechanical properties in a bone marrow stromal cell-collagen construct. *J Biomed Mater Res A* 93, 1132-1139.
- 249. Burla, F., Dussi, S., Martinez-Torres, C., Tauber, J., van der Gucht, J., and Koenderink, G.H. (2020). Connectivity and plasticity determine collagen network fracture. *Proceedings of the National Academy of Sciences of the United States of America* 117, 8326-8334.
- 250. Gu, L., Shan, T., Ma, Y.X., Tay, F.R., and Niu, L. (2019). Novel Biomedical Applications of Crosslinked Collagen. *Trends Biotechnol* 37, 464-491.
- 251. Nam, S., Hu, K.H., Butte, M.J., and Chaudhuri, O. (2016). Strain-enhanced stress relaxation impacts nonlinear elasticity in collagen gels. *Proceedings of the National Academy of Sciences of the United States of America* 113, 5492-5497.
- 252. Kishino, A., and Yanagida, T. (1988). Force measurements by micromanipulation of a single actin filament by glass needles. *Nature* 334, 74-76.
- 253. Meyer, R.K., and Aebi, U. (1990). Bundling of actin filaments by alpha-actinin depends on its molecular length. *The Journal of cell biology* 110, 2013-2024.

## **VITA**

Jing Li earned his BS degree in Bioengineering with a minor in Mathematics at Washington State University, WA, USA. He joined the Ph.D. program at the Weldon School of Biomedical Engineering in 2015. He is currently a Ph.D. candidate in the Molecular, Cellular, and Tissue Biomechanics lab, supervised by Dr. Tae Yoon Kim. He worked on a multitude of research from actomyosin polarization, remodeling, cell-matrix remodeling, and plant cortex array dynamics. He published seven research journal articles, one review article and one book chapter in Springer, with one paper ready to submit and one under preparation. This gives him a total of 10 publications during his Ph.D. study.

## PUBLICATIONS

### *In preparation*

9. Jing Li, Daniel Szymanski, Taeyoon Kim, “Patterning of cortical microtubule predicted by branched nucleation: a computational investigation,” in preparation

### *In submission*

8. Jing Li, Daniel Szymanski, Taeyoon Kim, “Cell wall stress pattern predicts ordering in the cortical microtubule array by regulating intrinsic dynamics,” in submission.

### *Published*

7. Brandon Slater\*, Jing Li\*, Dhiraj Indana\*, Yihao Xie, Ovijit Chaudhuri, and Taeyoon Kim, "Transient mechanical interactions between cells and viscoelastic extracellular matrix," *Soft Matter* (2021)
6. Wonyeong Jung\*, Jing Li\*, Ovijit Chaudhuri, and Taeyoon Kim, “Nonlinear elastic and inelastic properties of cells,” *Journal of Biomechanical Engineering* (2020) 142(10): 100806
5. Atsushi Matsuda\*, Jing Li\*, Peter Brumm, Taiji Adachi, Yasuhiro Inoue, and Taeyoon Kim, “Mobility of molecular motors regulates contractile behaviors of actin networks,” *Biophysical Journal* (2019) 116: 2161-2171.
4. Jing Li\*, Wonyeong Jung\*, Sungmin Nam, Ovijit Chaudhuri, and Taeyoon Kim, “Ch. 8: Roles of interactions between cells and extracellular matrices for cell migration and matrix remodeling” in *Multi-Scale Extracellular Matrix Mechanics and Mechanobiology* (2019) Springer
3. Jing Li, Taeyoon Kim, and Daniel B. Szymanski, “Multi-scale regulation of cell branching: Modeling morphogenesis,” *Developmental Biology* (2019) 451(1): 40-52
2. Qilin Yu\*, Jing Li\*, Michael P. Murrell, and Taeyoon Kim, “Balance between force generation and relaxation leads to pulsed contraction of actomyosin networks,” *Biophysical Journal* (2018) 115(10): 2003-2013

1. Jing Li\*, Thomas Biel\*, Pranith Lomada\*, Qilin Yu, and Taeyoon Kim, “Buckling-induced F-actin fragmentation modulates the contraction of active cytoskeletal networks,” *Soft Matter* (2017) 13: 3213-3220

\* indicates equal contribution.

Publication listed in chronological order.